



MONASH University

**Efficient Delivery of Oxygen Molecules by Magnetic
Framework Composites**

Leena Melag

Master of Engineering

A thesis submitted for the degree of Doctor of Philosophy at
Monash University in 2020
Department of Chemical Engineering

December 2020

Copyright Notice

© Leena Melag (2020).

I certify that I have made all reasonable efforts to secure copyright permissions for third-party content included in this thesis and have not knowingly added copyright content to my work without the owner's permission.

Abstract

Current oxygen separation technologies are either highly energy-intensive, i.e. cryogenic distillation, or; as is the case of zeolite adsorbents, they are based on the adsorption or isolation of nitrogen to separate oxygen. These size-selective sieving or separations based on the favourable quadrupole interactions of nitrogen with the adsorbates are unable to generate high purity oxygen. The difference in chemical properties between oxygen and nitrogen remains a relatively unexplored mechanism of isolating of oxygen from the air. Metal-organic frameworks (MOFs), with their intriguing network structures, large internal surface areas, and tunable pore properties offer the perfect yet largely unexplored alternative for selective adsorption of oxygen. Oxygen molecules can bind directly to the coordinatively unsaturated open metal sites of MOFs, leading to higher selectivity of oxygen over nitrogen. Whilst MOFs show extraordinary capacity to adsorb gas molecules, their thermally insulating nature and strong binding to stored molecules makes the desorption process quite challenging and energy-intensive. To overcome the high energy requirements associated with the regeneration of MOFs, it is possible to synthesise Magnetic Framework Composites (MFCs) by incorporating magnetic nanoparticles in the MOF framework. This process, known as Magnetic Induction Swing Adsorption (MISA), utilises the penetrative nature of magnetic fields to produce heat from the magnetic nanoparticles embedded within the MOF composites, enabling the adsorbent to be regenerated without the external application of heat or vacuum.

The primary objective of this study was to explore the potential of MOFs as effective adsorbents for oxygen and to use of MISA for its efficient and safe desorption. In the first part, owing to the strong affinity and temperature dependant reversible bindings of oxygen in Co^{2+} complexes, we explored the oxygen adsorption capacities of a cobalt-based Co-MOF-74. We then prepared a series of Co-MOF-74 MFCs using iron oxide magnetic nanoparticles. The highest oxygen uptake by the prepared cobalt-based MFCs was 4.8 mmol g^{-1} at 1.2 bar at 204 K, and when they were exposed to an alternating magnetic field of 17.4 mT, the MFC composite with 12.18 wt. % Fe_3O_4 nanoparticles achieved 100 % desorption of the adsorbed oxygen.

Due to the safety issues associated with handling and storing of a highly reactive gas like oxygen at high-pressure (ca. 140 Bar), for part two we investigated if it is possible to use simpler, stabler MOFs to adsorb and store oxygen at room temperature. Accordingly, using CuBTC (Copper (II) benzene-1,3,5-tricarboxylate), one of the widely used, easily scalable, and most commercially used MOFs, CuBTC/ MgFe_2O_4 composite pellets were prepared. The composite with 3 wt. % MgFe_2O_4 exhibited an oxygen uptake capacity of 0.34 mmol/g at 298 K and when exposed to a magnetic field of 31 mT, attained a temperature rise of $86 \text{ }^\circ\text{C}$ and released 100 % of adsorbed oxygen. Using MISA, the pelletised system can be regenerated within 10 minutes requiring less than 1 MJ/kg.

Building on our previous works on Co-MOF-74, we studied the impact of redox-active $\text{Fe}_x\text{-Co}_{1-x}\text{-MOF-74}$ ($x=0.9,0.5,0.1$) bimetallic MOFs for the room temperature adsorption of oxygen. The incorporation of secondary metal ions to the framework imparts added functionality to the single metal MOF. Fe-MOF-74 has been identified as an adsorbent capable of selective separation of O_2 from the air. The oxygen-binding capacity of Co-MOF-74 is not as high as Fe-MOF-74, it has better structural stability in air. These studies conducted at 298 K show that Fe-MOF-74 displays higher O_2/N_2 selectivity and large one-time oxygen uptake but limited cyclability, whereas Co-MOF-74 displays moderate oxygen adsorption but better cyclability. A series of $\text{Fe}_x\text{Co}_{1-x}\text{-MOF-74}$ frameworks with varying Fe: Co ion ratios were synthesised and the synergistic effect of incorporating the Fe^{2+} and Co^{2+} cations in one framework and how the charge transfers affect the adsorption capacity, cyclability and stability of the MOF is studied.

Further studies and improvements to the oxygen adsorption capabilities of MOFs, coupled with the energy-efficient potential of the MISA process in providing on-demand release of oxygen, would enable a step-wise improvement in the energy use and costs associated with the global oxygen industry.

Publications during Enrolment

1. **Melag, L.;**Sadiq, M. M.;Smith, S. J. D.;Konstas, K.;Suzuki, K. and Hill, M. R.,*Efficient delivery of oxygen via magnetic framework composites*, J. Mater. Chem. A, **2019**, **7**, 3790–3796.
2. **Melag, L.;**Sadiq, M. M.;Konstas, K.;Zadehahmadi, F.;Suzuki, K. and Hill, M. R.,*Performance evaluation of CuBTC composites for room temperature oxygen storage*, RSC Adv., **2020**, **10**, 40960-40968.

Conferences

1. Melag, L.;Sadiq, M. M.;Smith, S. J. D.;Konstas, K.;Suzuki, K. and Hill, M. R.,Efficient delivery of oxygen via magnetic framework composites, 8th annual CEPA conference, 2017, 26 October, Monash University (Oral)
2. Melag, L.;Sadiq, M. M.;Smith, S. J. D.;Konstas, K.;Suzuki, K. and Hill, M. R., Performance Evaluation of CuBTC composites for room temperature oxygen, 8th annual CEPA conference, 2018, 24 October, Monash University (Poster Presentation)
3. Melag, L.;Sadiq, M. M.;Smith, S. J. D.;Konstas, K.;Suzuki, K. and Hill, M. R.,Efficient delivery of oxygen via magnetic framework composites, iEESEP2019 (2th International Conference on Energy-Efficient Separation). 2019, 27-30 November, Melbourne (Oral)

Thesis Including Published Works Declaration

I hereby declare that this thesis contains no material which has been accepted for the award of any other degree or diploma at any university or equivalent institution and that, to the best of my knowledge and belief, this thesis contains no material previously published or written by another person, except where due reference is made in the text of the thesis.

This thesis includes 2 original papers published in peer-reviewed journals and 1 paper is ready for submission represented in **Chapters 4, 5 and 6** respectively. Further details of the general Methods used throughout this dissertation are included in **Chapter 3**. The core theme of this thesis is the selective separation and storage of oxygen using metal-organic frameworks and using magnetic framework composites for efficient desorption. The ideas, development and writing up of all the papers in the thesis were the principal responsibility of myself, the student, working within the *Department of Chemical Engineering (Monash University) and Manufacturing (CSIRO)* under the supervision of A. Prof. Matthew R. Hill, and Prof. Kiyonori Suzuki.

The inclusion of co-authors reflects the fact that the work came from active collaboration between researchers and acknowledges input into team-based research.

In the case of **Chapter 4**, my contribution to the work involved the following: experimental design, materials synthesis and characterization, conducting experiments and analysis of results, and preparation of the manuscript for publication. The project was conceived by my supervisors Matthew R. Hill and Kiyonori Suzuki who were also involved with the experimental design and set-up. The publication manuscript was reviewed by Matthew R. Hill, Stefan J. D. Smith, M. Munir Sadiq, Kristina Konstas and Kiyonori Suzuki before submission.

In the case of **Chapter 5**, my contribution to the work involved the following: project conception, experimental design, materials characterization, conducting experiments and analysis of results, and preparation of the manuscript for publication. M. Munir Sadiq, Kristina Konstas and Matthew R. Hill were involved with the conception of the project and experimental design. Kristina Konstas and Farnaz Zadehahmadi assisted with the synthesis. The publication manuscript was reviewed by Matthew R. Hill, M. Munir Sadiq, Kristina Konstas, Farnaz Zadehahmadi and Kiyonori Suzuki before submission.

In the case of **Chapter 6**, it is ready for submission and my contribution to the work involved the following: project conception, experimental design, materials synthesis and characterization, conducting experiments and analysis of results, and preparation of the manuscript for publication. Matthew R. Hill and Munir Sadiq were involved with the conception of the project. Kristina Konstas assisted with the synthesis. The publication manuscript was reviewed by Matthew R. Hill, M. Munir Sadiq, Kristina Konstas, J.S. Garitaonandia and Kiyonori Suzuki. Instrument operators assisted with the collection of experimental data for XPS (Yvonne Hora, Monash).

Thesis Chapter	Publication Title	Status (published, in press, accepted or returned for revision, submitted)	Nature and ° of student contribution	Co-author name(s) Nature and % of Co-author's contribution*	Co-author(s), Monash student Y/N*
4.2	Efficient delivery of oxygen via magnetic	Published	50 %, preparation of the review manuscript for publication	Input into manuscript Matthew R. Hill – 10% Stefan J. D. Smith– 10% M. Munir Sadiq– 10% Kristina Konstas– 10%	No

	framework composites			Kiyonori Suzuki– 10%	
5.2	Performance evaluation of CuBTC composites for room temperature oxygen storage	Published	70 %, experimental design, materials synthesis and characterization, conducting experiments and analysis of results, and preparation of the manuscript for publication	Matthew R. Hill - 8% M. Munir Sadiq- 6% Kristina Konstas- 7% Farnaz Zadehahmadi- 5% Kiyonori Suzuki- 4%	No

**If no co-authors, leave fields blank*

I ~~have not~~ have not renumbered sections of submitted or published papers in order to generate a consistent presentation within the thesis.

Student name: Leena Melag

Student signature:



Date: 22 December 2020

I hereby certify that the above declaration correctly reflects the nature and extent of the student's and co-authors' contributions to this work. In instances where I am not the responsible author, I have consulted with the responsible author to agree on the respective contributions of the authors.

Main Supervisor name: Matthew R Hill

Main Supervisor signature:

Date:

Acknowledgements

I would like to start by expressing my gratitude towards my supervisors Matthew R Hill & Kiyonori Suzuki for trusting me with this opportunity and for supporting me throughout this academic journey. Your encouragement, words of support and confidence have helped me stay motivated and focused. This year was challenging and unpredictable for all but on a personal level I faced some really tough times and I really appreciate you giving me enough time to cope with it and taking efforts to check on me.

I'm grateful to all my co-authors Kristina Konstas, Stefan J. D. Smith, M. Munir Sadiq and Farnaz Zadehahmadi for their help, inputs, advice and contributions towards the fulfilment of my research. I have learnt a lot from all of you. I would like to thank the staff of Monash Centre for Electron Microscopy, especially Jisheng Ma and Yvonne Vora for all their help. I would like to thank Lilyanne Price, Kim Phu, and Ian Wheeler for their help during my candidature. I'm grateful for the scholarship and financial support provided by Monash University.

A special Thank you to all my friends and colleagues from work, especially Rujing Hou, Marine Michel, Brandon He, Nathan Eden, Hamidreza Mahdavi, Areeb Shehzad, Ehsan Ghasemiestahbanati, Richard Parsons, Kenneth Ugochukwu, Luke Besley, Cara Doherty, Ruhani Singh, Mahdokht Shaibani, Marta Rubio, Micheal Batten, Aaron Thorton and Xavier Mullet. I appreciate and value your friendship and the times spent with you.

I would also like to take this opportunity to thank my very dear friends Juna and Genie for all the walks, talks, coffees and cakes. My life is sweeter because of friends like you.

Lastly, I want to thank my family, especially my mum, my husband and my kids. Thank you for all the love, trust, hope and faith in me. Dad must be so proud and so should we. We did it!!

Table of Contents

Preface-Efficient Delivery of Oxygen Molecules by Magnetic Framework Composites

Copyright Notice	ii
Abstract.....	iii
Publications during Enrolment.....	v
Conferences	vi
Thesis Including Published Works Declaration	vii
Acknowledgements	viii
Abbreviations and Nomenclature.....	xii
Chapter 1: Introduction	1
1.1 Background	2
1.2 Metal-Organic Frameworks	3
1.3 Magnetic Framework Composites (MFCs)	6
1.4 Aim of this thesis.....	7
1.5 Structure of this thesis.....	7
Chapter 2: Literature review	9
2.1 Introduction.....	10
2.2 Background	10
2.2.1 Separation of oxygen from air	10
2.2.2.1 Cryogenic Separation of air	11
2.2.2.2 Non-Cryogenic Separation of air.....	12
2.3 Metal-Organic Frameworks	16
2.3.1 Synthesis of MOFs.....	17
2.3.1.1 Conventional Synthesis of MOFs.....	18
2.3.1.2 Electrochemical synthesis.....	18
2.3.1.3 Microwave synthesis	19
2.3.1.4 Mechanochemical Synthesis.....	19
2.3.1.5 Flow chemistry	20
2.3.2 Synthesis of Bimetallic MOFs.....	21
2.3.3 Applications of MOFs for oxygen capture and storage.....	25
2.4 Magnetic Framework Composites (MFCs)	27
2.5 Desorption of Adsorbed molecules using MISA:	33
Chapter 3: Experimental Methods.....	34
3.1 Introduction.....	35
3.2 Materials.....	35
3.3 Synthesis	35
3.3.1 Magnetic nanoparticles	35
3.3.1.1 Fe ₃ O ₄ nanoparticles.....	35
3.3.1.2 MgFe ₂ O ₄ nanoparticles	35
3.3.2 Metal-Organic Frameworks (MOFs):	36
3.3.2.1 Co-MOF-74.....	36
3.3.2.2 Fe-MOF-74	36
3.3.2.3 MM-MOF-74	36
3.3.2.4 CuBTC MOF	37
3.3.3 Magnetic Framework Composites (MFCs):.....	37
3.3.3.1 Co-MOF-74-Fe ₃ O ₄ composite.....	37
3.3.3.2 Cu-BTC/MgFe ₂ O ₄ composite	38
3.4 Sample Characterisation.....	38
3.3.1 Powder X-ray diffraction (PXRD)	38
3.3.2 Scanning Electron Microscopy (SEM).....	39
3.3.3 Gas Adsorption Properties.....	39
3.3.4 Thermogravimetric Analysis (TGA).....	40

3.3.5	Thermo-magneto gravimetric analysis (TMGA)	40
3.3.6	X-ray photoelectron spectroscopy (XPS)	41
3.3.7	Magnetic property measurement	41
3.3.8	Specific Absorption Rate (SAR)	42
3.3.9	Desorption of Oxygen using MISA.....	42
3.3.10	Regeneration Energy Calculations.....	43
Chapter 4:	Efficient Delivery of Oxygen via Magnetic Framework Composites.....	45
4.1	Introduction.....	46
4.2	Published Work.....	46
4.2.1	Abstract	47
4.2.2	Introduction.....	47
4.2.3	Results and Discussion	50
4.2.4	Triggered Release Experiments:.....	53
4.2.5	Conclusions.....	57
4.3	Supporting Information and Acknowledgements	58
4.4	References.....	59
Chapter 5:	Performance evaluation of CuBTC composites for room temperature Oxygen storage	63
5.1	Introduction.....	64
5.2	Published Work.....	64
5.2.1	Abstract	65
5.2.2	Introduction.....	65
5.2.3	Experimental	67
5.2.3.1	Materials synthesis:.....	67
5.2.3.2	Characterisation of materials:	68
5.2.4	Results and Discussion	69
5.2.5	Conclusions.....	78
5.3	Supporting Information and Acknowledgements	78
5.4	References.....	80
Chapter 6:	The potential of bimetallic FeCo-MOF-74 for Oxygen adsorption at room temperature	85
6.1	Introduction.....	86
6.1.1	Abstract	87
6.1.2	Introduction.....	87
6.1.3	Experimental	89
6.1.3.1	Materials and Methods:.....	89
6.1.3.2	Synthesis.....	89
6.1.3.3	Characterisation.....	90
6.1.4	Results and discussion	91
6.1.4.1	Sample Characterisation	91
6.1.5	Conclusions.....	104
6.2	Supporting Information and Acknowledgements	105
6.3	References.....	106
Chapter 7:	Conclusions and Future Work.....	108
7.1	Summary of Dissertation Findings.....	109
7.2	Recommendation for Future Work	112
Appendix A	114
Appendix B	134
Appendix C	159
Appendix D	164

Abbreviations and Nomenclature

Å	Angstrom
AC	Alternating Current
ANG	Adsorbed Natural Gas
BDC	1-4 benzene-dicarboxylate
BET	Brunauer-Emmett-Teller
CCS	Carbon Capture and Storage
CPT	Composite
CTF	covalent triazine-based framework
DEA	diethanol amine
DFT	Density Functional Theory
DMF	dimethylformamide
DOBDC	2,5-dioxo-1,4 benzenedicarboxylate
DSC	Thermogravimetric - Differential Scanning Calorimeter
EDX	Energy Dispersive X-ray
EMF	Electromotive Force
GCMC	Grand canonical Monte Carlo
ICP	Inductive Coupled Plasma
IR	Infra-red
LISA	Light Induction Swing Adsorption
LNG	Liquefied Natural Gas
MEA	Monoethanolamine
MFC	Magnetic Framework Composites
MI	methyl imidazole
MISA	Magnetic Induction Swing Adsorption
MNP	Magnetic Nanoparticles
MOF	Metal Organic Frameworks
PSA	Pressure Swing Adsorption
PVA	Polyvinyl alcohol
PXRD	Powder X-ray Diffraction
SAR	Specific Absorption Rate
SEM	Scanning Electron Microscopy
TEM	Transmission Electron Microscopy
TMGA	Thermo-magneto Gravimetric Analysis
TPD	Temperature Programmed Desorption
TSA	Temperature Swing Adsorption
UiO-66	Zr(BDC) MOF
UV	Ultraviolet
VSA	Vacuum Swing Adsorption
VSM	Vibrating Sample Magnetometer
XPS	X-ray photoelectron spectroscopy

Chapter 1: Introduction

Chapter 1: Introduction	1
1.1 Background	2
1.2 Metal-Organic Frameworks	3
1.3 Magnetic Framework Composites (MFCs)	6
1.4 Aim of this thesis.....	7
1.5 Structure of this thesis.....	7

1.1 Background

The COVID-19 pandemic has re-emphasised the crucial importance of oxygen therapy treatments in saving lives. The dreaded coronavirus infects healthy human lungs causing respiratory distress, and if timely support of supplemental oxygen is not provided, can result in organ failures or death. Supply of high purity oxygen is usually facilitated using oxygen cylinders or oxygen concentrators. However, with the significant number of cases still soaring across the world, the enormous challenge has been the accessibility to oxygen supplies, especially in developing countries where its demand far exceeds its production and supply. Apart from COVID-19 patients, oxygen therapy is also a survival therapy for patients with respiratory ailments such as COPD (chronic obstructive pulmonary disease)¹⁻⁴. The significance of pure oxygen extends well beyond the healthcare industry. There is an ever-increasing demand of high purity oxygen for oxygen-enhanced combustion processes (OEC)^{5,6}, melting and smelting operations in the steel industry, for fermentation processes in food⁷⁻⁹, biotechnology and pharmaceutical industries¹⁰⁻¹², to aid wastewater treatments^{13,14}, as oxidising agents in chemical and fuel productions¹⁵⁻¹⁷, and as compressed quality breathing oxygen for aeronautical industries.

Most oxygen separation processes are based on the adsorption or isolation of nitrogen from the air to produce oxygen, and owing to their similar molecular sizes ($O_2=3.43 \text{ \AA}$, $N_2=3.68 \text{ \AA}$); this separation becomes complicated and challenging¹⁸. High purity oxygen is economically produced by the cryogenic liquefaction of air and separation of gases at their respective boiling temperatures ($O_2=-183 \text{ }^\circ\text{C}$, $N_2=-196 \text{ }^\circ\text{C}$). However, the complex plant setups and the energy requirements associated with the entire process limits its use to large scale productions only¹⁹. The non-cryogenic adsorption-based techniques using zeolites and carbon molecular sieves selectively retain nitrogen, allowing easy passage of oxygen whereas in membrane-based separations oxygen selectively permeates the membrane²⁰⁻²⁵. These processes are simpler, reversible, low cost and easily scalable for small scale separations, but their structural rigidity, pore heterogeneity, and low oxygen permeabilities impose limitations on the purity of the oxygen produced²⁶. The crucial factors that govern the choice of the oxygen-producing processes are the applications, purity required, the power, cost, capacity, complexity and maintenance of the infrastructure as well as the safety and transport of the bottled gases. With oxygen constituting only 21 vol.% of air, its direct capture from the air is more desirable and economical since smaller amounts of air would need to be processed for its selective separation²⁷⁻²⁹. An adsorption-based separation process relying on the differences in chemical properties of the two gases to isolate them can offer better selectivity and optimise direct capture of oxygen from the air at ambient temperatures.

1.2 Metal-Organic Frameworks

Metal-Organic frameworks are a class of crystalline, highly porous materials formed by the linking of inorganic metal nodes using coordinating ligands to construct a one, two or three-dimensional (1D, 2D and 3D) structure. Post synthesis, the activation or desolvation of the MOF removes any guest molecules (solvent or any chemicals used for the synthesis) from the MOF resulting in a highly porous scaffold-like structure with high internal surface areas and open coordination metal sites. The ordered, chemically stable and physically flexible frameworks have been used in a wide range of applications, such as gas sequestration and storage, catalysis, sensing and drug delivery³⁰⁻³⁴. Furthermore, the MOFs with coordinatively unsaturated metal sites, versatile chemical functionality, unique tunability and good thermal and mechanical stability hold an advantage over the conventional adsorbents and make them promising candidates for selective oxygen adsorption³⁵⁻³⁸.

For large volumetric gas storage capacity, especially at low pressures and at ambient temperature, MOFs should possess high porosity, and internal surface areas, suitable pore geometry and unsaturated open metal sites for strong interactions with the adsorbed gas molecules³⁹⁻⁴¹. The desired reactive properties can readily be incorporated in a MOF by altering its chemical composition and structure, only by changing the metal nodes, or the organic ligands, or both^{33,42,43}. Apart from these MOF precursors, the solvent systems, the metal: ligand ratio in the solvent, the reaction time and temperature, controlling of the inert atmospheres, as well as the activation conditions, also influence the structural, dimensional and functional characteristics of the resultant MOF. Here, Co-MOF-74, FeCo-MOF-74 and CuBTC are the candidate MOFs selected for oxygen adsorption, storage and desorption studies.

Co-MOF-74

The M-MOF-74 (M = Mg, Mn, Fe, Co, Ni, Cu, or Zn) series of isostructural, highly porous MOFs is an extensively studied MOFs with one of the highest reported concentrations of open metal sites accessible for guest-host interactions^{37,44-48}. The structure of $M_2(\text{dobdc})$ consists of one-dimensional metal oxide clusters linked by dobdc^{4-} ($\text{dobdc}^{4-} = 2,5\text{-dioxido-1,4-benzenedicarboxylate}$) ligands forming hexagonal channels that propagate along with the crystallographic *c*-axis. Five oxygen atoms from surrounding linkers octahedrally coordinate each metal in the cluster, and a solvent molecule occupies the sixth position in each octahedron. Desolvation of the MOF leads to removal of the solvent molecule exposing the M^{2+} cation sites for interactions with the gas molecules that results in enhanced selectivity at the site. The transition metal ions have been reported to react readily and form complexes with oxygen that are temperature dependant and bind reversibly. Figure 1.1 shows the building blocks and framework structure of Co-MOF-74. Similar to the oxygen binding in the natural oxygen carriers of haemoglobin and myoglobin, the iron centres of Fe-MOF-74 displays chemisorption, higher O_2/N_2

selectivity and an initial high uptake of oxygen. However, the strong binding between iron and oxygen impairs the reversibility of the adsorption capacity. It affects the chemical stability of the MOF^{47,49-51}. Cobalt complexes with oxygen have been known to have better cyclability and chemical stability than compared to iron^{21,52,53}.

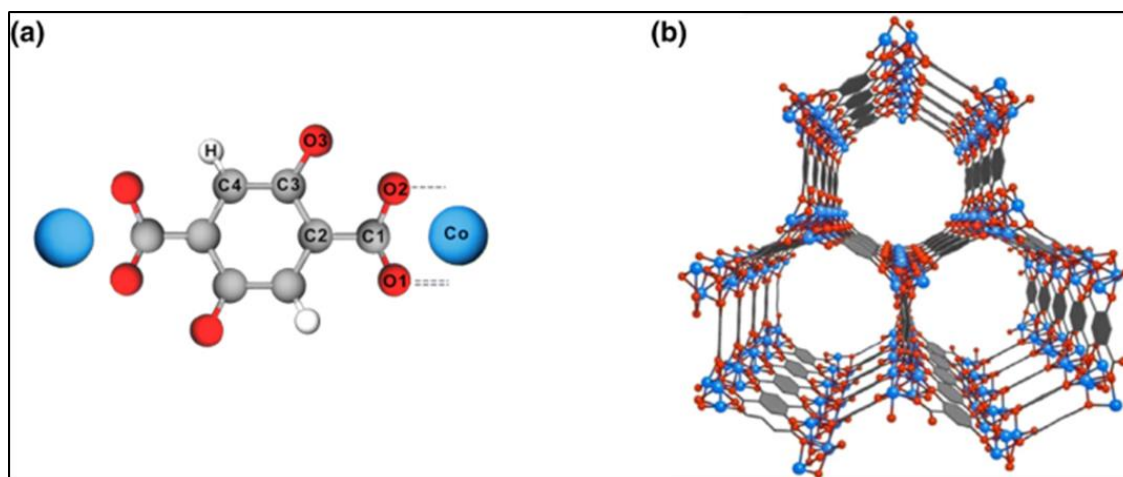


Figure 1.1: a) The Co-MOF-74 building blocks, b) the Co-MOF-74 framework structure. Reproduced from ref. 54 with permission⁵⁴

FeCo-MOF-74

MOFs structures offer the ability to incorporate different metal ions in their framework and exhibit enhanced properties and added functionality compared to the single metal MOFs. Fe-MOFs display higher O₂/N₂ selectivity and large uptake capacity of oxygen but limited cyclability⁴⁹. Compared to Fe-MOFs, the oxygen selectivity or adsorption characteristics of Co-MOFs are moderate⁵⁵, but their regeneration and cyclability properties are superior. It would be advantageous to have these properties for both iron and cobalt metal ions combined in a bimetallic Fe-Co-MOF framework to retain its oxygen adsorption capacity and maintain its chemical stability.

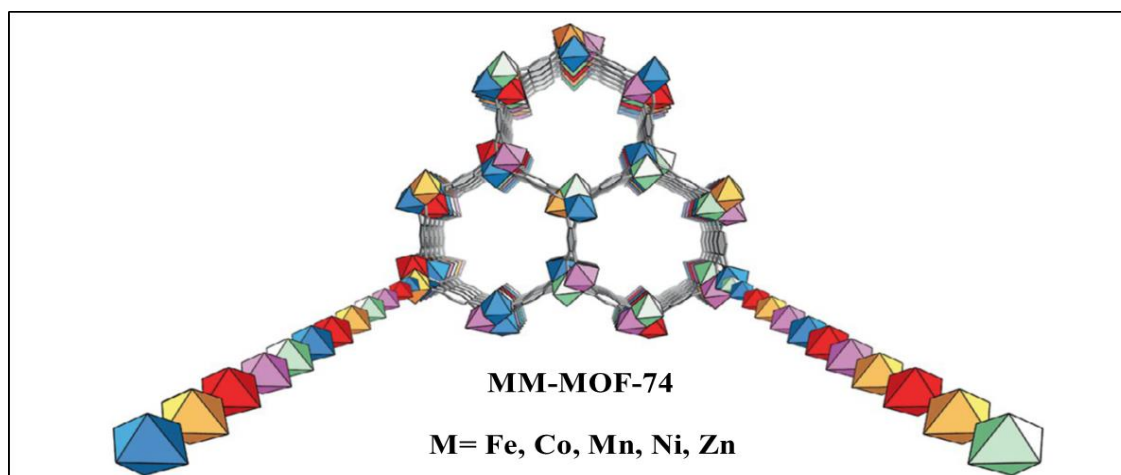


Figure 1.2: Schematic representation of metal variance in multivariate MOF-74 showing the spatial arrangement of metals. Reproduced from ref. 56 with permission. Copyright © 2020, Springer Nature Limited⁵⁶

CuBTC

CuBTC, also known as HKUST-1 or MOF-199, consists of coordinatively unsaturated copper ions, has previously been identified as one of the MOFs for oxygen storage applications^{28,57,58}. It is a very popular Cu(II) framework and as shown in Figure 1.3, the dimeric copper-tetracarboxylic unit of Cu-Cu (2.628 Å) acts as a centre and is connected by four oxygen atoms from the benzenetricarboxylate (BTC) linkers and water molecules. The interconnected Cu(II) paddlewheel unit and tridentate BTC linkers form a three-dimensional octahedral structure with square-shaped main channels of 9×9 Å and tetrahedral units of 5 Å openings that are connected to the main channels by triangular pockets of 3.5 Å. Its ease of synthesis, high surface areas (1500–2000 m²/g), excellent thermal and structural stability make it one of the most commercially used MOFs⁵⁹⁻⁶³.

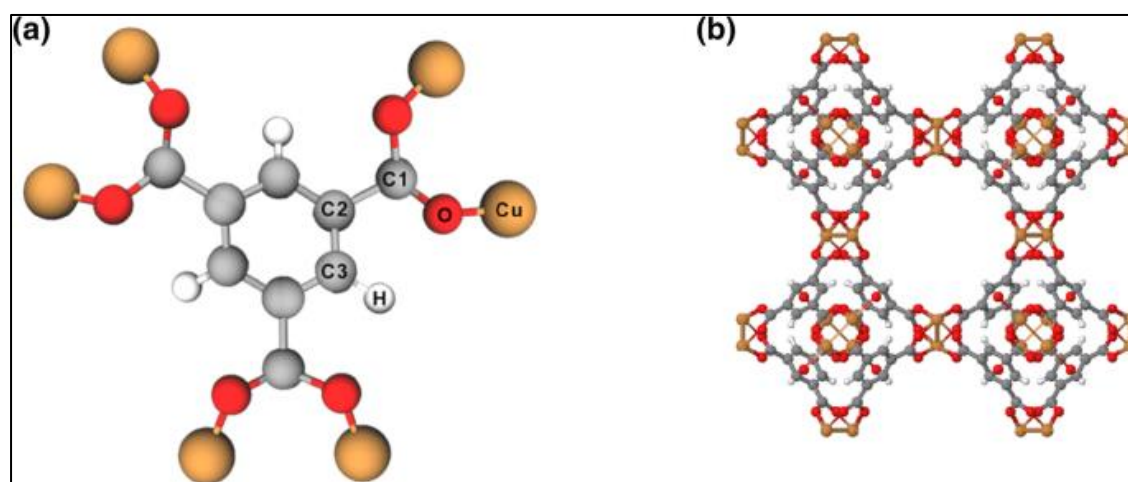


Figure 1.3: CuBTC building blocks, b) the activated CuBTC framework structure. Reproduced from ref. 54 with permission⁵⁴

1.3 Magnetic Framework Composites (MFCs)

In adsorption-based separations, apart from selectivity, adsorption and cyclic capabilities, the deliverable capacity of the adsorbent is equally essential. Whilst MOFs have an unprecedented ability to adsorb gas molecules, their thermally insulating nature and the strong binding of adsorbed molecules to their framework, limits their desorption capabilities. The regeneration processes of Temperature Swing Adsorption (TSA) and Pressure Swing Adsorption (PSA) carried out by changing the temperature or pressure is not energy-efficient and is not always suited for the application of the MOFs^{24,64,65}. The energy penalty associated with the regeneration processes can be overcome by the inclusion of 'stimuli-responsive' functional groups and nanoparticles in the MOF structures such that the stimulation of these groups can trigger the release of the trapped molecules. When magnetic nanoparticles are exposed to an alternating magnetic field, the reversal of the nanoparticles' magnetization causes power losses, resulting in the generation of localised heat. The magnetically induced heating is used to treat cancer cells⁶⁶⁻⁶⁸, for induction cooking, melting metals, heat treatment of alloys, positioning of MOF crystals in solution and for MOF synthesis⁶⁹⁻⁷¹. Based on this principle, Magnetic framework composites (MFCs), shown in Figure 1.4, are fabricated by four methods: 1) Embedding: the magnetic particles and the MOF precursor solution together results in magnetic nanoparticles embedded in MOF frameworks, 2) layer-by-layer: repetitive layer-by-layer growth of MOF crystal around functionalised magnetic particles, 3) Encapsulation: fast growth of the MOF around the functionalised magnetic nanoparticles (4) Mixing: mixing the pre-prepared MOFs and magnetic particles and binding them together using binders. The process of using the intense heat from magnetic nanoparticles to trigger desorption of bound gas molecules from within an adsorbent, efficiently and economically, is known as Magnetic induction swing adsorption (MISA) and has the potential to replace the conventional processes of desorption efficiently and economically^{33,70,72-76}.

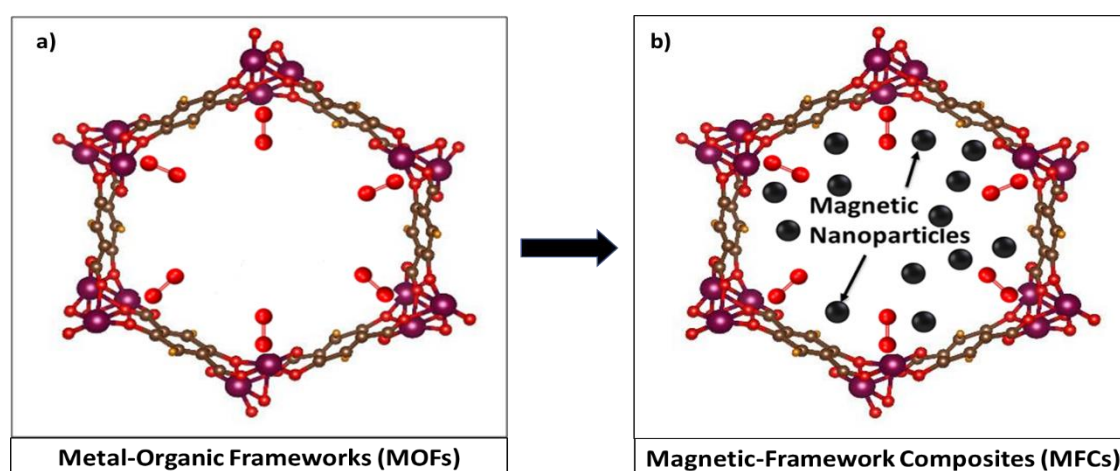


Figure 1.4: Schematic drawing of a) MOF with open metal sites and b) MFCs with magnetic nanoparticles incorporated in the framework of the MOF.

1.4 Aim of this thesis

Current oxygen separation techniques are either highly energy-intensive, i.e. cryogenic separation; or insufficiently selective for oxygen over nitrogen. The primary goal of this study is the separation and storage of oxygen using MOFs, an under-researched potential application of these advanced nanoporous materials. The difference in chemical properties between oxygen and nitrogen remains a relatively unexplored mechanism of isolating oxygen from air. This difference and the redox properties of MOFs can be exploited to achieve higher selectivity and storage for oxygen. To achieve regeneration of MOFs and to overcome the high energy requirements associated with the traditional regeneration processes, functional nanoparticles, like magnetic nanoparticles, can be used. This process known as magnetic induction swing adsorption (MISA), utilises the penetrative nature of magnetic fields to produce heat from the magnetic nanoparticles embedded within the composites, enabling the adsorbent to be regenerated without the external application of heat or vacuum. The objectives of this study are:

1. To identify, synthesise and evaluate oxygen adsorption capacities, stability and reversibility of different MOFs at different temperatures and to regenerate the MOFs using the MISA process.
2. To identify and synthesise simpler, stabler MOFs for oxygen adsorption at ambient temperatures and to calculate the energy requirements to regenerate the MOFs using the magnetic induction swing adsorption (MISA) process.
3. To understand the effect of varying Fe:Co ratios on the adsorptive and stability properties of the bimetallic FeCo-MOF-74.

1.5 Structure of this thesis

The thesis consists of seven chapters.

Chapter 1 gives brief information about the current oxygen separation processes, the prospect of employing MOFs as oxygen selective adsorbents, the suitability of the MOFs considered for the adsorption studies and the role of magnetic framework composites (MFCs) and MISA to facilitate on demand-supply of the oxygen.

Chapter 2 contains in-depth details of the literature reviewed on the current oxygen separation processes, the suitability, limitations, and prospects of MOFs as oxygen adsorbents and the importance of MFCs and MISA process in the efficient delivery of the stored oxygen from the adsorbent.

Chapter 3 consists of details of all the material characterisation techniques used to analyse the MOFs, and MFCs before and after oxygen adsorption and triggered release experiments.

Chapter 4 is the study of Co-MOF-74/ Fe₃O₄ MFCs that were synthesised by embedding varying concentrations of Fe₃O₄ nanoparticles in the Co-MOF-74 structures.

Chapter 5 describes the oxygen adsorption, and desorption capabilities of the CuBTC MOF at room temperature and how Cu-BTC/MgFe₂O₄ composite pellets were prepared and MISA was used to release the adsorbed oxygen quickly and efficiently at 298 K.

Chapter 6 consists of the study on synthesis and characterisation of the bimetallic Fe-Co-MOFs and how the concentration of a secondary metal ion in the framework affects the oxygen adsorption properties, and the chemical stabilities of the MOFs.

Chapter 7 provides a summary of each chapter, along with recommendations for future work.

For ease of reading and understanding, the structure of the thesis is presented in the form of a flow chart in Figure 1.5.

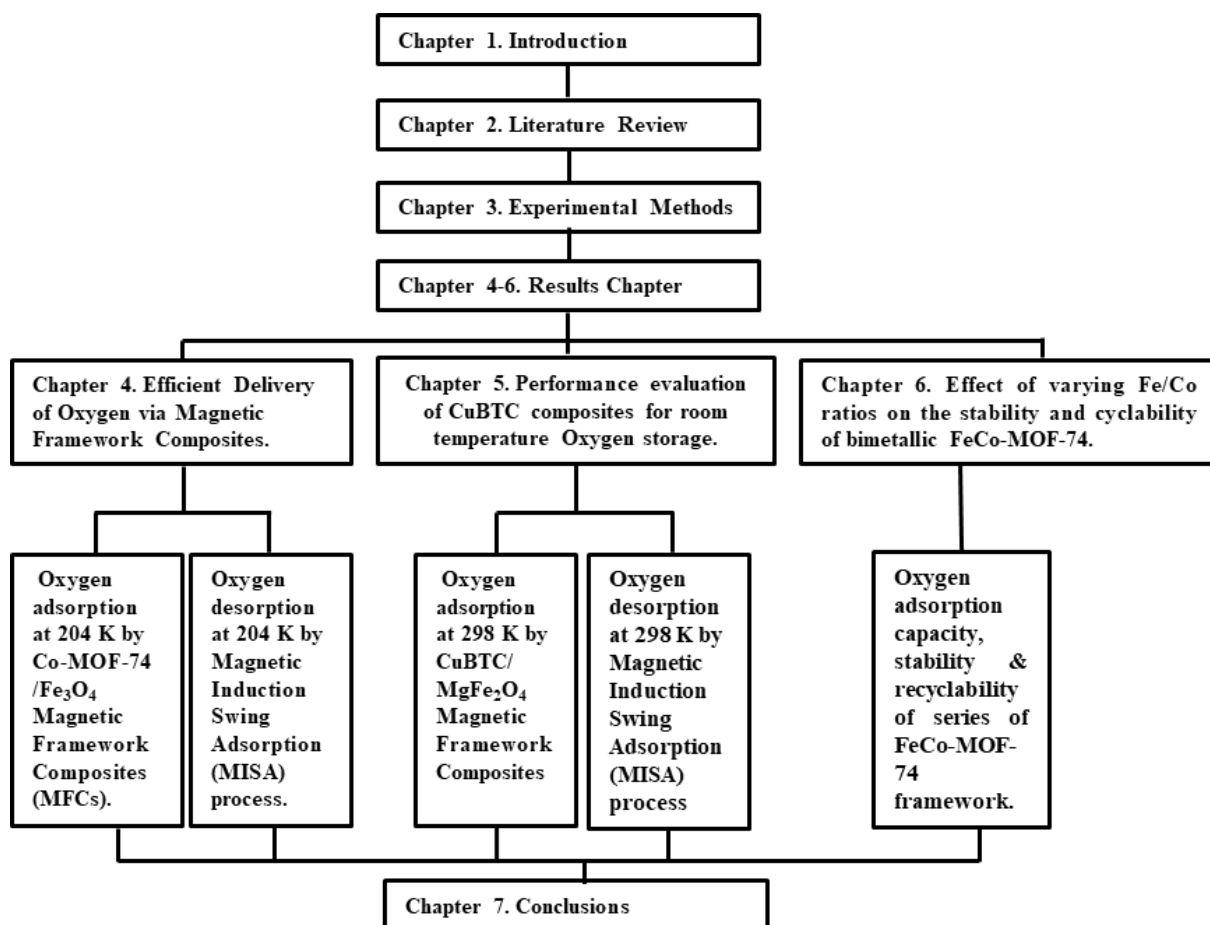


Figure 1.1: Flow chart of the structure of the thesis.

Chapter 2: Literature review

Chapter 2: Literature review	9
2.1 Introduction.....	10
2.2 Background	10
2.2.1 Separation of oxygen from air	10
2.2.2.1 Cryogenic Separation of air	11
2.2.2.2 Non-Cryogenic Separation of air	12
2.3 Metal-Organic Frameworks	16
2.3.1 Synthesis of MOFs	17
2.3.1.1 Conventional Synthesis of MOFs.....	18
2.3.1.2 Electrochemical synthesis.	18
2.3.1.3 Microwave synthesis	19
2.3.1.4 Mechanochemical Synthesis.....	19
2.3.1.5 Flow chemistry	20
2.3.2 Synthesis of Bimetallic MOFs.....	21
2.3.3 Applications of MOFs for oxygen capture and storage.....	25
2.4 Magnetic Framework Composites (MFCs)	27
2.5 Desorption of Adsorbed molecules using MISA:	33

2.1 Introduction

This literature review aims to provide an overview of the current air separation processes used for the production of high purity oxygen, the role of solid adsorbents in these processes and the advantages of using Metal-Organic Frameworks (MOFs) for direct capture and storage of oxygen. The main objective of this research is to explore oxygen capture and storage using MOFs. The coordinatively unsaturated metal centres of MOFs and their tunable chemistry can be utilised to exploit the differences in the chemical properties of oxygen and nitrogen to adsorb oxygen from air selectively^{22,24,28,49-51,77-79}. This section outlines the approach in identifying and synthesising these MOFs. The thermally insulating nature of the MOFs, aided by the strong host-guest interactions in the framework makes the desorption process from MOFs quite challenging and energy-intensive^{74,80-84}. The use of Magnetic Framework Composites (MFCs) in Magnetic Induction Swing adsorption (MISA) processes have shown promising potential in reducing the energy penalty associated with temperature, pressure or vacuum-based desorption techniques^{74,76,85,86}. In MISA, MFCs fabricated using magnetic nanoparticles are exposed to alternating magnetic fields. The responsive heat generated within the MFCs triggers the release of adsorbed molecules^{69,70,87-89}. This literature review presents an overview of oxygen-favouring MOFs, of magnetic nanoparticles, their properties, fabrication and advantages of MFCs and how these promising new adsorbents can be used effectively to improve the adsorption, storage and release of oxygen from the MOF framework.

2.2 Background

2.2.1 Separation of oxygen from air

Air is a mixture of gases, and oxygen is one of its most critical life-sustaining constituents. Nitrogen occupies approximately 78 percent of air, oxygen occupies 21 percent, and 1 percent is occupied by argon, carbon dioxide, trace amounts of other gases and water vapour. With more than 100 million tons consumed annually, production of pure oxygen consists of separating it from the rest of the constituents

of air^{18,90,91}. After separation of oxygen, it is compressed and stored in oxygen concentrators or high-pressure oxygen cylinders. Industrial oxygen is used for a wide range of applications from medical emergencies, to treat chronic obstructive pulmonary diseases (COPD), major traumas, and a wide range of other ailments^{4,92-95}, to facilitate the supply of oxygen to astronauts, mountaineers or scuba divers in oxygen-deficient atmospheres^{93,96-98}; for enhanced combustions and near-zero-emissions in oxyfuel combustion processes^{6,16,99-103}; in industries like melting and smelting in steel and aluminium industries¹⁰⁴⁻¹⁰⁶; for aerobic wastewater treatments^{13,107,108}; as oxidising agents for the production of chemicals and fuels¹⁰⁹⁻¹¹¹; for fermentation processes in the biotechnology and pharmaceutical industries^{10-12,112}. The global industrial growth, the development of oxyfuel combustion technology to curb greenhouse gas emissions and the recent COVID-19 crisis have heightened the importance and requirements of oxygen production. Currently, three separation processes are predominantly used for oxygen production from the air, and they are cryogenic air separation, adsorption-based separation and membrane-based air separation^{113,114}.

2.2.2.1 Cryogenic Separation of air

The traditional process of air liquefaction and distillation in cryogenic air separation units (ASUs) still dominates large scale production of ultra-high purity oxygen (99.8%). These units work on a process developed by Carl Von Linde in 1895 where he developed the process of cryogenic distillation of air to separate nitrogen and oxygen at their respective boiling points of -195.8 °C and -183 °C^{113,115}. Since then, with advancements in machinery and technology, these processes have evolved, and now the process parameters can be varied to produce the required volume of gas with the required level of gas purity. As illustrated in Figure 2.1, the air separation takes place in different stages. Initially, in air pretreatment, the ambient air is filtered, compressed and cooled to remove contaminants such as water vapour, carbon dioxide, and hydrocarbons. The heat exchangers help cool the compressed air to cryogenic temperatures and into the cold box that contains a multi-stage distillation column operating at different pressures. Due to the differences in their boiling points, the liquid mixture at the bottom of the distillation column is enriched with oxygen and can be separated as liquid oxygen, whereas the gas portion flowing upwards is rich in nitrogen and can be separated out from the top of the distillation

column. Since argon has a boiling point of $-185.8\text{ }^{\circ}\text{C}$ which is close to the boiling point of oxygen; a separate distillation column is used for separation of argon. On exit from the cold box, the separated gases are warmed by the heat exchangers and compressed to the final storage pressures. The complex plant set-ups and the energy penalty associated in achieving and maintaining such low temperatures is not economical unless it is to distil large volumes of high purity oxygen^{19,113}.

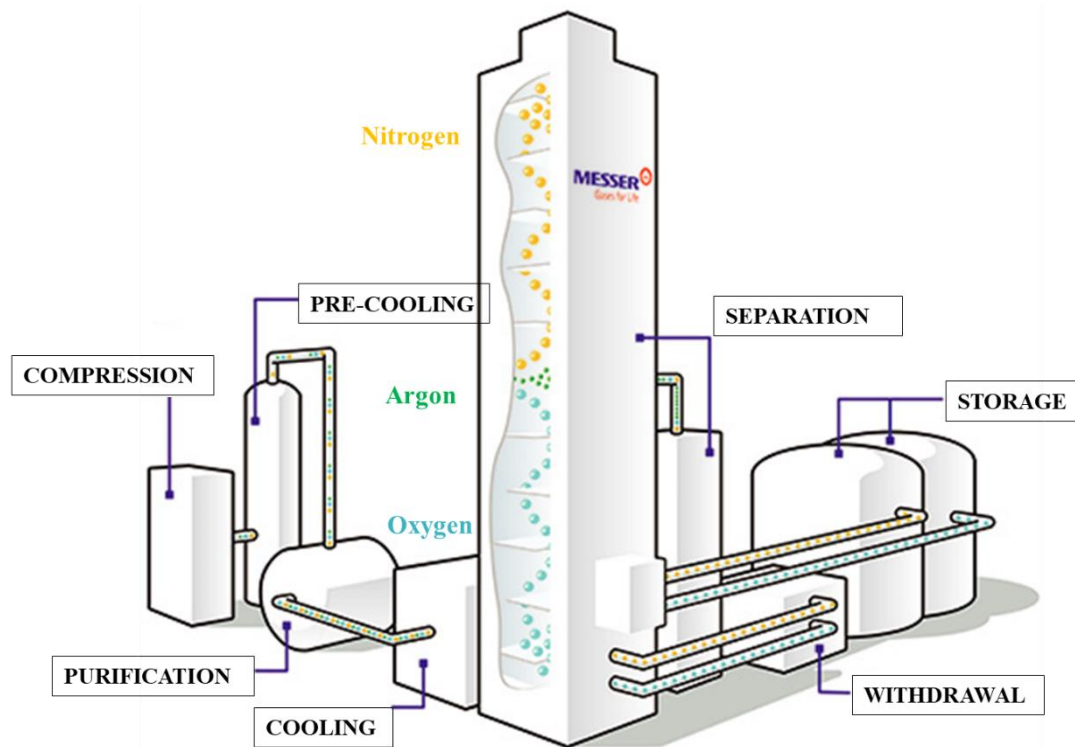


Figure 2.1: Cryogenic distillation to separate air into nitrogen, argon and oxygen © Messer Group¹¹⁶.

2.2.2.2 Non-Cryogenic Separation of air

Adsorption based separation process

Unlike the cryogenic air separation process, the non-cryogenic separations take place at ambient temperatures and pressures. Pressure swing adsorption (PSA) processes using adsorbents like zeolites or carbon molecular sieves are based on the interactions of the gas molecules with the adsorbents under

different pressures conditions¹¹⁷⁻¹²⁰. Different gases have different quadrupole moments and different quadrupole polarizabilities. When a gas mix passes through a bed of zeolite, the gas with a higher quadrupole moment interacts favourable with the non-uniform electric fields of the zeolite pores and gets adsorbed preferentially¹²¹⁻¹²³. In air separation using the PSA process, the air is passed under pressure through a pressure vessel filled with zeolite. Nitrogen from the air, having a higher quadrupole moment than oxygen gets preferentially retained in the pores of the zeolites and allows the passage of an oxygen-rich stream. Argon is not retained by the zeolites as it does not have a quadrupole moment and gets collected with the oxygen-rich stream affecting the purity of the oxygen (95% oxygen). When the zeolite gets saturated with nitrogen, the pressure vessels are switched with a new one. The saturated ones are regenerated by changing the pressures (Pressure swing adsorption), temperature (Temperature swing adsorption) or vacuum (Vacuum swing adsorption)^{113,124,125}. This results in desorption and collection of the adsorbed nitrogen and regeneration of the zeolite for the next cycle of adsorption. When two or more adsorbent vessels are employed, it establishes a continuous production cycle of oxygen, and the oxygen concentrators use this concept to provide oxygen-rich air^{2,93,126}. The separation using carbon molecular sieves is slightly different and is size-selective. It makes use of the narrow pore sizes of carbon molecular sieve and the differences in the kinetic diameters of oxygen and nitrogen to separate them¹²⁷⁻¹³⁰. The narrow pore sizes of carbon molecular sieves (3 to 12 Å) allow faster diffusion of the slightly smaller oxygen (3.43 Å) molecules into the pores of the sieves than nitrogen (3.68 Å) molecules⁷⁸. Thus, the adsorption-based air separation processes are simpler, reversible and scalable for small scale (typically 20–100 tons/day) separations of oxygen that do not require purities higher than 95%. Figure 2.2 shows the various processes involved in an adsorption-based oxygen separation plant. Higher oxygen productivity means mainly large adsorbent bed size meaning high capital investments and higher regeneration costs, so the scalability of the process to a large scale is not economical¹²⁴.

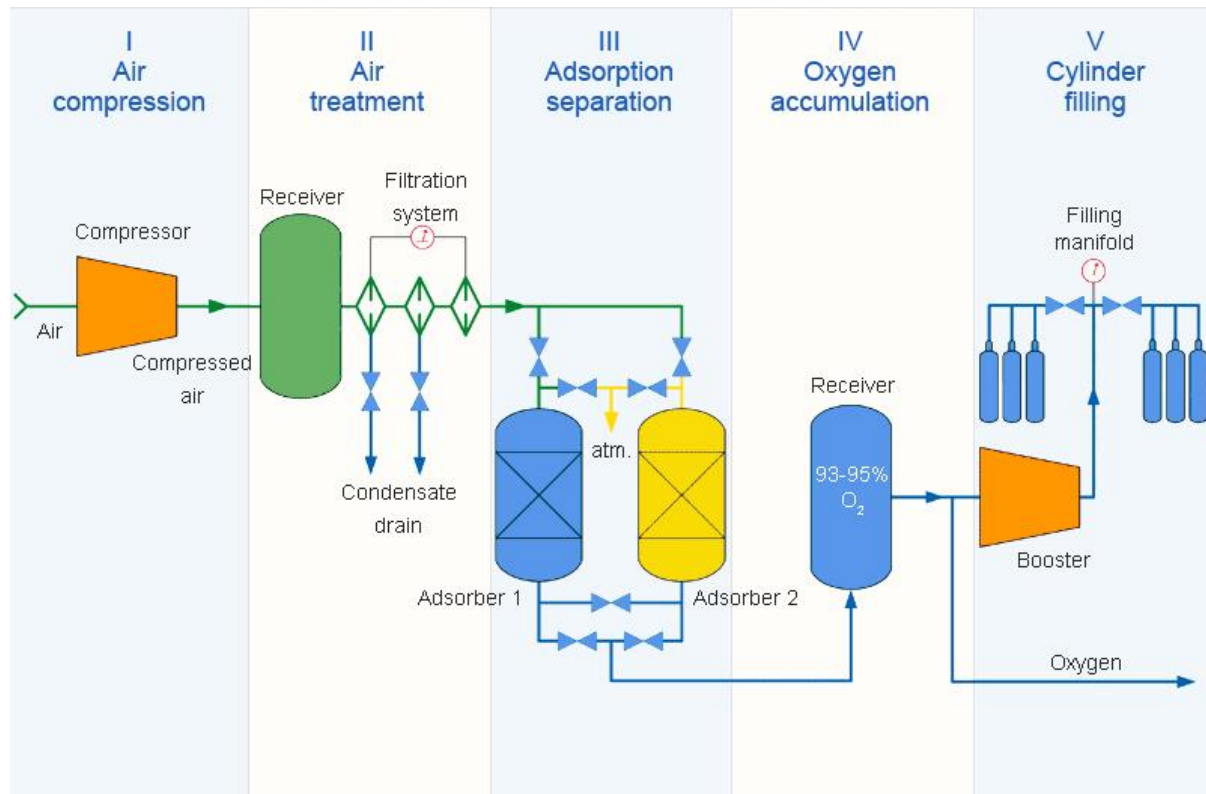


Figure 2.2: Adsorption based oxygen separation plant.¹³¹ © 2004–2020 GRASYS JSC

Membrane-based separation of air

Compared to cryogenic distillation processes and pressure swing adsorption processes, membrane technology is relatively new, more energy-efficient due to low energy consumptions and more economical due to low initial capital investment. Membrane technology makes use of the differences in diffusivity and solubility of oxygen and nitrogen through a membrane that separates high-pressure and low-pressure process streams. Flux and selectivity are membrane properties and determine the success of the membrane-based separation. Flux is the amount of permeate produced per unit area of the membrane surface, and selectivity of the membrane is the ratio of the permeabilities of the gases to be separated^{114,132}. Owing to their smaller size, oxygen molecules permeate through most membrane materials faster than nitrogen or argon. The membrane gas separation is straightforward where cleaned compressed ambient air is drawn through the membrane modules consisting of long hollow fibre membrane strands. While passing through the cylindrical membrane modules, due to high diffusivity oxygen is collected at the high-pressure end. Since carbon dioxide and water are more permeable than

oxygen, they collect along with oxygen-enriched air. Most membrane materials may be able to produce 25-50% oxygen-enriched air while large quantities of the nitrogen get contained at the low-pressure stream of the module. The polymeric membranes exhibit low O_2/N_2 selectivity resulting in limited productivity^{133,134}. Figure 2.3 depicts membrane-based air separations that have been reported to produce 10 - 25 tonnes of oxygen per day with the purity of 25 to 40% ^{135 20,135,136}.

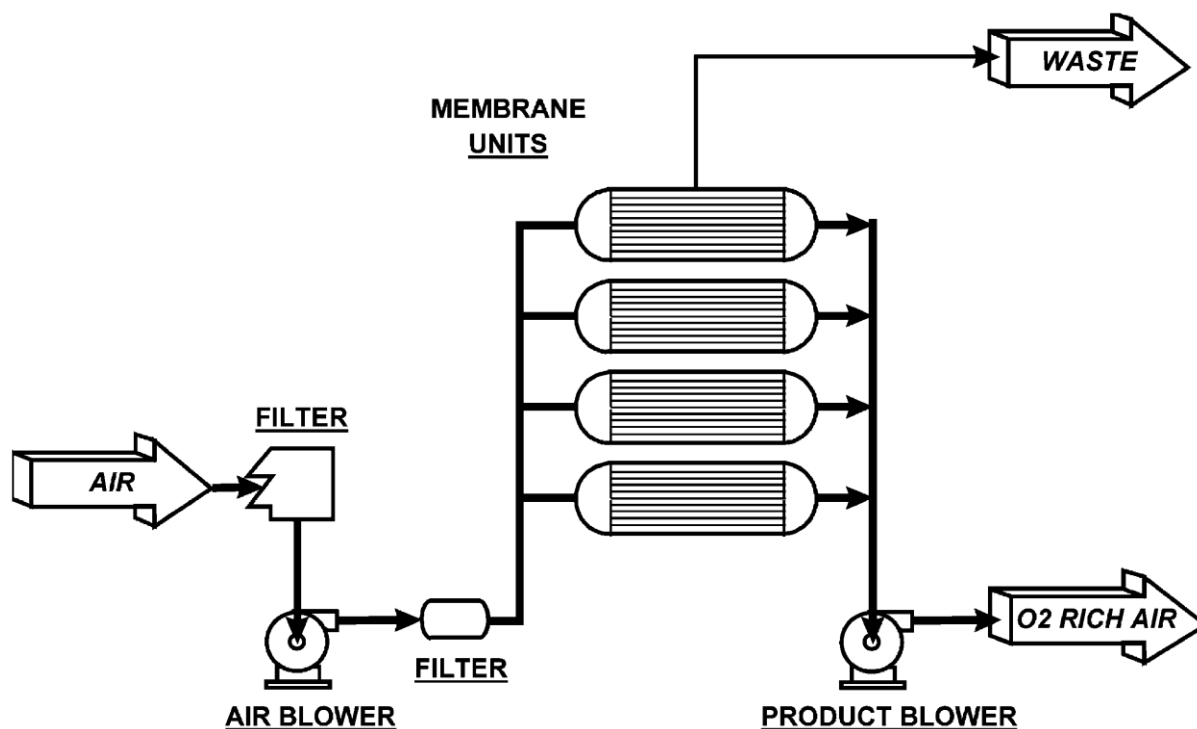


Figure 2.3: Membrane-based oxygen separation plant.¹¹⁴ Copyright © 2001 Published by Elsevier

Ceramic Membrane-based separation of air

The cryogenic distillation process separates oxygen at cryogenic temperatures. The pressure swing adsorption (PSA) based methods using zeolites or the membrane separation process using the polymeric membranes involves the separation of air at ambient temperatures. Oxygen ion-conducting materials, ceramic membranes, increase the oxygen selectivity of the membranes and produce oxygen of high purity at high temperatures of 800-900 °C¹³⁷. Oxygen can be transported from one side of the membrane to the other when a voltage is applied to pure oxygen conducting membranes. In the case of

mixed ionic electronic membranes, due to oxygen partial pressure differences, oxygen can be transported from high oxygen partial pressure side to the low oxygen partial pressure side¹³⁸. The ceramic membranes include Ion Transport Membranes (ITM) and Oxygen Transport Membranes (OTM). The advances in the ceramic membrane-based air separations technology at high temperatures are promising; however, membrane stability and low oxygen permeation rate affect its productivity. Since the ceramic membrane-based separation occurs at high temperatures, the membrane materials need to be stable and maintain high oxygen flux^{137,139-141}.

A summary of the air separation technologies concerning the purity of oxygen produced, the capacity of production, the energy requirements, the energy source and the possible by-products of the process are presented in Table 1.

Table 1. A summary of Air separation technologies.¹⁴²

Technology Development Stage	O₂ Purity [%]	Capacity (single train) [tonne/day]	Possible by-products, their quality	Driving force	Start-up time
Cryogenic Matured	>99	Up to 4000	Nitrogen, Argon, Xenon Very Good	Electricity	Hours/ Days
Adsorption Matured	~95	Up to 300	Nitrogen Bad, ca 11% O ₂	Electricity Heat (70-90 °C)	Minutes/ Hours
Membrane (polymer) Matured	~40	Up to 20	Nitrogen Bad	Electricity	Minutes
Membrane (ITM) R&D* Phase	>99	Laboratory scale	Nitrogen Bad	Electricity Heat (800 °C)	Hours

2.3 Metal-Organic Frameworks

Metal-Organic Frameworks (MOFs), are a unique class of highly crystalline, porous adsorbents constructed using metal nodes and organic linkers resulting in unique modular structures that are flexible, porous and offer high internal surface areas for gas sequestration and storage^{143-148 149-152}. As shown in Figure 2.4, the metal ions are pinned in position by the flexible organic ligands in a repetitive order to form a one, two or a three-dimensional structure called the secondary building units (SBUs)³⁰⁻

^{33,55,70,75,85,153}. The unique properties of MOFs can be readily altered by changing the metal nodes, organic ligands, or both; thus facilitating the targeted design and development of MOFs with tailored pore size, shapes, and host-guest interactions; ^{30,143,147} making them applicable for gas separations, ^{38,85,147,154-156} catalysis, ^{61,157,158} sensings, ^{33,48,50,85,154,155,159-161} and drug delivery. ^{88,162} Their ability to host functional nanoparticles within their structures also imparts added functionalities to their existing versatile properties ^{43,70,71,163}.

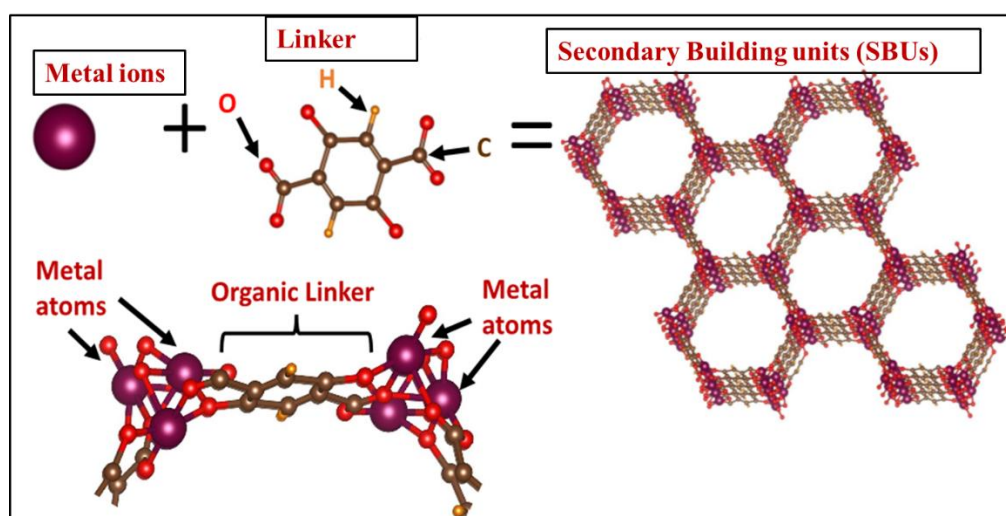


Figure 2.4: Formation of Metal-Organic Frameworks (MOFs).¹⁶⁴

2.3.1 Synthesis of MOFs

MOFs offer a tunable property such that their properties can readily be altered by changing the metal nodes, organic ligands, or both; to design a MOF with the desired pore size that would have favourable host-guest interactions for targeted separation of gases ^{52,71,165,166}. To successfully design and synthesise such a MOF the understanding of metal coordination environments, the functionality of the organic linker, the expected topologies, the sensitivity and stability of the reagents and the intended process parameters should be known. This helps in establishing the synthesis conditions for the successful formation of MOF crystals without the decomposition or degeneration of either of the reagents or formation of a different MOF.

2.3.1.1 Conventional Synthesis of MOFs

Conventional synthesis is the synthesis heated using conventional electric heating.¹⁶⁷ The mode of heating and the reaction temperatures are important process parameters and are distinguished into solvothermal synthesis and nonsolvothermal synthesis. In 1995, Omar Yaghi used solvothermal synthesis to obtain MOFs by mixing solutions of the inorganic salt and the organic linker in a sealed reactor and heating them to a definite temperature to promote the nucleation and growth of the MOF crystals^{143,168}. This solvothermal approach to synthesize MOFs by raising and maintaining the temperature and pressures of the synthesis above the boiling point of the solvents forces the reaction between the otherwise insoluble reagents to form fine MOF particles. The MIL series¹⁶⁹⁻¹⁷², MOF-74^{37,55,173-177}, UiOs^{74,178,179}, and PCNs¹⁸⁰⁻¹⁸² have been synthesised by solvothermal synthesis. The non-solvothermal approach to synthesize MOFs involves heating the reagents to below or at the boiling point of the solvents under ambient pressure, such that a precipitation reaction takes place followed by recrystallization or very slow evaporation of the solvent takes place, MOF-5^{183,184}, MOF-74⁴⁶, MOF-177¹⁸⁵, HKUST-1¹⁸⁶⁻¹⁸⁸ or ZIF-8^{189,190} have been synthesized at room temperature.

2.3.1.2 Electrochemical synthesis.

Electrochemical synthesis is when an electrical current brings about the required chemical changes required for the synthesis of MOFs. The first electrochemical synthesis of MOFs was reported in 2005 by researchers at BASF¹⁹¹. The synthesis was performed using the dissolved linker molecules from the reaction medium, the conducting salt and the metal ions available through anodic dissolution. The set-up of the electrochemically produced HKUST-1 consisted of a solution containing the organic linker, 1,3,5-benzenetricarboxylic acid (H₃BTC) and an electrolyte with a copper plate that acts as the electrode and supplies Cu(II) ions. When current or voltage was applied, the release Cu(II) ions from the copper electrode reacted with the dissolved linker. The surface area of this electrochemically synthesized HKUST-1 was reported to be 1820 m²/g. It was higher than that reported for the solvothermal synthesized HKUST-1 (1550 m²/g)¹⁹². Electrochemical synthesis of MOFs offers the possibility of continuous synthesis of MOFs with higher yield possibility under milder conditions than the usual

solvothermal or microwave syntheses with reduced reaction times of minutes or hours. It gives better control over the synthesis of MOF as it can be controlled by controlling the applied current or voltage to the reaction. The nature of the solvent, its conductivity, nature of the electrolyte also has a strong influence on the anodic dissolution synthesis of MOFs^{168,193-195}. Apart from HKUST-1, the electrochemical synthesis of MOF-5¹⁹⁵⁻¹⁹⁸ and ZIFs^{199,200} has also been investigated.

2.3.1.3 Microwave synthesis

The microwave-assisted synthesis of MOFs is based on the interactions between the electromagnetic waves and the conducting ions in the reagents and precursor solutions, and due to this direct interaction, the heating is faster and more efficient. In conventional methods, the nucleation and growth start at the wall of the reactor. In microwave-assisted synthesis, it starts at the hot spots formed due to non-uniform temperature distribution in the solvent mixture. This results in MOFs with finer particle sizes. Jhung *et al.* performed the microwave-assisted water-based synthesis of the chromium trimesate MIL-100 MOF in the presence of hydrofluoric acid at 220 °C²⁰¹. The resultant yield obtained after 4 h of microwave-assisted synthesis was 44%, which is nearly equal to the 45% yield achieved by the conventional synthesis after 4 days. It was also noted from the spherical nanocrystals of chromium terephthalate MIL-101 that with an increase in irradiation times, the crystal size of MOF increases²⁰². Khan *et al.* synthesized ZIF-8, with larger surface area and large micropore volume using microwave irradiation at 140 °C for 4 hours²⁰³. The studies on microwave synthesis of IRMOF-1, IRMOF-2 and IRMOF-3 show how the power level, the irradiation times, the irradiation temperatures, solvent concentration and substrate composition affected the crystallinity and morphology of the synthesised MOF^{204,205}.

2.3.1.4 Mechanochemical Synthesis

In mechanochemical synthesis, MOFs are formed by the chemical reactions induced due to mechanical breakage of intramolecular bonds during milling or grinding of the solids with the minimal presence of any solvents. The reaction times for these syntheses are short, 10-60 mins. These room-temperature syntheses can be solvent-free and reduce the need for organic solvents making the process environment friendly. Metal oxides have very low solubilities and are not used in conventional solvent-based

synthesis. But in some mechanochemical synthesis, instead of metal salts, metal oxides are used as the starting materials, and water is formed as a side product²⁰⁶⁻²⁰⁸. Liquid-Assisted Grinding (LAG) process involves additions of small amounts of solvents that leads to structure-directing properties and accelerates the synthesis reactions. Ion-and-Liquid Assisted Grinding (ILAG) is a modification to the LAG process; it involves the inclusion of ions and solvents which was found to be efficient for the fabrication of pillared-layered MOFs^{209,210}. As low melting point reagents, solvents or anion containing metal hydrated metal salts are used in these processes; acetic acid is one of the by-products that can easily be removed during thermal activation of the MOFs. Using these techniques, different MOFs has been synthesised and studied. The detailed study on the synthesis of HKUST-1 showed that the LAG process using copper acetate demonstrated higher crystallinity and better adsorption properties than the solvent-free technique²¹⁰⁻²¹³. The choice and ratios of metal salts, linker and solvent and the time and frequency of the grinding process are the key parameters that impact the properties of the MOF.

2.3.1.5 Flow chemistry

Flow chemistry is a technology that involves continuous chemical reaction occurring within flowing reagents in a tube or a pipe rather than in a reaction vessel. This synthesis method has advantages over the batch stationary modes of synthesis because, 1) of the scalability of the process, 2) better control on the process parameters, 3) as the surface to volume reaction is higher than a batch synthesis the heat and mass transfer is better than in batch synthesis and faster synthesis of MOFs is achieved, 4) due to the continuous synthesis less solvent consumption and more batches of synthesis can take place. The process consists of continuous pumping, mixing and flowing of the MOF precursor solutions and the organic ligand through the temperature-controlled flow reactors²¹⁴⁻²¹⁷. Ameloot *et al.* discovered this method of synthesis in 2011 and using the immiscibility properties of oil and water as a template they successfully formed hollow copper trimesate HKUST-1 microcapsules^{218,219}. In 2013, Faustini *et al.* synthesised, copper trimesate HKUST-1, zinc terephthalate MOF-5, zinc aminoterephthalate IRMOF-3 and zirconium terephthalate using oil microdroplets as reactors. In a two-step process, they also successfully incorporated iron oxide particles within core-shell Fe_3O_4 @ZIF-8 composite superstructures²²⁰. Unlike batch synthesis with reaction times of 12-24 h for the synthesis of MOFs,

using flow chemistry, UiO-66 was synthesized in 10 mins at 130 °C in 10 min at a flow rate of 2 mL·min⁻¹ and NOTT-400 at 85 °C in 15 min, at 2 mL·min⁻¹, using a total volume of 30 mL. Based on the modification to the process with respected to the flow reactors, it can be classified into the categories of 1) microfluidic reactors , where the reagents are constrained in the channels of the reactors, 2) plug flow reactors , where the reagents react as they are pumped through the tube and cover the entire length of the reactor and 3) stirred tank reactors, where the MOF precursor are introduced into tank reactors while products are continuously removed. Rubio-Martinez *et al.* proved the versatility of the process by synthesising good quality of the copper trimesate HKUST-1, the zirconium terephthalate UiO-66 and the scandium biphenyl-tetracarboxylate NOTT-400 MOFs, in 5, 10 and 15 minutes, respectively. It was also demonstrated that a bench-top reactor would help achieve a production rate greater than a kilogram per day and a Space-Time Yield (STY) of 4533 kg m⁻³ day⁻¹ ^{168,215,221}. Flow chemistry demonstrates the possibility of laboratory-scale to pilot-scale production of high-quality MOFs.

2.3.2 Synthesis of Bimetallic MOFs

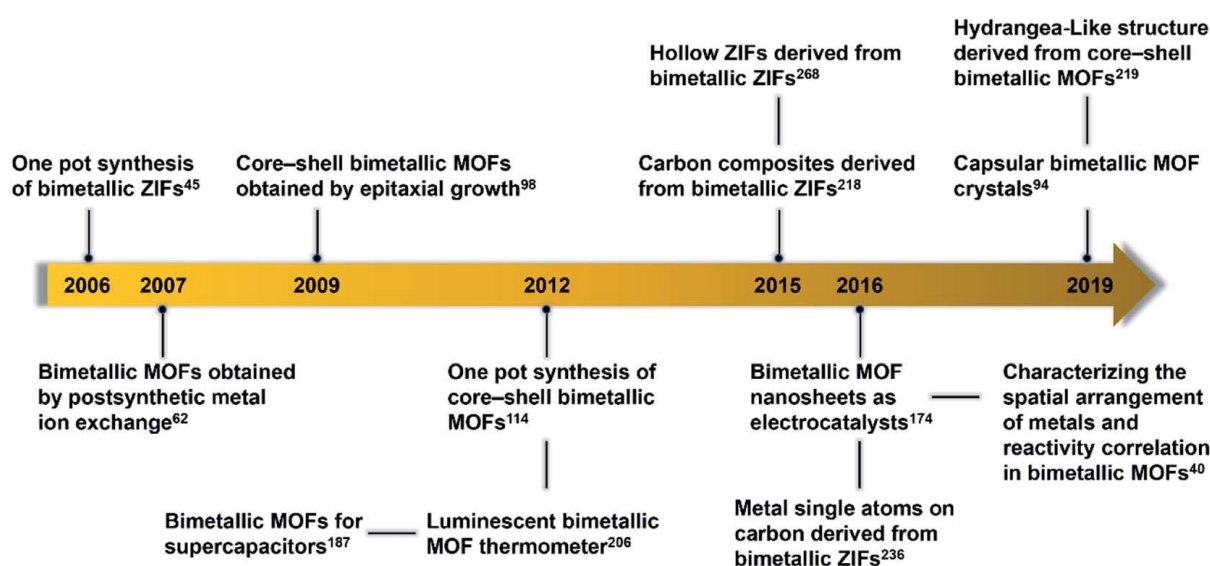


Figure 2.5: Timeline in the development and growth of bimetallic MOFs.²²²

The incorporation of secondary metal ions in the framework has been shown to improve the selectivity adsorption capacity, optical, electronic, and magnetic properties of the single metal-MOF and Figure

2.5 describes the development and growth of bimetallic MOFs over the years^{176,223-229}. The generation of defects along with the synergistic effects between different metal ions in the same framework is attributed to the enhancement in properties of the bimetallic MOFs. The inclusion of secondary metal ions might affect the stability of the MOF and make them fragile. Therefore, the choice of 1) secondary metal ions and the organic linkers; 2) the ratio of the different metal ions in the solution, 3) the synthesis of the bimetallic MOFs are important parameters that govern the resultant topologies and properties of the resultant MOFs^{177,224,225,228}. Bimetallic MOFs can be synthesised by 1) One-step synthesis, 2) Post-synthetic modifications, 3) using a template-based approach or 4) core-shell bimetallic MOF. The detailed reviews of these processes are described below.

- 1) One-step synthesis method involves mixing measured quantities of both the metal salts and solvents for the designated time and duration of the synthesis. Because of the random mixing process, the bimetallic MOF may have a fragile framework with unpredictable functionality and crystallinity. Metals ions having similar ionic radii and coordination geometries form less defective MOFs and show better stability, whereas lattice distortion due to non-similar ionic radii may result in a distorted MOF and limited adsorption capability. The bimetallic $\text{Cu}_{3-x}\text{Zn}_x(\text{btc})_2$ MOFs showed reduced surface areas with increasing Zn^{2+} cations because of the size differences between the two metal ions in the framework^{230,231}. However, the CO_2 adsorption capacity of HKUST-1 improved on the addition of the alkali metal cations Li^+ , Na^+ , and K^+ to the framework because the chemical heterogeneity imparted by the secondary metal ions enhanced their selectivity²³².

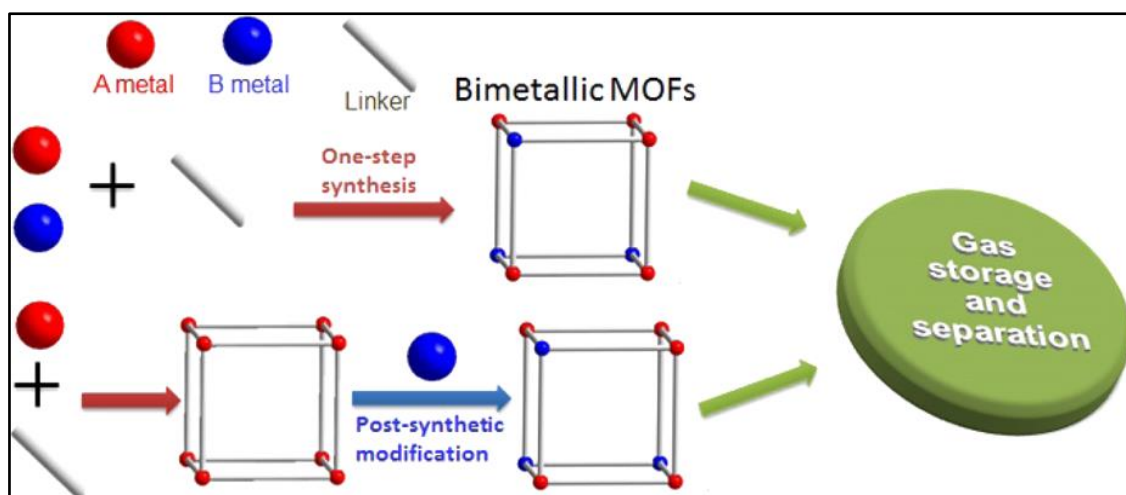


Figure 2.6: Synthesis of Bimetallic Metal-Organic Frameworks (MOFs).²²³ Copyright © 2017,

American Chemical Society

- 2) Post Synthetic Modification is the alteration to the framework by partial or major substitution of the secondary metal ion or organic linkers. As seen from Figure 2.6, this synthesis can also be used to synthesise hard to make bimetallic MOFs. Substitution of the primary metal nodes from an already formed framework needs extra stimulation. The diffusion and substitution of the secondary metal ions cause vacancies and defects in the framework that can enhance the adsorption properties of the post-synthetically modified bimetallic MOFs. The porous Mn(H₃O) [(Mn₄Cl)₃(hmtt)₈] (POST-65) MOF, containing Mn²⁺ centres was post-synthetically modified using N, N-dimethylformamide (DMF) solutions of Fe²⁺, Co²⁺, Ni²⁺, and Cu²⁺ for 12 days. This post-synthetic modification resulted in the formation of three complex frameworks, POST-65(Co/Ni/Cu), as well as a new framework, POST-65(Fe) that could not be synthesized by conventional methods. The Mn²⁺ ions were partially substituted only by the Cu²⁺ ions, forming CuMn-POST-65. However, rather than the bimetallic MOF, the highest H₂ adsorption uptake was recorded by the completely substituted POST-65(Fe) MOF²³³. The post-synthetic titanium exchange of the UiO-66's zirconium metal centres resulted in enhanced adsorption capabilities while maintaining the thermal, chemical and structural stabilities of UiO-66's through water adsorption and desorption cycles²³⁴.
- 3) In the previous methods of synthesis, the substitution of the secondary metal ion is randomly resulting in non-predictable properties. Using ordered substitutions of secondary metal ions,

the selectivity, adsorption and stability properties of MOFs can be predicted, designed and changed²²². Kim et al. synthesised a 1D Zn-based polymer with pre-defined binding sites as a structural template to grow the bimetallic Zn/M-MOF-74 (M = Mg, Ni) MOF structure²³⁵. The 1D $[\text{Zn}(\text{H}_2\text{O})_2(\text{C}_8\text{H}_4\text{O}_6)]_n$ polymer was synthesised using 2,5-dihydroxy-1,4-benzene dicarboxylic acid and ZnSO_4 . The 1D polymer was reported to possess ordered hydroxy and carbonyl sites for the secondary metal ions to bind. Weighed quantities of the polymer were suspended in the cosolvent mixture of DMF/EtOH/ H_2O with varying quantities of $\text{Mg}(\text{NO}_3)_2$ and $\text{Ni}(\text{NO}_3)_2$ to form corresponding 3D Zn/M-MOF-74 (M = Mg, Ni). It was reported that in spite of varying metal concentrations at the start of the reaction, once synthesised, the bimetallic MOFs displayed a uniform molar ratio of 1: 1. In the case of Fe-MOF-74, this technique can be used to avoid the irreversible Fe-peroxo complex formation by strategically planting a secondary metal ion to alter the arrangement of the secondary metal ion to alter the Fe-O-O bond^{47,49}.

- 4) The core–shell bimetallic MOFs are MOFs with different core and shell. These unique bimetallic MOFs can be synthesised using the seed-induced growth approach or the post-synthetic exchange approach, or the one-pot synthesis approach. The synthesis of core–shell bimetallic ZIFs can be explained using the ZIF-8@ZIF-67 MOF bimetallic MOF. Since Zn containing ZIF-8 and ZIF-67 have similar lattice parameters and owing to epitaxial growth, ZIF-8 acts as the core or the seed and ZIF-67 grows around it as the shell forming seed-induced bimetallic ZIF-8@ZIF-67 MOF^{222,236}. The epitaxial growth method is limited to the MOFs with similar crystallographic parameters because otherwise, dissimilar growth of core and shell MOFs in solution will take place.

In a synthesised MOF crystal, the metal ions at the core show different reactivities than to the metal ions at the surface. The different synthesis and growth of MOFs at the centre and at the surface take place due to these different post-synthetic metal exchanges. This results in formation of bimetallic core–shell MOFs through selective transmetalation²³⁷. The one pot synthesis of core–shell bimetallic MOFs involves mixing of the precursor solutions of core and shell and controlling their nucleation and growth to initiate the growth of the shell MOF on the

core MOF. This reactivity-driven nucleation and growth process of two different MOFs can be controlled by adjusting the experimental parameters like temperature, time, starting reagents, solvents and modulators^{238,239}.

2.3.3 Applications of MOFs for oxygen capture and storage

Metal-organic frameworks (MOFs), with their unique design, large surface areas, exceptional porosity, and diverse physical and chemical tunability have been used successfully in gas storage,^{72,85,240,241} selective separations,^{35,74,163,242} catalysis,^{61,219} sensing,^{33,48,85,154,155,159-161,243} drug delivery applications^{88,162} however, the successful use of MOFs in oxygen capture and storage has not been explored to its full potential. The properties of MOFs can be readily altered by changing the metal nodes, organic ligands; or both thus facilitating the targeted design and development of MOFs with tailored pore size, shapes, and host-guest interactions. Using computational techniques, the MOFs for these particular applications can be identified before they can be experimentally analysed. In 2014 DeCoste *et al.* conducted grand canonical Monte Carlo simulations (GCMC) on 10,000 MOFs to identify MOFs for the adsorption and storage of oxygen.⁵⁷ They identified HKUST-1 (Cu-BTC) and NU-125, the two MOFs with coordinatively unsaturated Cu sites, for oxygen adsorption study. The high-pressure oxygen isotherms measured for the MOFs HKUST-1, NU-125, zeolite NaX and Norit activated carbon showed that NU-125 has a 237% excess capacity for oxygen than the zeolite NaX, and 98% excess capacity than the activated carbon, Norit. Based on the GCMC simulations carried out by Moghadam *et al.* for more than 2900 MOFs in the CoRE MOF database, UMCM-152 was identified, synthesised and tested for its oxygen capacity. It showed 22.5% more oxygen capacity than the best oxygen storing material²⁸. GCMC simulations of gas uptakes are based on the force fields describing the intermolecular interactions of the gas molecules and their intramolecular interactions with the porous adsorbent framework. Zeitler *et al.* investigated 98 nanoporous framework structures for sensing applications using the classical Grand canonical Monte Carlo simulations for low-pressure oxygen adsorption. However, the general force field UFF was not able to calculate the interactions of the oxygen with open metal sites accurately²⁴⁴. Computational screening of metal-organic framework (MOF) materials for selective oxygen adsorption from air is used to identify new sorbents for the oxyfuel

combustion process feedstock streams. Parkes *et al.* conducted computational screening to study on the effect of metal chemistry on the oxygen and nitrogen binding energies with fourteen different metals gas binding energies using two frameworks, $M_2(\text{dobdc})$ and $M_3(\text{btc})$. They reported higher oxygen binding energies by the early transition metals due to side-on bonding, due to M-O bond lengthening, whereas there was no noticeable change in the nitrogen binding energies over all the transitional metal series. The study concluded that early transition metal MOFs are better suited for oxygen to nitrogen separations²⁴⁵. Wang *et al.* performed density functional theory calculations and studied the effect of metal ions on the adsorption behaviour of O_2 in $M_3(\text{BTC})_2$ -type materials ($M = \text{Cr, Mn, Fe, Co, Ni}$ and Cu ; $\text{BTC} = 1,3,5\text{-benzenetricarboxylate acid}$) and identified $\text{Ni}_3(\text{BTC})_2$ as the potential oxygen adsorbent with easier deoxygenation than $\text{Cr}_3(\text{BTC})_2$ ²⁴⁶. Demie *et al.* used GCMC simulations to study the four MOFs ($\text{UiO-66}(\text{Zr})$, Ce-UiO-66 , MOF-5 , and IRMOF-14) to DFT studies and metal catecholates ($\text{Mg, Co, Ni, Zn, and Cd}$) were added to Cd-catecholated showed promising results²⁷. Gallis *et al.* used a combination of DFT calculations, post synthetic metal substitutions, gas adsorption results using Cu-BTC (HKUST-1) to prove the effect of metal ion on their oxygen and nitrogen adsorption properties at cryogenic temperatures. The results show the correlation between O_2/N_2 selectivities at 77 K that were determined experimentally and the difference in O_2 and N_2 binding energies calculated from DFT modelling data: $\text{Mn} > \text{Fe} \approx \text{Co} \gg \text{Cu}$. Room temperature gas sorption studies were also performed and correlated with metal substitution. Interestingly, the Fe-exchanged sample showed higher nitrogen isosteric heat of adsorption showing favourable interactions between N_2 and coordinatively unsaturated Fe metal centres²⁴⁷. Xiao *et al.* demonstrated using Co-BTTri and Co-BDTriP, two cobalt-based frameworks, how the choice of framework structure and ligand basicity results in high O_2/N_2 selectivities⁷⁸. Bloch *et al.* identified and synthesised the open-metal $\text{Fe}_2(\text{dobdc})$ as the oxygen selective MOF with irreversible O_2 binding above 226 K. The partial switching of Fe^{2+} to Fe^{3+} changes to permanent switching resulting in reversibility and poor performance of this MOF at higher temperatures⁴⁹. Verma *et al.* used density functional theory to explain the reversible differential adsorption of N_2 and O_2 on $\text{Fe}_2(\text{dobdc})$ using spin-states, bond orders, vibrational frequencies, and orbital energies and highlight the stronger binding of O_2 over N_2 ²⁴⁸. Murray *et al.* used $\text{Cr}_3(\text{BTC})_2$ for selective O_2 over N_2 adsorptions at Cr^{2+} open metal sites. However, this MOF also exhibits decreasing

uptake with for repeated cycles⁷⁹. Bloch *et al* used the coordinatively unsaturated, redox-active Cr^{2+} cation sites from the chromium (II)-based metal–organic framework $\text{Cr}_3[(\text{Cr}_4\text{Cl})_3(\text{BTT})_8]_2$ (Cr-BTT; BTT^{3-} =1,3,5-benzenetristetrazolate) to show higher O_2/N_2 selectivity and room temperature O_2 reversibility and explained this mechanism by the selective electron transfer to Cr^{III} superoxide²⁴⁹. Co-BTTri and Co-BDTriP, the sodalite-type metal-organic framework coordinatively unsaturated Co^{2+} metal-centers displayed high O_2/N_2 selectivities at low temperatures of 230 K. The calculated oxygen capacities of Co-BTTri were reported to be 1.2 mmol/g and for Co-BDTriP it was 0.6 mmol/g^{27,250}. MOF-177, a zinc benzenetribenzoate MOF was reported to display an O_2/N_2 selectivity of ~ 1.8 at 1 atm and at 298 K making it a prospective candidate for oxygen separation and storage. However, the framework was not stable in ambient conditions and decomposed after exposure to ambient air in 3 days²⁵¹.

2.4 Magnetic Framework Composites (MFCs)

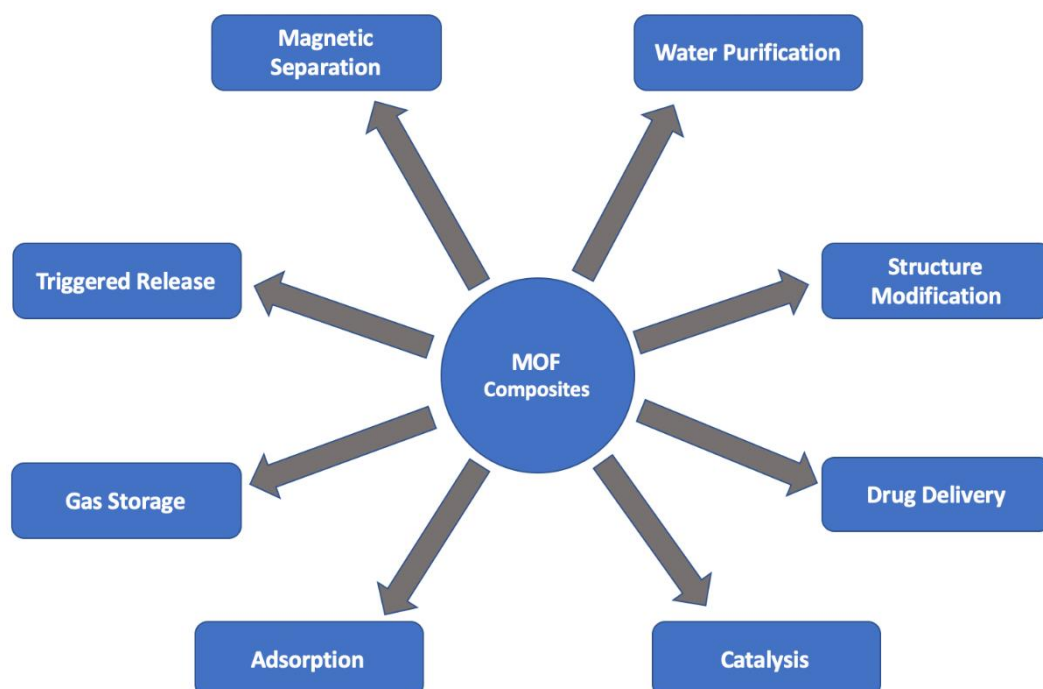


Figure 2.7: Applications of Magnetic Framework Composites (MFCs).

The ability of MOFs to host stimuli-responsive functional nanoparticles in their structure imparts added functionalities to their nanocomposites^{43,69,87}. The thermally insulating nature of the MOFs, aided by the strong host-guest interactions in the framework makes the entire desorption process quite challenging and energy intensive^{25,125,175,252,253}. To negate the energy penalty associated with temperatures, pressures or vacuum based desorption techniques, magnetic induction swing adsorption (MISA) is used where the penetrative radiations intrinsic to magnetic fields are utilized to induce remote and localised heating that is high enough to trigger the release of the adsorbed molecules. This is achieved by fabricating magnetic framework composites. MFCs are formed by incorporation of magnetic nanoparticles with or within the porous and flexible frameworks of MOFs. They offer efficient response to external stimuli providing a rapid, localised and controllable heating when exposed to an alternating magnetic field and as shown in Figure 2.7 they find applications in adsorption, catalysis, gas storage, triggered release, magnetic separations and water purification^{88,254}. MFCs can be synthesized using four techniques:

- 1) **Mixing:** The magnetic nanoparticles and MOF are synthesized separately and later sonicated together to give a coarse mix or mixed together using a binder²⁵⁵,
- 2) **Embedding:** The magnetic particles are added into the MOF solution of metal salts and ligands, heated and the composite allowed to grow^{70,72},
- 3) **Encapsulation:** A carrier medium acts as an interface between the nanoparticles and the growing MOF, allowing the MOF to encapsulate and grow around the magnetic particles^{70,72},
- 4) **Layer-by-layer:** The surfaces of the nanoparticles are functionalized and MOF is grown on them layer-by-layer²⁵⁶.

The success of the MISA process depends on the properties of the magnetic nanoparticles. Magnetic nanoparticles exhibit many unique properties that depend on their size, shape, surface chemistry and size distribution. Depending on the orientations of their magnetic dipoles and their responses to a magnetic field, materials can be classified as diamagnetic, paramagnetic, ferromagnetic and ferrimagnetic materials and antiferromagnetic^{257,258}. The orbitals of diamagnetic materials are filled

with unpaired electrons. Therefore, when exposed to a magnetic field, they are slightly repelled but there is no permanent magnetic moment. The orbitals of paramagnetic materials contain randomly oriented magnetic moments. In the presence of a magnetic field these get aligned and exhibit slightly magnetic properties but exhibit zero magnetization when the external magnetic field is removed. The orientation of the individual magnetic moments is random owing to the lack of the exchange interaction²⁷⁷. Ferromagnetic materials are materials that exhibit a long-range magnetic order and spontaneous magnetization. They have unpaired electrons and their strong magnetic properties are due to the presence of magnetic domains. In presence of the magnetic field, these domains get aligned to and produce a strong magnetic field within the part. These orientations and alignments get disrupted with increase in temperatures and above the Curie Temperature the magnetization stops. Ferrimagnetic materials show spontaneous magnetization. But the exchange interaction in ferromagnetic materials is negative. Similar to ferromagnetism, ferrimagnetic materials undergo magnetic transition at the Curie temperature. Figure 2.8 shows the different responses of the Diamagnetic, Paramagnetic, Ferromagnetic, Ferrimagnetic and Antiferromagnetic materials to a magnetic field.

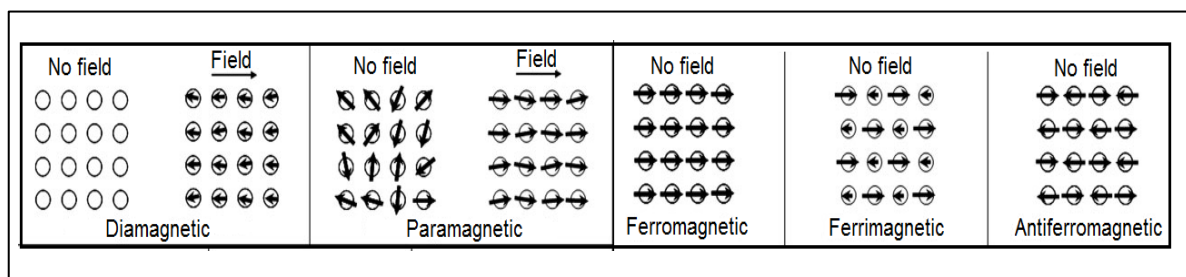


Figure 2.8: Classification of magnetic materials as per their responses to a magnetic field. ^{67,258}

Saturation Magnetization

In the presence of a magnetic field, the randomly aligned magnetic dipoles in ferro and ferromagnetic materials align themselves in one direction and produce a magnetization (M). With an increase in the magnetic field strength, the magnetic flux density (B) also increases until a saturation magnetization (M_s , maximum magnetization) is reached. The path traced by this flux density defines the initial non-linear magnetization curve. When the magnetic field is removed, the realignment of the magnetic dipoles takes a bit longer and so instead of following the initial curve, the magnetic flux density traces

a new but slower travel path. Owing to this, even when the applied field is zero, there is still some retained magnetic flux density in the material, the remnant magnetization (M_r , induced magnetization). This loop depicting the ‘lack of retraceability’ of the original magnetization curve is called the hysteresis loop. The area under the curve in Figure 2.9 represents the amount of thermal energy absorbed from the field and dissipated by the material ^{67,259,260}.

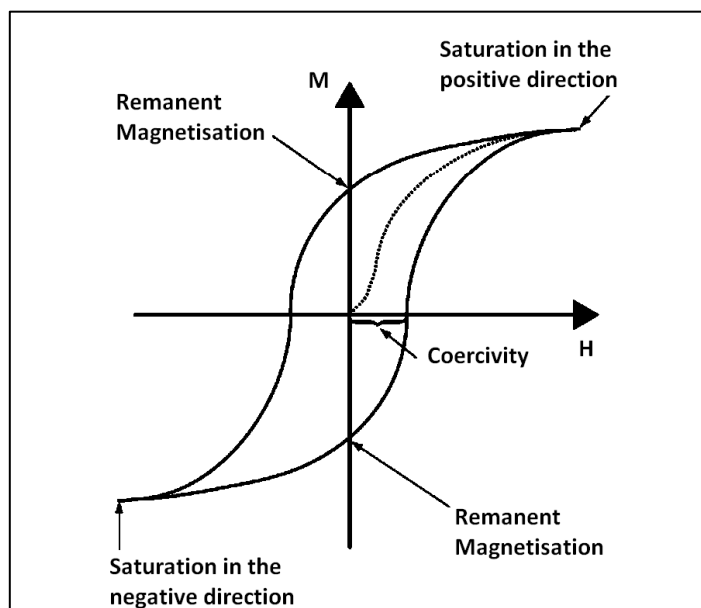


Figure 2.9: The hysteresis curve for ferro and ferrimagnetic materials ²⁶⁰

Super-paramagnetism

Magnetic domains are separated by interfaces called the domain walls, where the direction of magnetization in one domain is different from the other domain. Domain walls have a definite width and a set amount of energy is required to maintain the width. In ferro and ferrimagnetic nanoparticles, if the grain sizes are decreased and maintained below a critical size, they act as single domain structures. On exposure to a magnetic field, the thermal fluctuations produced in single domain structures are high enough to overcome the domain wall energy barrier and cause rapid flipping of their magnetic dipoles. Acting as single structures they get magnetized to their saturation magnetization, and exhibit super paramagnetic behaviour. This behaviour is unique because on removal of the electric field they exhibit

zero magnetism. Unlike their intrinsic characteristic these nanoparticles avoid agglomeration due to paramagnetism. Regulating the field strength can control the property change from super paramagnetism to zero magnetism. This paramagnetic behaviour is of high importance in biomedical applications because it ensures that even in absence of a magnetic field, the nanoparticles don't agglomerate and cause clogging of blood vessels ²⁶¹.

Relaxation Losses

In response to an applied magnetic field, either as a result of the domain wall displacement or due to the rotation of their magnetic moments, the nanoparticles release energy. For larger particles these losses, called hysteresis losses, are due to the domain wall displacement. In smaller or super paramagnetic particles, this release of heat can be attributed to the rotation: either of their magnetic moments or to their own rotation, around themselves. This generation of thermal energy by magnetic nanoparticles is explained by three size-dependent mechanisms: Hysteresis losses (particle sizes ~20 nm), Neel relaxation (particles sizes < 7.5 nm), and Brownian relaxations (particle sizes > 7.5 nm)²⁶¹⁻²⁶³. Figure 2.10 depicts the relaxation losses by Neel relaxation and Brownian motion.

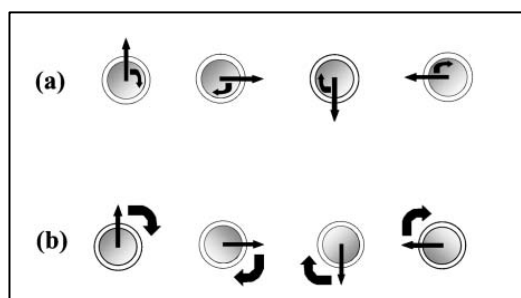


Figure 2.10: The relaxation losses: a) when the particles are stationary (Neel relaxation), b) when the particles rotate (Brownian relaxation) ²⁶¹.

Specific Adsorption Rate (SAR)

The rate at which the magnetic nanoparticles will absorb the magnetic energy and convert it into thermal energy can be predicted using Specific adsorption rate, (SAR). Apart from the diameter, shape and

composition of the nanoparticles, SAR is strongly governed by the frequency of the applied magnetic field. In hyperthermia treatments nanoparticles with high SAR values are preferred because it means a higher absorption rate even at low concentrations.

It has been observed that the heating efficiency of single-domain ferromagnetic nanoparticles is more than the heating efficiency of super paramagnetic particles²⁶³. Therefore, it has been proposed that the particle with the highest SAR will have a diameter slightly above the super paramagnetic diameter, i.e. ~15-20nm, where both the weakened Neels mechanism and the significant hysteresis effects contribute towards the heat loss²⁶²⁻²⁶⁴.

SAR is calculated by dispersing the particles in a liquid medium and the measuring:

$$SAR = C_s \frac{m_s}{m_m} \left(\frac{dT}{dt} \right)_{t=0} \quad 2.1$$

Where C_s is the specific heat capacity of suspension, dT/dt at $t=0$ is the initial gradient of the heating curve, m_s and m_m are the specific masses of the suspension and magnetic particles, respectively. The units of SAR are watts per kilogram (W/kg)²⁶⁴⁻²⁶⁷.

Curie Temperature

In the presence of the magnetic fields, the nanoparticles heat up efficiently until the Curie point temperature, T_c , is reached. Above this point the heating effect due to the magnetic field stops and the material becomes paramagnetic and loses all its otherwise strong magnetic properties. When the temperatures cool down below their Curie temperatures, the particles resume their normal magnetic behavior and start to heat up again^{263,267}. This self-controlling heating property is used as a control to avoid overheating by the nanoparticles and is especially important in the hyperthermia treatments where overheating of the nanoparticles above 46 °C can destroy the healthy cells in the body¹⁷⁴.

2.5 Desorption of Adsorbed molecules using MISA:

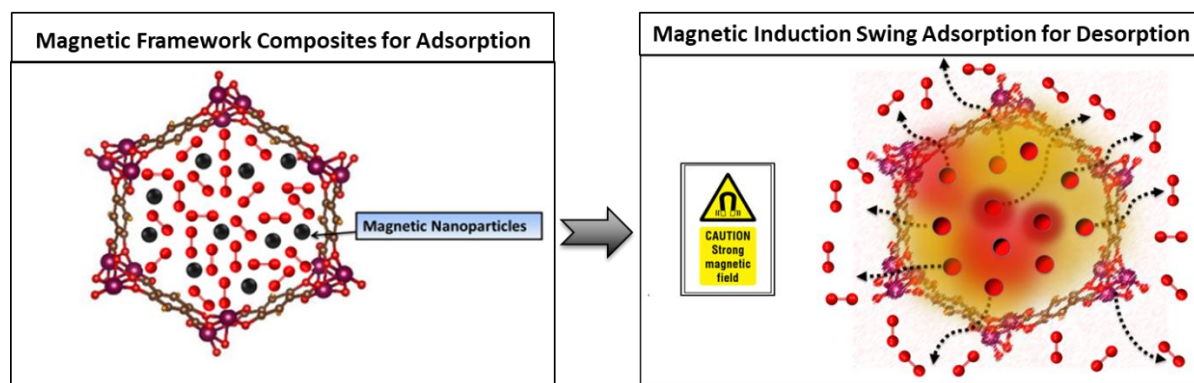


Figure 2.11: Desorption of adsorbed molecules using Magnetic Induction Swing Adsorption (MISA).

As illustrated in Figure 2.11, magnetic induction swing adsorption harnesses the heating abilities of magnetic nanoparticles to trigger the release of stored gas molecules from the framework in energy-efficient ways. The adsorption potential of the MOFs and the heating abilities of the magnetic nanoparticles are combined to develop the MFCs. This is to enable efficient heat transfer in the MOF by overcoming their low thermal conductivities and achieved using ferrimagnetic nanoparticles. The heat generation in the nanoparticles is a result of hysteresis observed in the magnetization vs applied field plot when the ferrimagnets are exposed to an alternating current magnetic field. A magnetization-demagnetization process is induced with the magnitude of the heat generated equivalent to the area within the hysteresis loop. Consequently, in MFCs, this rapid and localised heat generation leads to instability in the guest-host bond of the adsorbed gas and the framework that triggers the release of the gas molecules. The selection of the MOF, the ratio of magnetic nanoparticles, and the strength of the applied magnetic field are essential features of the MISA process. The heat generation capability of the MFCs are measured by recording their temperature rise profile at different magnetic fields. For triggered release of gases, desorption is initiated using an induction machine to trigger the remote and rapid heating within the MFCs that enables the complete release of the adsorbed molecules.

Chapter 3:

Experimental Methods

Chapter 3: Experimental Methods	34
3.1 Introduction	35
3.2 Materials	35
3.3 Synthesis	35
3.3.1 Magnetic nanoparticles	35
3.3.1.1 Fe₃O₄ nanoparticles	35
3.3.1.2 MgFe₂O₄ nanoparticles	35
3.3.2 Metal-Organic Frameworks (MOFs):	36
3.3.2.1 Co-MOF-74	36
3.3.2.2 Fe-MOF-74	36
3.3.2.3 MM-MOF-74	36
3.3.2.4 CuBTC MOF	37
3.3.3 Magnetic Framework Composites (MFCs):	37
3.3.3.1 Co-MOF-74-Fe₃O₄ composite	37
3.3.3.2 Cu-BTC/MgFe₂O₄ composite	38
3.4 Sample Characterisation	38
3.3.1 Powder X-ray diffraction (PXRD)	38
3.3.2 Scanning Electron Microscopy (SEM)	39
3.3.3 Gas Adsorption Properties	39
3.3.4 Thermogravimetric Analysis (TGA)	40
3.3.5 Thermo-magneto gravimetric analysis (TMGA)	40
3.3.6 X-ray photoelectron spectroscopy (XPS)	41
3.3.7 Magnetic property measurement	41
3.3.8 Specific Absorption Rate (SAR)	42
3.3.9 Desorption of Oxygen using MISA	42
3.3.10 Regeneration Energy Calculations	43

3.1 Introduction

This chapter briefly discusses the synthesis and various characterisation techniques used to study the structural, optical, adsorption, and magnetic properties of the samples, and it also provides a brief overview of the triggered release experiments setup.

3.2 Materials

All chemical reagents used for these experiments were of analytical grade and were used as received without any further purification. All ultra-high purity (UHP, 99.999% purity) grades of N₂, O₂, and CO₂ gases were used for the surface area analysis, gas adsorption studies, and the triggered release experiments. More details on the materials used in each experiment are detailed in the materials and methods section of the respective chapter.

3.3 Synthesis

3.3.1 Magnetic nanoparticles

3.3.1.1 Fe₃O₄ nanoparticles

The Fe₃O₄ nanoparticles were synthesised by mixing 1 mmol of sodium citrate dihydrate (C₆H₅Na₃O₇ · 2H₂O), 4 mmol of sodium hydroxide (NaOH), and 0.2 mol of sodium nitrate (NaNO₃) to 19 mL of deionised water and heating this mixture to 100 °C. Once a transparent solution was formed, 1 mL of 2mmol iron sulphate tetrahydrate (FeSO₄ · 4H₂O) was added to it, and this solution was kept at 100 °C for 1 h. When cooled to room temperature, the Fe₃O₄ nanoparticles were then magnetically separated and washed multiple times by water ²⁶⁸.

3.3.1.2 MgFe₂O₄ nanoparticles

MgFe₂O₄ nanoparticles were synthesised using a solvothermal method by mixing of 3.6 g, 0.027 moles of sodium acetate trihydrate (CH₃COONa · 3H₂O), 2.5 mmol of magnesium chloride hexahydrate (MgCl₂ · 6H₂O) and 5 mmol of ferric chloride hexahydrate (FeCl₃ · 6H₂O) together. Around 2.00 g of polyethylene glycol (MW = 4000) was added as a surfactant. The mixture was stirred vigorously to form a homogeneous solution and then heated under reflux at 180 °C for 16 h. On cooling, the black magnetic nanoparticles were magnetically separated and washed alternately with distilled water and ethanol, dried in a vacuum oven at 80 °C for 8 h, and stored in a glove bag ²⁶⁹.

3.3.2 Metal-Organic Frameworks (MOFs):**3.3.2.1 Co-MOF-74**

0.75 g of 2,5-Dihydroxyterephthalic acid (3.78 mmol) and 3.0 g of cobalt nitrate hexahydrate (11 mmol) was dissolved in 150 mL of DMF. The mixture was sonicated in a tightly capped 250 mL Schott bottle and placed in an oven at 110 °C for 20 h. The sample was cooled down to room temperature, the mother liquor decanted, the products washed with DMF three times, and then immersed in 200 mL of methanol. The methanol exchange was carried out for the next six days, and then the samples were activated at 250 °C under vacuum for 24 h before storing them in an N₂ filled glove bag.

3.3.2.2 Fe-MOF-74

1.1 g of anhydrous ferrous chloride (9.0 mmol), 0.71 g of 2,5-dihydroxyterephthalic acid (3.6 mmol), 300 mL of DMF, and 36 mL of methanol were all added to a 500 mL Schlenk flask and heated under reflux at 120 °C for 18 h. The red-orange coloured precipitate was collected by filtration, washed with DMF, and soaked in DMF at 120 °C for 24 h. The solid was collected after filtration, then washed with methanol, and soaked in methanol at 70 °C for 24 h. This methanol exchange was repeated three times before the sample was activated at 160 °C under vacuum for 24 h before storing them in an Ar filled glove box ⁴⁹.

3.3.2.3 MM-MOF-74

The synthesis of the bimetallic MM-MOF-74 was similar to the synthesis of the Fe-MOF-74 with varied Fe/Co molar ratios of Fe_xCo_{1-x}-MOF-74.

Fe_{0.9}Co_{0.1}-MOF-74

1 g of anhydrous ferrous chloride (8.1 mmol), 0.1 g of cobalt chloride (0.7 mmol), 0.071 g of 2,5-dihydroxyterephthalic acid (3.6 mmol), 300 mL of DMF and 36 mL of methanol were all added.

Fe_{0.5}Co_{0.5}-MOF-74

0.5 g of anhydrous ferrous chloride (4.1 mmol), 0.5 g of cobalt chloride (3.5 mmol), 0.71 g of 2,5-dihydroxyterephthalic acid (3.6 mmol), 300 mL of DMF and 36 mL of methanol were all added.

Fe_{0.1}Co_{0.9}-MOF-74

0.1 g of anhydrous ferrous chloride (0.8 mmol), 1 g of cobalt chloride (6.9 mmol), 0.71 g of 2,5-dihydroxyterephthalic acid (3.6 mmol), 300 mL of DMF and 36 mL of methanol were all added.

The mixture was heated under reflux at 120 °C for 18 h in a 500 mL Schlenk flask. The precipitates were collected by filtration, washed with DMF, and soaked in DMF at 120 °C for 24 h. The solid was collected by filtration, washed with methanol, and soaked in methanol at 70 °C for 24 h. The methanol exchange was repeated three times, and then the sample was activated at 160 °C under vacuum for 24 h before storing them in Ar filled glove box ^{49,177,270}.

3.3.2.4 CuBTC MOF

0.7 g of copper acetate monohydrate (3.5mmol) dissolved in 14 mL of deionised water was mixed with 0.6 g of trimesic acid (H₃BTC, 2.8 mmol) dissolved in 14 mL of ethanol. This mixture was stirred for 30 min, transferred into an autoclave, and heated to 85 °C for 24 h. On cooling, the blue CuBTC MOF was washed three times with ethanol and dried in a vacuum oven at 140 °C for 24 h.

3.3.3 Magnetic Framework Composites (MFCs):

3.3.3.1 Co-MOF-74-Fe₃O₄ composite

As shown in Figure 3.1, the pre-synthesised Fe₃O₄ nanoparticles were weighed and added in different proportions to the Co-MOF-74 precursor solution and subjected to continuous mechanical stirring for 24 h at 100 °C. MFCs with 0.08 wt % (MC1) , 8.8 wt % (MC2) , 11.8 wt % (MC3) , 12.18 wt % (MC4) , 12.6 wt % (MC5) , and 15 wt % (MC6) of Fe₃O₄ nanoparticles were synthesized. On cooling, the samples were magnetically separated, washed with DMF three times, and then immersed in 200 mL of methanol. The methanol exchange was carried out for the next six days, and then the samples were activated at 250 °C under vacuum for 24 h and stored in an N₂ filled glove bag.

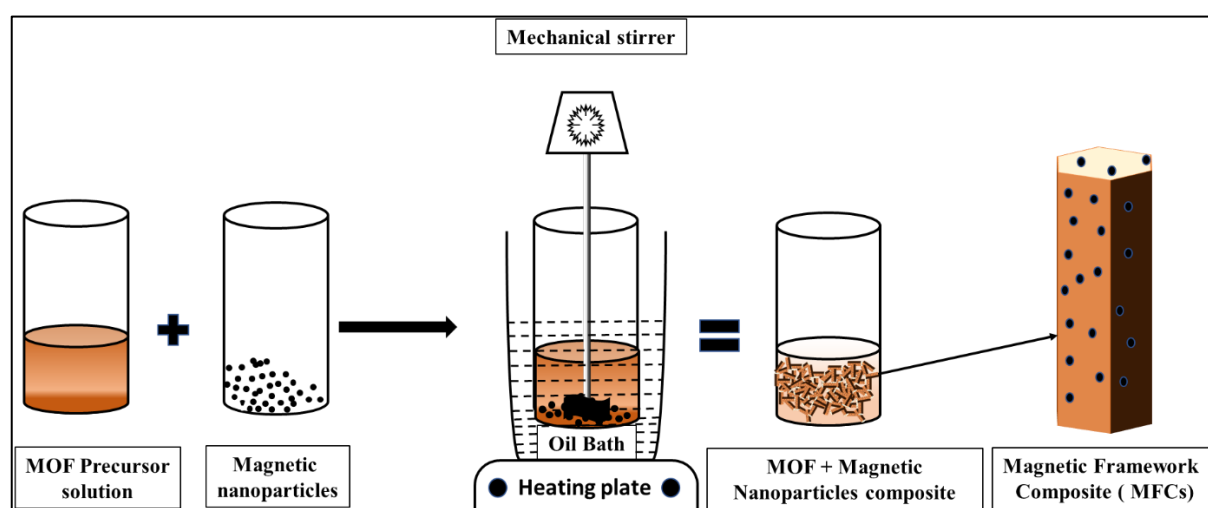


Figure 3.1: Schematic showing synthesis of MFCs.

3.3.3.2 Cu-BTC/MgFe₂O₄ composite

The objective behind the shaping of MOFs is to increase the amount of gas stored per unit volume. For practical applications, pelletising MOFs is favourable and can be achieved by either applying a certain amount of pressure on the powdered MOFs to shape them into pellets or by mixing the MOF powder with specific binders (typically, polyvinyl alcohol (PVA)) and solvent. Figure 3.2 illustrates how the Cu-BTC/MgFe₂O₄ MFCs were pelletised by extruding a paste made using measured quantities of CuBTC MOF, binder, and MgFe₂O₄ nanoparticles, through a 5 mL syringe. The extruded MFC noodles were cut into 8-10 mm pellets and allowed to dry in ambient air before drying them in a vacuum oven at 140 °C for 24 hrs. To select an MFC having an optimal balance between adsorption capacities, heating abilities, and structural stability, different MFCs with varying binder concentrations (1, 2, 3, 4 wt. %) and varying magnetic content (1, 2, 3, 4 wt. % of MgFe₂O₄ nanoparticles) were fabricated and investigated for their surface area and oxygen adsorption properties.

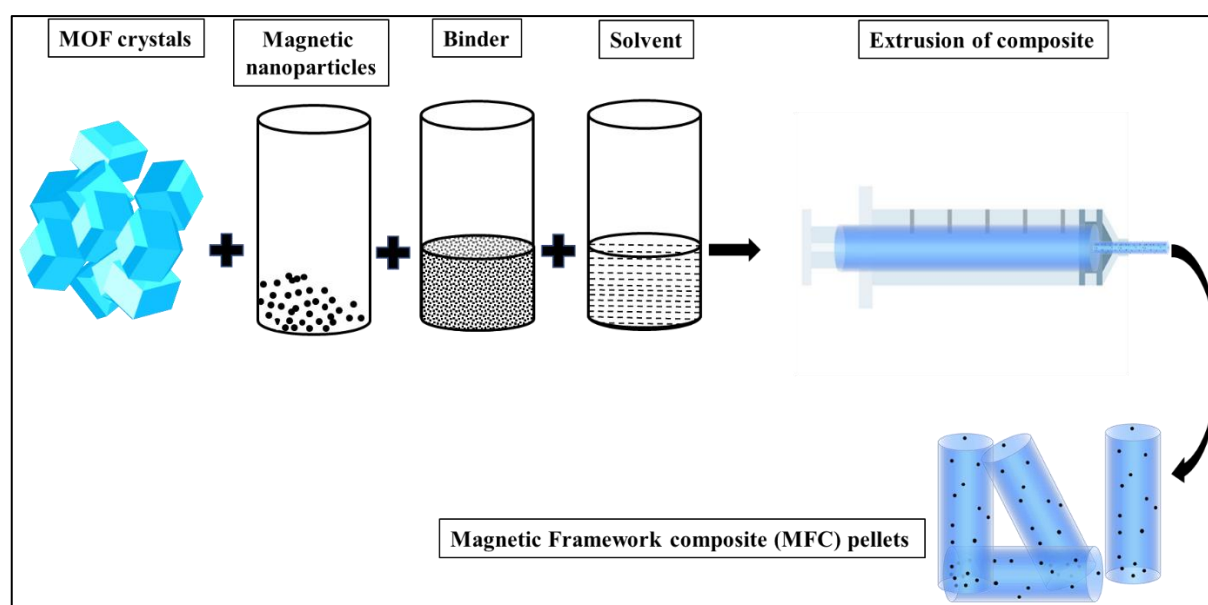


Figure 3.2: Schematic showing the pelletising process of MFCs.

3.4 Sample Characterisation

3.3.1 Powder X-ray diffraction (PXRD)

X-Ray diffraction is a characterisation technique used for phase identification, mean size measurements, and to determine the presence of dislocations, defects, impurities, or stresses within the crystallites. In crystalline materials, atoms are arranged periodically in long-range orders. When an incident X-ray beam irradiates a sample, the interactions between the X-rays and these atomic arrangements produce

distinct diffraction patterns distinctive to their crystallographic structures. They are plotted as intensity versus 2θ , the angle between the incident and reflected rays. In a diffraction pattern, each peak position and intensity depends on the wavelength of the X-rays, which in turn is representative of the d-spacings and provides information about the location of lattice planes in the crystal structure²⁷¹. The wavelength of the X-ray, λ , is relative to the distance between atoms and Bragg's law, $n\lambda=2d(\sin \theta)$, defines the relationship between these X-ray wavelengths, the angle between the incident beam θ and the lattice planes, and, the distance between the crystallographic planes, d , where n is the order of reflection. All PXRD measurements on samples were conducted using a Bruker D8 Advance X-ray diffractometer, using a Co K-alpha radiation (40 kV, 25 mA) equipped with a LYNXEYE detector.

3.3.2 Scanning Electron Microscopy (SEM)

Scanning electron microscopy (SEM) was used for surface and compositional characterisation of the samples, such as its particle size, shape, the topography of the surface (SEI), chemical compositions, phase homogeneity (BSE), phase identification and crystallographic orientations (EBSD). The scanning electron microscope uses an electron gun to accelerate a beam of high-intensity electrons through a series of lenses onto the sample surface under a high vacuum. When the electron beam impacts the samples, electrons penetrate and travel into the surface. The sample reacts by emitting out its electrons in the form of secondary electrons, backscattered electrons, X-rays, and visible light that are acquired and used for the microstructural analysis of the samples. During sample preparation, a tiny amount of the sample is dispersed by sonification in a solvent. Then a drop of it is pipetted onto a silicon wafer that has been secured tightly on the mounting metal stubs with a double-sided conducting adhesive tape. To avoid charging of the nonconductive MOF samples, they were coated with a thin platinum/iridium coating. Special care was taken to protect the objective lens of the microscope during the study of magnetic nanoparticles because they being magnetic they can get sucked up in the column chamber and affect the settings and the overall performance of the SEM. All microstructural, morphological studies on the samples were carried out using the JEOL 7001F Scanning Electron Microscope. The backscattered images (BSE) were used to highlight the contrast between the MOF and magnetic nanoparticles in an MFC, and the Energy Dispersive X-ray Spectroscopy (EDS) mapping was used to demonstrate the distribution of the magnetic nanoparticles within the composites.

3.3.3 Gas Adsorption Properties

A Micrometrics ASAP 2420 machine was used to carry out the surface area and pore size distribution measurements of the MOF and MFC samples by nitrogen (N_2) gas adsorption at 77 K. During the synthesis of MOFs and MFCs, solvent molecules get trapped in the framework and to have complete access to the pores and surface areas within the framework, the MOFs and MFCs are activated. For activation, the sample to be analysed is transferred into a clean, dry, pre-weighed analysis tube, fitted

with a transeal cap and activated using heat and vacuum at recommended temperatures and times. For reliable results, accurate weights of the samples are required, and therefore after activation, the tubes are weighed again to know the exact mass of the desolvated samples. They are attached to the analysis ports of the ASAP machine, and their surface area properties and pore volumes are measured by nitrogen (N_2) adsorption-desorption isotherms at 77 K using liquid nitrogen baths.

Micrometrics Tristar and 3Flex surface characterisation analyser machines were used to study the oxygen adsorption properties of the MOFs and MFCs. The sample activation and the oxygen adsorption measurements are similar to the nitrogen adsorption measurements except for the temperatures. The oxygen adsorption studies were carried out at 204, 273, and 298 K by using acetone + dry ice bath, ice bath, and water bath, respectively. To achieve and maintain these temperatures during the adsorption-desorption cycles, a slightly bigger glass tube encircling the analysis tube was used as a dewar to hold the bath mixture.

3.3.4 Thermogravimetric Analysis (TGA)

Thermogravimetric analysis (TGA) is the technique used to analyse the thermal stability of the samples. It is achieved by heating a known mass of sample at a constant rate under a controlled atmosphere and recording the weight change with respect to time and temperature. With MOFs and MFCs, the TGA curve helps establish the time and temperature settings required for the activation of the samples. The thermal stability of every MOF sample is different and depends on the type of solvents and organic linkers used for synthesising the MOF. The TGA curves reveal how the decomposition of the samples occurs over multiple steps. The first weight loss step usually corresponds to the loss of trapped water or solvent molecules followed by the second and or third weight loss steps that occur due to the decomposition of the organic linker or the disintegration of the MOF itself. All thermal analysis studies were carried out on SENSYS evo TG-DSC machine equipped with a refrigeration cooling system Julabo FL-601 and operating in the temperature range from room temperature (RT) to 800 °C. Weighed amounts of MOF samples were placed into the alumina crucible and then heated to 800 °C at a heating rate of 10 °C /min in an N_2 atmosphere ³¹.

3.3.5 Thermo-magneto gravimetric analysis (TMGA)

Thermo-magneto gravimetric analysis (TMGA) is a very efficient technique to ascertain the magnetic transitions in magnetic nanoparticles by measuring their Curie points (T_c). The Curie point is a temperature at which magnetic materials undergo loss of their magnetic properties and become paramagnetic. This sharp change in magnetic properties is measured by measuring the weight change of the samples as a function of temperature. These measurements are acquired by placing a high strength permanent magnet outside the temperature-controlled chamber of a TGA setup and collecting the

weight loss data over the required temperature range. The Curie temperature measurements were carried out on a Perkin Elmer TGA 7 machine, where the sample to be analysed was wrapped in an aluminium foil and gently placed on a platinum pan connected to a microbalance. A horseshoe magnet of 1 mT magnetic field strength was placed around the pan in such a manner to get the maximum magnetic weight of the sample. The sample chamber was flushed with argon before heating the sample to 800 °C at a constant heating rate of 40 °C, and the resultant weight loss of the sample was recorded as a function of temperature²⁷².

3.3.6 X-ray photoelectron spectroscopy (XPS)

X-ray photoelectron spectroscopy (XPS) is a very powerful technique to analyse both elemental and compositional chemistry of a wide range of materials. It is a surface-selective analysis where the surface of the sample to be analysed is irradiated with monochromatic X-rays, and an electron energy analyser studies the electrons emitted from the surface. The intensity of the emitted photoelectrons can reveal the elemental details of the sample, whereas the binding energies of the emitted electrons will reveal the chemical state of the sample. An initial survey scan covering the entire energy range allows identification and quantification of the elements and based on this scan, high-resolution scans can be collected to quantify the surface chemistry. An electron spectrometer consists of the source of radiation and an electron energy analyser all contained within a vacuum chamber held under high vacuum because, for detection of photoelectrons, an ultrahigh vacuum is required²⁷³. X-ray photoelectron spectroscopy (XPS) analysis of MOF and MFC samples was carried out using Nexsa Surface Analysis System X-ray photoelectron spectrometer with a micro-focused, monochromated Al K- α X-ray source and high-efficiency electron lens, hemispherical analyser and detector and uses Avantage Software for instrument control, data processing, and reporting. Since the samples were air-sensitive, the samples were transferred from the glove box to the spectrometer via a vacuum transfer module.

3.3.7 Magnetic property measurement

A vibrating sample magnetometer (VSM) is used to measure the magnetic properties of materials and to study the response of magnetic nanoparticles to an applied magnetic field. When exposed to an applied magnetic field, the magnetization (M) of the nanoparticles increases with an increase in the magnetic field until it becomes saturated, and any increase in the magnetic field cannot increase its magnetization anymore. A reverse magnetic field brings the magnetization back to zero. This response is plotted in the form of a magnetization curve. Vibrating-sample magnetometer (VSM) is used to measure magnetic properties by oscillating the sample between fixed coils of the magnetometer. It exposes the sample to the magnetic field generated by the coils, and it will get magnetised, which will directly affect the magnetic flux in the coils. According to Faraday's Law of Induction, this magnetic change will affect the electric field in the coils and will be proportional to the magnetization of the

sample. The generated electric field can easily be measured and analysed for information about the magnetic field, the magnetization, hysteresis, and coercivity of the samples⁶⁷. The magnetic property studies of saturation magnetization (Ms), coercivity (Hc), and magnetization curves were studied on a vibrating sample magnetometer (VSM, RIKEN DENSHI). The samples for the study were prepared by embedding weighed quantities of samples in an epoxy resin and hardener mix and allowing it to set. Once it was all set, the measurements were carried out at room temperature.

3.3.8 Specific Absorption Rate (SAR)

Specific Absorption Rate, SAR, describes the heating efficiency of the magnetic materials and indicates the rate at which the magnetic nanoparticles will absorb the magnetic energy and convert it into thermal energy. Apart from the diameter, shape, and composition of the nanoparticles, SAR is strongly governed by the frequency of the applied magnetic field. In hyperthermia treatments, nanoparticles with high SAR values are preferred because it means a higher absorption rate even at low concentrations⁶⁷. SAR is calculated by dispersing the particles in a liquid medium and then measuring the heat capacity and applying the following equation:

$$\text{SAR} = C_s \frac{m_s}{m_m} \left(\frac{dT}{dt} \right)_{t=0} \quad 3.1$$

Where C_s is the specific heat capacity of suspension, dT/dt at $t=0$ is the initial gradient of the heating curve, m_s , and m_m are the specific masses of the suspension and magnetic particles, respectively. The units of SAR are watts per kilogram (W/kg).^{265,266} To measure SAR, the nanoparticles were dispersed in water at a concentration of 5mg/ml. This magnetic suspension was placed in a dewar flask and exposed to an induction heating system (EASY HEAT 0224–Ambrell) with a heating coil of 8 turns (N) of 2.5 cm diameter (D) and 4 cm in length (L). The amplitude of the AC magnetic field was fixed at $H = 13.09$ kA/m. The temperature rise attained by the samples for the next 30 minutes is noted as the heat generation capacity of the samples. An IR thermal camera (FLIR E5) was used to capture these changes in the temperatures.

3.3.9 Desorption of oxygen using MISA

The heat generation capability of the MFCs was measured by recording their temperature rise profile while exposing them to different magnetic field strengths. The oxygen adsorption isotherms were collected using a Micrometrics Tristar and Micrometrics 3Flex gas sorption analyser at pre-set equilibration times allowing enough time for the system to equilibrate at each pressure point, and the targeted pressures for desorption were set at 200, 400, 600, 800, and 1000 mBar. The experiment was designed to alternate between adsorption and desorption phases continuously, with minimal activation and degassing taking place between each cycle. The desorption was generated with an EASY HEAT

Ambrell induction machine to trigger the remote, rapid, and localised heating enabling the complete release of the adsorbed oxygen at the desired pressure. Typically, the experiment program is run to adsorb oxygen from 0.1 mbar to 1200 mbar. The experiment is monitored, and at 200 mbar pressure range, the remote magnetic heating is activated to trigger the release of the adsorbed oxygen molecules. The process is repeated at 400, 600, 800, and 1000 mbar. As depicted in Figure 3.3, the triggered release setup consisted of the activated and weighed samples filled in a Tristar / 3Flex tube and attached to the Tristar/3Flex machine while a slightly wider glass dewar holding the bath mixture encircled it. This was fitted through an induction coil such that the sample sits in the centre of the 8-turn coil to ensure uniform exposure of the sample to the magnetic field. The effects of the magnetic field were contained using a Faradays cage.

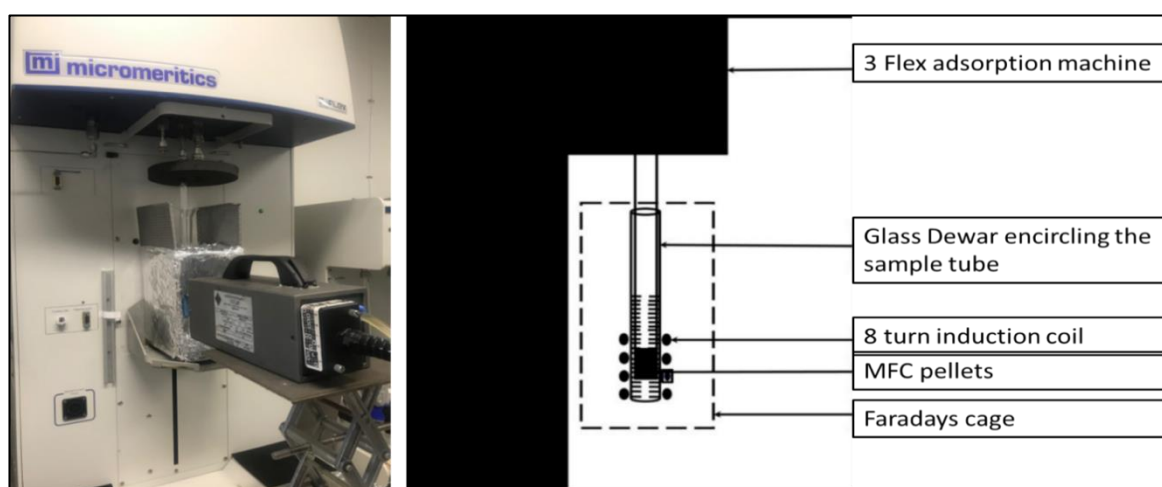


Figure 3.3: Schematic showing the setup for room temperature oxygen adsorption measurements consisting of the 3Flex machine and the EASY HEAT Ambrell induction machine with an 8 turn coil that is strategically placed around the sample tube so that the sample is uniformly exposed to the magnetic field, b) the graphical representation of the triggered release experiments.

3.3.10 Regeneration Energy Calculations

The regeneration energy is the energy utilised by the adsorbent to undo the adsorption process. It depends on the heat of adsorption, specific heat capacity, and working capacity of the adsorbents. It is directly proportional to the heat of adsorption because strong interaction between the adsorbent and adsorbate results in a higher heat of adsorption and consequently higher regeneration energy would be required to overcome this strong interaction¹⁷⁵, leading to a high energy penalty^{76,85,175}. Furthermore, MOFs are generally known to be thermal insulators and require high temperatures to trigger the release of adsorbed species.

Specific regeneration energy (Q_{thermal}) is the sum of the energy needed to heat the adsorbent to the desorption temperature, and the energy required to desorb bound gas species from the adsorbent ⁷⁴, according to the equation:

$$Q_{\text{thermal}} = \frac{c_p m_{\text{sorbent}} \Delta T + (\Delta h O_2 \Delta q O_2)}{m O_2}$$

Where,

C_p = specific heat capacity of adsorbent ($\text{Jg}^{-1}\text{K}^{-1}$)

$m_{\text{adsorbent}}$ = mass of adsorbent (g)

ΔT = Temperature difference between adsorption and desorption conditions (K)

Δh = heat of adsorption (kJmol^{-1})

Δq = working capacity, it can be defined as the difference between the O_2 loadings at adsorption and O_2 loadings at the end of desorption ⁵¹.

$m O_2$ = mass of oxygen adsorbed at that pressure (g)

The remote, localised, and targeted heating nature of the MISA process makes it most suitable for Oxygen capture and storage applications while minimising the energy penalty required to operate the process ^{74,75,85,86}.

Chapter 4:
**Efficient Delivery of Oxygen via Magnetic
Framework Composites**

Chapter 4: Efficient Delivery of Oxygen via Magnetic Framework Composites.....	45
4.1 Introduction.....	46
4.2 Published Work.....	46
4.2.1 Abstract	47
4.2.2 Introduction.....	47
4.2.3 Results and Discussion	50
4.2.4 Triggered Release Experiments:.....	53
4.2.5 Conclusions.....	57
4.3 Supporting Information and Acknowledgements.....	58
4.4 References.....	59

4.1 Introduction

Metal organic frameworks are crystalline, highly porous scaffold like structures formed by the linking of organic ligands and inorganic metal nodes, and due to their chemical stability and high internal surface areas they have generated a lot of interest for gas sequestration and storage. However, their potential in separation and storage of oxygen is yet to be explored fully.

Currently oxygen separation techniques are either highly energy intensive, i.e. cryogenic distillation; or insufficiently selective for oxygen, as is the case of zeolite adsorbents which are selective for nitrogen and are unable to generate a high purity gas stream. The difference in chemical properties between oxygen and nitrogen remains a relatively unexplored mechanism of isolating of oxygen from air. The tunable properties of MOFs, this difference in quadrupole moment and redox properties can be exploited to achieve higher selectivity and storage for oxygen, enabling direct capture from air. This is the first detailed study on the use of MISA for the separation and storage of oxygen using MOFs.

In particular, this study reports the oxygen adsorption capacities of a cobalt-based Co-MOF-74, owing to the strong affinity and temperature dependant reversible bindings of oxygen in Co^{2+} complexes. A series of Co-MOF-74 composites containing iron oxide magnetic nanoparticles were used to magnetically trigger the release of bound oxygen from the composite adsorbent and use this process to overcome the high energy requirements associated with regeneration of MOFs. This process known as Magnetic Induction Swing adsorption (MISA), utilises the penetrative nature of magnetic fields to produce heat from the magnetic nanoparticles embedded within the MOF composites, enabling the adsorbent to be regenerated without the external application of heat or vacuum.

Chapter 4 is based on the manuscript titled, “*Efficient Delivery of Oxygen via Magnetic Framework Composites*” published in Journal of Materials Chemistry A on 10th January 2019. This proof of concept study demonstrates the potential of MOFs as effective adsorbents for the oxygen purification.

4.2 Published Work

This section discusses work previously published in a journal article, reproduced with permission from Melag *et al.*[28] © Royal Society of Chemistry 2019. Figures and references from this publication have been renumbered for consistency with the Chapter. A copy of this work is included as **Appendix A**.

Efficient Delivery of Oxygen via Magnetic Framework Composites

Leena Melag, M. Munir Sadiq, Stefan J. D. Smith, Kristina Konstas,
Kiyonori Suzuki and Matthew R. Hill

J. Mater. Chem. A, 2019, <https://pubs.rsc.org/en/content/articlelanding/2019/TA/C8TA07739H>

4.2.1 Abstract

Metal-organic frameworks (MOFs), with their intriguing network structures, large internal surface areas, and tunable pore properties offer the perfect yet largely unexplored alternative for selective adsorption of oxygen. Owing to their thermally insulating nature and often favorable binding of guest species, controlled desorption of the adsorbed molecules from such frameworks can be challenging and energy intensive. To find an energy efficient means for release of these gas molecules, here, we have made use of the heating effect of magnetic nanoparticles to achieve desorption using the Magnetic Induction Swing Adsorption (MISA) process. Magnetic nanoparticles when exposed to a high-frequency magnetic field, heat up instantly; and when present within a MOF, this localised heating is enough to drive the release of adsorbed molecules. Here Co-MOF-74 based Magnetic Framework Composites (MFCs), containing varying concentrations of Fe₃O₄ nanoparticles, were trialed for triggered oxygen capture. The greatest oxygen adsorption achieved by the prepared Cobalt based MFCs was 4.8 mmol g⁻¹ at 1.2 bar, with a Type I adsorption isotherm. For the effective desorption was then triggered by exposure to a magnetic field, with 100 % desorption of oxygen accomplished by MFC4, the MOF composite with 12.18 wt. % Fe₃O₄ nanoparticles.

4.2.2 Introduction

With more than 100 million tons consumed annually, oxygen separation from air is one of the most energy demanding industrial processes. One that is primarily achieved by the cryogenic distillation of air¹, where air is compressed between 4 and 10 atm, cooled to ambient temperatures before passing it through the pre-purification Unit to remove the trace contaminants, especially water, carbon dioxide, and heavy hydrocarbons. The purified air is passed through the main heat exchanger, cooled to near its liquefaction temperature before entering the distillation columns to separate oxygen, nitrogen and argon. Achieving and maintaining column temperatures of -183 °C (boiling point of oxygen) to distil large volumes of high purity oxygen is complex and consumes vast amounts of energy.

Most other oxygen separation techniques rely on the adsorption or isolation of nitrogen from air to produce oxygen; however, as air is only 21 % O₂, there is significant room for improvement¹⁻³. Non-cryogenic separation processes, including membrane and adsorption-based technologies are less energy intensive, but are not yet industrially competitive^{4,5}.

Adsorption techniques make use of the differences in the quadrupole moments and the kinetic diameters of gases to separate a specific component from a mixture of gases. Zeolites, for example, preferentially adsorb nitrogen due to the interaction between its extra framework cations and the N₂ molecule's larger quadrupole moment⁶. Through this mechanism, nitrogen molecules are retained in vacant pores of the

adsorbent, allowing gaseous oxygen to be collected⁷. Alternatively, molecular sieve carbons are able to selectively adsorb oxygen by size, with only the smaller oxygen molecules ($3.43 \pm \text{\AA}$ vs. $3.68 \pm \text{\AA}$) able to access the adsorbent's pore cavities. Unfortunately, material properties such as structural rigidity, heterogeneity of pores, the inability to alter their pore geometry, as well as regeneration energy costs, impose significant limitations on these methods^{8,9}.

Instead, separation processes that exploit differences in the chemical properties of oxygen and nitrogen may offer the selectivity required for direct capture of oxygen from air. Over the last decade, metal organic frameworks, (MOFs), have been successfully deployed for the selective separation and storage of a range of gases¹⁰⁻¹⁵; making them applicable in diverse fields of selective adsorption processes, to catalysis to drug delivery, and leading to their scale up from laboratory trials to commercial productions¹⁶⁻²³. In spite of all these advances, very few reports have highlighted the potential of MOFs for oxygen capture or storage^{7, 24-26}. So far, oxygen separation using MOFs has relied on MOFs containing uncoordinated redox-active metal centers^{26, 27}. In these cases, oxygen reacts with the exposed metal cation within the MOF, causing selective adsorption by chemically binding to a molecule of oxygen^{7, 10, 28}. While offering high adsorption capacities in ambient conditions, the key challenge is in overcoming the irreversible nature of the adsorption. Working capacity, defined as the difference in the amount adsorbed under uptake conditions and the amount left in the adsorbent under desorption conditions is an important parameter used in selecting materials for separation and storage applications, remains prohibitively low. Unfortunately, MOFs' strong host-guest interactions and low thermal conductivity make desorption by high temperature and/or vacuum, slow and energy intensive²⁹⁻³³. Ultimately, the efficiency of a separation process depends on the energy required to desorb bound guest molecules³³.

Recently, the energy penalty associated with the regeneration stage of Temperature Swing Adsorption (TSA) and Pressure Swing Adsorption (PSA) processes has been overcome by the inclusion of 'stimuli-responsive' functional groups and nanoparticles in MOFs³⁴⁻³⁶. Stimulation of these groups trigger property changes within the MOF, causing adsorbent regeneration without the application of external heat or vacuum³⁴⁻³⁶.

One such method is the incorporation of magnetic nanoparticles into MOFs, resulting in magnetic framework composites (MFCs); which add magnetic induction heating properties to the adsorbent, as well as magnetically driven isolation and positioning of MOF crystals in solution^{20, 21, 37}. Induction heating is a controllable method of heating where energy from an alternating magnetic field is converted into heat within a magnetic material. The magnetically induced heating effect has successfully been

used for heat treatment of metals and alloys³⁸, hyperthermia treatment of cancer cells³⁹⁻⁴², and more recently, as the heat source for MOF synthesis^{20, 21, 37}.

MFCs are prepared by growing MOF crystals around preformed magnetic nanoparticles^{43, 44}. When exposed to an alternating magnetic field, these ‘nanoheaters’ provide rapid, localised heating throughout the framework. By using localised heat sources, the efficacy of applied regeneration energy can be greatly improved by overcoming MOF’s inherently low thermal conductivity. This process of using the intense heating of magnetic nanoparticles to trigger desorption of bound gas molecules from within an adsorbent is known as magnetic induction swing adsorption (MISA)^{39-41, 43-49}.

Unlike the traditional cyclic adsorption-based separation techniques of temperature swing adsorption (TSA), and or pressure swing adsorption (PSA), the MISA process regenerates the entire adsorbent while greatly reducing the energy inefficiencies associated with the conduction of externally applied heat and or through an insulating MOF. In studies carried out by Li *et al.*^{43, 46}, the composite of Mg-MOF-74 and Fe₃O₄ nanoparticles, showed a ~ 9.8 % increase in CO₂ uptake as compared to a bare Mg-MOF-74 and on application of a magnetic field of 81 mT, the heating of the Fe₃O₄ nanoparticles resulted in efficient release of ~ 49 % of adsorbed CO₂ molecules. Sadiq *et al.*⁴⁴, further demonstrated the potential of MISA by incorporating MgFe₂O₄ nanoparticles in zirconium-based UiO-66 to synthesize an MFC that achieved a 100 % release of CO₂ at a magnetic field of 32 and 42 mT. Together, these works prove MISA’s potential for low energy desorption using MFCs for carbon capture applications. In this work, using the MISA process, we examine the potential of MFCs for oxygen capture.

The M-MOF-74 series of MOFs has the highest density of unsaturated open metal centres which are needed to bind oxygen. Since cobalt exhibits a strong affinity and a temperature-dependant reversible binding to oxygen in Co²⁺ complexes we selected Co-MOF-74 as the candidate MOF to demonstrate MISA triggered release of oxygen^{7, 10, 25, 50-56}. Synthesis of Co-MOF-74 in the presence of pre-synthesized Fe₃O₄ magnetic nanoparticles successfully resulted in composites with the magnetic nanoparticle firmly embedded in the MOF. Subsequent to synthesis of composites with varying concentrations of Fe₃O₄ nanoparticles, the triggered release MISA experiments were carried out.

In non-cryogenic conditions, the Fe₃O₄@Co-MOF-74 MFC had a maximum oxygen uptake of 4.8 mmol g⁻¹ at 1.2 bar. The **MFC4** with 12.18 wt. % Fe₃O₄ nanoparticles was able to release 100 % of the adsorbed oxygen molecules when exposed to a magnetic field of 17.4 mT at 270 kHz.

4.2.3 Results and Discussion

The size and morphology of the synthesized Fe_3O_4 nanoparticles was investigated using a scanning electron microscope (SEM). The nanoparticles had a spherical morphology with nanoparticle size of ~ 30 to ~ 50 nm (see Figure S2-a). The nanoparticles showed excellent stability in water with no change in properties for one month^{48, 57-60}.

The magnetic properties of the Fe_3O_4 nanoparticles were studied at room temperature using a vibrating sample magnetometer (VSM) with a maximum applied field of ± 1 T. The hysteresis curve of the Fe_3O_4 nanoparticles shows a saturation magnetization (M_s) of 58 emu g^{-1} and very little coercivity (Figure S6-a). Thermo-magneto gravimetric analysis (TMGA) of the nanoparticles revealed the Curie temperature of the particles to be $T_c = 570^\circ \text{C}$ (Figure S7). At the T_c , there is a phase transition from the ferrimagnetic state to the paramagnetic state that results in a loss of heating capability of the NPs and thus could serve as a switch to regulate the temperature rise.

The heat generation capacity of the nanoparticles was estimated by recording the temperature rise profile of a known concentration of NPs solution and estimating the specific absorption rate (SAR) in W/g ^{41, 44}. All the induction heating experiments were carried out at 270 kHz except where otherwise stated. At $\mu_0 H$ of 16.4 mT, 5 mg/ml of Fe_3O_4 nanoparticles in water attained a maximum temperature rise of 85.0°C and the SAR was calculated to be 74.5 W g^{-1} (Figure S8). These synthesised nanoparticles were then used to fabricate composites with varying concentrations of magnetic nanoparticles simply by adding weighed quantities of Fe_3O_4 nanoparticles to the MOF precursor solutions and mechanically stirring it for the course of the synthesis. (See Section S1-III). The concentrations of these composites were checked using the inductive coupled plasma mass spectrometry (ICP-MS) analysis and the results are listed below in Table 1.

	MFC 1	MFC 2	MFC 3	MFC 4	MFC 5	MFC 6
Wt.% Fe_3O_4	0.08	8.8	11.8	12.18	12.6	15

Table 1. Results from the ICP analysis of the synthesized composites show the concentration of magnetic content within the MFCs.

As observed from the XRD patterns in Figure 4.1, for all the composites **MFC1-MFC6**, the peaks of bare Co-MOF-74 match the diffraction peaks of the composites. For magnetic measurements, as

expected, the composites with higher concentrations of magnetic nanoparticles show higher saturation magnetization .

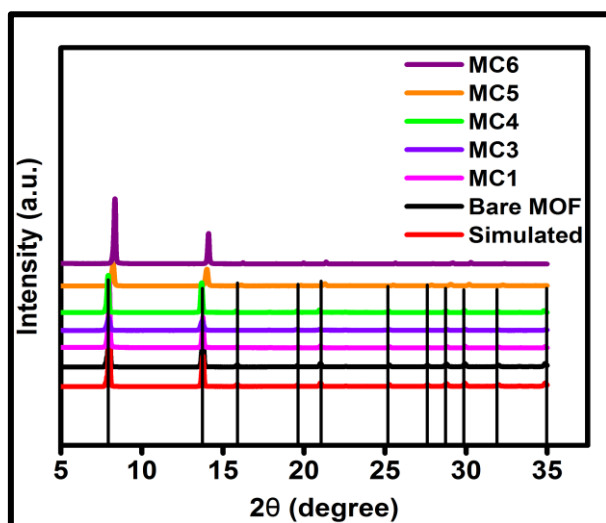


Figure 4.1: The XRD pattern of the Co-MOF-74 and the MFCs compared with the simulated data of M-MOF-74.

The scanning electron microscope images reveal that the nanoparticles are uniformly embedded over the entire surface of the composite. As observed from Figure 4.2e and 4.2f, the EDX mapping analysis on the samples confirm the presence of the Fe_3O_4 nanoparticles in the composites.

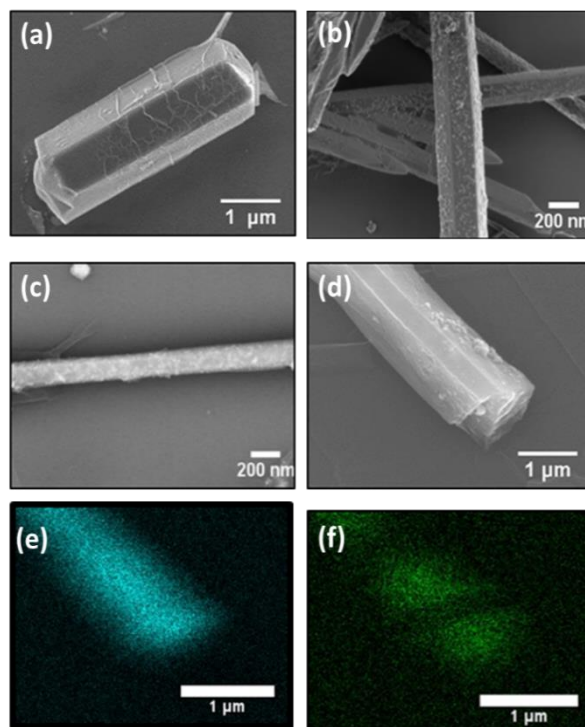


Figure 4.2: The SEM micrographs of a) Bare Co-MOF-74, b) Co-Based composite with Fe_3O_4 nanoparticles embedded in it, c) The contrast in the BSE image confirms the presence and uniform

distribution of Fe_3O_4 nanoparticles throughout the composite, d) Sample used for the EDX mapping, e) EDX mapping results of sample showing the cobalt content and f) Fe content in the composite.

For gas measurements, low-pressure gas adsorption isotherms in the range of 0-1 bar were measured and Type I nitrogen isotherm, was obtained for the bare Co-MOF-74 and the composites. The measured Brunauer–Emmett–Teller (BET) and Langmuir surface areas of the bare Co-MOF-74 were $1449 \text{ m}^2 \text{ g}^{-1}$ and $1764 \text{ m}^2 \text{ g}^{-1}$ respectively.

In case of **MFC1** with 0.08 wt. % Fe_3O_4 , the measured BET surface area of $1478 \text{ m}^2 \text{ g}^{-1}$ is actually higher than that of the bare Co-MOF-74. This may be attributed to some heterogeneous nucleation with the nanoparticles acting as nuclei and aiding the nucleation of the composite. But for **MFC3-MFC6**, increasing the content of magnetic NPs in the framework directly and adversely affects the surface area with **MFC3**- $1082 \text{ m}^2 \text{ g}^{-1}$, **MFC4**- $1008 \text{ m}^2 \text{ g}^{-1}$, **MFC5**- $952 \text{ m}^2 \text{ g}^{-1}$ and **MFC6**- $713 \text{ m}^2 \text{ g}^{-1}$ respectively (Figure S4). With the MFCs, to establish the optimum time and temperature conditions for maximum adsorption of oxygen, the trials were conducted at three different temperatures of 204 K, 273 K and 298 K. Figure 4.3 shows the oxygen adsorption isotherm of the composite **MFC3**, at a temperature of 204 K, that achieved maximum adsorption of oxygen of 3.5 mmol g^{-1} at 1.2 bar at an equilibration time of 5 secs.

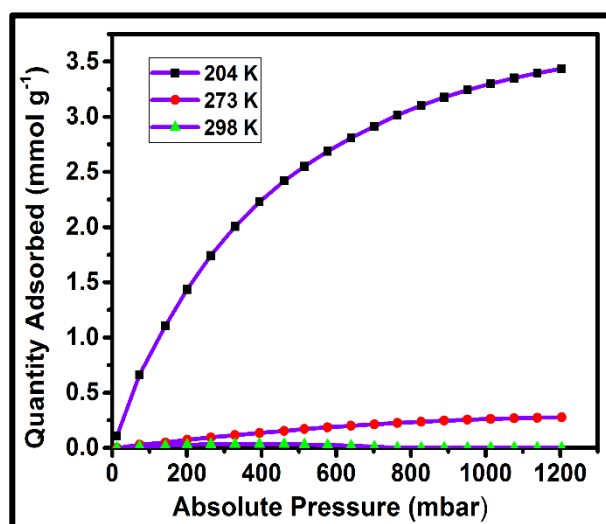


Figure 4.3: Oxygen adsorption isotherms of the composite **MFC3** measured at temperatures of 204 K, 273 K and 298 K at an equilibration time of 5 secs.

4.2.4 Triggered Release Experiments:

The triggered release of bound oxygen from the MFCs was achieved using the Tristar Micromeritics adsorption equipment in conjunction with an induction-heating machine. The requirement from the induction machine was to pass a current high enough to generate a large magnetic field and cause heating of the nanoparticles to their maximum capacity. If the heating of these nanoheaters is high enough, it would cause instability in the intermolecular bond between the adsorbed oxygen molecules and the adsorbing MFCs and trigger the release of the oxygen molecules. To know the maximum temperature rise attained by both, the Fe₃O₄ nanoparticles by themselves and the Fe₃O₄ nanoparticles from the composite, individual samples of each were placed in a dewar flask and exposed to a magnetic field of 16.5 mT. The responsive temperature rise profile was noted for 30 minutes. The bare Fe₃O₄ nanoparticles stabilized at a temperature of 85.0 °C whereas the ones from within the MFCs exhibited a maximum temperature of 63.7 °C. According to these temperature rise profiles obtained at room temperature, when the MFC is exposed to a magnetic field of 16.5 mT, the magnetic nanoparticles from within it should heat up to 63.7 °C.

The oxygen adsorption consisted of the dynamic uptake of oxygen by the composites and for desorption, at preset points the magnetic field was activated triggering the release of the adsorbed oxygen molecules. When the magnetic field would be turned off, the composites would resume their normal oxygen uptake up until the point the magnetic field was activated again. With 200 mbar being the approximate partial pressure of oxygen in air, the periodic switching was set at 200, 400, 800 and 1000 mbar.

The concentration of nanoparticles in the composite determined the adsorption and desorption properties of the MOFs. Composites with high content of magnetic nanoparticles affected the adsorption capacities but provided higher heating rates whereas composites with low nanoparticle concentration had good adsorption properties but insufficient heating and therefore could not achieve full desorption. Consequently **MFC4**, a composite with a comparatively right balance of adsorption properties and heating abilities, was selected to study the effect of magnetic field strengths on the desorption properties of the composites and Figure 4.4 demonstrates the effect of magnetic field strengths on the release of oxygen molecules from **MFC4** composite.

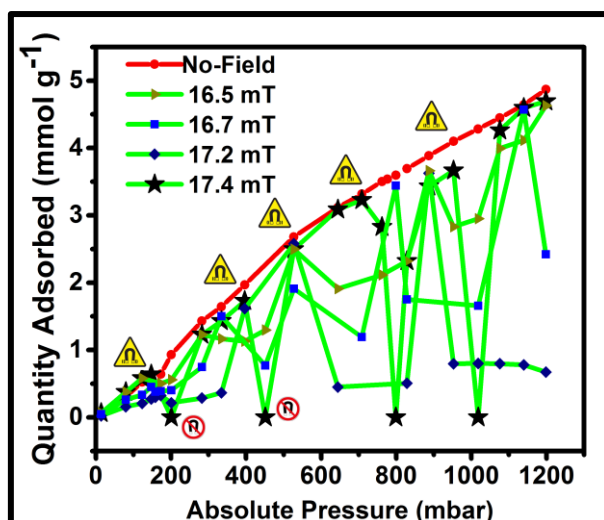


Figure 4.4: Effect of magnetic field strengths, 16.5 mT, 16.7 mT, 17.2 mT and 17.5 mT on the release of oxygen molecules from MFC4 composite.

The induction coil settings from the temperature rise studies were replicated to heat up the MFC to its maximum of 63.7 °C. However, unlike the room temperature measurement settings, for the oxygen adsorption trials, the sample tube was submerged in a bath of acetone/dry ice which reduced the heating effect of the induction coil causing incomplete desorption of the adsorbed oxygen. To attain the right temperature, the applied field was gradually increased from 16.4 mT to the maximum value of 17.4 mT that caused a full desorption of the oxygen molecules. As demonstrated in Figure 4.5, with increase in magnetic field strengths, the desorption capacity of the composites increased with 21 %, 49 %, 74 % and 100 % desorption achieved at 16.4, 16.7, 17.2 and 17.4 mT respectively.

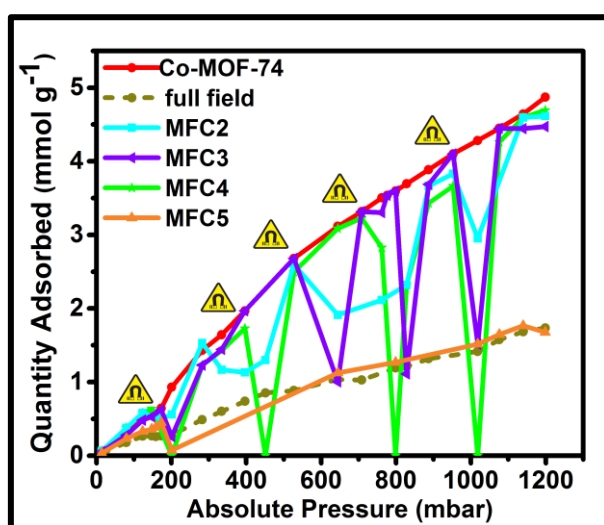


Figure 4.5: Results of the triggered release of oxygen molecules from MFC2 to MFC5 by employing a magnetic field of 17.4 mT. The composite MFC4 released 100 % of the adsorbed oxygen molecules.

For composite **MFC2**, a desorption efficiencies of 16 %, 25.8 %, 25 % and 24.6 % was observed whereas for **MFC3** it was 71 %, 73 %, 78 % and 72.5 % at the preset points of 200, 400, 600 and 800 mbar respectively. **MFC4** achieved a full 100 % desorption of oxygen molecules at all points. Contrary to the desorption trend established by the composites **MFC2** to **MFC4**, the composite, with 12.6 wt. % magnetic nanoparticles, **MFC5**, achieved a near complete desorption at 200 mbar followed by which it neither adsorbed oxygen nor reacted to the applied magnetic field in any way.

The specific regeneration energy (Q_{thermal}) can be defined as the amount of energy required to heat the adsorbent to the desorption temperature^{44, 61}, was calculated for **MFC4**. Figure 4.6 shows the effect of increase in working capacity on regeneration energy with increase in pressure. As highlighted by Zhang et al.,⁶¹ the higher working capacity results in lower regeneration energies with **MFC4** achieving the lowest regeneration energy of 1.1 MJ/kg at 1 bar. While this calculation does not include process considerations and cooling the temperature of air from room temperature to 204 K, we expected this energy requirement to be less than half of that required for cryogenic distillation at 92 K. For a cryogenic distillation based air separation unit producing 110 to 350 tonnes of oxygen per day, the specific energy requirement is reported to be 1.11 MJ/kg- 1.82 MJ/kg at 40 bar⁶².

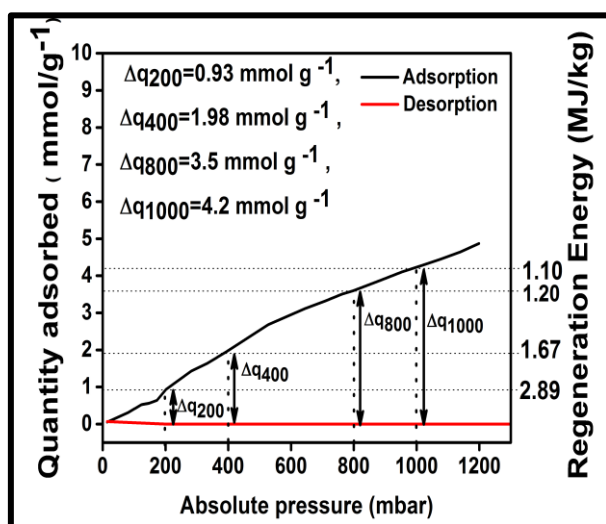


Figure 4.6: Working capacities of **MFC4** at 204 K adsorption temperatures.

The isosteric heat of adsorption is a measure to understand the intensity of the interaction between the gas molecules and the porous framework and is highly time and temperature dependent. The rate of oxygen adsorption in a MOF is decided by the pore dimensions and the available number of unsaturated

metal centers. As shown in Figure 4.7, the initial isosteric heat of adsorption for oxygen was calculated to be -30 kJ mol^{-1} that decreased with surface coverage and stabilized at -19 kJ mol^{-1} . Owing to their higher surface curvatures, at lower loadings, oxygen gets adsorbed into the smaller pores of the MOF and also on the exposed, unsaturated Co^{2+} metal centers. At higher loadings, as all the favorable sites get preferentially occupied, the adsorption proceeds through the larger pores resulting in lower isosteric heat of adsorption^{63, 64 65}.

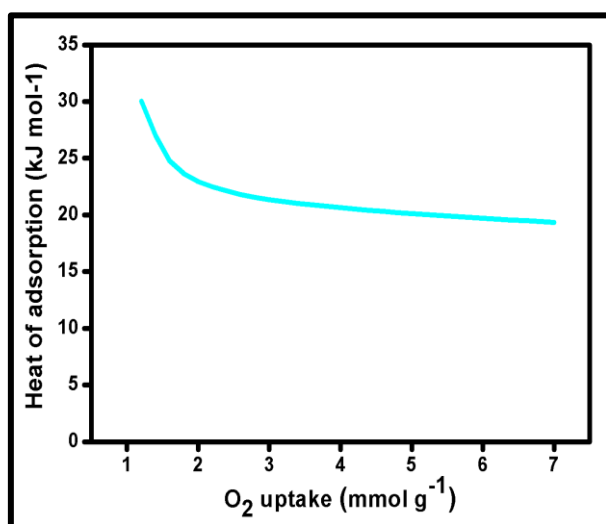


Figure 4.7: *Isosteric heat of adsorption for oxygen, calculated from the oxygen isotherms of MFC2 collected at 204 and 273 K.*

To understand the reversibility of the oxygen bindings at 204 K, the composite MFC4, was exposed to ten consecutive oxygen adsorption and desorption cycles and as observed in Figure 4.8, with each cycle a 10 % drop in the adsorption capacity was noted. Even though the adsorptions were carried out at 204 K, where the reversible binding of oxygen in Co^{2+} complexes still exist, the heat from the magnetic nanoparticles that was used to trigger the molecules out of the composite may possibly have caused oxidation of the metal centres. Post-experiment XRD results showed loss of crystallinity and gradual decomposition of the composite.

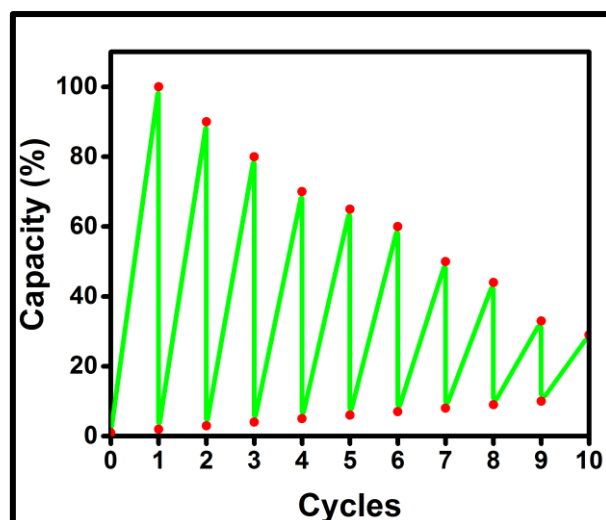


Figure 4.8: The results of the oxygen adsorption-desorption cyclic experiments conducted on the composite *MFC4*, at temperatures of 204 K.

4.2.5 Conclusions

The high capital and production costs associated with the setup and operations of the current air separation processes has led to the search for a new, better and energy efficient technique for separation of oxygen. This can be provided for by the formation of MFCs that make use of the reactive heating ability of the nanoparticles in a magnetic field to trigger the release of the adsorbed molecules by magnetic induction swing adsorption (MISA).

In this study the capacity of cobalt-based MFCs to adsorb oxygen molecules was evaluated. Desorption trials were conducted by exposing the composites it to an alternating magnetic field resulting in release of the bound oxygen molecules. A composite with 12.18 wt. % Fe_3O_4 nanoparticles was able to release 100 % of the adsorbed oxygen when exposed to a magnetic field of 17.4 mT at 270 kHz. The repetitive adsorption and desorption cycles revealed the dependency of time and temperature on the performance and stability of the composite. This is a proof-of-concept experiment carried out to prove the oxygen adsorption capability of MFCs and to establish the efficiency of the magnetic induction heating in successfully achieving the release of most of the adsorbed oxygen molecules.

Future work will include the study and development of prospective new MOFs for the capture of oxygen, the subsequent synthesis of the MFCs by encapsulation of high magnetization nanoparticles in these MOFs and the stimuli responsive triggering of the oxygen molecules by the MISA process.

4.3 Supporting Information and Acknowledgements

Supporting Information

The Electronic Supplementary Information (ESI) accompanying this publication has been reproduced with permission from Melag *et al.*[28] © 2019 American Chemical Society. A copy of this document is included in **Appendix A**.

Acknowledgements

The authors acknowledge the use of instruments and scientific and technical assistance at the Monash Centre For Electron Microscopy, a Node of Microscopy Australia.

4.4 References

References cited in this Chapter text reproduced from the publication “*Efficient Delivery of Oxygen via Magnetic Framework Composites*” included as **Appendix A**, are consolidated here for completeness.

1. Emsley, J., *Nature's building blocks: an AZ guide to the elements*, Oxford University Press, 2011.
2. Smith, A. and Klosek, J., *A review of air separation technologies and their integration with energy conversion processes*, Fuel Process. Technol., 2001, **70**, 115-134.
3. Dobson, M., *Oxygen concentrators and cylinders*, The international journal of tuberculosis and lung disease: the official journal of the International Union against Tuberculosis and Lung Disease, 2001, **5**, 520-523.
4. Zhu, Y.; Legg, S. and Laird, C. D., *Optimal design of cryogenic air separation columns under uncertainty*, Computers & chemical engineering, 2010, **34**, 1377-1384.
5. Castle, W. F., *Air separation and liquefaction: recent developments and prospects for the beginning of the new millennium*, International Journal of Refrigeration, 2002, **25**, 158-172.
6. Watanabe, K.; Austin, N. and Stapleton, M. R., *Investigation of the Air Separation Properties of Zeolites Types A, X and Y by Monte Carlo Simulations*, Molecular Simulation, 1995, **15**, 197-221.
7. Xiao, D. J.; Gonzalez, M. I.; Darago, L. E.; Vogiatzis, K. D.; Haldoupis, E.; Gagliardi, L. and Long, J. R., *Selective, tunable O₂ binding in cobalt (II)-triazolate/pyrazolate metal-organic frameworks*, J. Am. Chem. Soc., 2016, **138**, 7161-7170.
8. Lastoskie, C.; Gubbins, K. E. and Quirke, N., *Pore size heterogeneity and the carbon slit pore: a density functional theory model*, Langmuir, 1993, **9**, 2693-2702.
9. Reid, C. R. and Thomas, K. M., *Adsorption of Gases on a Carbon Molecular Sieve Used for Air Separation: Linear Adsorptives as Probes for Kinetic Selectivity*, Langmuir, 1999, **15**, 3206-3218.
10. Sumida, K.; Rogow, D. L.; Mason, J. A.; McDonald, T. M.; Bloch, E. D.; Herm, Z. R.; Bae, T.-H. and Long, J. R., *Carbon dioxide capture in metal-organic frameworks*, Chem. Rev., 2011, **112**, 724-781.
11. Koh, H. S.; Rana, M. K.; Wong-Foy, A. G. and Siegel, D. J., *Predicting Methane Storage in Open-Metal-Site Metal-Organic Frameworks*, The Journal of Physical Chemistry C, 2015, **119**, 13451-13458.
12. Lin, Y.; Kong, C.; Zhang, Q. and Chen, L., *Metal-Organic Frameworks for Carbon Dioxide Capture and Methane Storage*, Advanced Energy Materials, 2017, **7**, 1601296-n/a.
13. Li, J.-R.; Sculley, J. and Zhou, H.-C., *Metal-organic frameworks for separations*, Chem. Rev., 2011, **112**, 869-932.
14. Rosi, N. L.; Eckert, J.; Eddaoudi, M.; Vodak, D. T.; Kim, J.; Keeffe, M. and Yaghi, O. M., *Hydrogen Storage in Microporous Metal-Organic Frameworks*, Science, 2003, **300**, 1127.
15. Liu, Y.; Wang, Z. U. and Zhou, H.-C., *Recent advances in carbon dioxide capture with metal-organic frameworks*, Greenhouse Gases: Science and Technology, 2012, **2**, 239-259.
16. Rubio-Martinez, M.; Avci-Camur, C.; Thornton, A. W.; Imaz, I.; Maspoch, D. and Hill, M. R., *New synthetic routes towards MOF production at scale*, Chemical Society Reviews, 2017, **46**, 3453-3480.
17. Rowsell, J. L. and Yaghi, O. M., *Strategies for hydrogen storage in metal-organic frameworks*, Angew. Chem. Int. Ed., 2005, **44**, 4670-4679.
18. Zhou, H.-C.; Long, J. R. and Yaghi, O. M., *Journal*, 2012.
19. Kuppler, R. J.; Timmons, D. J.; Fang, Q.-R.; Li, J.-R.; Makal, T. A.; Young, M. D.; Yuan, D.; Zhao, D.; Zhuang, W. and Zhou, H.-C., *Potential applications of metal-organic frameworks*, Coord. Chem. Rev., 2009, **253**, 3042-3066.
20. Doherty, C. M.; Buso, D.; Hill, A. J.; Furukawa, S.; Kitagawa, S. and Falcaro, P., *Using functional nano- and microparticles for the preparation of metal-organic framework composites with novel properties*, Acc. Chem. Res., 2013, **47**, 396-405.

21. Ricco, R.;Malfatti, L.;Takahashi, M.;Hill, A. J. and Falcaro, P.,*Applications of magnetic metal–organic framework composites*, Journal of Materials Chemistry A, 2013, **1**, 13033-13045.
22. Adhikari, A. K. and Lin, K.-S.,*Improving CO₂ adsorption capacities and CO₂/N₂ separation efficiencies of MOF-74(Ni, Co) by doping palladium-containing activated carbon*, Chem. Eng. J., 2016, **284**, 1348-1360.
23. Falcaro, P.;Ricco, R.;Yazdi, A.;Imaz, I.;Furukawa, S.;Maspoth, D.;Ameloot, R.;Evans, J. D. and Doonan, C. J.,*Application of metal and metal oxide nanoparticles@MOFs*, Coord. Chem. Rev., 2016, **307**, 237-254.
24. Bloch, E. D.;Murray, L. J.;Queen, W. L.;Chavan, S.;Maximoff, S. N.;Bigi, J. P.;Krishna, R.;Peterson, V. K.;Grandjean, F. and Long, G. J.,*Selective binding of O(2) over N(2) in a redox-active metal-organic framework with open iron(II) coordination sites*, J. Am. Chem. Soc., 2011, **133**, 14814-14822.
25. Märzc, M.;Johnsen, R. E.;Dietzel, P. D. C. and Fjellvåg, H.,*The iron member of the CPO-27 coordination polymer series: Synthesis, characterization, and intriguing redox properties*, Microporous and Mesoporous Materials, 2012, **157**, 62-74.
26. Sumida, K.;Rogow, D. L.;Mason, J. A.;McDonald, T. M.;Bloch, E. D.;Herm, Z. R.;Bae, T.-H. and Long, J. R.,*Carbon Dioxide Capture in Metal–Organic Frameworks*, Chem. Rev., 2012, **112**, 724-781.
27. Bae, Y.-S.;Spokoyny, A. M.;Farha, O. K.;Snurr, R. Q.;Hupp, J. T. and Mirkin, C. A.,*Separation of gas mixtures using Co(ii) carborane-based porous coordination polymers*, Chem. Commun., 2010, **46**, 3478-3480.
28. Murray, L. J.;Dinca, M.;Yano, J.;Chavan, S.;Bordiga, S.;Brown, C. M. and Long, J. R.,*Highly-selective and reversible O₂ binding in Cr³⁺ (1, 3, 5-benzenetricarboxylate) ₂*, J. Am. Chem. Soc., 2010, **132**, 7856-7857.
29. Tlili, N.;Grévillet, G. and Vallières, C.,*Carbon dioxide capture and recovery by means of TSA and/or VSA*, International Journal of Greenhouse Gas Control, 2009, **3**, 519-527.
30. Mason, J. A.;Sumida, K.;Herm, Z. R.;Krishna, R. and Long, J. R.,*Evaluating metal-organic frameworks for post-combustion carbon dioxide capture via temperature swing adsorption*, Energy & Environmental Science, 2011, **4**, 3030-3040.
31. Hedin, N.;Andersson, L.;Bergström, L. and Yan, J.,*Adsorbents for the post-combustion capture of CO₂ using rapid temperature swing or vacuum swing adsorption*, Applied Energy, 2013, **104**, 418-433.
32. Songolzadeh, M.;Soleimani, M.;Takht Ravanchi, M. and Songolzadeh, R.,*Carbon Dioxide Separation from Flue Gases: A Technological Review Emphasizing Reduction in Greenhouse Gas Emissions*, The Scientific World Journal, 2014, **2014**, 828131.
33. Morris, R. E. and Wheatley, P. S.,*Gas Storage in Nanoporous Materials*, Angew. Chem. Int. Ed., 2008, **47**, 4966-4981.
34. Lyndon, R.;Konstas, K.;Evans, R. A.;Keddie, D. J.;Hill, M. R. and Ladewig, B. P.,*Tunable Photodynamic Switching of DArE@PAF-1 for Carbon Capture*, Adv. Funct. Mater., 2015, **25**, 4405-4411.
35. Lyndon, R.;Konstas, K.;Thornton, A. W.;Seeber, A. J.;Ladewig, B. P. and Hill, M. R.,*Visible Light-Triggered Capture and Release of CO₂ from Stable Metal Organic Frameworks*, Chemistry of Materials, 2015, **27**, 7882-7888.
36. Lyndon, R.;Konstas, K.;Ladewig, B. P.;Southon, P. D.;Kepert, P. C. J. and Hill, M. R.,*Dynamic Photo-Switching in Metal–Organic Frameworks as a Route to Low-Energy Carbon Dioxide Capture and Release*, Angew. Chem. Int. Ed., 2013, **52**, 3695-3698.
37. Falcaro, P.;Lapierre, F.;Marmiroli, B.;Styles, M.;Zhu, Y.;Takahashi, M.;Hill, A. J. and Doherty, C. M.,*Positioning an individual metal–organic framework particle using a magnetic field*, Journal of Materials Chemistry C, 2013, **1**, 42-45.
38. Lucia, O.;Maussion, P.;Dede, E. J. and Burdío, J. M.,*Induction heating technology and its applications: past developments, current technology, and future challenges*, IEEE Transactions on Industrial Electronics, 2014, **61**, 2509-2520.
39. Bañobre-López, M.;Teijeiro, A. and Rivas, J.,*Magnetic nanoparticle-based hyperthermia for cancer treatment*, Reports of Practical Oncology & Radiotherapy, 2013, **18**, 397-400.

40. Ma, M.;Zhang, Y.;Shen, X.;Xie, J.;Li, Y. and Gu, N.,*Targeted inductive heating of nanomagnets by a combination of alternating current (AC) and static magnetic fields*, Nano Research, 2015, **8**, 600-610.
41. Kolhatkar, A.;Jamison, A.;Litvinov, D.;Willson, R. and Lee, T.,*Tuning the Magnetic Properties of Nanoparticles*, Int. J. Mol, 2013, **14**, 15977.
42. Rudolf, H.;Silvio, D.;Robert, M. and Matthias, Z.,*Magnetic particle hyperthermia: nanoparticle magnetism and materials development for cancer therapy*, J. Phys.: Condens. Matter, 2006, **18**, S2919.
43. Li, H.;Sadiq, M. M.;Suzuki, K.;Ricco, R.;Doblin, C.;Hill, A. J.;Lim, S.;Falcaro, P. and Hill, M. R.,*Magnetic Metal–Organic Frameworks for Efficient Carbon Dioxide Capture and Remote Trigger Release*, Adv. Mater., 2016, **28**, 1839-1844.
44. Sadiq, M. M.;Li, H.;Hill, A. J.;Falcaro, P.;Hill, M. R. and Suzuki, K.,*Magnetic Induction Swing Adsorption: An Energy Efficient Route to Porous Adsorbent Regeneration*, Chemistry of Materials, 2016, **28**, 6219-6226.
45. Li, H.;Sadiq, M. M.;Suzuki, K.;Doblin, C.;Lim, S.;Falcaro, P.;Hill, A. J. and Hill, M. R.,*MaLISA—a cooperative method to release adsorbed gases from metal–organic frameworks*, Journal of Materials Chemistry A, 2016, **4**, 18757-18762.
46. Li, H.;Sadiq, M. M.;Suzuki, K.;Falcaro, P.;Hill, A. J. and Hill, M. R.,*Magnetic Induction Framework Synthesis: A General Route to the Controlled Growth of Metal–Organic Frameworks*, Chem. Mater., 2017, **29**, 6186-6190.
47. Lyndon, R.;Konstas, K.;Ladewig, B. P.;Southon, P. D.;Kepert, P. C. J. and Hill, M. R.,*Dynamic Photo-Switching in Metal–Organic Frameworks as a Route to Low-Energy Carbon Dioxide Capture and Release*, Angew. Chem. Int. Ed., 2013, **52**, 3695-3698; Angew. Chem. 2013, 3125, 3783-3786.
48. Barreto, A. C. H.;Santiago, V. R.;Freire, R. M.;Mazzetto, S. E.;Denardin, J. C.;Mele, G.;Cavalcante, I. M.;Ribeiro, M. E. N. P.;Ricardo, N. M. P. S.;Gonçalves, T.;Carbone, L.;Lemos, T. L. G.;Pessoa, O. D. L. and Fachine, P. B. A.,*Magnetic Nanosystem for Cancer Therapy Using Oncocalyxone A, an Antitumor Secondary Metabolite Isolated from a Brazilian Plant*, International Journal of Molecular Sciences, 2013, **14**, 18269-18283.
49. Ke, F.;Yuan, Y.-P.;Qiu, L.-G.;Shen, Y.-H.;Xie, A.-J.;Zhu, J.-F.;Tian, X.-Y. and Zhang, L.-D.,*Facile fabrication of magnetic metal-organic framework nanocomposites for potential targeted drug delivery*, J. Mater. Chem., 2011, **21**, 3843-3848.
50. Rosi, N. L.;Kim, J.;Eddaoudi, M.;Chen, B.;O’Keeffe, M. and Yaghi, O. M.,*Rod packings and metal–organic frameworks constructed from rod-shaped secondary building units*, J. Am. Chem. Soc., 2005, **127**, 1504-1518.
51. Dietzel, P. D.;Besikiotis, V. and Blom, R.,*Application of metal–organic frameworks with coordinatively unsaturated metal sites in storage and separation of methane and carbon dioxide*, J. Mater. Chem., 2009, **19**, 7362-7370.
52. Dietzel, P. D.;Georgiev, P. A.;Eckert, J.;Blom, R.;Strässle, T. and Unruh, T.,*Interaction of hydrogen with accessible metal sites in the metal–organic frameworks M₂(dhtp)(CPO-27-M; M= Ni, Co, Mg)*, Chem. Commun., 2010, **46**, 4962-4964.
53. Dietzel, P. D.;Johnsen, R. E.;Fjellvåg, H.;Bordiga, S.;Groppo, E.;Chavan, S. and Blom, R.,*Adsorption properties and structure of CO₂ adsorbed on open coordination sites of metal–organic framework Ni₂(dhtp) from gas adsorption, IR spectroscopy and X-ray diffraction*, Chem. Commun., 2008, 5125-5127.
54. Southon, P. D.;Price, D. J.;Nielsen, P. K.;McKenzie, C. J. and Kepert, C. J.,*Reversible and selective O₂ chemisorption in a porous metal–organic host material*, J. Am. Chem. Soc., 2011, 133, 10885-10891.
55. Sugimoto, H.;Nagayama, T.;Maruyama, S.;Fujinami, S.;Yasuda, Y.;Suzuki, M. and Uehara, A.,*Thermodynamic study on dioxygen binding of diiron (II) and dicobalt (II) complexes containing various dinucleating ligands*, Bull. Chem. Soc. Jpn., 1998, **71**, 2267-2279.
56. Suzuki, M.;Kanatomi, H. and Murase, I.,*Synthesis and Properties of binuclear Cobalt (II) Oxygen Adduct with 2, 6-bis [bis (2-pyridylmethyl) aminomethyl]-4-methylphenol*, Chem. Lett., 1981, **10**, 1745-1748.

57. Hui, C.;Shen, C.;Yang, T.;Bao, L.;Tian, J.;Ding, H.;Li, C. and Gao, H. J.,*Large-Scale Fe₃O₄ Nanoparticles Soluble in Water Synthesized by a Facile Method*, The Journal of Physical Chemistry C, 2008, **112**, 11336-11339.
58. Yang, T.;Shen, C.;Li, Z.;Zhang, H.;Xiao, C.;Chen, S.;Xu, Z.;Shi, D.;Li, J. and Gao, H.,*Highly Ordered Self-Assembly with Large Area of Fe₃O₄ Nanoparticles and the Magnetic Properties*, The Journal of Physical Chemistry B, 2005, **109**, 23233-23236.
59. Sun, S.;Zeng, H.;Robinson, D. B.;Raoux, S.;Rice, P. M.;Wang, S. X. and Li, G.,*Monodisperse MFe₂O₄ (M = Fe, Co, Mn) nanoparticles*, J. Am. Chem. Soc., 2004, **126**, 273-279.
60. Popa, C.;Prodan, A.;Chapon, P.;Turculec, C. and Predoi, D.,*Inhibitory effect evaluation of glycerol-iron oxide thin films on methicillin-resistant Ataphylococcus aureus*, Journal of Nanomaterials, 2015, **2015**, 5.
61. Zhang, W.;Liu, H.;Sun, Y.;Cakstins, J.;Sun, C. and Snape, C. E.,*Parametric study on the regeneration heat requirement of an amine-based solid adsorbent process for post-combustion carbon capture*, Applied Energy, 2016, **168**, 394-405.
62. Construction, A. L. E.,*Standard Plants*, 04-2017.
63. Xiao, D. J.;Gonzalez, M. I.;Darago, L. E.;Vogiatzis, K. D.;Haldoupis, E.;Gagliardi, L. and Long, J. R.,*Selective, Tunable O₂ Binding in Cobalt(II)-Triazolate/Pyrazolate Metal-Organic Frameworks*, J. Am. Chem. Soc., 2016, **138**, 7161-7170.
64. Kloutse, A.;Zacharia, R.;Cossement, D.;Chahine, R.;Balderas-Xicohtencatl, R.;Oh, H.;Streppel, B.;Schlichtenmayer, M. and Hirscher, M.,*Isosteric heat of hydrogen adsorption on MOFs: comparison between adsorption calorimetry, sorption isosteric method, and analytical models*, Applied Physics A, 2015, **121**, 2.
65. Schmitz, B.;Müller, U.;Trukhan, N.;Schubert, M.;Férey, G. and Hirscher, M.,*Heat of Adsorption for Hydrogen in Microporous High-Surface-Area Materials*, ChemPhysChem, 2008, **9**, 2181-2184.

Chapter 5:
**Performance evaluation of CuBTC composites for
room temperature Oxygen storage**

Chapter 5: Performance evaluation of CuBTC composites for room temperature Oxygen storage
..... 63

5.1 Introduction..... 64

5.2 Published Work..... 64

5.2.1 Abstract 65

5.2.2 Introduction..... 65

5.2.3 Experimental 67

5.2.3.1 Materials synthesis:..... 67

5.2.3.2 Characterisation of materials: 68

5.2.4 Results and Discussion 69

5.2.5 Conclusions..... 78

5.3 Supporting Information and Acknowledgements 78

5.4 References..... 80

5.1 Introduction

Oxygen is most commonly separated from air using cryogenic liquefaction and the inherent energy penalties of a phase change inspire the search for more energy efficient separation processes. The safety hazards associated with the handling and storing of a highly reactive gas like oxygen, equal emphasis is required on finding alternate means to counter the current high-pressure (ca. 140 Bar) storage of oxygen; a safe, lightweight alternative that would store oxygen in high volumes but at much lower pressures.

As discussed in **Chapter 4**, Metal-Organic Frameworks offer the alternative process for separations and storage of oxygen by forming a bond with the metal cations from the framework, leading to higher selectivity of oxygen over other gases, especially nitrogen. As observed from the oxygen adsorption isotherms of the Co-MOF-74 at 204 K, the adsorption capacity of the MOF is higher at low temperatures. Using MISA, 100 % desorption of adsorbed oxygen molecules was achieved at 204 K. The real challenge with a reactive gas like oxygen is its adsorption and storage at room temperatures. And if the energy requirements associated with cryogenic temperatures are to be overcome, the adsorption should be targeted at room temperature. Therefore, in **Chapter 5**, the aim is to explore the potential of Cu-BTC MOFs for room temperature storage of oxygen. CuBTC (Copper (II) benzene-1,3,5-tricarboxylate) MOF is one of the most popular and widely used MOFs in various applications. To target the release of the adsorbed oxygen molecules at room temperature, CuBTC composite pellets were synthesised with MgFe₂O₄ nanoparticles. The composite with 3 wt.% nanoparticles exhibited an Oxygen uptake capacity of 0.34 mmol/g at 298 K. When exposed to a magnetic field of 31 mT, the magnetic nanoparticles heated up and attained a temperature rise of 86 °C and released 100 % of adsorbed Oxygen. Using MISA, the composite was regenerated for the next adsorption cycle within 10 minutes requiring around 5.6 MJ/kg.

Chapter 5 is based on the manuscript titled, “*Performance evaluation of CuBTC composites for room temperature Oxygen storage*” published in RSC Advances on 27th October 2020. This demonstrates the room temperature storage potential of CuBTC MOF and the versatility of the MISA process in achieving 100 % desorption of the stored oxygen and 100% regeneration of the MOF within 10 minutes.

5.2 Published Work

This section discusses work previously published in a journal article, reproduced with permission from Melag *et al.*[12] © Royal Society of Chemistry 2020. Figures and references from this publication have been renumbered for consistency with the Chapter. A copy of this work is included as **Appendix B**. RSC Adv., 2020, <https://doi.org/10.1039/D0RA07068H>

Performance evaluation of CuBTC composites for room temperature Oxygen storage

Leena Melag, M. Munir Sadiq, Kristina Konstas, Farnaz Zadehahmadi, Kiyonori Suzuki and

Matthew R. Hill

RSC Adv., 2020, <https://doi.org/10.1039/D0RA07068H>

5.2.1 Abstract

Oxygen is most commonly separated from air using cryogenic liquefaction. The inherent energy penalties of a phase change inspire the search for more energy-efficient separation processes. Adsorption and release by Metal-Organic Frameworks (MOFs) are an attractive alternative due to their high capacity at ambient conditions, lowering the energy requirements. Much progress has been made at cryogenic temperatures or high pressures, but examples of cyclable materials at room temperature are rare. Many require high nitrogen loadings, which present safety issues when saturated with oxygen. Here, an alternative approach is presented, where we determine whether it is possible to utilize simpler, stable materials in the right process to achieve overall energy efficiency. Cu-BTC/MgFe₂O₄ composites were prepared, and magnetic induction swing adsorption (MISA) used to release adsorbed oxygen quickly and efficiently. The composite with 3 wt. % MgFe₂O₄ exhibited an oxygen uptake capacity of 0.34 mmol/g at 298 K and when exposed to a magnetic field of 31 mT, attained a temperature rise of 86 °C and released 100 % of adsorbed oxygen. The pelletised system, which is stable to water vapor, can be filled and emptied within 10 minutes requiring around 5.6 MJ/kg.

5.2.2 Introduction

The demand for high purity oxygen is on the rise owing to its increased consumption by the healthcare, steel, food, water, chemical, and pharmaceutical industries and this, in turn, has influenced research into more energy-efficient ways to capture, separate and store oxygen^{1, 2}. The traditional process of cryogenic liquefaction of air³ produces ultra-high purity oxygen and still dominates the industrial methods of oxygen separation, but the complex plant setups and the energy requirements associated with the entire process limits its use for large scale productions only. The membrane-based separations and adsorption-based processes using zeolites and carbon molecular sieves are simpler, reversible, low cost and easily scalable for small scale separations of oxygen, but their structural rigidity, pore heterogeneity, and low oxygen permeabilities impose limitations on the purity of the oxygen produced⁴. Once produced, compressed or liquefied oxygen is bottled up in storage tanks for subsequent use in varied applications^{2, 5-7}. Taking into account the safety hazards associated with the handling and storing of a highly reactive gas like oxygen, equal emphasis is required on finding alternate means to counter

the current high-pressure (ca. 140 Bar) storage of oxygen; a safe, lightweight alternative that would store oxygen in high volumes but at much lower pressures⁸⁻¹⁰.

Metal-Organic Frameworks (MOFs) are porous nanomaterials that have been explored for gas separations¹¹⁻¹⁴, catalysis¹⁵, sensing^{11, 16-23}, and drug delivery applications^{24, 25}. They are constructed using metal nodes and organic linkers resulting in unique modular structures that are flexible, porous and offer the distinctive chemical tunability needed for gas storage²⁶⁻²⁸. Their ability to host functional nanoparticles within their structures imparts added diverse functionalities to their existing versatile properties²⁹. Similar to most adsorption processes, separations in MOFs are based on the guest-host interactions where the adsorbents can either physically adsorb gas molecules on its surface or can bind to them chemically³⁰. For selective separations using MOFs, the selectivity between the different gas molecules relies on preferential size-selective sieving or favorable quadrupole interactions or strong chemical affinities with either of the adsorbates³¹. Most oxygen separation processes are nitrogen selective and are based on the adsorption or isolation of nitrogen from the air to separate oxygen. However, using MOFs, selective oxygen separation has been studied through a process that relies on oxygen molecules directly binding to the metal cations in the framework leading to higher selectivity over other gases, mainly nitrogen³²⁻³⁵. Accordingly, to investigate the role of MOFs in oxygen separation and storage, DeCoste *et al.* conducted simulation studies on 10,000 hypothetical MOFs and recorded NU-125 as the MOF with the highest oxygen adsorption capacity of 17.4 mol/kg at 140 Bar pressure. Computational studies by Moghadam *et al.* on 2932 existing MOFs reported UMCM-152 as the MOF with the highest oxygen uptake of 20.4 mmol/kg. Similarly, various other MOFs like IRMOFs, UiO-66, Cr₃(BTC)₂^{33, 35, 36}, Cr-BTT³⁷, and M₂(dobdc) (M = Cr, Mn, Fe, Co), especially Co₂(dobdc)³⁸⁻⁴⁰ and Fe₂(dobdc)^{35, 41, 42} have been investigated in detail as oxygen selective adsorbents for separation and storage of oxygen. Apart from specially designed and developed MOFs, the existing range of MOFs need to be explored for a simpler, stable and recyclable solution for room temperature oxygen storage. This paper investigates a widely used copper-based MOF, CuBTC, also known as HKUST-1 or MOF-199, previously identified by both DeCoste *et al.* and Moghadam *et al.* for oxygen storage applications.

CuBTC, Copper (II) benzene-1,3,5-tricarboxylate, is one of the widely explored, easily scalable, and most commercially used MOFs in various applications. Its ease of synthesis, high surface areas (1500–2000 m²/g), and excellent thermal and structural stability make it applicable for gas adsorption⁴³⁻⁴⁷, separation^{44, 48-51}, and sensors^{17, 52, 53} applications. It is a very popular Cu (II) framework where the dimeric copper-tetracarboxylic unit of Cu-Cu (2.628Å) acts as a centre and is connected by four oxygen atoms from the benzenetricarboxylate (BTC) linkers and water molecules⁵⁴⁻⁵⁷. The interconnected Cu (II) paddlewheel unit and tridentate BTC linkers form a three-dimensional octahedral structure with

square-shaped main channels of $9 \times 9 \text{ \AA}$ and tetrahedral units of 5 \AA openings that are connected to the main channels by triangular pockets of 3.5 \AA .

Temperature Swing Adsorption (TSA) and Pressure Swing Adsorption (PSA) are the most commonly used regeneration processes for MOFs. However, their strong host-guest interactions with the adsorbed molecules, particularly the strong adsorption at lower partial pressures and their thermally insulating nature, limit the uniform transfer of the applied heat throughout the MOF, making the regeneration process very challenging and energy-intensive^{11, 58-62}. To address this, our group has demonstrated the potentials of incorporating stimuli-responsive materials in MOFs to achieve energy-efficient release of the trapped gases^{11, 39, 58, 59, 63-67}. In this paper, we discuss how rapid and remote heat generation can be achieved through the fabrication of magnetic framework composites (MFCs) and how their interactions with a magnetic field can be used efficiently for release of the adsorbed molecules. Magnetic induction swing adsorption (MISA) is a magnetically induced heating process aimed at regeneration of MOFs⁶⁸⁻⁷⁰. In our previous paper, we have demonstrated the efficiency of the MISA process by desorption of 4.8 mmol/g of adsorbed oxygen from Co-MOF-74/ Fe_3O_4 systems. To build upon these results obtained at cryogenic temperatures of 204 K , we intend to explore the possibility of simpler, stabler, cyclable MOFs for Oxygen adsorption at room temperature. This paper looks into the relative stability and capacity of CuBTC MOF for oxygen storage, and the feasibility of oxygen release using magnetic induction swing adsorption (MISA) at room temperatures.

The exposure of CuBTC MFC pellets formed using 3 wt. \% of MgFe_2O_4 nanoparticles, to a magnetic field of 33 mT , triggered a 100 \% release of the 0.30 mmol/g oxygen molecules stored at 1 Bar pressure. The ease of use and control of the MISA process was demonstrated by triggering an on-demand release of Oxygen at $200, 400, 600, 800, \text{ and } 1000 \text{ mBar}$ pressures and achieving 100 \% desorption each time. Three continuous cycles of adsorption and magnetically triggered desorption cycles helped to establish the structural rigidity, thermal stability, and adsorption capacity of the CuBTC MFC. The effect of atmospheric exposure, and the effect of exposure to water vapour on the structural stability of the MFCs, was also investigated.

5.2.3 Experimental

5.2.3.1 Materials synthesis:

All the reagents including 1,3,5-benzenetricarboxylic acid (H_3BTC), copper acetate monohydrate $\text{Cu}(\text{OAc})_2 \cdot \text{H}_2\text{O}$, sodium acetate trihydrate ($\text{CH}_3\text{COONa} \cdot 3\text{H}_2\text{O}$), magnesium chloride hexahydrate ($\text{MgCl}_2 \cdot 6\text{H}_2\text{O}$), Ferric chloride hexahydrate ($\text{FeCl}_3 \cdot 6\text{H}_2\text{O}$), PEG and the solvents, N, N-

dimethylformamide (DMF) and ethanol used for the synthesis were of analytical grade, obtained from commercial vendors and used as received.

Synthesis of CuBTC MOF:

0.7 g of copper acetate monohydrate (3.5 mmol) dissolved in 14 mL of deionized water was mixed with 0.6 g of trimesic acid (H₃BTC, 2.8 mmol) dissolved in 14 mL of ethanol. This mixture was stirred for 30 min, transferred into an autoclave, and heated to 85 °C for 24 hrs. On cooling, the blue CuBTC MOF was washed three times with ethanol and dried in a vacuum oven at 140 °C for 24 hrs^{50, 71}.

Synthesis of MgFe₂O₄ nanoparticles:

MgFe₂O₄ nanoparticles were synthesized using a solvothermal method by mixing of 3.6 g, 0.027 moles of sodium acetate trihydrate, 2.5 mmol MgCl₂·6H₂O and 5 mmol FeCl₃·6H₂O together and adding 2.00 g of polyethylene glycol (MW = 4000) as a surfactant. The mixture is stirred vigorously to form a homogeneous solution and then heated under reflux at 180 °C for 16 hrs. On cooling, the black magnetic nanoparticles are magnetically separated and washed alternately with distilled water and ethanol and dried in a vacuum oven at 80 °C for 8 hrs⁷².

Fabrication of CuBTC pellets:

The objective behind the shaping of MOFs is to pack maximum amounts of adsorbents in the storage tank compactly, to increase the amount of gas stored per unit volume. For practical applications, shaping MOFs is favourable. Still, the shaping technique should not adversely affect the stability and or adsorption capacity of the MOFs, and it should be feasible for large scale productions too. The most common shaping technique, pelletising, can be achieved by either applying a certain amount of pressure on the powdered MOFs to shape them into pellets or by mixing the MOF powder with specific binders (typically, polyvinyl alcohol (PVA)) and solvent to make a paste that can be further extruded into pellets^{50, 71}. The Cu-BTC/MgFe₂O₄ MFCs were pelletised by extruding a paste made using measured quantities of CuBTC MOF, binder, and MgFe₂O₄ nanoparticles, through a 5 mL syringe. The extruded MFC noodles were cut into 8-10 mm pellets and allowed to dry in ambient air before drying them in a vacuum oven at 140 °C for 24 hrs. To select an MFC having an optimal balance between adsorption capacities, heating abilities, and structural stability, different MFCs with varying binder concentrations (1, 2, 3, 4 wt. %) and varying magnetic content (1, 2, 3, 4 wt. % of MgFe₂O₄ nanoparticles) were fabricated and investigated for their surface area and oxygen adsorption properties.

5.2.3.2 Characterisation of materials:

The samples were characterised using X-Ray Powder Diffraction (XRD), Scanning Electron Microscopy (SEM), Energy Dispersive Spectroscopy (EDS) and Thermogravimetric analysis (TGA). Fourier-Transform Infrared (FTIR) spectra for all samples were collected using a Thermo Scientific NICOLET 6700 FT-IR. XRD measurements analysed the crystal structure of the samples on a D8 ADVANCE Eco X-ray powder diffractometer with a Co K_{α} radiation source of 1.79Å with a scan rate of 0.05 sec per step at 40 kV and 25 mA. JOEL 7001F Scanning Electron Microscope was used for the morphological size-shape study of all the samples. The surface area measurements were carried out using Micromeritics ASAP 2420 instruments, and the Oxygen adsorption studies were carried out on a 3Flex surface and catalyst characterisation instrument. For the triggered release experiments, the 3Flex was paired with an induction machine (EASY HEAT 0224–Ambrell) with an 8 turns heating coil of 2.5 cm diameter and 4 cm in length.

5.2.4 Results and Discussion

Figure 5.1-a. presents the diffraction patterns of the synthesized powdered CuBTC MOF, the magnetic nanoparticles, and the MFCs fabricated with 1 wt.%, 2 wt.%, and 3 wt.%, $MgFe_2O_4$ nanoparticles. The diffraction peaks from the synthesized CuBTC sample corresponds to the face centred cubic (FCC) CuBTC structure, that matches well with the peaks of the simulated CuBTC (Figure S1-a). The clear, distinct sharp peaks confirm the excellent crystallinity of the sample. The morphology of the bare CuBTC and composite was investigated with Scanning Electron Microscopy (SEM) analysis. SEM micrographs presented in Figure 5.1- b and d) reveal octahedral shaped CuBTC particles with an average particle size of about 5 μm . Figure 5.1-c shows a uniform, spherical morphology for $MgFe_2O_4$ nanoparticles with a diameter of 150-170 nm. The nanoparticles were used to fabricate the MFCs by varying their concentrations during the pelletization process. Figure 5.1-e is a micrograph of the MFC with 3 wt.%, $MgFe_2O_4$ nanoparticles which reveal the magnetic nanoparticles firmly bound to the surfaces of the MOF particles. The XRD analysis of the synthesized $MgFe_2O_4$ nanoparticles (Figure S2- a) shows the diffraction peaks of planes (2 2 0), (3 1 1), (4 0 0), (5 1 1) and (4 4 0), for a cubic spinel $MgFe_2O_4$ phase, that matches the standard powder diffraction data (ICSD #00-036-0398) of the $MgFe_2O_4$ phase from literature ⁷² with a calculated mean crystallite size of 10.2 nm.

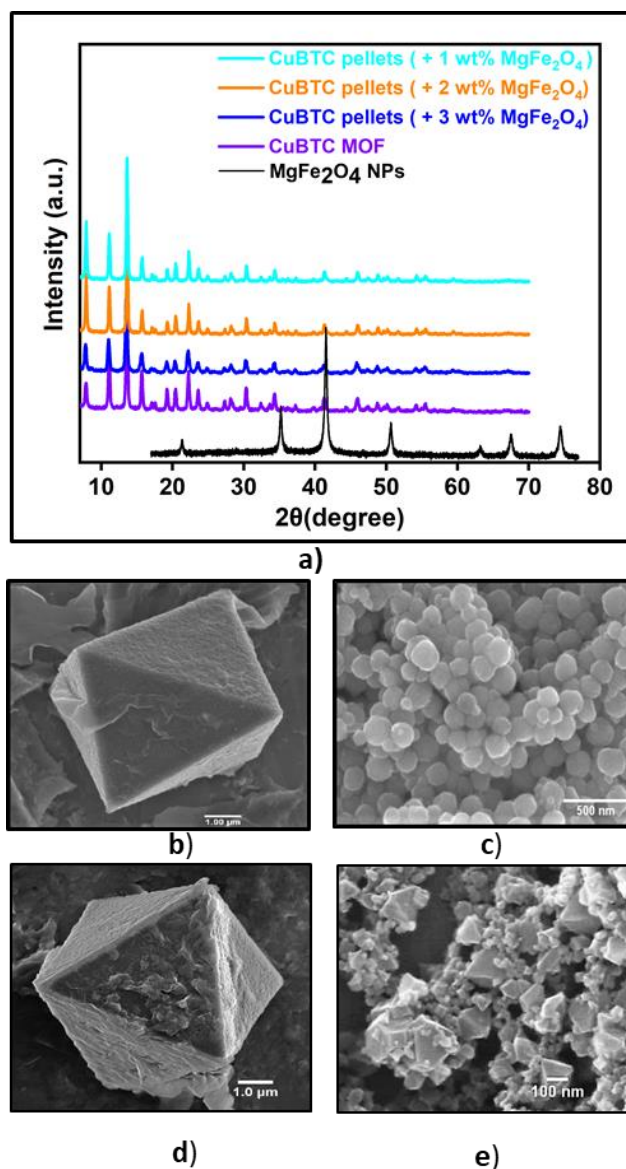


Figure 5.1: a) The powder diffraction pattern of bare CuBTC MOF, MgFe₂O₄ nanoparticles, CuBTC-MgFe₂O₄ composite with 1 wt.%, 2 wt.%, 3 wt.% magnetic content, and SEM images of b) bare CuBTC c) the MgFe₂O₄ nanoparticles d) bare CuBTC e) 3 wt.% CuBTC-MgFe₂O₄ composite.

Vibrating sample magnetometer (RIKEN DENSHI VSM) was used to study the response of MgFe₂O₄ nanoparticles to an applied magnetic field. When exposed to an applied magnetic field, the magnetization (M), of the MgFe₂O₄ nanoparticles increases with an increase in the magnetic field until it becomes saturated and any increase in the magnetic field cannot increase its magnetization anymore. A reverse magnetic field brings the magnetization back to zero. This response is plotted in the form of a magnetization curve, and the magnetization curve of the synthesized MgFe₂O₄ nanoparticles shows a saturation magnetization (M_s) of 65 emu g⁻¹ (Figure S3-a). The Curie temperature (T_c) of the MgFe₂O₄ nanoparticles, defined as the temperatures above which the ferrimagnetic magnetic nanoparticles lose their magnetic properties and become paramagnetic^{12, 73-76}, was evaluated through Thermo-magneto

gravimetric analysis (TMGA) (Figure S4-c). This was estimated to be 566 °C. This agrees with T_c values reported in the literature for $MgFe_2O_4$ ^{58, 65, 68}. Specific adsorption rate, SAR, is a parameter used in estimating the magnitude of the heating effect generated by magnetic nanoparticles when exposed to alternating current magnetic field^{11, 58, 65, 68}. The SAR is a valuable parameter that can be used to estimate the rate of conversion of a magnetic field to thermal energy with a high SAR indicating rapid heating. The SAR of the synthesized $MgFe_2O_4$ nanoparticles was calculated to be 130 W/g.

For gas adsorption measurements, the CuBTC samples were activated at 140 °C for 24 hrs under vacuum. N_2 adsorption isotherms obtained at 77 K show a type I adsorption that is typically observed in microporous solids. The calculated Brunauer–Emmett–Teller (BET) surface areas of the bare CuBTC MOF and MFCs are summarized in Table S1 and Figure S5-a. The BET surface area of the bare CuBTC MOF was 1495 m²/g, and upon addition of 1 wt.% binder, a drop of 23 % in surface area was noticed. This loss in surface area can be attributed to the process of pelletising where the binders, that are essential to enable cohesion and densification of the MOFs, cause partial blockage of some pores in the MOF resulting in lower surface areas and pore volumes⁷⁷. Based on such effects of different binder concentrations and varying magnetic contents on the surface area properties of the MFC, the Cu-BTC/ $MgFe_2O_4$ composites with 3 wt.% binder concentration and 3 wt.% $MgFe_2O_4$ nanoparticles were selected fabricated for all the experiments.

To evaluate the potential of these Cu-BTC/ $MgFe_2O_4$ MFCs for room temperature oxygen storage applications, it is crucial to establish their moisture stability in ambient atmospheric conditions⁷⁸. Water adsorption experiments were conducted to test the water stability of the MFCs using Micromeritics 3Flex gas sorption analyser for the range ($P/P_0 = 0.001-0.9$) at 298 K with dry N_2 as the carrier gas. Prior to the vapour adsorption measurements, the CuBTC samples were activated at 140 °C for 12 hrs. The initial steep slope (0.001-0.2), the intermediate shallow plateau (0.2- 0.7) and the last steep slope (0.7- 0.9) of the water adsorption isotherm are all indicative of the strong interactions between the water molecules and the copper centres from the initial adsorption in the CuBTC cages to the final micropore filling of the side pockets. The water vapour adsorption capacity of 28.4 mmol/g of the CuBTC MOF matches well with the results reported in the literature⁴⁵. The water vapour adsorption capacity of the 3 wt.% CuBTC- $MgFe_2O_4$ composite pellets plotted in Figure 5.2, was found to be 28.9 mmol/g. Post water adsorption experiments, the structural stability of the MOF and MFC were analysed by powder X-ray diffraction (PXRD), and the matching XRD peak intensities of the activated samples and the hydrated samples confirm the structural stability .

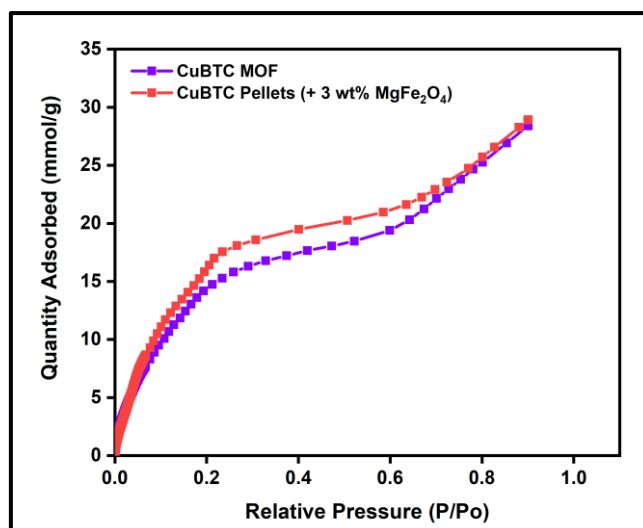


Figure 5.2: Water vapour adsorption isotherms of CuBTC MOF and 3 wt.% CuBTC-MgFe₂O₄ composite pellets measured at 298 K.

Oxygen adsorption:

To evaluate the oxygen adsorption properties of CuBTC pellets, single-component oxygen adsorption measurements were carried out at 204, 273 and 298 K (pressures loadings between 0 to 1 Bar), where around 80 mg of weighed CuBTC pellets were activated at 140 °C for 24 hrs under vacuum. The adsorption temperatures of 204, 273, and 298 K were stabilized using acetone and dry-ice bath, ice bath, and water bath, respectively. The results from the oxygen adsorption at these three temperatures reveal that at 204 K, the pellets displayed the highest adsorption capacity of 4.2 mmol/g of oxygen, followed by 0.5 mmol/g oxygen at 273 K and 0.34 mmol/g of oxygen was adsorbed at 298 K (Figure 5.3). These results confirm the adsorption capacity of the MOF at all three temperatures. The isosteric heat of adsorption, Q_{st} , reveals the extent of interaction between the adsorbed molecules and the adsorbate under constant loading conditions. In the case of CuBTC MOF¹³, this interaction that is primarily dependant on the reactions at the exposed cationic Cu²⁺ sites and adsorption at the windows sites of the octahedral CuBTC cage is calculated to be -15.3 kJ/mol. This near-constant Q_{st} curve was plotted using the adsorption data measured at 204, 273, and 298 K and shows that irrespective of the loading conditions the binding energies remain constant.

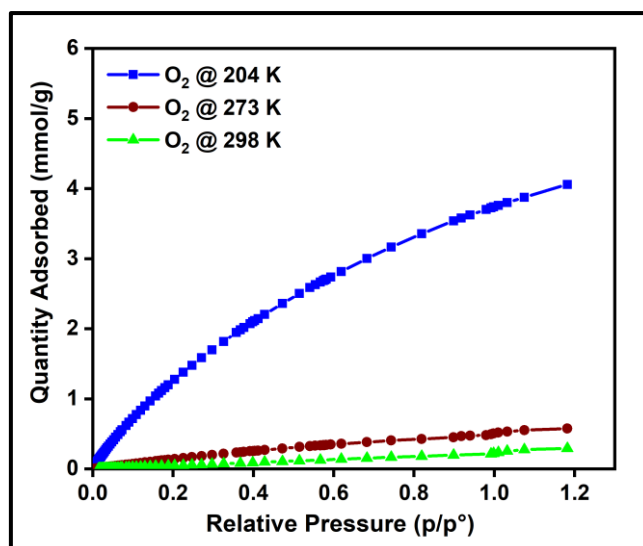


Figure 5.3: Oxygen adsorption isotherms of CuBTC MOF measured at 204, 273, and 298 K.

To study the reversibility and reusability of the MFC pellets after their interactions with oxygen at room temperature, cyclic studies were carried out on the same sample. Between every oxygen adsorption cycle, the sample was regenerated at 140 °C for 12 hrs. As observed from Figure 5.4, over twenty continuous cycles the MFC pellets displayed a consistent oxygen adsorption capacity and did not show any signs of material degradation even after the 20th cycle which was later confirmed by PXRD (Figure S-10). Thermal stabilities and decomposition temperatures of the samples were also studied by thermal gravimetric analysis (TGA) using weighed samples that were heated from 25 °C to 800 °C at a heating rate of 10 °C/min (Figure S7-a).

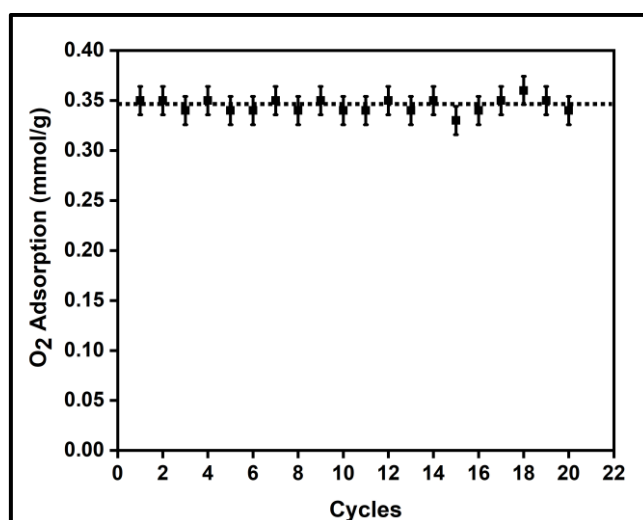


Figure 5.4: Twenty oxygen adsorption-desorption cycles on the 3 wt.% CuBTC-MgFe₂O₄ composite pellets at 298 K.

Desorption of Oxygen using MISA:

The adsorption potential of the MOFs and the heating abilities of the magnetic nanoparticles are combined to develop the MFCs. This is to enable efficient heat transfer in the MOF by overcoming their low thermal conductivities. It is achieved using ferrimagnetic nanoparticles capable of remote, targeted, and localised heat generation capabilities upon exposure to a magnetic field^{59, 79, 80}. The heat generation in the nanoparticles is a result of hysteresis observed in the magnetization vs applied field plot when the ferrimagnets are exposed to an alternating current magnetic field. A magnetization-demagnetization process is induced with the magnitude of the heat generated equivalent to the area within the hysteresis loop^{68,81, 82}. Consequently, in MFCs, this rapid and localised heat generation leads to instability in the guest-host bond of the adsorbed gas and the framework that triggers the release of the gas molecules. The selection of the MOF, the ratio of magnetic nanoparticles, and the strength of the applied magnetic field are essential features of the MISA process. The heat generation capability of the MFCs was measured by recording their temperature rise profile while exposing them to different magnetic field strengths. While studying the 3 wt.% Cu-BTC/MgFe₂O₄ MFCs, it was noted that on application of 25 mT magnetic field, from the initial temperatures of 25 °C the pellets attained a maximum temperature rise of 78 °C, with 31 mT magnetic field the temperature reached was 86 °C and with 33 mT, the MFCs reached a temperature of 92 °C. (Figure S4-d).

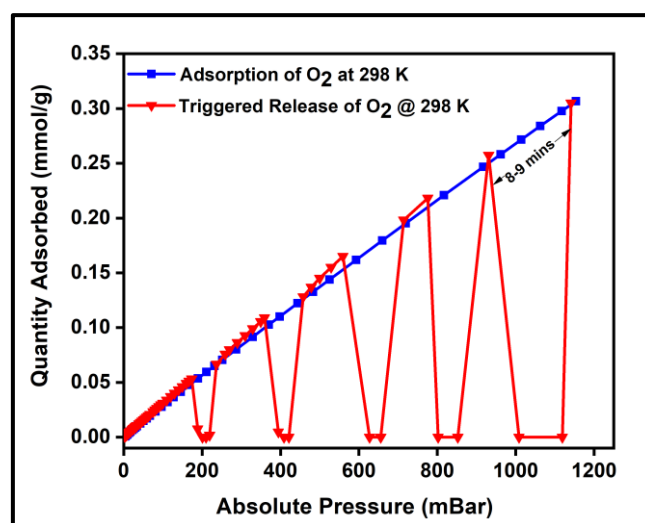


Figure 5.5: Oxygen adsorption isotherm of 3 wt.% CuBTC-MgFe₂O₄ composite pellets at 298 K and the magnetically triggered desorption at 200, 400, 600, 800 and 1000 mBar.

The oxygen adsorption isotherms were collected using a Micrometrics 3Flex gas sorption analyser at pre-set equilibration times allowing enough time for the system to equilibrate at each pressure point, and the targeted pressures for desorption were set at 200, 400, 600, 800, and 1000 mBar. The experiment was designed to alternate between adsorption and desorption phases continuously with minimal activation and degassing taking place between each cycle. The desorption was induced with an EASY

HEAT Ambrell induction machine (Figure S9) to trigger the remote, rapid and localised heating enabling the complete release of the adsorbed oxygen at the desired pressure. Typically, 3Flex experiment program is run to adsorb oxygen from 0.1 mbar to 1200 mbar. The experiment is monitored, and at 200 mbar pressure range, the remote magnetic heating is activated to trigger the release of the adsorbed oxygen molecules. The process is repeated at 400, 600, 800, and 1000 mbar. For the 3 wt. % MFC a magnetic field of 31 mT was applied, and at 188 mBar a 100 % release of the 0.06 mmol/g of adsorbed oxygen was released in 5 minutes. Once complete desorption was achieved, the applied magnetic field was switched off to stop the remote heating process, thereby allowing the MFC to resume adsorption of oxygen. The MFC pellets showed a similar uptake performance relative to the bare MOF. The triggered release of the MFC was repeated again at 400 mBar (0.12 mmol/g), 600 mBar (0.17 mmol/g), 800 mBar (0.22 mmol/g), and 1000 mBar (0.26 mmol/g) and achieved 100 % release of oxygen molecules within 5 mins time except for the 1000-1200 mBar range where it took 8-9 mins for the adsorption-desorption-adsorption cycle to finish (Figure 5.5). To investigate the post-MISA stability of the MFC, its regeneration, and adsorption capacities of the MFC pellets, they were activated at 140 °C for 6 hrs after each triggered release experiment, and after twenty MISA cycles (Figure 5.4), the XRD results corroborate their structural stability(Figure -S10).

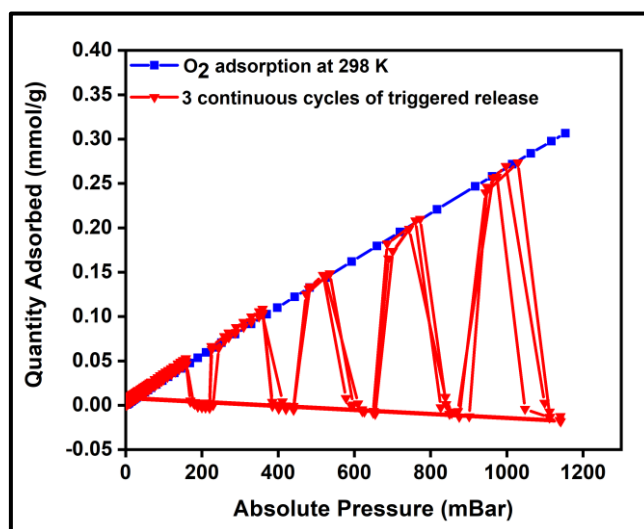


Figure 5.6: Oxygen adsorption isotherm of 3 wt.% CuBTC-MgFe₂O₄ composites at 298 K and three continuous desorption cycles of oxygen at 200, 400, 600, 800, and 1000 mBar.

In order to evaluate regeneration capability and the cyclic performance of the composite pellets over multiple closed MISA cycles, upon achieving the maximum oxygen uptake of 0.34 mmol/g at 1140 mBar, the pellets were reactivated for 10 minutes by remote magnetic heating at 33 mT (92 °C) and simultaneously evacuating the sample from 1200 – 0 mBar. Figure 5.6 presents the results of three continuous closed MISA cycles on the 3 flex with a sample pressure of 0.007 mBar achieved when the magnetic heating and vacuum activation steps were combined. Upon switching off the magnetic field,

oxygen adsorption and MISA- based desorption second cycle continued precisely like the first cycle at 200, 400, 600, 800 and 1000 mBar and 31 mT (86 °C) applied magnetic field. The results from three continuous adsorptions and MISA regeneration of the MFCs revealed that the oxygen adsorption capacity of the composite pellets was not adversely affected by the heat from the nanoparticles and each desorption cycle achieved a consistent result of complete desorption of bound oxygen molecules.

To highlight the easy accessibility of oxygen at any targeted pressures and to signify the versatility of the MISA process in regenerating the MFC after every adsorption cycle we ran a closed MISA adsorption-desorption-regeneration cyclic run across all pressures. This experiment was planned to alternate between adsorption, desorption and regeneration between each cycle. The experiment was conducted with the usual oxygen adsorption by the MFCs, that was followed by desorption at 200 mBar using a magnetic field of 31 mT (86 °C), and the 200-0 mBar regeneration was achieved within 6 mins by the magnetic heating from 33 mT (92 °C) magnetic field and evacuation from the system. Once 0 mBar pressure was reached, the MFC resumed its oxygen adsorption until the desorption and regeneration steps were activated again at 400, 600, 800 and 1000 mBar pressures. The regeneration times varied between 6-10 minutes with 200-0 mBar reached in 6 minutes whereas it took 10 minutes for the 1200-0 mBar step. The reactivation step of heating at 140 °C for 12 hrs heating plus vacuum reactivation step was replaced by heating at 92 °C for 10 mins, using 33 mT applied field at the end of each pressure point (downward-facing arrows at 1,2,3,4 and 5 in Figure 5.7). The success of this new adsorbent regeneration method can be validated by the consistent oxygen adsorption capacities shown by the composite in consecutive cycles.

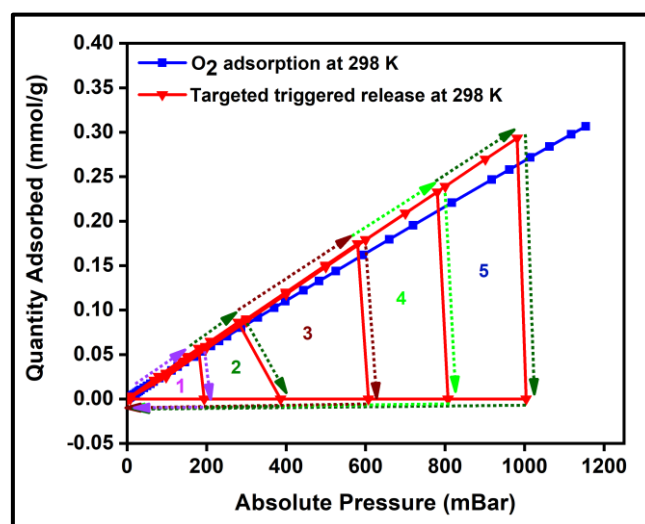


Figure 5.7: The performance of 3 wt.% CuBTC-MgFe₂O₄ composites at 298 K in a closed MISA cyclic adsorption-desorption-regeneration process with the combined vacuum and magnetic heating triggered desorption at 200, 400, 600, 800 and 1000 mBar and the magnetic heating triggered regeneration from 200-0 mBar (1), 400-0 mBar (2), 600-0 mBar (3), 800-0 mBar (4) and 1000-0 mBar (5).

Regeneration energy:

For efficient and economic adsorption-based separations, the adsorbent selection is primarily governed by its selectivity, adsorption capabilities, regeneration ability, and stability. The regeneration energy is the energy utilized by the adsorbent to reverse the adsorption process and depends on the heat of adsorption, specific heat capacity, and working capacity of the adsorbents. It is directly proportional to the heat of adsorption because strong interaction between the adsorbent and adsorbate results in a higher heat of adsorption and consequently higher regeneration energy would be required to overcome this strong interaction⁸³, leading to a high energy penalty^{11, 83, 84}. Furthermore, MOFs are generally known to be thermal insulators and require high temperatures to trigger the release of adsorbed species. The remote, localised and targeted heating nature of the MISA process makes it most suitable for oxygen capture and storage applications while minimising the energy penalty required to operate the process^{11, 58, 59, 85}.

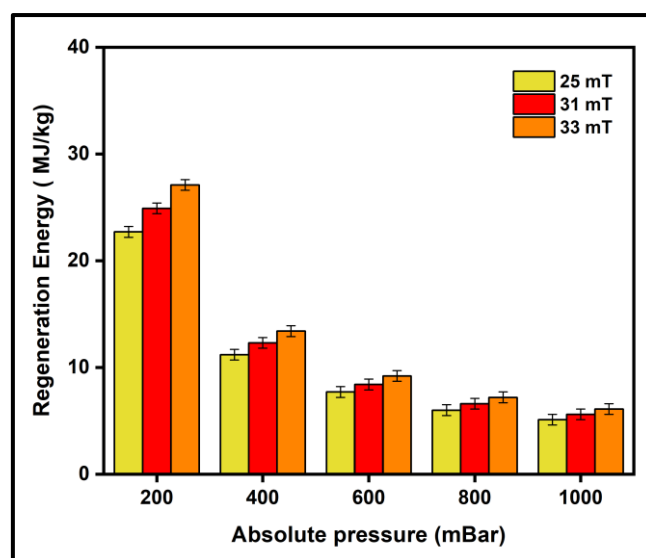


Figure 5.8: Regeneration energy as a function of varying magnetic fields of 25 mT, 31 mT, and 33 mT used to trigger desorption of Oxygen from the 3 wt.% CuBTC-MgFe₂O₄ MFCs.

Furthermore, results show that the efficiency of the process is primarily dependant on the area of the induction coil and the changes in the magnetic fields. Figure 5.8 depicts the regeneration energy requirements with varying magnetic fields of 25 mT, 31 mT, and 33 mT. Stronger interactions between the adsorbed molecules and the framework at low pressures require higher regeneration energies for desorption at 200 mBar. Energy requirements by the MISA process were evaluated for two different masses of the MFC pellets. When 0.3 g and 0.6 g of the 3 wt. % MFC pellets were exposed to a magnetic field of 31 mT; the MFC pellets experienced a temperature rise of 86 °C and the energy utilized for the regeneration of 0.26 mmol /g of Oxygen adsorbed at 1000 mBar was calculated to be 5.1 MJ /kgO₂ for 0.3 g weight sample and 5.6 MJ /kgO₂ for 0.6 g sample (Figure S-11b).

Additionally, the energy used to drive the magnetic induction heating in the MISA process was determined by monitoring the electrical power consumption of the EASY HEAT Ambrell induction machine. A power meter connected to the machine estimated the power consumption when the MFC is in and out of the magnetic field at 25 mT, 31 mT, and 33 mT. For the 0.6 g of the MFC pellets, the energy consumed to regenerate the pellets at 1000 mbar was calculated from the power (W) consumed by the induction unit, the time (s) it took to release the adsorbed molecules and the mass (g) of the released molecules (Table-S2). Despite the relatively high regeneration energy requirement of the MFC pellets, the energy input to the induction system was calculated to be 0.15 kWh/kgO₂ (Table-S1) highlighting a lower energy requirement when compared to conventional cryogenic oxygen producing systems where energy requirement of 0.3-0.35 kWh/kgO₂ has been reported⁸⁶.

5.2.5 Conclusions

MOFs are known to be thermally insulating, and this can be overcome by utilizing the rapid, localised, and easily controllable magnetic induction heating effect. MISA is a technology that can be harnessed to achieve an efficient process for on-demand oxygen delivery. Particularly, miniaturized oxygen concentrators can be engineered with MFCs for room temperature oxygen storage and on-demand supply of oxygen. The results demonstrate the versatility and potential of the MISA process in exploiting a readily available MOF incorporated with magnetic nanoparticles for safe storage and on-demand release of oxygen at ambient conditions. Here, the powdered CuBTC MOF was transformed into CuBTC-MgFe₂O₄ MFCs by mixing them with different amounts of MgFe₂O₄ nanoparticles and pelletising them with the help of a binder. To understand the purity and properties of the synthesized CuBTC MOF, MgFe₂O₄ nanoparticles, and the fabricated CuBTC-MgFe₂O₄ MFCs, they were analysed using different characterisation techniques and depending on the outcome the pellets with 3 wt.% magnetic content were selected for further oxygen studies. These pellets showed an adsorption capacity of 0.03 mmol/g at 1 Bar pressure at 298 K. When they were exposed to a magnetic field of 31 mT; the MgFe₂O₄ nanoparticles attained a temperature rise to 86 °C causing full desorption of the oxygen molecules. The composite exhibited good thermal stability and excellent cyclability by maintaining its adsorption properties over three continuous adsorption-desorption cycles. Oxygen capture, storage and supply using ambient temperature processes can be simpler, efficient, safer and considerably less complex and further development of this concept is expected to revolutionize the safe storage, handling, transport, and release of oxygen under ambient conditions.

5.3 Supporting Information and Acknowledgements

Supporting Information

The Electronic Supplementary Information (ESI) accompanying this publication has been reproduced with permission from Melag [12]. A copy of this document is included in **Appendix B**.

Acknowledgements

The authors acknowledge the use of instruments and scientific and technical assistance at the Monash Centre For Electron Microscopy, a Node of Microscopy Australia.

5.4 References

References cited in this Chapter text reproduced from the publication “*Performance evaluation of CuBTC composites for room temperature oxygen storage*” included as Appendix B, are consolidated here for completeness.

1. Allam, R. J., *Improved oxygen production technologies*, Energy Procedia, 2009, **1**, 461–470.
2. Dobson, M., *Oxygen concentrators and cylinders*, Int J Tuberc Lung Dis, 2001, **5**, 520–523.
3. Emsley, J., *Nature's building blocks: an AZ guide to the elements*, Oxford University Press, 2011.
4. Gulcay, E. and Erucar, I., *Biocompatible MOFs for Storage and Separation of O₂: A Molecular Simulation Study*, Ind. Eng. Chem. Res., 2019, **58**, 3225–3237.
5. Dobson, M., *Oxygen concentrators offer cost savings for developing countries*, Anaesthesia, 1991, **46**, 217–219.
6. Arnold, E.; Bruton, A.; Donovan-Hall, M.; Fenwick, A.; Dibb, B. and Walker, E., *Ambulatory oxygen: why do COPD patients not use their portable systems as prescribed? A qualitative study*, BMC Pulm. Med., 2011, **11**, 9.
7. Dubois, A.; Bodelin, P. and Vigor, X., *Portable oxygen concentrator.*, US Patent 6,520,176, 18 Feb. 2003.
8. Moghadam, P. Z.; Islamoglu, T.; Goswami, S.; Exley, J.; Fantham, M.; Kaminski, C. F.; Snurr, R. Q.; Farha, O. K. and Fairen-Jimenez, D., *Computer-aided discovery of a metal–organic framework with superior oxygen uptake*, Nat. Commun., 2018, **9**, 1378.
9. DeCoste, J. B.; Weston, M. H.; Fuller, P. E.; Tovar, T. M.; Peterson, G. W.; LeVan, M. D. and Farha, O. K., *Metal–organic frameworks for oxygen storage*, Angew. Chem. Int. Ed., 2014, **53**, 14092–14095.
10. Weston, M. H., *Metal-organic frameworks for oxygen storage and air separation*, U.S. Patent 20150105250, April 16, 2015.
11. Sadiq, M. M.; Suzuki, K. and Hill, M. R., *Towards energy efficient separations with metal organic frameworks*, Chem. Commun., 2018, **54**, 2825–2837.
12. Falcaro, P.; Lapierre, F.; Marmiroli, B.; Styles, M.; Zhu, Y.; Takahashi, M.; Hill, A. J. and Doherty, C. M., *Positioning an individual metal–organic framework particle using a magnetic field*, J Mater Chem C, 2013, **1**, 42–45.
13. Mason, J. A.; Veenstra, M. and Long, J. R., *Evaluating metal–organic frameworks for natural gas storage*, Chem Sci, 2014, **5**, 32–51.
14. Bazer-Bachi, D.; Assié, L.; Lecocq, V.; Harbuzaru, B. and Falk, V., *Towards industrial use of metal-organic framework: Impact of shaping on the MOF properties*, Powder Technology, 2014, **255**, 52–59.
15. Kim, J.; Cho, H.-Y. and Ahn, W.-S., *Synthesis and Adsorption/Catalytic Properties of the Metal Organic Framework CuBTC*, Catal. Surv. Asia, 2012, **16**, 106–119.
16. Mendes, R. F. and Almeida Paz, F. A., *Transforming metal-organic frameworks into functional materials*, Inorg. Chem. Front, 2015, **2**, 495–509.
17. Peterson, G. W.; Britt, D. K.; Sun, D. T.; Mahle, J. J.; Browe, M.; Demasky, T.; Smith, S.; Jenkins, A. and Rossin, J. A., *Multifunctional Purification and Sensing of Toxic Hydride Gases by CuBTC Metal–Organic Framework*, Ind. Eng. Chem. Res., 2015, **54**, 3626–3633.
18. Bloch, E. D.; Queen, W. L.; Krishna, R.; Zadrozny, J. M.; Brown, C. M. and Long, J. R., *Hydrocarbon separations in a metal-organic framework with open iron (II) coordination sites*, Science, 2012, **335**, 1606–1610.
19. Li, H.; Wang, K.; Sun, Y.; Lollar, C. T.; Li, J. and Zhou, H.-C., *Recent advances in gas storage and separation using metal–organic frameworks*, Mater. Today, 2018, **21**, 108–121.
20. Li, J.-R.; Kuppler, R. J. and Zhou, H.-C., *Selective gas adsorption and separation in metal-organic frameworks*, Chem. Soc. Rev., 2009, **38**, 1477–1504.
21. Li, J.-R.; Sculley, J. and Zhou, H.-C., *Metal–organic frameworks for separations*, Chem. Rev., 2011, **112**, 869–932.

22. Parkes, M. V.; Sava Gallis, D. F.; Greathouse, J. A. and Nenoff, T. M., *Effect of metal in M3 (btc) 2 and M2 (dobdc) MOFs for O₂/N₂ separations: A combined density functional theory and experimental study*, J. Phys. Chem. C, 2015, **119**, 6556–6567.
23. Queen, W. L.; Bloch, E. D.; Brown, C. M.; Hudson, M. R.; Mason, J. A.; Murray, L. J.; Ramirez-Cuesta, A. J.; Peterson, V. K. and Long, J. R., *Hydrogen adsorption in the metal-organic frameworks Fe₂(dobdc) and Fe₂(O₂)(dobdc)*, Dalton Trans, 2012, **41**, 4180–4187.
24. Gangu, K. K.; Maddila, S.; Mukkamala, S. B. and Jonnalagadda, S. B., *A review on contemporary Metal–Organic Framework materials*, Inorg. Chim. Acta, 2016, **446**, 61–74.
25. Ke, F.; Yuan, Y.-P.; Qiu, L.-G.; Shen, Y.-H.; Xie, A.-J.; Zhu, J.-F.; Tian, X.-Y. and Zhang, L.-D., *Facile fabrication of magnetic metal-organic framework nanocomposites for potential targeted drug delivery*, J. Mater. Chem., 2011, **21**, 3843–3848.
26. Yaghi, O. M.; Li, G. and Li, H., *Selective binding and removal of guests in a microporous metal-organic framework*, nature, 1995, **378**, 703.
27. Furukawa, H.; Cordova, K. E.; O’Keeffe, M. and Yaghi, O. M., *The chemistry and applications of metal-organic frameworks*, Science, 2013, **341**, 1230444.
28. Eddaoudi, M.; Moler, D. B.; Li, H.; Chen, B.; Reineke, T. M.; O’Keeffe, M. and Yaghi, O. M., *Modular Chemistry: Secondary Building Units as a Basis for the Design of Highly Porous and Robust Metal–Organic Carboxylate Frameworks*, Acc. Chem. Res., 2001, **34**, 319–330.
29. Doherty, C. M.; Buso, D.; Hill, A. J.; Furukawa, S.; Kitagawa, S. and Falcaro, P., *Using functional nano- and microparticles for the preparation of metal-organic framework composites with novel properties*, Acc. Chem. Res., 2014, **47**, 396–405.
30. Hendon, C. H.; Rieth, A. J.; Korzyński, M. D. and Dincă, M., *Grand Challenges and Future Opportunities for Metal–Organic Frameworks*, ACS Cent. Sci, 2017, **3**, 554–563.
31. Li, J.-R.; Kuppler, R. J. and Zhou, H.-C., *Selective gas adsorption and separation in metal–organic frameworks*, Chem. Sov. Rev. , 2009, **38**, 1477–1504.
32. Xiao, D. J.; Gonzalez, M. I.; Darago, L. E.; Vogiatzis, K. D.; Haldoupis, E.; Gagliardi, L. and Long, J. R., *Selective, tunable O₂ binding in cobalt (II)–triazolate/pyrazolate metal–organic frameworks*, J. Am. Chem. Soc, 2016, **138**, 7161–7170.
33. Murray, L. J.; Dinca, M.; Yano, J.; Chavan, S.; Bordiga, S.; Brown, C. M. and Long, J. R., *Highly-selective and reversible O₂ binding in Cr³⁺ (1, 3, 5-benzenetricarboxylate) 2*, J. Am. Chem. Soc., 2010, **132**, 7856–7857.
34. Southon, P. D.; Price, D. J.; Nielsen, P. K.; McKenzie, C. J. and Kepert, C. J., *Reversible and selective O₂ chemisorption in a porous metal–organic host material*, J. Am. Chem. Soc., 2011, **133**, 10885–10891.
35. Bloch, E. D.; Murray, L. J.; Queen, W. L.; Chavan, S.; Maximoff, S. N.; Bigi, J. P.; Krishna, R.; Peterson, V. K.; Grandjean, F.; Long, G. J.; Smit, B.; Bordiga, S.; Brown, C. M. and Long, J. R., *Selective Binding of O₂ over N₂ in a Redox–Active Metal–Organic Framework with Open Iron(II) Coordination Sites*, J. Am. Chem. Soc, 2011, **133**, 14814–14822.
36. Bloch, E. D.; Queen, W. L.; Hudson, M. R.; Mason, J. A.; Xiao, D. J.; Murray, L. J.; Flacau, R.; Brown, C. M. and Long, J. R., *Hydrogen Storage and Selective, Reversible O₂ Adsorption in a Metal–Organic Framework with Open Chromium(II) Sites*, Angew. Chem. Int. Ed, 2016, **55**, 8605–8609.
37. Xiao, D. J.; Gonzalez, M. I.; Darago, L. E.; Vogiatzis, K. D.; Haldoupis, E.; Gagliardi, L. and Long, J. R., *Selective, Tunable O₂ Binding in Cobalt(II)–Triazolate/Pyrazolate Metal–Organic Frameworks*, J. Am. Chem. So., 2016, **138**, 7161–7170.
38. Nagar, H.; Vadthya, P.; Prasad, N. S. and Sridhar, S., *Air separation by facilitated transport of oxygen through a Pebax membrane incorporated with a cobalt complex*, RSC Adv., 2015, **5**, 76190–76201.
39. Melag, L.; Sadiq, M. M.; Smith, S. J. D.; Konstas, K.; Suzuki, K. and Hill, M. R., *Efficient delivery of oxygen via magnetic framework composites*, J. Mater. Chem. A, 2019, **7**, 3790–3796.
40. Sugimoto, H.; Nagayama, T.; Maruyama, S.; Fujinami, S.; Yasuda, Y.; Suzuki, M. and Uehara, A., *Thermodynamic study on dioxygen binding of diiron (II) and dicobalt (II) complexes containing various dinucleating ligands*, Bull. Chem. Soc. Jpn., 1998, **71**, 2267–2279.
41. Moeljadi, A. M. P.; Schmid, R. and Hirao, H., *Dioxygen binding to Fe-MOF-74: microscopic insights from periodic QM/MM calculations*, Can. J. Chem., 2016, **94**, 1144–1150.

42. Märcz, M.;Johnsen, R. E.;Dietzel, P. D. C. and Fjellvåg, H.,*The iron member of the CPO-27 coordination polymer series: Synthesis, characterization, and intriguing redox properties*, Micropor. Mesopor. Mater, 2012, **157**, 62–74.
43. Skoulidas, A. I.,*Molecular Dynamics Simulations of Gas Diffusion in Metal– Organic Frameworks: Argon in CuBTC*, J. Am. Chem. So., 2004, **126**, 1356–1357.
44. Liu, J.;Wang, Y.;Benin, A. I.;Jakubczak, P.;Willis, R. R. and LeVan, M. D.,*CO₂/H₂O adsorption equilibrium and rates on metal– organic frameworks: HKUST-1 and Ni/DOBDC*, Langmuir, 2010, **26**, 14301–14307.
45. Al-Janabi, N.;Hill, P.;Torrente-Murciano, L.;Garforth, A.;Gorgojo, P.;Siperstein, F. and Fan, X.,*Mapping the Cu-BTC metal–organic framework (HKUST-1) stability envelope in the presence of water vapour for CO₂ adsorption from flue gases*, Chem. Eng. J., 2015, **281**, 669–677.
46. Sun, B.;Kayal, S. and Chakraborty, A.,*Study of HKUST (Copper benzene-1, 3, 5-tricarboxylate, Cu-BTC MOF)-1 metal organic frameworks for CH₄ adsorption: An experimental Investigation with GCMC (grand canonical Monte-carlo) simulation*, Energy, 2014, **76**, 419–427.
47. Gutiérrez-Sevillano, J. J.;Vicent-Luna, J. M.;Dubbeldam, D. and Calero, S.,*Molecular Mechanisms for Adsorption in Cu-BTC Metal Organic Framework*, J. Phys. Chem. C, 2013, **117**, 11357–11366.
48. Yang, Q.;Xue, C.;Zhong, C. and Chen, J. F.,*Molecular simulation of separation of CO₂ from flue gases in CU-BTC metal-organic framework*, AIChE journal, 2007, **53**, 2832–2840.
49. Hulvey, Z.;Lawler, K. V.;Qiao, Z.;Zhou, J.;Fairen-Jimenez, D.;Snurr, R. Q.;Ushakov, S. V.;Navrotsky, A.;Brown, C. M. and Forster, P. M.,*Noble gas adsorption in copper trimesate, HKUST-1: an experimental and computational study*, J. Phys. Chem. C, 2013, **117**, 20116–20126.
50. Rubio-Martinez, M.;Batten, M. P.;Polyzos, A.;Carey, K.-C.;Mardel, J. I.;Lim, K.-S. and Hill, M. R.,*Versatile, High Quality and Scalable Continuous Flow Production of Metal-Organic Frameworks*, Sci. Rep., 2014, **4**, 5443.
51. Liang, Z.;Marshall, M. and Chaffee, A. L.,*CO₂ adsorption-based separation by metal organic framework (Cu-BTC) versus zeolite (13X)*, Energy & Fuels, 2009, **23**, 2785–2789.
52. Travlou, N. A.;Singh, K.;Rodríguez-Castellón, E. and Bandosz, T. J.,*Cu–BTC MOF–graphene-based hybrid materials as low concentration ammonia sensors*, J. Mater. Chem. A, 2015, **3**, 11417–11429.
53. Hosseini, M.;Zeinali, S. and Sheikhi, M.,*Fabrication of capacitive sensor based on Cu-BTC (MOF-199) nanoporous film for detection of ethanol and methanol vapors*, Sens. Actuators, B, 2016, **230**, 9–16.
54. Bouson, S.;Krittayavathananon, A.;Phattharasupakun, N.;Siwayaprahm, P. and Sawangphruk, M.,*Antifungal activity of water-stable copper-containing metal-organic frameworks*, R. Soc. Open Sci, 2017, **4**, 170654.
55. Vishnyakov, A.;Ravikovitch, P. I.;Neimark, A. V.;Bülow, M. and Wang, Q. M.,*Nanopore structure and sorption properties of Cu– BTC metal– organic framework*, Nano Lett., 2003, **3**, 713–718.
56. Lin, K.-S.;Adhikari, A. K.;Ku, C.-N.;Chiang, C.-L. and Kuo, H.,*Synthesis and characterization of porous HKUST-1 metal organic frameworks for hydrogen storage*, Int. J. Hydrog. Energy, 2012, **37**, 13865–13871.
57. Lestari, W. W.;Adreane, M.;Purnawan, C.;Fansuri, H.;Widiastuti, N. and Rahardjo, S. B., 2016.
58. Sadiq, M. M.;Li, H.;Hill, A. J.;Falcaro, P.;Hill, M. R. and Suzuki, K.,*Magnetic Induction Swing Adsorption: An Energy Efficient Route to Porous Adsorbent Regeneration*, Chem. Mater., 2016, **28**, 6219–6226.
59. Li, H.;Sadiq, M. M.;Suzuki, K.;Ricco, R.;Doblin, C.;Hill, A. J.;Lim, S.;Falcaro, P. and Hill, M. R.,*Magnetic Metal–Organic Frameworks for Efficient Carbon Dioxide Capture and Remote Trigger Release*, Adv. Mater., 2016, **28**, 1839–1844.
60. Huang, B. L.;McGaughey, A. J. H. and Kaviani, M.,*Thermal conductivity of metal-organic framework 5 (MOF-5): Part I. Molecular dynamics simulations*, Int. J. Heat Mass Transfer, 2007, **50**, 393-404.
61. Huang, B. L.;Ni, Z.;Millward, A.;McGaughey, A. J. H.;Uher, C.;Kaviani, M. and Yaghi, O.,*Thermal conductivity of a metal-organic framework (MOF-5): Part II. Measurement*, Int. J. Heat Mass Transfer, 2007, **50**, 405-411.

62. Zhang, X. and Jiang, J., *Thermal Conductivity of Zeolitic Imidazolate Framework-8: A Molecular Simulation Study*, J. Phys. Chem. C, 2013, **117**, 18441-18447.
63. Li, H.;Sadiq, M. M.;Suzuki, K.;Doblin, C.;Lim, S.;Falcaro, P.;Hill, A. J. and Hill, M. R., *MaLISA – a cooperative method to release adsorbed gases from metal–organic frameworks*, J. Mater. Chem. A, 2016, **4**, 18757–18762.
64. Li, H.;Sadiq, M. M.;Suzuki, K.;Falcaro, P.;Hill, A. J. and Hill, M. R., *Magnetic Induction Framework Synthesis: A General Route to the Controlled Growth of Metal–Organic Frameworks*, Chem. Mater., 2017, **29**, , 6186–6190.
65. Sadiq, M. M.;Rubio-Martinez, M.;Zadehahmadi, F.;Suzuki, K. and Hill, M. R., *Magnetic Framework Composites for Low Concentration Methane Capture*, Ind. Eng. Chem. Res., 2018, **57**, 6040–6047.
66. Ricco, R.;Konstas, K.;Styles, M. J.;Richardson, J. J.;Babarao, R.;Suzuki, K.;Scopece, P. and Falcaro, P., *Lead (II) uptake by aluminium based magnetic framework composites (MFCs) in water*, J. Mater. Chem. A, 2015, **3**, 19822–19831.
67. Ricco, R.;Malfatti, L.;Takahashi, M.;Hill, A. J. and Falcaro, P., *Applications of magnetic metal–organic framework composites*, J. Mater. Chem. A, 2013, **1**, 13033–13045.
68. Kolhatkar, A.;Jamison, A.;Litvinov, D.;Willson, R. and Lee, T., *Tuning the Magnetic Properties of Nanoparticles*, Int. J. Mol, 2013, **14**, 15977.
69. Bañobre-López, M.;Teijeiro, A. and Rivas, J., *Magnetic nanoparticle-based hyperthermia for cancer treatment*, Rep Pract Oncol Radiother, 2013, **18**, 397–400.
70. Harris, I. and Williams, A., *Magnetic materials*, Mater. Sci. Eng. C, 2009, **2**, 49–84.
71. Rubio-Martinez, M.;Avci-Camur, C.;Thornton, A. W.;Imaz, I.;Maspoeh, D. and Hill, M. R., *New synthetic routes towards MOF production at scale*, Chem. Soc. Rev., 2017, **46**, 3453–3480.
72. Maensiri, S.;Sangmanee, M. and Wiengmoon, A., *Magnesium ferrite (MgFe₂O₄) nanostructures fabricated by electrospinning*, Nanoscale Res. Lett, 2009, **4**, 221.
73. Bakoglidis, K.;Simeonidis, K.;Sakellari, D.;Stefanou, G. and Angelakeris, M., *Size-dependent mechanisms in AC magnetic hyperthermia response of iron-oxide nanoparticles*, IEEE Trans. Magn, 2012, **48**, 1320–1323.
74. Sun, S.;Zeng, H.;Robinson, D. B.;Raoux, S.;Rice, P. M.;Wang, S. X. and Li, G., *Monodisperse MFe₂O₄ (M = Fe, Co, Mn) nanoparticles*, J Am Chem Soc, 2004, **126**, 273–279.
75. Deatsch, A. E. and Evans, B. A., *Heating efficiency in magnetic nanoparticle hyperthermia*, J. Magn. Magn. Mater, 2014, **354**, 163–172.
76. Ebrahimi, M., *On the temperature control in self-controlling hyperthermia therapy*, J. Magn. Magn. Mater, 2016, **416**, 134–140.
77. Yang, S. J.;Choi, J. Y.;Chae, H. K.;Cho, J. H.;Nahm, K. S. and Park, C. R., *Preparation and Enhanced Hydrostability and Hydrogen Storage Capacity of CNT@MOF-5 Hybrid Composite*, Chem. Mater., 2009, **21**, 1893-1897.
78. Gelfand, B. S. and Shimizu, G. K. H., *Parameterizing and grading hydrolytic stability in metal–organic frameworks*, Dalton Trans., 2016, **45**, 3668-3678.
79. Mu, B. and Walton, K. S., *Thermal Analysis and Heat Capacity Study of Metal–Organic Frameworks*, J. Phys. Chem. C, 2011, **115**, 22748–22754.
80. Bhardwaj, S. K.;Bhardwaj, N.;Kaur, R.;Mehta, J.;Sharma, A. L.;Kim, K.-H. and Deep, A., *An overview of different strategies to introduce conductivity in metal–organic frameworks and miscellaneous applications thereof*, J. Mater. Chem. A, 2018, **6**, 14992-15009.
81. Rudolf, H.;Silvio, D. and Matthias, Z., *Validity limits of the Néel relaxation model of magnetic nanoparticles for hyperthermia*, Nanotechnology, 2010, **21**, 015706.
82. Sung, H. W. F.;Rudowicz, C.;Physics, C. U. o. H. K. D. o. and Science, M., *A Closer Look at the Hysteresis Loop for Ferromagnets: A Survey of Misconceptions and Misinterpretations in Textbooks*, City University of Hong Kong, Department of Physics and Materials Science, 2002.
83. Mason, J. A.;Sumida, K.;Herm, Z. R.;Krishna, R. and Long, J. R., *Evaluating metal-organic frameworks for post-combustion carbon dioxide capture via temperature swing adsorption*, Energy Environ. Sci., 2011, **4**, 3030–3040.

84. Li, H.;Sadiq, M. M.;Suzuki, K.;Doblin, C.;Lim, S.;Falcaro, P.;Hill, A. J. and Hill, M. R.,*MaLISA– a cooperative method to release adsorbed gases from metal–organic frameworks*, J. Mater. Chem. A, 2016, **4**, 18757–18762.
85. Sadiq, M. M.;Rubio-Martinez, M.;Zadehahmadi, F.;Suzuki, K. and Hill, M. R.,*Magnetic Framework Composites for Low Concentration Methane Capture*, Ind. Eng. Chem. Res., 2018, **57**, 6040-6047.
86. Twort, A. C., *Water supply*, London : Arnold/IWA Pub., London, 5th ed. edn., 2000.

Chapter 6:
The potential of bimetallic FeCo-MOF-74 for
Oxygen adsorption at room temperature

Chapter 6: The potential of bimetallic FeCo-MOF-74 for Oxygen adsorption at room temperature	85
6.1 Introduction.....	86
6.1.1 Abstract	87
6.1.2 Introduction.....	87
6.1.3 Experimental.....	89
6.1.3.1 Materials and Methods:.....	89
6.1.3.2 Synthesis.....	89
6.1.3.3 Characterisation.....	90
6.1.4 Results and discussion	91
6.1.4.1 Sample Characterisation	91
6.1.5 Conclusions.....	104
6.2 Supporting Information and Acknowledgements.....	105
6.3 References.....	106

6.1 Introduction

In **Chapter 4**, the adsorption capacity of Co-MOF-74 to adsorb oxygen at 204 K was demonstrated. By synthesizing varying combinations of Co-MOF-74/Fe₃O₄ MFC, the targeted triggered release of oxygen was achieved at 204 K. The cobalt based MFCs steadily adsorbed 4.8 mmol g⁻¹ Oxygen at 1.2 bar. For desorption when it was exposed to a 17.4 mT magnetic field, the MFC with 12.18 wt% Fe₃O₄ nanoparticles released 100% of oxygen.

Chapter 5 presented the results from the room temperature storage of oxygen using the CuBTC–MgFe₂O₄ MFC pellets. These pellets showed an adsorption capacity of 0.3 mmol g⁻¹ at 1 bar pressure at 298 K and when they were exposed to a magnetic field of 31mT at 269 kHz; the MgFe₂O₄ nanoparticles heated up causing full desorption of the oxygen molecules. It was proved that the storage, usage and transport of oxygen at ambient temperatures and pressures can be made simpler, efficient and safer, using cyclable MOFs. This, accompanied by the energy-efficient MISA process, can revolutionize the safe storage, handling, transport, and on-demand supply of oxygen.

Chapter 6 discusses the implications of adding a secondary metal ion in oxygen adsorption capabilities of single metal MOFs. Fe-MOF-74 shows enhanced affinity for oxygen but after an initial high oxygen uptake its cyclability drops. This irreversible Fe-peroxo complex formation at high temperatures is due to the irreversible binding of the O₂ molecule by two iron centres, Fe-O-Fe. It has been reported that the inclusion of different M²⁺ metal centres affects the oxygen-binding capability at the Fe²⁺ metal centres of the Fe-MOF-74. Co-MOF-74 displays moderate oxygen adsorption but better cyclability. In this study the effect of Fe/Co, Co²⁺/Co³⁺ and the Fe²⁺/Fe³⁺ ratios on oxygen uptake capacities of MOFs is investigated.

The potential of bimetallic FeCo-MOF-74 for Oxygen adsorption at room temperature.

Leena Melag, M. Munir Sadiq, Kristina Konstas, Kiyonori Suzuki, J. S. Garitaonandia
and Matthew R. Hill

6.1.1 Abstract

The potential of redox-active bimetallic MOFs for the room temperature adsorption of oxygen is studied. Herein, we have successfully synthesised a series of $\text{Fe}_x\text{-Co}_{1-x}\text{-MOF-74}$ ($x=0.9,0.5,0.1$) in an air-free environment, using controlled compositions of iron salts, cobalt salts and 2,5-dihydroxyterephthalic acid in a one-step solvothermal process. The synthesised samples were thoroughly characterised using X-ray diffraction (XRD), scanning electron microscopy (SEM), N_2 adsorption isotherms, X-ray photoelectron spectroscopy (XPS), thermogravimetric analysis (TGA) and Mössbauer spectroscopy and confirm the successful inclusion of both Fe and Co cations in the bimetallic MOF-74 framework. The Fe/Co, $\text{Co}^{2+}/\text{Co}^{3+}$ and the $\text{Fe}^{2+}/\text{Fe}^{3+}$ ratios were thoroughly investigated to understand the synergistic effect of bimetallic cations on oxygen uptake properties of MOFs. The oxygen adsorption isotherms were measured at 298 K, and the results show that the $\text{Fe}_{0.5}\text{-Co}_{0.5}\text{-MOF-74}$ shows favourable oxygen adsorption uptake of 0.6 mmol/g over seven consecutive cycles.

6.1.2 Introduction

Oxygen constitutes only 21 vol.% of air and yet to separate it from the mixture of air gases, large volumes of air need to be processed. The cryogenic method of oxygen separation process works on air liquefaction and separation of nitrogen and oxygen using their different boiling points whereas the non-cryogenic adsorption-based techniques, using zeolites, carbon molecular sieves or membranes are based on using the physical differences of molecular sizes to either selectively adsorb or permeate oxygen or nitrogen. An efficient and economical method of oxygen production should rely on the chemical properties of oxygen for high O_2/N_2 selectivity to separate it from the air mixture. The selective adsorption method would also need to process only small amounts of air for oxygen production. The structural rigidity and pore heterogeneity of the conventional adsorbents limit their applications for chemisorption. In contrast, the new age adsorbents, Metal-Organic Frameworks (MOFs), with their coordinatively unsaturated metal sites, versatile chemical functionality, unique tunability and good thermal and mechanical stabilities present as promising candidates for selective oxygen adsorption¹⁻⁴.

Metal-Organic frameworks are a promising class of crystalline, highly porous materials formed due to linking of metal cations by organic ligands into a one, two or three-dimensional (1D, 2D and 3D) framework with large internal surface areas⁵⁻⁸. These ordered, chemically stable and physically flexible structures offer high selectivity, adsorption and storage capacities making them applicable in a diverse

Chapter 6: The potential of bimetallic FeCo-MOF-74 for Oxygen adsorption at room temperature

range of applications from gas sequestration and storage⁹⁻¹⁷, to catalysis^{18, 19}, sensing and drug delivery^{9, 19-22}. While the metal cations, provide the activity sites and the linkers offer the stability and volume to accommodate the guest molecules, the choice to change the metal cations or modify the coordinating linkers for enhanced selectivity, catalytic, optical and magnetic properties provide the unique tunability to the MOF and imparts a versatile chemical functionality to it. The accessible coordinatively unsaturated metal sites (CUS) or open metal sites (OMS) formed by the vacant Lewis acid sites on the metal cations during the desolvation process of the MOF acts as the reactive site for host-guest interactions towards gases leading to higher selective gas adsorption and higher storage capacities^{3, 13, 23-28}. M-MOF-74 (M = Mg, Mn, Fe, Co, Ni, Cu, or Zn) series of isostructural, highly porous MOFs are an extensively studied MOFs with one of the highest reported concentrations of open metal sites accessible for guest-host interactions^{3, 26, 29-32}. The structure of M₂(dobdc) consists of one-dimensional metal oxide clusters linked by dobdc⁴⁻ (dobdc⁴⁻ = 2,5-dioxido-1,4-benzene dicarboxylate) ligands forming hexagonal channels that propagate along with the crystallographic c-axis. Five oxygen atoms from surrounding linkers octahedrally coordinate each metal in the cluster, and a solvent molecule occupies the sixth position in each octahedron^{3, 10, 23, 29, 33-35}. Desolvation of the MOF leads to removal of the solvent molecule exposing the M²⁺ cation sites for interactions with the gas molecules that results in enhanced selectivity at the site. The transition metal ions are redox-active and bind preferentially to oxygen to form temperature dependant complexes. In nature, iron acts as the oxygen-binding atom in the heme proteins that bind or releases molecular oxygen and this reversible binding in haemoglobin and myoglobin have generated interest in iron as promising oxygen-binding adsorbents³⁶⁻³⁸. Additionally, the temperature-dependent oxidation states of iron make it reactive for redox reactions. The oxygen adsorption studies conducted by E.D. Bloch *et al.* using the synthesised Fe-MOF-74 showed temperature dependant complete reversibility at 211 K and preferential oxygen-binding over nitrogen at 298 K with an irreversible adsorption capacity of 9.3 wt.%²³. The iron centres of Fe-MOF-74 initiate chemisorption and influence O₂/N₂ selectivity. However, the binding between iron and oxygen is so strong that it impairs the reversibility of the adsorption capacity and affects the chemical stability of the MOF^{23, 31, 39, 40}. Cobalt complexes with oxygen have been known to have better cyclability and chemical stability as compared to iron. In our previous work, we studied the oxygen adsorption capacity of Co-MOF-74 at 204 K. We observed a strong affinity and temperature dependant reversible binding to oxygen and though its oxygen uptake is moderate compared to Fe-MOF-74²⁸, its regeneration capacity and cyclability is better than Fe-MOF-74⁴¹⁻⁴³. The properties of Co-MOF-74 and Fe-MOF-74 can be included together in a bimetallic MOF⁴⁴. The incorporation of different metal ions to the same Framework results in bimetallic or multi-metallic MOFs and as the synergistic effects of the multi-metallic cations add more functionality to the intrinsic properties of the single metal MOF. It imparts added functionality to the MOF and maintains the stability and reusability of the MOF. The

choice of the secondary metal, their ratio in the solvent and the method of their incorporation are essential parameters to consider avoiding and minimising defects in the structure^{40, 45-48}.

Fe-MOF-74 displays higher O₂/N₂ selectivity and large oxygen capacity but limited cyclability, whereas Co-MOF-74 displays moderate oxygen adsorption but better cyclability^{23, 28, 31, 41}. In this work, we have synthesised a series of Fe_xCo_{1-x}-MOF-74 frameworks with varying Fe: Co ion ratios via a one-step solvothermal process to study the synergistic effects of iron and cobalt metal ions on the oxygen adsorption capacity and cyclability of the resultant MOF.

6.1.3 Experimental

6.1.3.1 Materials and Methods:

The synthesis of all MOFs was performed under inert conditions using Schlenk techniques or in an argon-filled glovebox. The chemical reagents for these experiments, including the air-sensitive anhydrous N, N-dimethylformamide (DMF) and methanol were purchased from commercial vendors. It was ensured that all the glassware used for the procedures are clean and dry. Before using them or before transferring them to the glovebox, the chemicals were further deoxygenated by prolonged N₂ gas bubbling. All ultra-high purity (UHP, 99.999% purity) grades of N₂ and O₂ gases were used for the surface area analysis and gas adsorption studies.

6.1.3.2 Synthesis

Synthesis of Fe-MOF-74

1.1 g of anhydrous ferrous chloride, FeCl₂ (9.0 mmol), 0.71 g of 2,5-dihydroxyterephthalic acid (DHTA) (3.6 mmol), 300 mL of DMF, and 36 mL of methanol were all added to a 500 mL Schlenk flask and heated under reflux at 120 °C for 18 h. The red-orange coloured precipitate was collected by filtration, washed with DMF, and soaked in DMF at 120 °C for 24 h. The solid was collected by filtration and washed with methanol before soaking it in methanol at 70 °C for 24 h. This methanol exchange was repeated three times before the sample was activated at 160 °C under vacuum for 24 h before storing them in an Ar filled glove box.

Synthesis of Bimetallic FeCo-MOF-74

A range of bimetallic FeCo-MOF-74 was synthesised using the same synthesis procedure of Fe-MOF-74 using varying molar ratios of Fe and Co. Initially different amounts of metal salts of FeCl₂ and CoCl₂ along with 0.71 g of DHTA (3.6 mmol) were dissolved in the 336 ml of a solvent mixture of DMF and

methanol by continuous stirring for 30 mins. The rest of the synthesis was carried out by following the same procedure used for the synthesis of Fe-MOF-74. The samples were labelled as Fe_xCo_{1-x}MOF-74, where x represents the molar ratio in the sample.

6.1.3.3 Characterisation

All the synthesised samples were characterised by X-ray diffraction using a D8 ADVANCE Eco X-ray powder diffractometer with a Cu K α radiation source of 1.79 Å with a scan rate of 0.005 sec per step at 40 kV and 25 mA, and the diffraction patterns were analysed with DIFFRAC EVA diffraction software. SEM analysis was carried out to study the morphologies and uniformity of the synthesised samples using the JOEL 7001F Scanning Electron Microscope. The information from the SEM images was supported by the data from EDS mapping and line mapping.

The surface area properties and pore size distribution of the synthesised samples were measured using nitrogen gas adsorption Micromeritics ASAP 2010 analyser, and oxygen gas adsorption measurements were carried out on the Micromeritics 3Flex surface and catalyst characterisation instrument.

The metal content in MOF samples was analysed using an Agilent 730 inductively coupled plasma optical emission spectrometry (ICP-OES) where the samples were first digested using 6mL of 69% HNO₃ and 1mL of 30% H₂O₂ at 200 °C.

X-ray photoelectron spectroscopy (XPS) analysis of MOF and MFC samples was carried out using Nexsa Surface Analysis System X-ray photoelectron spectrometer with a micro-focused, monochromated Al K- α X-ray source and high-efficiency electron lens, hemispherical analyser and detector and used the Avantage Software for data processing.

The thermal stability studies on all the samples were carried out on SENSYS evo TG-DSC machine equipped with a refrigeration cooling system Julabo FL-601 and operating in the temperature range from room temperature (RT) to 800 °C. Weighed amounts of the were placed into the alumina crucible and then heated to 800 °C at a heating rate of 10 °C /min in an N₂ atmosphere⁴⁹.

The magnetic properties of saturation magnetization (M_s), coercivity (H_c), and magnetization curves were studied on a vibrating sample magnetometer (VSM, RIKEN DENSHI). The samples were prepared by embedding weighed quantities of samples in an epoxy resin and hardener mix and allowing it to set. Once it was set, the measurements were carried out at room temperature.

Chapter 6: The potential of bimetallic FeCo-MOF-74 for Oxygen adsorption at room temperature

Fe Mössbauer spectra were acquired at 295 K using a constant acceleration, transmission spectrometer with a CoRh source and the NORMOS software package was used for fitting of these spectra.

6.1.4 Results and discussion

6.1.4.1 Sample Characterisation

XRD

The crystallinity of the synthesised samples was analysed using powder X-ray diffraction (PXRD) analysis. Figure 6.1 shows the comparable PXRD peak patterns of the synthesised FeCo-MOF-74 samples that show identical characteristic peaks of the parent MOFs that matches well with the peaks of simulated MOF-74 confirming the successful synthesis of Co-MOF-74, Fe-MOF-74, $\text{Fe}_{0.9}\text{Co}_{0.1}$ -MOF-74, $\text{Fe}_{0.5}\text{Co}_{0.5}$ -MOF-74 and $\text{Fe}_{0.1}\text{Co}_{0.9}$ -MOF-74.

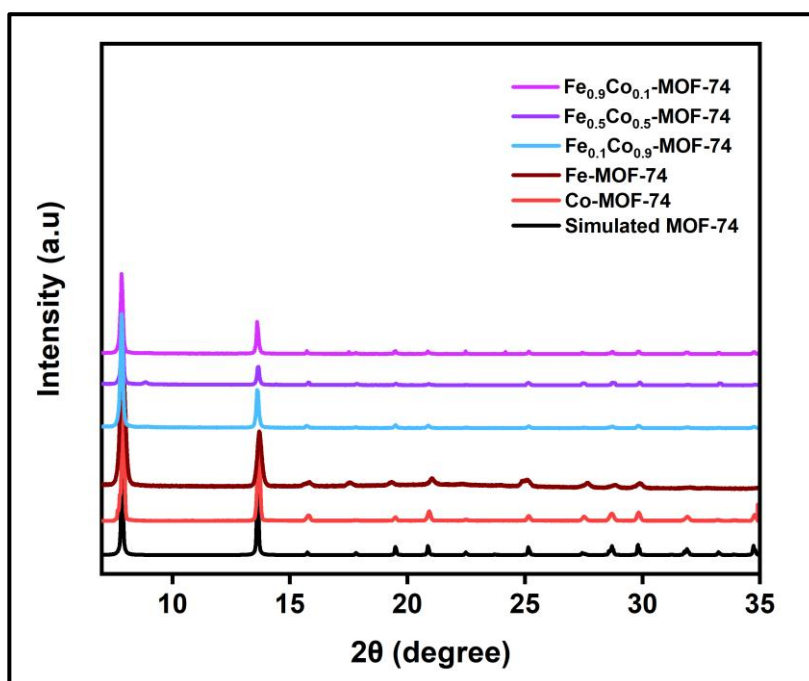


Figure 6.1: The PXRD patterns of the synthesised Fe-MOF-74, Co-MOF-74, and the bimetallic $\text{Fe}_{0.9}\text{Co}_{0.1}$ -MOF-74, $\text{Fe}_{0.5}\text{Co}_{0.5}$ -MOF-74, $\text{Fe}_{0.1}\text{Co}_{0.9}$ -MOF-74.

SEM & EDS

SEM analysis was used to study the morphology of the synthesised MOF samples. As seen in Figure 6.2, the SEM micrographs of Co-MOF-74, Fe-MOF-74 and mostly all the bimetallic $\text{Fe}_{0.9}\text{Co}_{0.1}$ -MOF-74, $\text{Fe}_{0.5}\text{Co}_{0.5}$ -MOF-74 and $\text{Fe}_{0.1}\text{Co}_{0.9}$ -MOF-74 show hexagonal-shaped MOF measuring 5-10 μm in length. The SEM micrographs of $\text{Fe}_{0.9}\text{Co}_{0.1}$ -MOF-74 reveals the coexistence of the elliptical-shaped

Chapter 6: The potential of bimetallic FeCo-MOF-74 for Oxygen adsorption at room temperature

MOF crystal agglomerates and the hexagonal prism-like MOF crystals. While the $\text{Fe}_{0.9}\text{Co}_{0.1}$ -MOF-74 micrographs show petal-like structures formed by the hexagonal MOF prism, the $\text{Fe}_{0.1}\text{Co}_{0.9}$ -MOF-74 samples exhibit a rodlike morphology.

The energy-dispersive X-ray spectroscopy (EDX) mapping results seen in Figure 6.2, confirmed the presence and uniform distribution of carbon, oxygen, cobalt and iron in the bimetallic MOFs. The uniform distribution of Fe and Co species in the EDS maps confirm the formation of a bimetallic MOF. EDX line scan was conducted on the magnetically separated $\text{Fe}_{0.9}\text{Co}_{0.1}$ -MOF-74 crystals, and the results indicate the presence of both Fe and Co (Figure S-3). The Fe/Co molar ratios of all the FeCo-MOF-74 samples determined using the EDX analysis are slightly different from the intended initial molar ratios used in the synthesis, but they compare well with ICP and XPS detected Fe/Co values (Table 1).

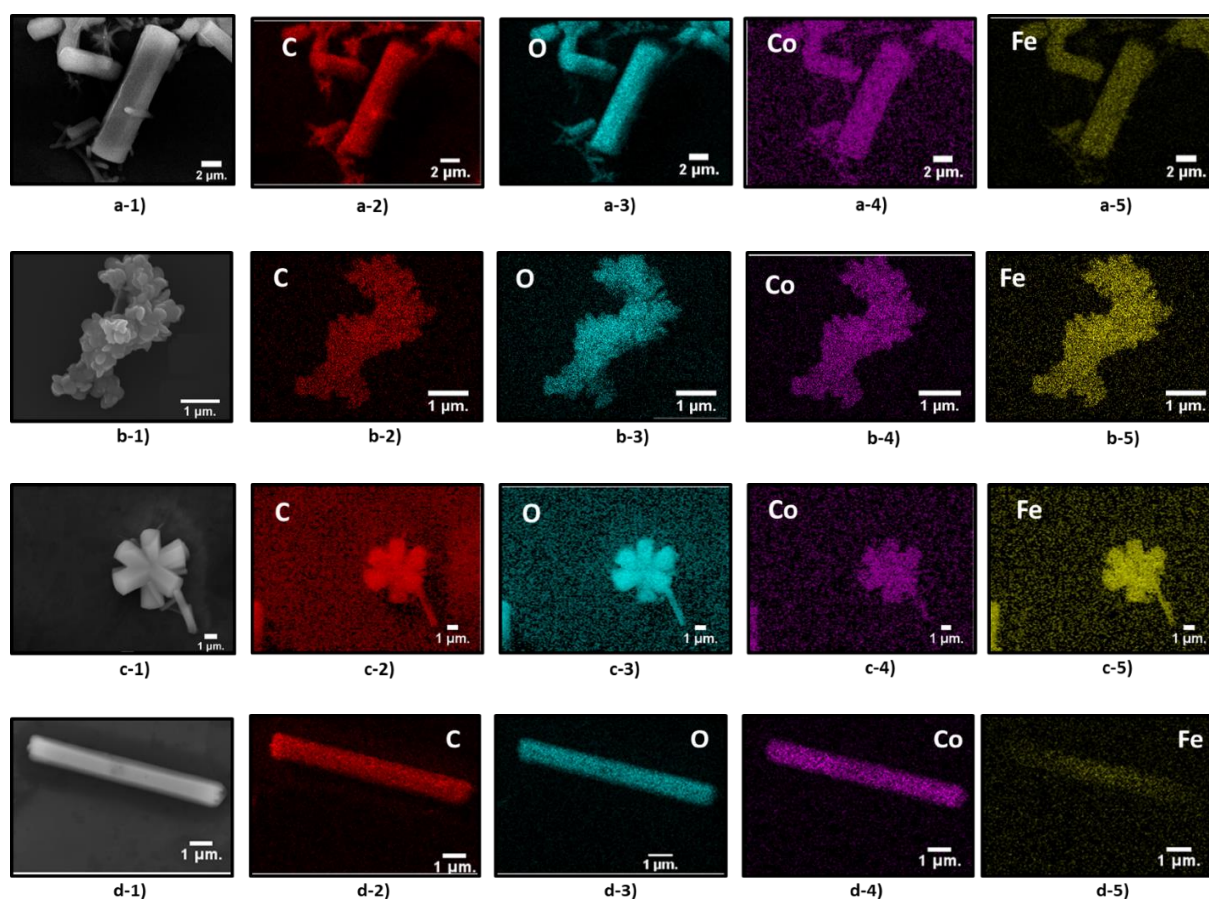


Figure 6.2: The SEM images and with corresponding EDX mapping areas confirming the presence of carbon, oxygen, cobalt and iron in a-1) the $\text{Fe}_{0.9}\text{Co}_{0.1}$ -MOF-74, b-1) the spherical $\text{Fe}_{0.9}\text{Co}_{0.1}$ -MOF-74, c-1) the $\text{Fe}_{0.5}\text{Co}_{0.5}$ -MOF-74, and d-1) the $\text{Fe}_{0.1}\text{Co}_{0.9}$ -MOF-74.

N_2 adsorption isotherms

Leena Melag

The surface area and porosity measurements were carried out using Micromeritics ASAP2020. 100-120 mg of MOF sample was transferred in a pre-weighed analysis tube, capped with a transeal and using Smart Vacprep, evacuated under vacuum by heating it to at 160 °C ramp rate of 0.5 °C min⁻¹ for 20 h. After activation, the sample carrying analysis tubes were weighed again to calculate the actual mass of the sample being analysed before transferring them to the analysis port to be held under vacuum for further 3-4 h. Analyses at 77 K were performed using liquid-nitrogen baths. All MOF samples show the type I adsorption isotherms when measured using nitrogen at 77 K. The surface area of Fe-MOF-74 is calculated to be 1129 m²/g and of Co-MOF-74 to be 1090 m²/g, which is lower than mentioned in the literature^{23, 24, 35, 50}.

Table 1. The BET surface area, Langmuir surface area and the pore volume of Fe-MOF-74, Co-MOF-74, and the bimetallic Fe_{0.9}Co_{0.1}-MOF-74, Fe_{0.5}Co_{0.5}-MOF-74, Fe_{0.1}Co_{0.9}-MOF-74 (Figure S3).

Sample	BET surface area (m ² /g)	Langmuir surface area (cm ² /g)	Pore volume (cm ³ /g)
Fe-MOF-74	1129	1459	0.87
Co-MOF-74	1090	1410	0.84
Fe _{0.9} Co _{0.1} -MOF-74	943	1240	0.74
Fe _{0.5} Co _{0.5} -MOF-74	763	919	0.63
Fe _{0.1} Co _{0.9} -MOF-74	749	967	0.68

VSM

A small percentage of the synthesised bimetallic MOF samples exhibited magnetic properties. They were magnetically separated, and their magnetic properties were measured at room temperature by employing vibrating sample magnetometer. As seen from Figure 6.3, the hysteresis curve of the Fe_{0.9}Co_{0.1}-MOF-74 shows the higher saturation magnetization (Ms) of 0.25 emu g⁻¹ as compared to Fe_{0.5}Co_{0.5}-MOF-74 and Fe_{0.1}Co_{0.9}-MOF-74 that show saturation magnetization (Ms) less than 0.05 emu g⁻¹.

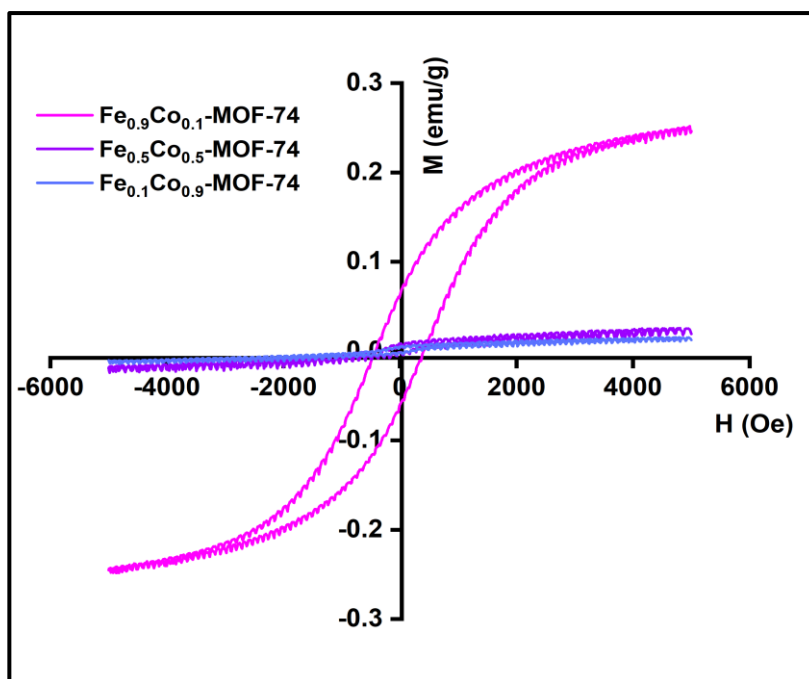


Figure 6.3: The VSM data of the $Fe_{0.9}Co_{0.1}$ -MOF-74, $Fe_{0.5}Co_{0.5}$ -MOF-74 and the $Fe_{0.1}Co_{0.9}$ -MOF-74.

Oxygen adsorption isotherms

Single-component oxygen adsorption measurements on Fe-MOF-74, Co-MOF-74 and FeCo-MOF-74 samples were conducted at 204, 273 and 298 K at pressures loadings of 0-1 Bar on a Micromeritics 3Flex gas adsorption analyser. The adsorption temperatures at 204, 273, and 298 K were performed using acetone and dry-ice bath, ice bath, and water bath, respectively. 100-120 mg of MOF sample was evacuated under vacuum by heating it to at 160 °C ramp rate of $0.5^{\circ}\text{C min}^{-1}$ for 20 h and weighed again to know the exact mass of the desolvated samples. Free space measurements were carried out using helium at the end of the analysis.

It can be seen from Figure 6.4-a) that at 204 K the Co-MOF-74 reversibly adsorbs 4.2 mmol/g of oxygen, at 273 K it adsorbs 0.9 mmol/g and at 298 K its oxygen adsorption capacity is 0.36 mmol/g. As expected, the oxygen adsorption capacities of the Co-MOF-74 decreases with increasing temperatures. For the second oxygen adsorption cycle at 298 K, the MOF adsorbs 0.32 mmol/g that further reduces to 0.26 mmol/g for the third cycle. At higher temperatures, the strong affinity of the Co atoms to the oxygen molecules causes oxidation of the metal sites resulting in reduced cyclability of the MOF, as shown in Figure 6.4-c²⁸.

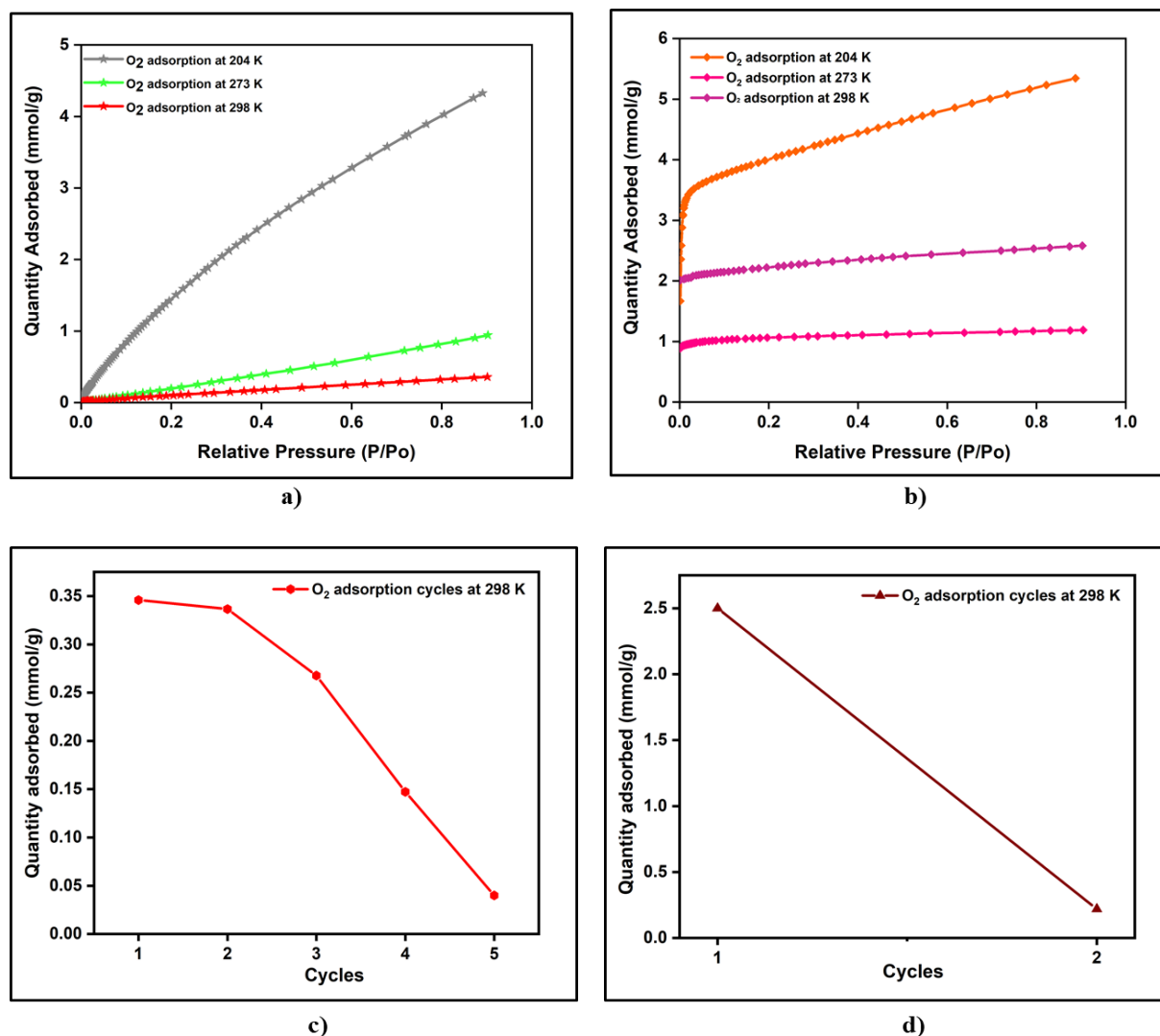


Figure 6.4: Low-pressure O_2 adsorption isotherms of a) Co-MOF-74 and b) Fe-MOF-74 at 204, 273 and 298 K, c) O_2 adsorption cycles by Co-MOF-74 at 298 K and d) cyclability of Fe-MOF-74 at 298 K.

The oxygen adsorption isotherms of the synthesised Fe-MOF-74 in Figure 6.4 b) shows an oxygen uptake of 5.2 mmol/g at 204 K, 1.2 mmol/g at 273 K and 2.5 mmol/g at 298 K. The high uptake of oxygen at 204 K can be attributed to the open metal framework and the high surface area of the MOF because the adsorption at this temperature is reversible and repeatable. At higher temperatures, the oxygen adsorption uptake can be attributed to the porous framework and the high surface area. However, it is mainly due to the strong chemical affinity between the Fe atoms and the oxygen molecules resulting in the irreversible chemisorption of oxygen. The oxidation of metal centres affects cyclability and structural stability of the MOFs (Figure S4).

The oxygen adsorption isotherms of the synthesised bimetallic MOFs show different oxygen uptake, and at room temperature, the interactions between the Fe atoms and the oxygen molecules govern the adsorption performance of the MOFs. The $Fe_{0.9}Co_{0.1}$ -MOF-74 shows an oxygen uptake of 1.6 mmol/g

Chapter 6: The potential of bimetallic FeCo-MOF-74 for Oxygen adsorption at room temperature

in the first cycle, but it drops down to 0.4 mmol/g in the second cycle and reduces rapidly in consecutive cycles. The oxygen adsorption isotherms of the $\text{Fe}_{0.5}\text{Co}_{0.5}\text{-MOF-74}$ shows an initial uptake of 0.8 mmol/g in the first cycle that drops down to 0.6 mmol/g in the second cycle and maintains an oxygen uptake of 0.6 mmol/g for a further seven consecutive cycles. The $\text{Fe}_{0.1}\text{Co}_{0.9}\text{-MOF-74}$ shows an oxygen uptake of 0.6 mmol/g in the first cycle and maintains an uptake of 0.5-0.6 mmol/g for the next five cycles. $\text{Fe}_{0.1}\text{Co}_{0.9}\text{-MOF-74}$ and $\text{Fe}_{0.5}\text{Co}_{0.5}\text{-MOF-74}$ were exposed to more cycles of oxygen adsorption, and the $\text{Fe}_{0.5}\text{Co}_{0.5}\text{-MOF-74}$ continued with a consistent 0.6 mmol/g uptake for seven consecutive cycles whereas the adsorption capacity of $\text{Fe}_{0.1}\text{Co}_{0.9}\text{-MOF-74}$ dropped down to 0.2 mmol/g by the seventh cycle.

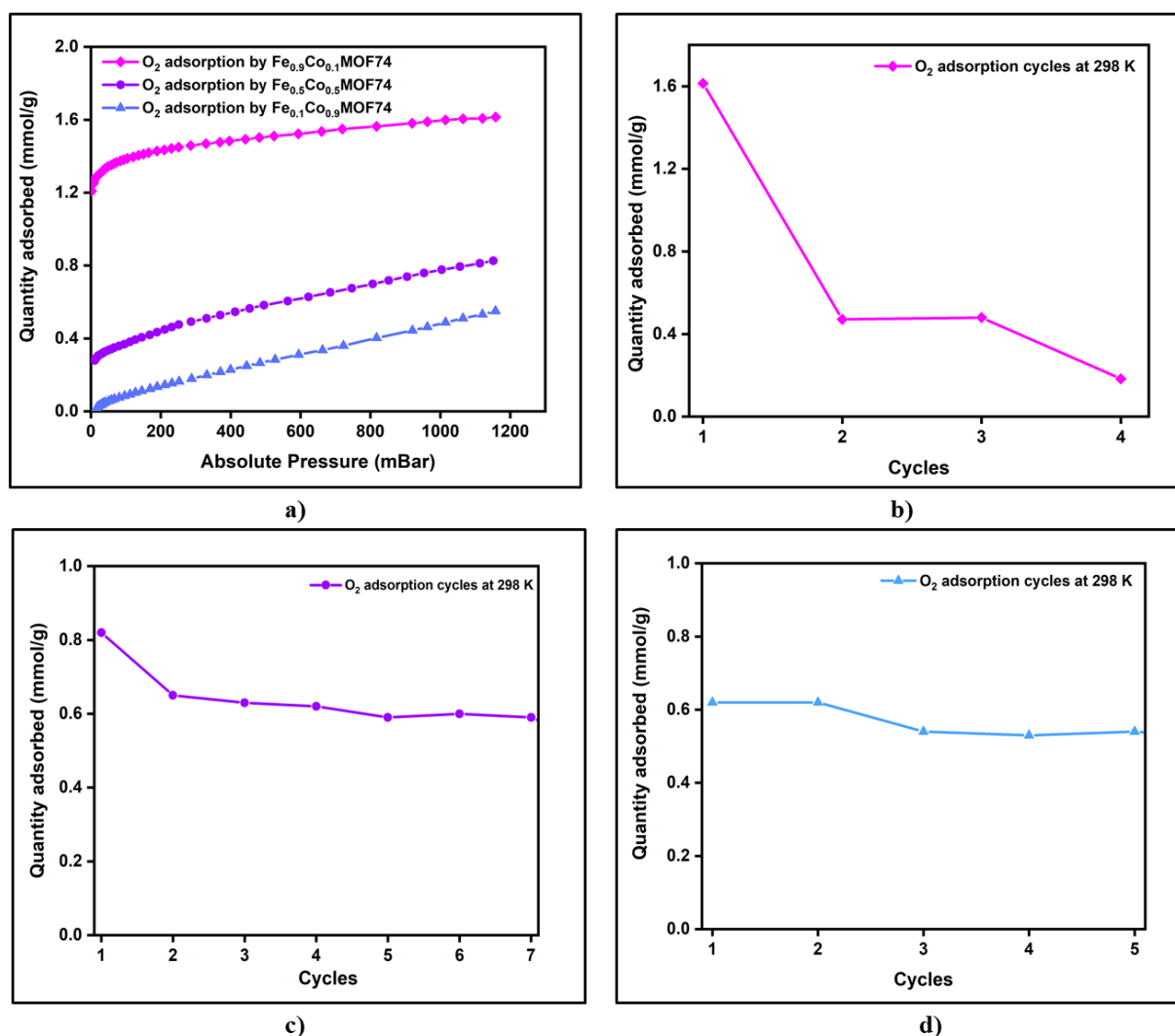


Figure 6.5: Low-pressure oxygen adsorption isotherms by a) the bimetallic $\text{Fe}_{0.9}\text{Co}_{0.1}\text{-MOF-74}$, $\text{Fe}_{0.5}\text{Co}_{0.5}\text{-MOF-74}$ and $\text{Fe}_{0.1}\text{Co}_{0.9}\text{-MOF-74}$, oxygen adsorption cycles of b) $\text{Fe}_{0.9}\text{Co}_{0.1}\text{-MOF-74}$, c) $\text{Fe}_{0.5}\text{Co}_{0.5}\text{-MOF-74}$ and d) of $\text{Fe}_{0.1}\text{Co}_{0.9}\text{-MOF-74}$ at 298 K.

Mössbauer Spectra

Oxygen binds to the open metal sites of Fe-MOF-74 differently at different temperatures.^{23, 24, 31} Mössbauer spectroscopy was used to study the oxidation state of iron before and after oxygen adsorption at different temperatures. ⁵⁷Fe Mössbauer spectroscopy was carried out at room temperature using a conventional constant-acceleration spectrometer in standard transmission geometry with a ⁵⁷CoRh source. A simultaneous fit of a crystalline spectrum and an amorphous phase characterised by a distribution of hyperfine fields B_{hf} with probability $P(B_{\text{hf}})$ has been performed, and the NORMAS software package was used for fitting the spectra. The quadrupole interactions of ⁵⁷Fe leave the groundstate spin $I = 1/2$ unsplit but split the excited state, $I = 3/2$ into two substates creating a doublet. These quadrupole interactions are different for Fe^{3+} and Fe^{2+} . The quadrupole splittings for Fe^{3+} are usually in the low range of 0.8-1.6 mm/s because the spherical half-filled outer $3d^5$ shells of Fe^{3+} limit their interactions resulting in small electric field gradients. The non-spherical $3d^6$ electron configuration of Fe^{2+} ions cause large electric gradients, and therefore, the quadrupole interactions of Fe^{2+} ions are in the range of 0.8- 3.0 mm/s range. Change in oxidation states of Fe affects the electron densities at the nucleus bringing about an isomer shift.

It can be seen from Figure 6.4-a) that at 204 K the Co-MOF-74 reversibly adsorbs 4.2 mmol/g of oxygen, at 273 K it adsorbs 0.9 mmol/g and at 298 K its oxygen adsorption capacity is 0.36 mmol/g. As expected, the oxygen adsorption capacities of the Co-MOF-74 decreases with increasing temperatures. For the second oxygen adsorption cycle at 298 K, the MOF adsorbs 0.32 mmol/g that further reduces to 0.26 mmol/g for the third cycle. At higher temperatures, the strong affinity of the Co atoms to the oxygen molecules causes oxidation of the metal sites resulting in reduced cyclability of the MOF, as shown in Figure 6.4-c²⁸. The quadrupole splitting and the isomer shifts help identify the oxidation states of Fe. In Fe-MOF-74 the quadrupole splitting represents the bindings at Fe^{2+} centres, the $\text{Fe}^{2+/3+}$ centres and the Fe^{3+} centres. The Mössbauer spectrum of the bare Fe-MOF-74 exhibits an isomer shift in the range of 0.57-1.15 mm/s with the corresponding quadrupole doublets ranges from 0.65–2.34 mm/s. These values are indicative of the presence of both the high-spin Fe^{2+} and high-spin Fe^{3+} in the sample. The estimated molar ratio of $[\text{Fe}^{2+}]/[\text{Fe}^{3+}]$ calculated from the spectra before methanol wash was estimated to be 0.93:0.07. After the methanol wash at 70 °C, the Mössbauer spectra exhibited an isomer shift of 0.47-1.14 mm/s; a quadrupole splitting range from 0.73–2.02 mm/s and the molar ratio of $[\text{Fe}^{2+}]/[\text{Fe}^{3+}]$ changed to 0.8:0.2 This is due to the conversion of trapped methanol molecules into formaldehyde by heat. After exposure to O_2 at 204 K, the doublet shows an isomer shift from 0.39–2.0 mm/s; a quadrupole splitting range from 0.70–1.93 mm/s and the molar ratio of $[\text{Fe}^{2+}]/[\text{Fe}^{3+}]$ is 0.2:0.8. The partial transfer of electrons between the Fe^{2+} and O_2 molecules result in a weak bond at low temperatures of at 204 K resulting in the reversible uptake of O_2 by the Fe-MOF-74.

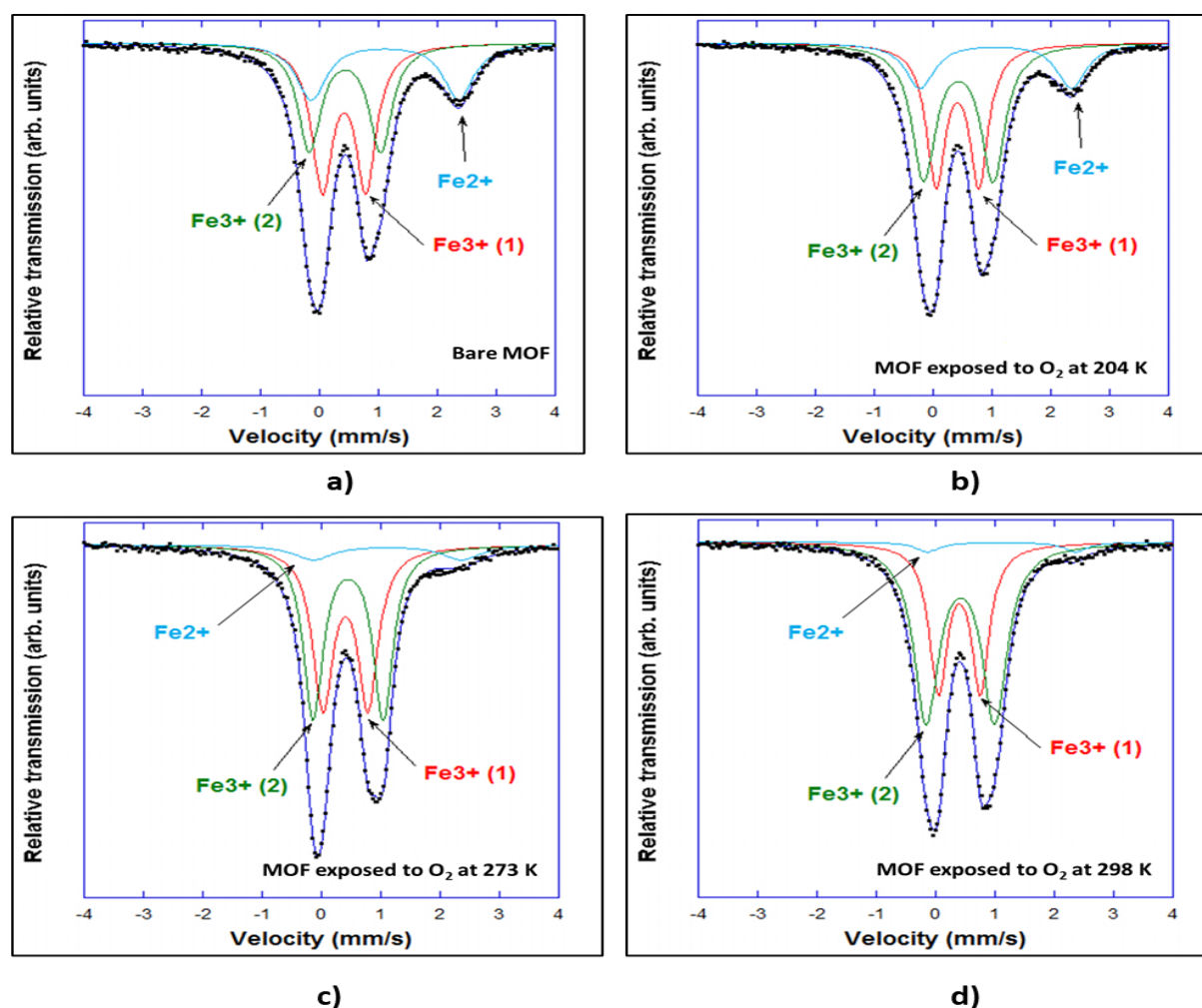


Figure 6.6: The Mössbauer spectra of Fe-MOF-74 samples a) the bare sample, the samples exposed to O_2 at b) 204 K, c) 273 K and d) after exposure to O_2 at 298 K.

The concentration of Fe^{3+} increases with an increase in oxidation temperatures and the spectra for sample exposed to O_2 at 273 K, showing a molar ratio of $[Fe^{2+}]/[Fe^{3+}]$ to 0.1:0.9. After an irreversible O_2 uptake at 298 K, the doublet exhibited an isomer shift of 0.40-1.32 mm/s; a quadrupole splitting from 0.652.33 mm/s and the molar ratio of $[Fe^{2+}]/[Fe^{3+}]$ changed to 0.06:0.94.

XPS

XPS analysis was performed to determine the composition and changes in the chemical states of the sample.

1. Fe-MOF-74:

The Fe 2p and Fe 3p peaks of Fe-MOF-74 were studied before and after exposure to O_2 at 204 K, 273 K and 298 K. The peak values of Fe 2p for Fe_2O_3 has been reported to be between 710.6 and 711.2 eV

Chapter 6: The potential of bimetallic FeCo-MOF-74 for Oxygen adsorption at room temperature

⁵¹⁻⁵³. The Fe 2p peak of the pristine Fe-MOF-74 can be deconvoluted into Fe2p_{3/2} and Fe2p_{1/2} at 710.3 and 722.9 eV respectively. Their distinct satellite peaks are located at 715 eV and 727.2 eV respectively.
⁵¹. The Fe 2p_{3/2} peak can be deconvoluted into two peaks at 709.6 and 711 eV revealing the presence of Fe²⁺. After Oxygen adsorption at 298 K, there is a chemical shift in Fe 2p peaks peak positions resulting in Fe 2p_{3/2} and Fe 2p_{1/2} at 714.5 eV and 725.3 eV, respectively. The characteristic satellite peaks for Fe₂O₃ are absent. The deconvoluted Fe 2p peaks confirm the presence of Fe₃O₄ ^{44, 54, 55}. The O 1s spectrum shows the binding peak at 532.1 eV for the pristine Fe-MOF-74. This major peak can be separated into three peaks at 530 eV (Fe-O), 532.1 eV (Fe-OH) and 533.1 eV(O=C-O). On exposure to O₂ at 298 K, the O 1s binding energy increases with increasing metal-binding energy causing the peaks to shift to higher binding energies at 530.7 eV, 532 eV and 533.3 eV, respectively. The Fe 3p peak of the pristine Fe-MOF-74 is observed at 56.41 eV and after O₂ adsorption at 298 K the peak moves to higher binding energies of 57.75 eV (Figure S5). Though Fe 3p peaks consist of both Fe²⁺ and Fe³⁺ ions, it is generally presented as a single peak due to minimal peak separations. The molar ratios of the [Fe²⁺]/[Fe³⁺] for samples were calculated by measuring the areas of each identified Fe²⁺, and Fe³⁺ peaks from the deconvoluted peaks of Fe 2p spectrum and the results are consistent with the Mössbauer results.

Chapter 6: The potential of bimetallic FeCo-MOF-74 for Oxygen adsorption at room temperature

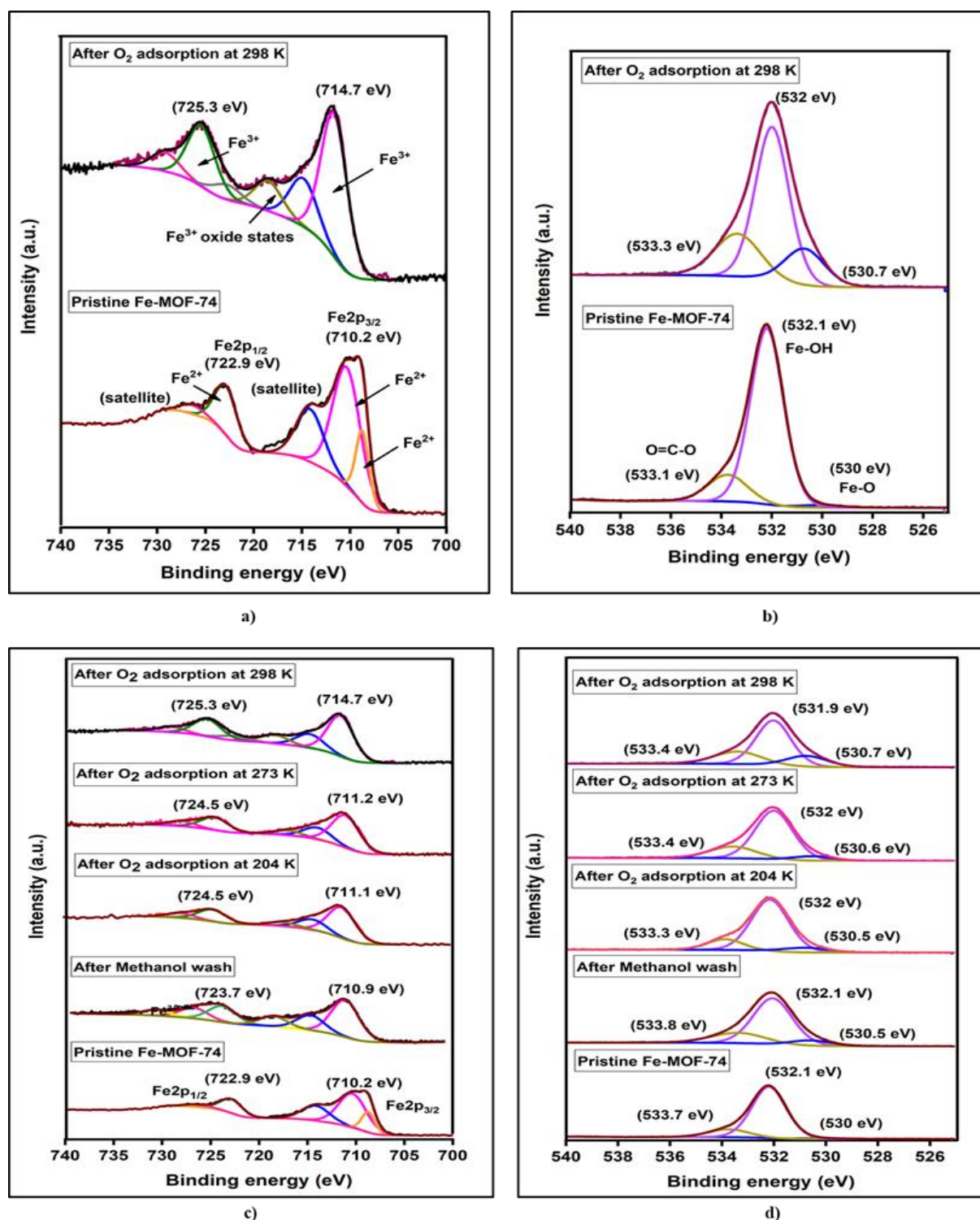


Figure 6.7: The XPS spectrum of a) Fe 2p from the pristine Fe-MOF-74 and before and after it was exposed to O₂ at 298 K, b) The corresponding O 1s spectrum that moves to higher binding energies with an increase in interaction between the Fe cations and Oxygen molecules, c) Fe 2p from the pristine Fe-MOF-74, the MOF exposed to O₂ at 204 K, 273 K and 298 K and d) corresponding O 1s spectrum of the samples.

2. Co-MOF-74

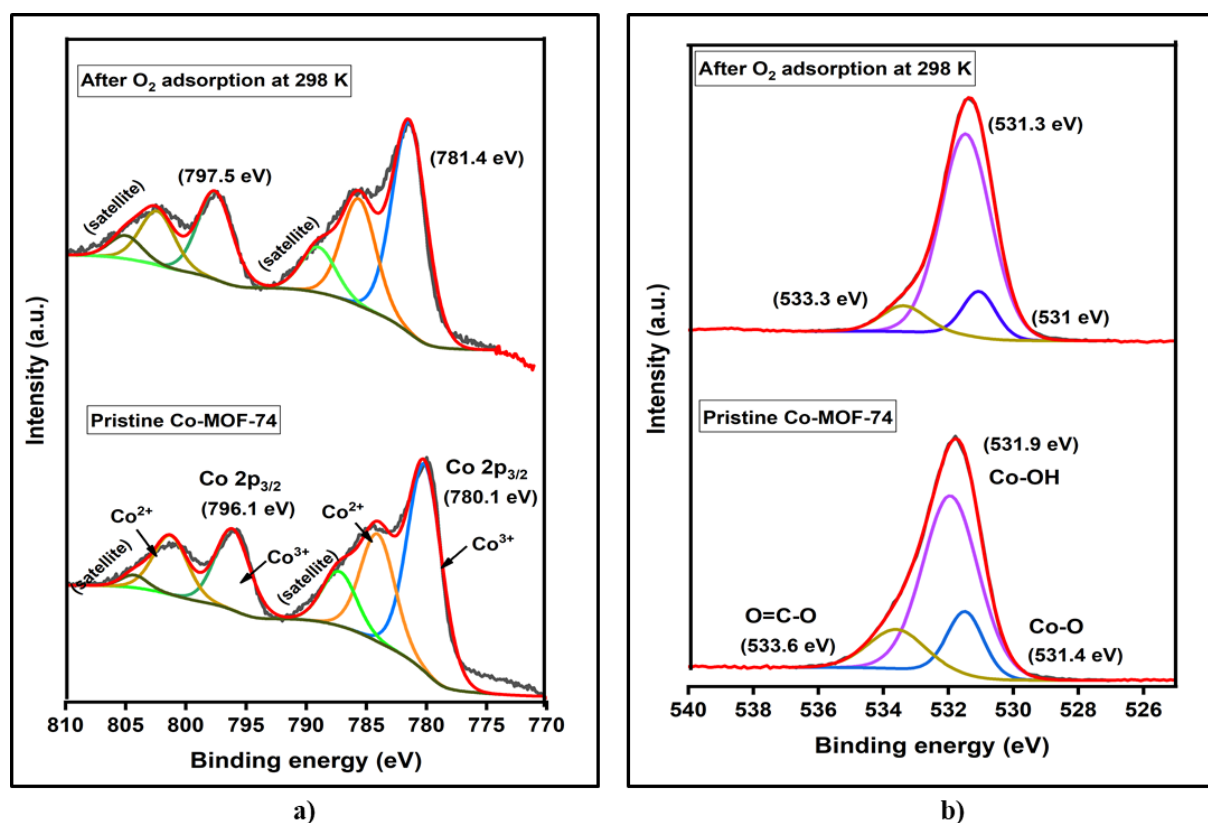


Figure 6.8: The XPS spectrum of a) Co 2p from the pristine Co-MOF-74 and before and after it was exposed to O₂ at 298 K, b) The corresponding O 1s spectrum that moves to lower binding energies with an increase in interaction between the Co cations and Oxygen molecules.

The Co 2p spectra of the pristine Co-MOF-74 consists of the peaks for Co 2p_{3/2} and Co 2p_{1/2} at 780.1 and 796.1 eV with the spin-orbit splitting difference of 15.8 eV^{44, 54, 56}, whereas the shake-up satellite peaks are observed at 787.2 and 804.2 eV. On oxygen adsorption at 298 K, there is a positive shift in the binding energies of Co 2p, and a negative shift in the binding energies of the O 1s spectra showing the increased donor-acceptor interaction with oxygen. The Co 2p^{3/2} and Co 2p^{1/2} peaks move to higher binding energies of 781.4, and 797.5 eV, respectively and their satellite peaks are observed at 788 eV and 804.1 eV. On the integration of the deconvoluted fitting curves, the Co²⁺/Co³⁺ ratio of the pristine sample was 4, and after exposure to oxygen, it reduced to 1.7.

3. Bimetallic Fe_xCo_{1-x}-MOF-74

The XPS spectra of the bimetallic Fe_xCo_{1-x} samples confirm the presence of Fe, Co, O, C, N in all three samples (Figure S6). The final Fe/Co molar ratios in the synthesised MOFs were determined using the XPS and the ICP analysis and compared against the intended initial molar ratios used in the synthesis.

MOF	Intended Fe/Co ratio	ICP detected Fe/Co ratio	XPS detected Fe/Co ratio	EDX detected Fe/Co ratio
Fe-MOF-74	1:0	—	—	1
Fe _{0.9} Co _{0.1} -MOF-74	9:1	8.3	8.5	8.7
Fe _{0.5} Co _{0.5} -MOF-74	1:1	0.73	0.87	1:1
Fe _{0.1} Co _{0.9} -MOF-74	1:9	0.08	0.09	0.08
Co-MOF-74	0:1	—	—	1

Table 2. Comparison of the intended with the detected Fe/Co ratios in the FeCo-MOF-74, using ICP, XPS and EDX analysis.

The XPS analysis was performed to study the effect of the secondary metal ion on the compositional states of the sample. The multiplet peak analysis was carried out using the Shirley method, and the peak fittings were carried out using the Gauss-Lorentz method. To quantify the results, using the peak positions and the relative areas of every peak designated to the Fe²⁺, Fe³⁺, Co²⁺ and Co³⁺, the effect of Oxygen exposure on each of the samples is summarised in Table 3.

Pristine MOFs								
Name	Fe 2p _{3/2}	Fe 2p _{1/2}	Co 2p _{3/2}	Co 2p _{1/2}	Fe ²⁺	Fe ³⁺	Co ²⁺	Co ³⁺
Fe _{0.1} Co _{0.9} -MOF-74	711.2	723.2	780.7	796.9	0.08	0.02	0.63	0.27
Fe _{0.5} Co _{0.5} -MOF-74	711.1	723.2	781.1	797.0	0.12	0.39	0.13	0.38
Fe _{0.9} Co _{0.1} -MOF-74	710.8	723.0	781.1	797.1	0.20	0.70	0.02	0.08
After O ₂ adsorption at 298 K								
Name	Fe 2p _{3/2}	Fe 2p _{1/2}	Co 2p _{3/2}	Co 2p _{1/2}	Fe ²⁺	Fe ³⁺	Co ²⁺	Co ³⁺
Fe _{0.1} Co _{0.9} -MOF-74	713.3	723.3	781.2	797.1	0.06	0.04	0.47	0.43
Fe _{0.5} Co _{0.5} -MOF-74	713.3	723.4	781.1	796.9	0.09	0.41	0.11	0.39
Fe _{0.9} Co _{0.1} -MOF-74	713.9	723.8	781.0	797.0	0.06	0.84	0.01	0.09

Table 3. The Molar fractions of Fe²⁺, Fe³⁺, Co²⁺ and Co³⁺ using the peak positions and relative peak areas of each element from the XPS data.

Based on the results from the XPS data from Table 3, Table 4. presents the rate of oxidation of Fe²⁺ into Fe³⁺ and Co²⁺ and Co³⁺ for all three compositions of bimetallic MOFs.

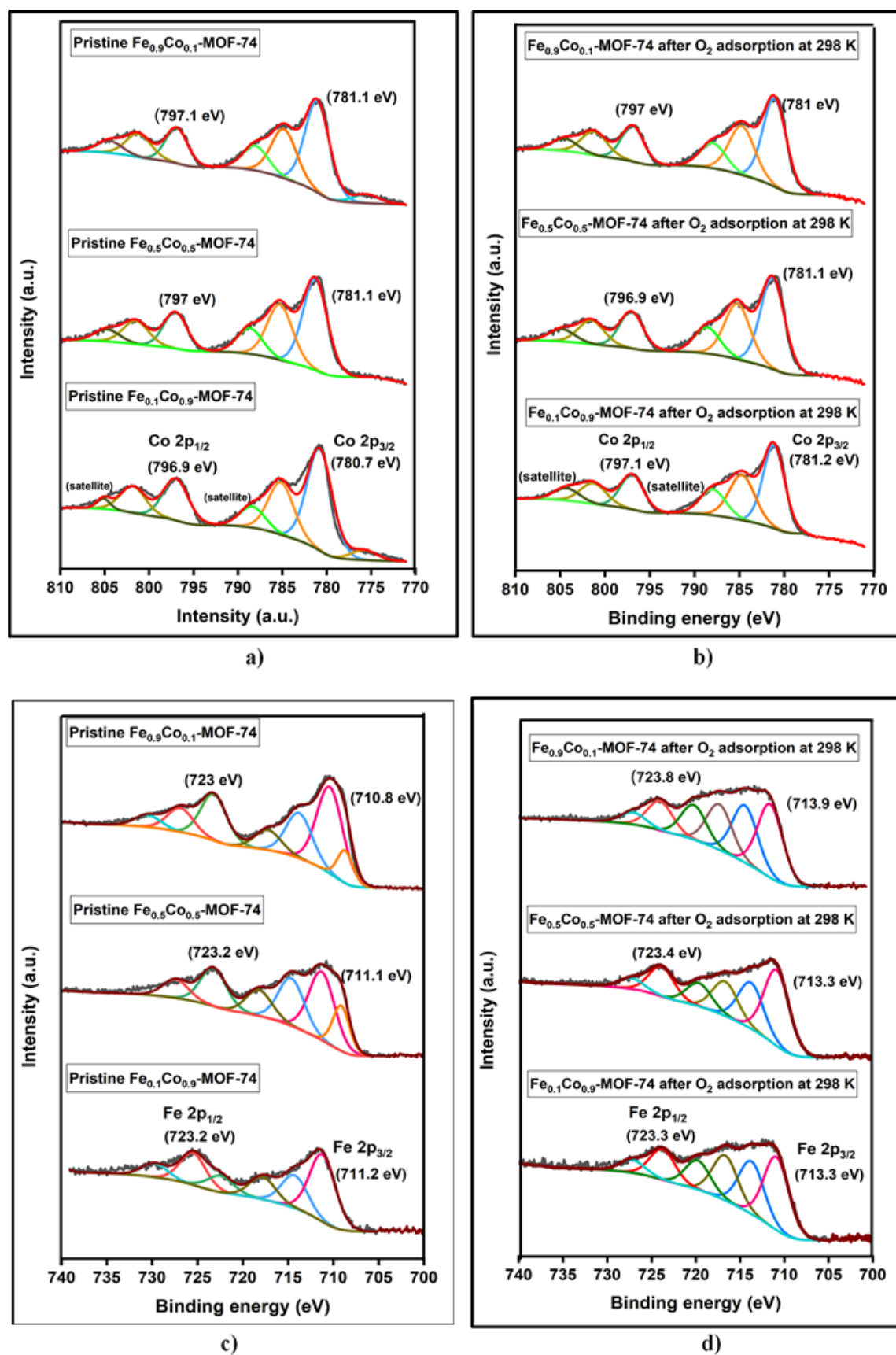


Figure 6.9: High-resolution XPS spectra of Co 2p a) before and b) after, and Fe 2p spectra of bimetallic Fe_xCo_{1-x}-MOF-74s c) before and d) after O₂ adsorption at 298 K.

Chapter 6: The potential of bimetallic FeCo-MOF-74 for Oxygen adsorption at room temperature

Name	Fe ²⁺ converted to Fe ³⁺	Co ²⁺ converted to Co ³⁺
Fe _{0.1} Co _{0.9} -MOF-74	25.0%	25.7%
Fe _{0.5} Co _{0.5} -MOF-74	21.7%	12.0%
Fe _{0.9} Co _{0.1} -MOF-74	68.2%	33.3%

Table 4. The molar fractions of Fe²⁺, Fe³⁺, Co²⁺ and Co³⁺ using the peak positions and relative peak areas of each element from the XPS data.

The iron-oxygen binding is temperature dependant and favours the reversible Fe-superoxo formation at low temperatures by the binding of a single iron centre to a single oxygen molecule, Fe-O. The irreversible Fe-peroxo complex formation at high temperatures is due to the irreversible binding of the O₂ molecule by two iron centres, Fe-O-Fe. It has been reported that the inclusion of different M²⁺ metal centres affects the oxygen-binding capability at the Fe²⁺ metal centres of the Fe-MOF-74.³¹ The interlacement of Fe and Co in the same framework is favourable because both are redox-active transition metals with similar charge and similar sizes; ionic radius of Co²⁺ is 0.74 Å and Fe²⁺ is 0.76 Å. The cyclability shown by Fe_{0.1}Co_{0.9}-MOF-74 and Fe_{0.5}Co_{0.5}-MOF-74 suggests the partial substitution of Fe by Co in the Fe-O-Fe bond and hinder the formation of peroxide anion. The adsorption performance of Fe_{0.9}Co_{0.1}-MOF-74 is similar to Fe-MOF-74, with around 68% of the Fe²⁺ in the framework getting oxidised to Fe³⁺. However, with increasing concentration of Co²⁺ in Fe_{0.5}Co_{0.5}-MOF-74, the Fe²⁺ to Fe³⁺ conversion reduced to 21% and maintained its adsorption capacity of 0.6 mmol/g over seven consecutive cycles. In Fe_{0.1}Co_{0.9}-MOF-74 the Fe²⁺ to Fe³⁺ conversion is 25% and the O₂ uptake capacity of this MOF is consistent for five consecutive cycles. The change in the oxidation of Co²⁺ to Co³⁺ in the MOF samples proves that the substitution of the secondary metal ion, Fe²⁺ impacts the oxidation kinetics of cobalt complexes too.

6.1.5 Conclusions

In this study, we have explored the potential of the bimetallic metal-organic framework with open iron-cobalt coordination sites for adsorption of oxygen due to electron transfer interactions. Fe-MOF-74 has been identified as an adsorbent capable of selective separation of O₂ from the air. Unfortunately, due to the irreversible iron-oxygen bonding, desorption of oxygen from the framework is not possible, and this one-time high-capacity uptake is not repeatable. The oxygen-binding capacity of Co-MOF-74 is not as high as Fe-MOF-74, but comparatively, it has better structural and chemical stability in air. The synergistic effect of incorporating the Fe²⁺ and Co²⁺ cations in one framework and how the charge transfers affect the adsorption capacity, cyclability and stability of the MOF is studied. We synthesised bimetallic Fe_x-Co_{1-x}-MOF-74 (x=0.9,0.5,0.1) in an air-free environment in a one-step solvothermal process. We studied its structural, morphological and adsorption properties using XRD, SEM-EDS,

Chapter 6: The potential of bimetallic FeCo-MOF-74 for Oxygen adsorption at room temperature

VSM, XPS, Mössbauer and N₂ adsorption. The oxygen adsorption capabilities and recyclable properties were measured at room temperature, and the results indicated that the Fe_{0.5}Co_{0.5}-MOF-74 has an uptake capacity of 0.6 mmol/g, and this adsorption capacity is consistent over seven consecutive cycles. The Fe_{0.1}Co_{0.9}-MOF-74 showed consistent uptake of 0.5 mmol/g for five cycles. These bimetallic MOFs displayed magnetic properties as well, and the Fe_{0.9}Co_{0.1}-MOF-74 showed the highest saturation magnetization (M_s) of 0.25 emu g⁻¹. With optimum tuning of Fe/Co ratio, an intrinsically magnetic MOF can be designed such that the magnetic properties can be utilised for the timely supply of the stored oxygen. The versatility, functionality and stability of Fe-MOF-74 and Co-MOF-74 can be enhanced by the interlacement of the Fe and Co metal ions in the framework. Owing to the promising results obtained by the heterogeneous dispersion of Fe and Co in the framework, the outcome from a more ordered dispersion will be explored.

6.2 Supporting Information and Acknowledgements

Supporting Information

The Electronic Supplementary Information (ESI) accompanying this publication document is included in **Appendix D**.

Acknowledgements

The authors acknowledge the use of instruments and scientific and technical assistance at the Monash Centre For Electron Microscopy, a Node of Microscopy Australia.

6.3 References

References cited in this Chapter text reproduced from the publication “*Efficient Delivery of Oxygen via Magnetic Framework Composites*” included as **Appendix D**, are consolidated here for completeness.

1. Sumida, K.; Rogow, D. L.; Mason, J. A.; McDonald, T. M.; Bloch, E. D.; Herm, Z. R.; Bae, T.-H. and Long, J. R., *Chem. Rev.*, 2012, **112**, 724–781.
2. Bae, Y.-S.; Spokoyny, A. M.; Farha, O. K.; Snurr, R. Q.; Hupp, J. T. and Mirkin, C. A., *Chem. Commun.*, 2010, **46**, 3478–3480.
3. Grant Glover, T.; Peterson, G. W.; Schindler, B. J.; Britt, D. and Yaghi, O., *Chem. Eng. Sci.*, 2011, **66**, 163–170.
4. Britt, D.; Furukawa, H.; Wang, B.; Glover, T. G. and Yaghi, O. M., *PNAS*, 2009, **106**, 20637–20640.
5. Yaghi, O. M.; Li, G. and Li, H., *Nature*, 1995, **378**, 703.
6. Yaghi, O. M.; O’Keeffe, M.; Ockwig, N. W.; Chae, H. K.; Eddaoudi, M. and Kim, J., *Nature*, 2003, **423**, 705–714.
7. Rosi, N. L.; Kim, J.; Eddaoudi, M.; Chen, B.; O’Keeffe, M. and Yaghi, O. M., *J. Am. Chem. Soc.*, 2005, **127**, 1504–1518.
8. Zhou, H.-C.; Long, J. R. and Yaghi, O. M., *Journal*, 2012.
9. Rosi, N. L.; Eckert, J.; Eddaoudi, M.; Vodak, D. T.; Kim, J.; Keffe, M. and Yaghi, O. M., *Science*, 2003, **300**, 1127.
10. Dietzel, P. D.; Besikiotis, V. and Blom, R., *J. Mater. Chem.*, 2009, **19**, 7362–7370.
11. Lin, K.-S.; Adhikari, A. K.; Ku, C.-N.; Chiang, C.-L. and Kuo, H., *Int. J. Hydrog. Energy*, 2012, **37**, 13865–13871.
12. Melag, L.; Sadiq, M. M.; Konstas, K.; Zadehahmadi, F.; Suzuki, K. and Hill, M. R., *RSC Adv.*, 2020, **10**, 40960–40968.
13. Weston, M. H., *U.S. Patent 20150105250*, April 16, 2015.
14. DeCoste, J. B.; Weston, M. H.; Fuller, P. E.; Tovar, T. M.; Peterson, G. W.; LeVan, M. D. and Farha, O. K., *Angew. Chem. Int. Ed.*, 2014, **53**, 14092–14095.
15. Mason, J. A.; Veenstra, M. and Long, J. R., *Chem Sci*, 2014, **5**, 32–51.
16. Sadiq, M. M.; Rubio-Martinez, M.; Zadehahmadi, F.; Suzuki, K. and Hill, M. R., *Ind. Eng. Chem. Res.*, 2018, **57**, 6040–6047.
17. Konstas, K.; Osl, T.; Yang, Y.; Batten, M.; Burke, N.; Hill, A. J. and Hill, M. R., *J. Mater. Chem.*, 2012, **22**, 16698–16708.
18. Kim, J.; Cho, H.-Y. and Ahn, W.-S., *Catal. Surv. Asia*, 2012, **16**, 106–119.
19. Doherty, C. M.; Buso, D.; Hill, A. J.; Furukawa, S.; Kitagawa, S. and Falcaro, P., *Acc. Chem. Res.*, 2014, **47**, 396–405.
20. Furukawa, H.; Cordova, K. E.; O’Keeffe, M. and Yaghi, O. M., *Science*, 2013, **341**, 1230444.
21. Ke, F.; Yuan, Y.-P.; Qiu, L.-G.; Shen, Y.-H.; Xie, A.-J.; Zhu, J.-F.; Tian, X.-Y. and Zhang, L.-D., *J. Mater. Chem.*, 2011, **21**, 3843–3848.
22. Falcaro, P.; Ricco, R.; Yazdi, A.; Imaz, I.; Furukawa, S.; Maspoch, D.; Ameloot, R.; Evans, J. D. and Doonan, C. J., *Coord. Chem. Rev.*, 2016, **307**, 237–254.
23. Bloch, E. D.; Murray, L. J.; Queen, W. L.; Chavan, S.; Maximoff, S. N.; Bigi, J. P.; Krishna, R.; Peterson, V. K.; Grandjean, F.; Long, G. J.; Smit, B.; Bordiga, S.; Brown, C. M. and Long, J. R., *J. Am. Chem. Soc.*, 2011, **133**, 14814–14822.
24. Märcz, M.; Johnsen, R. E.; Dietzel, P. D. C. and Fjellvåg, H., *Micropor. Mesopor. Mater.*, 2012, **157**, 62–74.
25. Yang, D.-A.; Cho, H.-Y.; Kim, J.; Yang, S.-T. and Ahn, W.-S., *Energy Environ. Sci.*, 2012, **5**, 6465–6473.
26. Villajos, J. A.; Jagorel, N.; Reinsch, S. and Emmerling, F. L., *Front. Mater.*, 2019, **6**, 230.
27. Becker, T. M.; Heinen, J.; Dubbeldam, D.; Lin, L.-C. and Vlugt, T. J. H., *J. Phys. Chem. C*, 2017, **121**, 4659–4673.

Chapter 6: The potential of bimetallic FeCo-MOF-74 for Oxygen adsorption at room temperature

28. Melag, L.; Sadiq, M. M.; Smith, S. J. D.; Konstas, K.; Suzuki, K. and Hill, M. R., *J. Mater. Chem. A*, 2019, **7**, 3790–3796.
29. Vitillo, J. G.; Regli, L.; Chavan, S.; Ricchiardi, G.; Spoto, G.; Dietzel, P. D.; Bordiga, S. and Zecchina, A., *J. Am. Chem. Soc.*, 2008, **130**, 8386-8396.
30. Díaz-García, M.; Mayoral, Á.; Díaz, I. and Sánchez-Sánchez, M., *Cryst. Growth Des.*, 2014, **14**, 2479–2487.
31. Moeljadi, A. M. P.; Schmid, R. and Hirao, H., *Can. J. Chem.*, 2016, **94**, 1144–1150.
32. Parkes, M. V.; Sava Gallis, D. F.; Greathouse, J. A. and Nenoff, T. M., *J. Phys. Chem. C*, 2015, **119**, 6556–6567.
33. Kapelewski, M. T.; Geier, S. J.; Hudson, M. R.; Stück, D.; Mason, J. A.; Nelson, J. N.; Xiao, D. J.; Hulvey, Z.; Gilmour, E.; FitzGerald, S. A.; Head-Gordon, M.; Brown, C. M. and Long, J. R., *J. Am. Chem. Soc.*, 2014, **136**, 12119–12129.
34. Wu, H.; Zhou, W. and Yildirim, T., *J. Am. Chem. Soc.*, 2009, **131**, 4995–5000.
35. Dietzel, P. D.; Georgiev, P. A.; Eckert, J.; Blom, R.; Strässle, T. and Unruh, T., *Chem. Commun.*, 2010, **46**, 4962–4964.
36. Anneser, M. R.; Haslinger, S.; Pöthig, A.; Cokoja, M.; D'Elia, V.; Högerl, M. P.; Basset, J.-M. and Kühn, F. E., *Dalton Trans.*, 2016, **45**, 6449-6455.
37. Kepp, K. P., *Coord. Chem. Rev.*, 2017, **344**, 363-374.
38. Carlsen, C. U.; Møller, J. K. S. and Skibsted, L. H., *Coord. Chem. Rev.*, 2005, **249**, 485-498.
39. Li, J.-R.; Kuppler, R. J. and Zhou, H.-C., *Chem. Sov. Rev.*, 2009, **38**, 1477–1504.
40. Zhang, W.; Banerjee, D.; Liu, J.; Schaef, H. T.; Crum, J. V.; Fernandez, C. A.; Kukkadapu, R. K.; Nie, Z.; Nune, S. K. and Motkuri, R. K., *Adv. Mater.*, 2016, **28**, 3572–3577.
41. Xiao, D. J.; Gonzalez, M. I.; Darago, L. E.; Vogiatzis, K. D.; Haldoupis, E.; Gagliardi, L. and Long, J. R., *J. Am. Chem. So.*, 2016, **138**, 7161–7170.
42. Sugimoto, H.; Nagayama, T.; Maruyama, S.; Fujinami, S.; Yasuda, Y.; Suzuki, M. and Uehara, A., *Bull. Chem. Soc. Jpn.*, 1998, **71**, 2267–2279.
43. Nagar, H.; Vadthya, P.; Prasad, N. S. and Sridhar, S., *RSC Adv.*, 2015, **5**, 76190–76201.
44. Sun, J.; Zhang, X.; Zhang, A. and Liao, C., *Int. J. Environ. Sci*, 2019, **80**, 197–207.
45. Zhong, M.; Yang, D.-H.; Kong, L.-J.; Shuang, W.; Zhang, Y.-H. and Bu, X.-H., *Dalton Trans.*, 2017, **46**, 15947-15953.
46. Sun, Q.; Liu, M.; Li, K.; Han, Y.; Zuo, Y.; Chai, F.; Song, C.; Zhang, G. and Guo, X., *Inorg. Chem. Front*, 2017, **4**, 144-153.
47. Yuan, Q.; Yu, Y.; Sherrell, P. C.; Chen, J. and Bi, X., *Chem. Asian J.*, 2020, **15**, 1728-1735.
48. Sun, H.; Ren, D.; Kong, R.; Wang, D.; Jiang, H.; Tan, J.; Wu, D.; Chen, S. and Shen, B., *Microporous Mesoporous Mater.*, 2019, **284**, 151-160.
49. Howarth, A. J.; Peters, A. W.; Vermeulen, N. A.; Wang, T. C.; Hupp, J. T. and Farha, O. K., *Chem. Mater.*, 2017, **29**, 26–39.
50. Mason, J. A.; Sumida, K.; Herm, Z. R.; Krishna, R. and Long, J. R., *Energy Environ. Sci.*, 2011, **4**, 3030–3040.
51. Yamashita, T. and Hayes, P., *Appl. Surf. Sci.*, 2008, **254**, 2441-2449.
52. Graat, P. C. and Somers, M. A., *Appl. Surf. Sci.*, 1996, **100**, 36-40.
53. Roosendaal, S.; Van Asselen, B.; Elsenaar, J.; Vredenberg, A. and Habraken, F., *Surf. Sci.*, 1999, **442**, 329-337.
54. C. Carvalho, C. L.; B. Silva, A. T.; Luz, R. A.; Castro, G. M. B.; da Luz Lima, C.; Mastelaro, V. R.; da Silva, R. R.; Oliveira Jr, O. N. and Cantanhêde, W., *ACS Appl. Nano Mater.*, 2018, **1**, 4283-4293.
55. Jain, S.; Shah, J.; Dhakate, S.; Gupta, G.; Sharma, C. and Kotnala, R., *J. Phys. Chem. C*, 2018, **122**, 5908-5916.
56. Liu, C.; Wang, J.; Wan, J.; Cheng, Y.; Huang, R.; Zhang, C.; Hu, W.; Wei, G. and Yu, C., *Angew. Chem. Int. Ed.*, 2020, **59**, 3630-3637.

Chapter 7: Conclusions and Future Work

Chapter 7: Conclusions and Future Work.....	108
7.1 Summary of Dissertation Findings.....	109
7.2 Recommendation for Future Work	112

7.1 Summary of Dissertation Findings

In this chapter, the key findings of this project are summarised. This thesis focused on the adsorption and storage of oxygen using MOFs and to use the heating capability of the Magnetic Framework Composites to achieve energy-efficient and safe release of the oxygen.

Objective 1 was to identify, synthesise and evaluate oxygen adsorption capacities, stability and reversibility of MOFs at different temperatures. In nature, heme proteins are the recognised biological oxygen carriers, and so iron complexes have always been preferred for oxygen studies. Previous oxygen adsorption studies conducted by Bloch, *et al.*, using Fe-MOF-74 showed chemisorption and selectivity adsorbed oxygen over nitrogen at 298 K. However, the adsorption was very strong and not reversible. Cobalt complexes exhibit both a strong affinity and reversible binding to oxygen in Co^{2+} complexes, and the M-MOF-74 series of MOFs has the highest density of unsaturated open metal centres. Therefore Co-MOF-74 was selected as the candidate MOF, synthesised and oxygen adsorption studies were carried out at 204 K, 273 K and 298 K. Co-MOF-74/ Fe_3O_4 MFCs were synthesised. As observed from Figure 7.1-a) at 204 K, the Co-MOF-74 showed an oxygen uptake capacity of 4.8 mmol g^{-1} at 1.2 Bar, and 100 % release of oxygen molecules was accomplished when the composite with 12.18 wt. % Fe_3O_4 nanoparticles were exposed to a magnetic field of 17.4 m. Prolonged exposure to oxygen at elevated temperatures adversely affected the cyclability and stability of this MOF composite. This proof-of-concept experiment proved the oxygen adsorption capability of MFCs. It established the efficiency of the magnetic induction heating in successfully achieving the release of most of the adsorbed oxygen molecules.

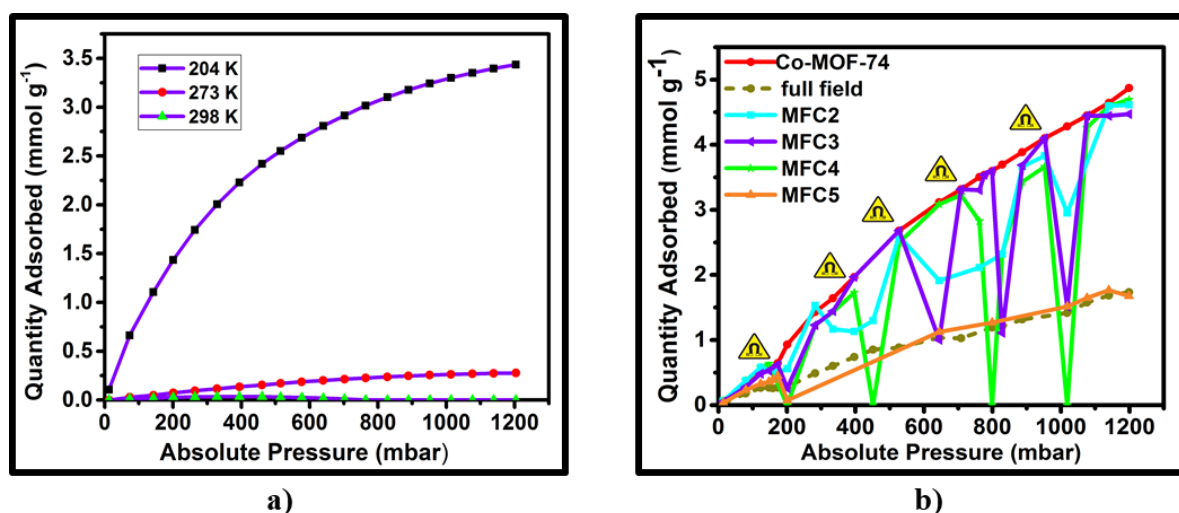


Figure 7.1: a) Oxygen adsorption isotherms of Co-MOF-74/ Fe_3O_4 measured at 204 K, 273 K and 298 K, b) Triggered release of 4.8 mmol g^{-1} of adsorbed oxygen at 204 K using MISA.

Figure reproduced from **Figure 4.3** and **Figure 4.5**.

Objective 2 was to identify and synthesise simpler, Stabler MOFs for oxygen adsorption and storage at ambient temperatures and to calculate the energy requirements to regenerate the MOFs using the magnetic induction swing adsorption (MISA) process. MOFs can be a safe, lightweight alternative that can store oxygen in high volumes and at much lower pressures. Accordingly, CuBTC one of the widely explored, easily scalable, and most commercially used MOFs was used to fabricate Cu-BTC/MgFe₂O₄ composite pellets. The and 3 wt.% CuBTC-MgFe₂O₄ composite pellets showed an adsorption capacity of 0.03 mmol/g at 1 Bar pressure at 298 K. As shown in Figure 7.2-a), when they were exposed to a magnetic field of 31 mT, the MgFe₂O₄ nanoparticles attained a temperature rise to 86 °C causing full desorption of the adsorbed oxygen molecules. To highlight the versatility of the MISA process, it was used to regenerate the MFC in a closed cyclic process across all pressures. This experiment was planned to alternate between adsorption, desorption and regeneration between each cycle. The investigation was conducted with the usual oxygen adsorption by the MFCs followed by desorption using a magnetic field of 31 mT (86 °C), and the 200-0 mBar regeneration was achieved within 6 mins by the magnetic heating from 33 mT (92 °C) magnetic field. For the energy calculations when 0.3 g and 0.6 g of the 3 wt. % MFC pellets were exposed to a magnetic field of 31 mT; the MFC pellets experienced a temperature rise of 86 °C and the energy utilised for the regeneration of 0.26 mmol /g of oxygen adsorbed at 1000 mBar was calculated to be 5.1 MJ /kg_{O₂} for 0.3 g weight sample and 5.6 MJ /kg_{O₂} for 0.6 g sample. This experiment proved that the pelletised system of CuBTC-MgFe₂O₄, which is stable to water vapour, can be filled and emptied within 10 minutes requiring around 5.6 MJ/kg.

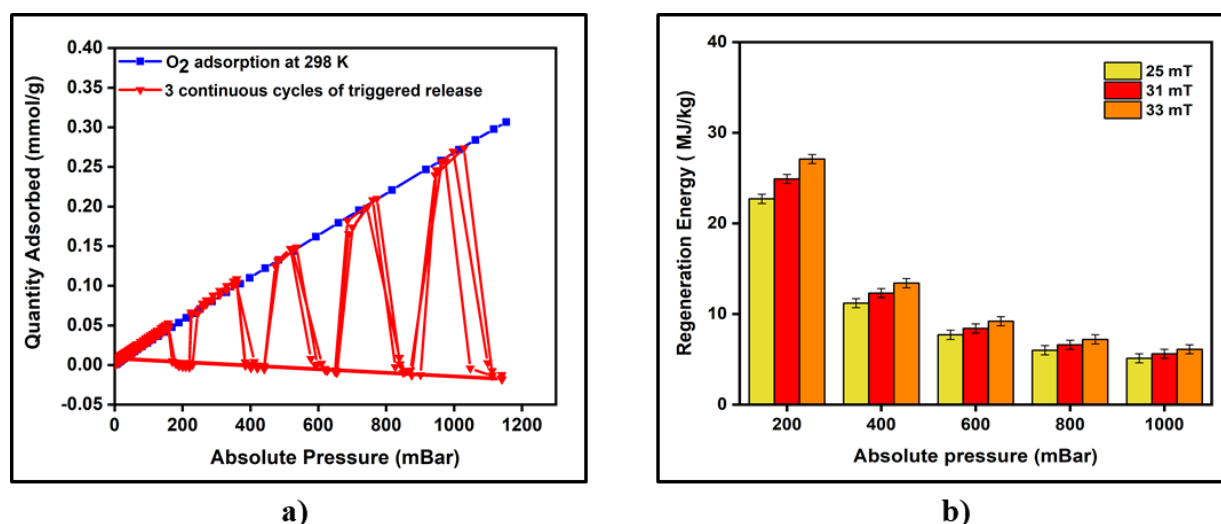


Figure 7.2: a) Cyclic Oxygen adsorption-desorption-regeneration isotherms of CuBTC-MgFe₂O₄ measured at 298 K, b) Regeneration energy as a function of varying magnetic fields of 25 mT, 31 mT, and 33 mT used for desorption of oxygen from the 3 wt.% CuBTC-MgFe₂O₄ MFCs. Figure reproduced from **Figure 5.6** and **Figure 5.8**.

Objective 3 was to understand the effect of varying Fe: Co ratios on the adsorptive and stability properties of the bimetallic FeCo-MOF-74. A series of $\text{Fe}_x\text{-Co}_{1-x}\text{-MOF-74}$ ($x=0.9,0.5,0.1$) were synthesised, and the Fe/Co, $\text{Co}^{2+}/\text{Co}^{3+}$ and the $\text{Fe}^{2+}/\text{Fe}^{3+}$ ratios were thoroughly investigated to understand the synergistic effect of bimetallic cations on oxygen uptake properties of MOFs. As shown in Figure 7.3, The oxygen adsorption isotherms were measured at 298 K, and the results show that the $\text{Fe}_{0.5}\text{-Co}_{0.5}\text{-MOF-74}$ shows favourable oxygen adsorption uptake of 0.6 mmol/g over seven consecutive cycles. The iron-oxygen binding is temperature dependant and favours the reversible Fe-superoxo formation at low temperatures and the irreversible Fe-peroxo complex formation at high temperatures. It has been reported that the inclusion of different M^{2+} metal centres affects the oxygen-binding capability at the Fe^{2+} metal centres of the Fe-MOF-74 and the interplacement of Fe and Co is possible because both are redox-active transition metals with similar charge and similar sizes; ionic radius of Co^{2+} is 0.74 Å and Fe^{2+} is 0.76 Å.

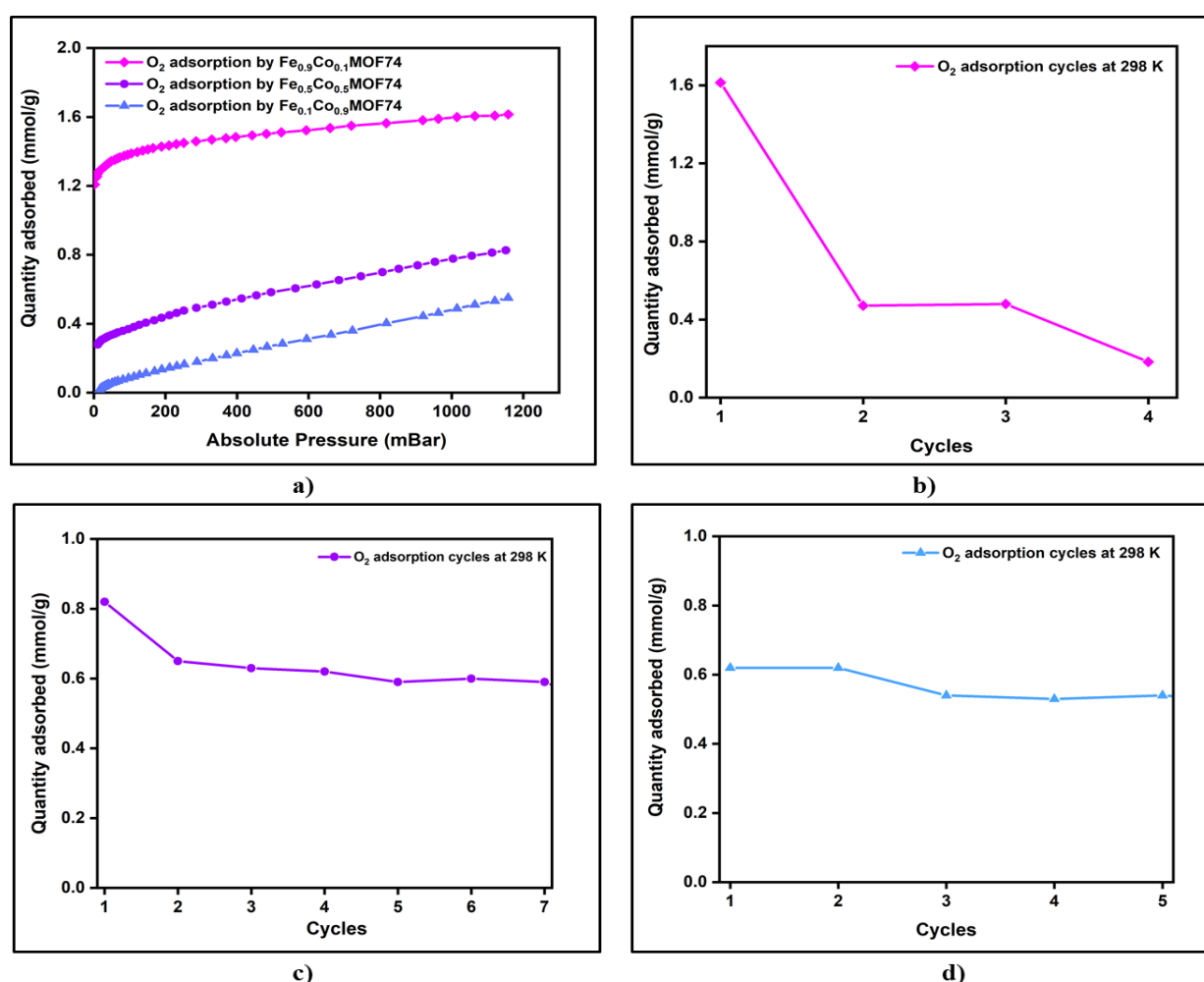


Figure 7.3: Low-pressure oxygen adsorption isotherms by a) the bimetallic $\text{Fe}_{0.9}\text{Co}_{0.1}\text{-MOF-74}$, $\text{Fe}_{0.5}\text{Co}_{0.5}\text{-MOF-74}$ and $\text{Fe}_{0.1}\text{Co}_{0.9}\text{-MOF-74}$, oxygen adsorption cycles of b) $\text{Fe}_{0.9}\text{Co}_{0.1}\text{-MOF-74}$, c) $\text{Fe}_{0.5}\text{Co}_{0.5}\text{-MOF-74}$ and d) of $\text{Fe}_{0.1}\text{Co}_{0.9}\text{-MOF-74}$ at 298 K. Figure reproduced from **Figure 6.5**.

The cyclability shown by $\text{Fe}_{0.1}\text{Co}_{0.9}\text{-MOF-74}$ and $\text{Fe}_{0.5}\text{Co}_{0.5}\text{-MOF-74}$ suggests the partial substitution of Fe by Co in the Fe-O-Fe bond and hinder the formation of peroxide anion. The adsorption performance of $\text{Fe}_{0.9}\text{Co}_{0.1}\text{-MOF-74}$ is similar to Fe-MOF-74, with around 68% of the Fe^{2+} in the framework getting oxidised to Fe^{3+} . However, with increasing concentration of Co^{2+} in $\text{Fe}_{0.5}\text{Co}_{0.5}\text{-MOF-74}$, the Fe^{2+} to Fe^{3+} conversion reduced to 21% and maintained its adsorption capacity of 0.6 mmol/g over seven consecutive cycles. In $\text{Fe}_{0.1}\text{Co}_{0.9}\text{-MOF-74}$ the Fe^{2+} to Fe^{3+} conversion is 25% and the O_2 uptake capacity of this MOF is consistent for five consecutive cycles. The change in the oxidation of Co^{2+} to Co^{3+} in the MOF samples proves that the substitution of the secondary metal ion, Fe^{2+} impacts the oxidation kinetics of cobalt complexes also.

7.2 Recommendation for Future Work

1. The oxygen adsorption capability of Co-MOF-74 and the efficiency of the magnetic induction heating in successfully achieving the release of most of the oxygen molecules have been proved here. Preliminary work on the oxygen adsorption capacities of the first row transition metal towards oxygen showed promising results that need to be studied further (Figure 7.4). Using the selectivity of the early transition metal ions, the framework of the MOFs, MFCs should be fabricated that can capture and store oxygen at or near ambient temperatures. The magnetic content of the MFCs can be tuned to achieve efficient and safe on-demand release of the adsorbed oxygen molecules.

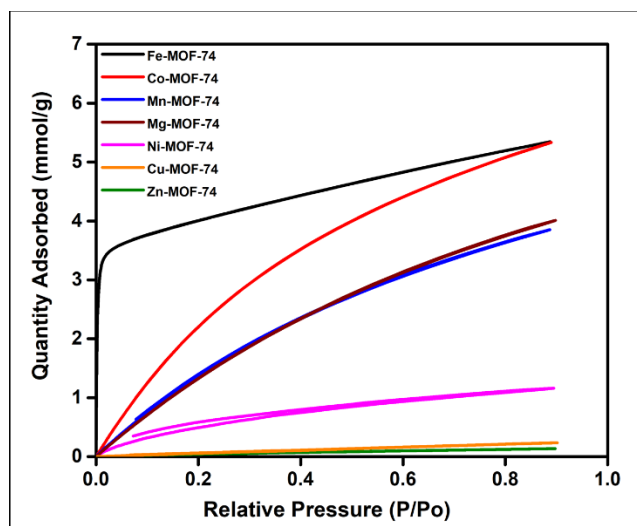


Figure 7.4: Oxygen adsorption isotherms of the synthesised $M\text{-MOF-74}$ ($M = \text{Fe}, \text{Co}, \text{Mn}, \text{Mg}, \text{Ni}, \text{Cu}, \text{Zn}$) at 204 K.

2. Apart from specially designed MOFs to chemisorb oxygen, the existing family of MOFs need to be explored more for a stable and recyclable solution for room temperature oxygen storage. Thoughtfully synthesised bi or multimetallic MOFs are believed to impart the selectivity and the stability required to capture and store a reactive gas like oxygen.

3. Fe-MOF-74 demonstrates high oxygen uptake capacity, but the irreversible Fe-peroxo complex formation at high temperatures affects the cyclability of the MOF due to the irreversible binding of the oxygen molecule by two iron centres, Fe-O-Fe. If the inclusion of different M^{2+} metal centres can disrupt the Fe-O-Fe bond, it should maintain the oxygen-binding capability at the Fe^{2+} metal centres of the Fe-MOF-74. The planned substitution of the M^{2+} ions in a MOF can be targeted using a template-based synthesis such that the favourable M^{2+} ions get placed between the two Fe^{2+} ions and avoid the formation of the peroxide anion while maintaining its oxygen selectivity and capacity.

Appendix A

Efficient Delivery of Oxygen via Magnetic Framework Composites

Leena Melag, M. Munir Sadiq, Stefan J. D. Smith, Kristina Konstas,
Kiyonori Suzuki and Matthew R. Hill

Cite this: *J. Mater. Chem. A*, 2019, 7, 3790Received 9th August 2018
Accepted 10th January 2019
DOI: 10.1039/c8ta07739h
rsc.li/materials-a

Efficient delivery of oxygen via magnetic framework composites†

Leena Melag,^a M. Munir Sadiq,^{*ab} Stefan J. D. Smith,^{id b} Kristina Konstas,^b Kiyonori Suzuki^{id *c} and Matthew R. Hill^{id *ab}

Metal–organic frameworks (MOFs), with their intriguing network structures, large internal surface areas, and tunable pore properties offer the perfect yet largely unexplored alternative for selective adsorption of oxygen. Owing to their thermally insulating nature and often favorable binding of guest species, controlled desorption of the adsorbed molecules from such frameworks can be challenging and energy intensive. To find an energy efficient means for release of these gas molecules, here, we have made use of the heating effect of magnetic nanoparticles to achieve desorption using the Magnetic Induction Swing Adsorption (MISA) process. Magnetic nanoparticles when exposed to a high-frequency magnetic field, heat up instantly; and when present within a MOF, this localized heating is enough to drive the release of adsorbed molecules. Here Co-MOF-74 based Magnetic Framework Composites (MFCs), containing varying concentrations of Fe₃O₄ nanoparticles, were trialed for triggered oxygen capture. The greatest oxygen adsorption achieved by the prepared cobalt based MFCs was 4.8 mmol g⁻¹ at 1.2 bar, with a Type I adsorption isotherm. For the effective desorption was then triggered by exposure to a magnetic field, with 100% desorption of oxygen accomplished by MFC4, the MOF composite with 12.18 wt% Fe₃O₄ nanoparticles.

Introduction

With more than 100 million tons consumed annually, oxygen separation from air is one of the most energy demanding industrial processes, one that is primarily achieved by the cryogenic distillation of air, where air is compressed between 4 and 10 atm, cooled to ambient temperatures before passing it through the pre-purification unit to remove the trace contaminants, especially water, carbon dioxide, and heavy hydrocarbons. The purified air is passed through the main heat exchanger, cooled to near its liquefaction temperature before entering the distillation columns to separate oxygen, nitrogen and argon. Achieving and maintaining column temperatures of –183 °C (boiling point of oxygen) to distil large volumes of high purity oxygen is complex and consumes vast amounts of energy.

Most other oxygen separation techniques rely on the adsorption or isolation of nitrogen from air to produce oxygen; however, as air is only 21% oxygen, there is significant room for improvement.^{1–3} Non-cryogenic separation processes, including

membrane and adsorption based technologies are less energy intensive, but are not yet industrially competitive.^{4,5}

Adsorption techniques make use of the differences in the quadrupole moments and the kinetic diameters of gases to separate a specific component from a mixture of gases. Zeolites, for example, preferentially adsorb nitrogen due to the interaction between its extra framework cations and the N₂ molecule's larger quadrupole.⁶ Through this mechanism, nitrogen molecules are retained in vacant pores of the adsorbent, allowing gaseous oxygen to be collected.⁷ Alternatively, molecular sieve carbons are able to selectively adsorb oxygen by size, with only the smaller oxygen molecules (3.43 Å vs. 3.68 Å) able to access the adsorbent's pore cavities. Unfortunately, material properties such as structural rigidity, heterogeneity of pores, the inability to alter their pore geometry, as well as regeneration energy costs, impose significant limitations on these methods.^{8,9}

Instead, separation processes that exploit differences in the chemical properties of oxygen and nitrogen may offer the selectivity required for direct capture of oxygen from air. Over the last decade, metal organic frameworks, (MOFs), have been successfully deployed for the selective separation and storage of a range of gases,^{10–15} making them applicable in diverse fields of selective adsorption processes, to catalysis to drug delivery, and leading to their scale up from laboratory trials to commercial productions.^{16–23} In spite of all these advances, very few reports have highlighted MOFs' potential for oxygen capture or storage.^{7,24–26} So far, oxygen separation using MOFs has relied on

^aDepartment of Chemical Engineering, Monash University, Clayton, VIC 3168, Australia. E-mail: matthew.hill@csiro.au

^bDepartment of Materials Science and Engineering, Monash University, Clayton, VIC 3168, Australia

^cCSIRO, Private Bag 33, Clayton South MDC, VIC 3169, Australia

† Electronic supplementary information (ESI) available. See DOI: 10.1039/c8ta07739h

MOFs containing partially uncoordinated redox-active metal centers.^{26,27} In these cases, oxygen reacts with the exposed metal cation within the MOF, causing selective adsorption by chemically binding to a molecule of oxygen.^{7,10,28} While offering high adsorption capacities in ambient conditions, the key challenge is in overcoming the irreversible nature of the adsorption. Working capacity, defined as the difference in the amount adsorbed under uptake conditions and the amount left in the adsorbent under desorption conditions is an important parameter used in selecting materials for separation and storage applications, remains prohibitively low. Unfortunately, MOFs' strong host-guest interactions and low thermal conductivity make desorption by high temperature and/or vacuum, slow and energy intensive.²⁹⁻³³ Ultimately, the efficiency of a separation process depends on the energy required to desorb bound guest molecules.³³

Recently, the energy penalty associated with the regeneration stage of Temperature Swing Adsorption (TSA) and Pressure Swing Adsorption (PSA) processes has been overcome by the inclusion of 'stimuli-responsive' functional groups and nanoparticles in MOFs.³⁴⁻³⁶ Stimulation of these groups trigger property changes within the MOF, causing adsorbent regeneration without the application of external heat or vacuum.³⁴⁻³⁶

One such method is the incorporation of magnetic nanoparticles into MOFs, resulting in magnetic framework composites (MFCs); which add magnetic induction heating properties to the adsorbent, as well as magnetically driven isolation and positioning of MOF crystals in solution.^{20,21,37} Induction heating is a controllable method of heating where energy from an alternating magnetic field is converted into heat within a magnetic material. Magnetically induced heating effect has successfully been used for heat treatment of metals and alloys,³⁸ hyperthermia treatment of cancer cells,³⁹⁻⁴² and more recently, as the heat source for MOF synthesis.^{20,21,37}

MFCs are prepared by growing MOF crystals around pre-formed magnetic nanoparticles,^{43,44} which ensure they are dispersed uniformly within MOF. When exposed to an alternating magnetic field, these 'nanoheaters' provide rapid, localized heating throughout the framework. By using localised heat sources, the efficacy of applied regeneration energy can be greatly improved by overcoming MOF's inherently low thermal conductivity. This process of using the intense heating of magnetic nanoparticles to trigger desorption of bound gas molecules from within an adsorbent is known as magnetic induction swing adsorption (MISA).^{39-41,43-49}

Unlike the traditional cyclic adsorption based separation techniques of temperature swing adsorption (TSA), and or pressure swing adsorption (PSA), the MISA process regenerates the entire adsorbent while greatly reducing the energy inefficiencies associated with the conduction of externally applied heat and or through an insulating MOF. In studies carried out by Li *et al.*^{43,46} the composite of Mg-MOF-74 and Fe₃O₄ nanoparticles, showed a ~9.8% increase in CO₂ uptake as compared to a bare Mg-MOF-74 and on application of a magnetic field of 81 mT, the heating of the Fe₃O₄ nanoparticles resulted in efficient release of ~49% of adsorbed CO₂ molecules. Sadiq *et al.*⁴⁴ further demonstrated the MISA's potential by incorporating

MgFe₂O₄ nanoparticles in zirconium-based UiO-66 to synthesize an MFC that achieved a 100% release of CO₂ at a magnetic field of 32 and 42 mT. Together, these works prove MISA's potential for low energy desorption using MFCs for carbon capture applications. In this work, using the MISA process, we examine the potential of Magnetic Framework Composites (MFCs) for oxygen capture.

The M-MOF-74 series of MOFs has the highest density of unsaturated open metal centres, needed to bind oxygen and since cobalt exhibits both, a strong affinity and a temperature-dependant reversible binding to oxygen in Co²⁺ complexes hence we selected Co-MOF-74 as the candidate MOF to demonstrate MISA triggered release of oxygen.^{7,10,25,50-56} Synthesis of Co-MOF-74 in the presence of pre-synthesized Fe₃O₄ magnetic nanoparticles successfully resulted in composites with the magnetic nanoparticle firmly embedded in the MOF. Subsequent to synthesis of composites with varying concentrations of Fe₃O₄ nanoparticles, the triggered release MISA experiments were carried out.

In non-cryogenic conditions, the Fe₃O₄@Co-MOF-74 MFC had a maximum oxygen uptake of 4.8 mmol g⁻¹ at 1.2 bar. The MFC4 with 12.18 wt% Fe₃O₄ nanoparticles was able to release 100% of the adsorbed oxygen molecules when exposed to a magnetic field of 17.4 mT at 270 kHz.

Results and discussion

The size and morphology of the synthesized Fe₃O₄ nanoparticles was investigated using a scanning electron microscope (SEM). The nanoparticles had a spherical orientation with nanoparticle size of ~30 to ~50 nm (see Fig. S2a†). The nanoparticles showed excellent stability in water with no change in properties for one month.^{48,57-60}

The magnetic properties of the Fe₃O₄ nanoparticles were studied at room temperature using a vibrating sample magnetometer (VSM) with a maximum applied field (μ_0H) of ± 1 T. The hysteresis curve of the Fe₃O₄ nanoparticles shows a saturation magnetization (M_s) of 58 emu g⁻¹ and very little coercivity (Fig. S6a†). Thermo-magneto gravimetric analysis (TMGA) of the nanoparticles revealed the Curie temperature of the particles to be $T_c = 570$ °C (Fig. S7†). At the T_c , there is a phase transition from the ferrimagnetic state to the paramagnetic state that results in a loss of heating capability of the NPs and thus could serve as a switch to regulate the temperature rise.

The heat generation capacity of the nanoparticles was estimated by recording the temperature rise profile of a known concentration of NPs solution and estimating the specific absorption rate (SAR) in W g⁻¹.^{41,44} All the induction heating experiments were carried out at 270 kHz except where otherwise stated. At μ_0H of 16.4 mT, 5 mg ml⁻¹ of Fe₃O₄ nanoparticles in water attained a maximum temperature rise of 85.0 °C and the SAR was calculated to be 74.5 W g⁻¹ (Fig. S8†). These synthesised nanoparticles were then used to fabricate composites with varying concentrations of magnetic nanoparticles simply by adding weighed quantities of Fe₃O₄ nanoparticles to the MOF precursor solutions and mechanically stirring it for the course of the synthesis (see Section S1-III). The concentrations

of these composites were checked using the inductive coupled plasma (ICP) analysis and the results are listed below in Table 1.

As observed from the XRD patterns in Fig. 1, for all the composites **MFC1–MFC6**, the peaks of bare Co-MOF-74 match the diffraction peaks of the composites. For magnetic measurements, as expected, the composites with higher concentrations of magnetic nanoparticles show higher saturation magnetization (Fig. S6b†).

The scanning electron microscope images reveal that the nanoparticles are uniformly embedded over the entire surface of the composite. As observed from Fig. 2e and f, the EDX mapping analysis on the samples confirm the presence of the Fe_3O_4 nanoparticles in the composites.

For gas measurements, low-pressure gas adsorption isotherms in the range of 0–1 bar were measured and Type I nitrogen isotherm, corresponding to a monolayer adsorption, was obtained for the bare Co-MOF-74 and the composites. The measured Brunauer–Emmett–Teller (BET) and Langmuir surface areas of the bare Co-MOF-74 were $1449 \text{ m}^2 \text{ g}^{-1}$ and $1764 \text{ m}^2 \text{ g}^{-1}$ respectively.

In case of **MFC1** with 0.08 wt% Fe_3O_4 , the measured BET surface area of $1478 \text{ m}^2 \text{ g}^{-1}$ is actually higher than that of the bare Co-MOF-74. This may be attributed to some heterogeneous nucleation with the nanoparticles acting as nuclei and aiding the nucleation of the composite. But for **MFC3–MFC6**, increasing the content of magnetic NPs in the framework directly and adversely affects the surface area with **MFC3**– $1082 \text{ m}^2 \text{ g}^{-1}$, **MFC4**– $1008 \text{ m}^2 \text{ g}^{-1}$, **MFC5**– $952 \text{ m}^2 \text{ g}^{-1}$ and **MFC6**– $713 \text{ m}^2 \text{ g}^{-1}$ respectively (Fig. S4†).

With the MFCs, to establish the optimum time and temperature conditions for maximum adsorption of oxygen, the trials were conducted at three different temperatures of 204 K, 273 K and 298 K. The composite **MFC3**, at a temperature of 204 K, achieved maximum adsorption of oxygen of 3.5 mmol g^{-1} at 1.2 bar at an equilibration time of 5 s (Fig. 3).

Triggered release experiments

The triggered release of bound oxygen from the MFCs was achieved using the Tristar Micromeritics adsorption equipment in conjunction with an induction-heating machine. The requirement from the induction machine was to pass a current high enough to generate a large magnetic field and cause heating of the nanoparticles to their maximum capacity. If the heating of these nanoheaters is high enough, it would cause instability in the intermolecular bond between the adsorbed oxygen molecules and the adsorbing MFCs and trigger the release of the oxygen molecules. To know the maximum temperature rise attained by both, the Fe_3O_4 nanoparticles in itself and the Fe_3O_4 nanoparticles from the composite,

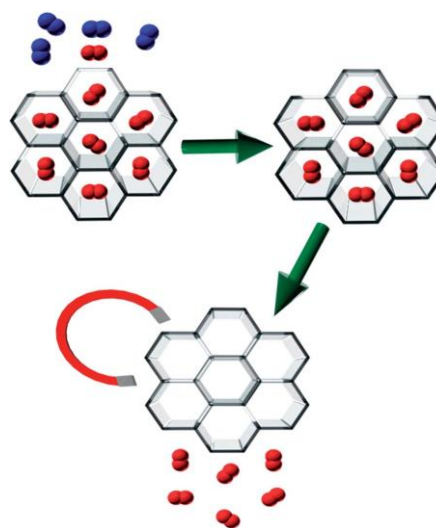


Fig. 1 The XRD pattern of the Co-MOF-74 and the MFCs compared with the simulated data of M-MOF-74.

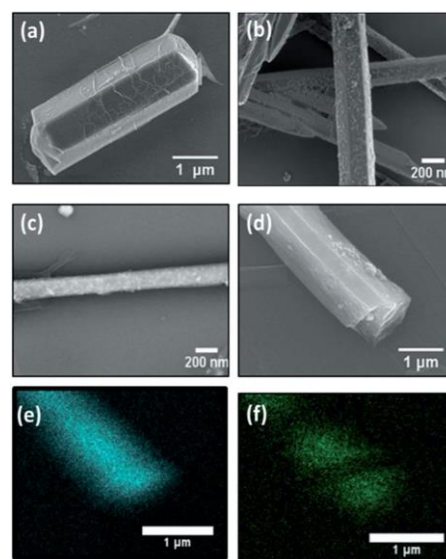


Fig. 2 The SEM micrographs of (a) bare Co-MOF-74, (b) Co-based composite with Fe_3O_4 nanoparticles embedded in it, (c) the contrast in the BSE image confirms the presence and uniform distribution of Fe_3O_4 nanoparticles throughout the composite, (d) sample used for EDX mapping, (e) EDX mapping results of sample showing the cobalt content and (f) Fe content in the composite.

Table 1 Results from the ICP analysis of the synthesized composites show the concentration of magnetic content within the MFCs

	MFC1	MFC2	MFC3	MFC4	MFC5	MFC6
Wt%, Fe_3O_4	0.08	8.8	11.8	12.18	12.6	15

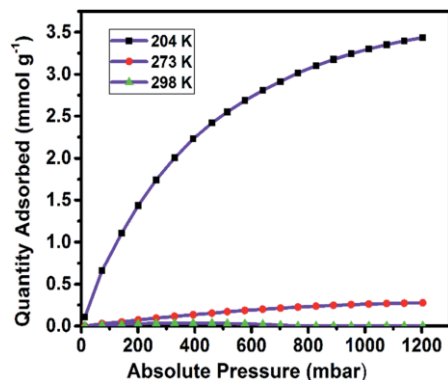


Fig. 3 Oxygen adsorption isotherms of the composite MFC3 measured at temperatures of 204 K, 273 K and 298 K at an equilibration time of 5 s.

individual samples of each were placed in a dewar flask and exposed to a magnetic field of 16.5 mT. The responsive temperature rise profile was noted for 30 minutes. The bare Fe_3O_4 nanoparticles stabilized at a temperature of 85.0 °C whereas the ones from within the MFCs exhibited a maximum temperature of 63.7 °C. According to these temperature rise profiles obtained at room temperature, when the MFC is exposed to a magnetic field of 16.5 mT, the magnetic nanoparticles from within it should heat up to 63.7 °C.

The oxygen adsorption consisted of the dynamic uptake of oxygen by the composites and for desorption, at preset points the magnetic field was activated triggering the release of the adsorbed oxygen molecules. When the magnetic field would be turned off, the composites would resume their normal oxygen uptake up until the point the magnetic field was activated again.

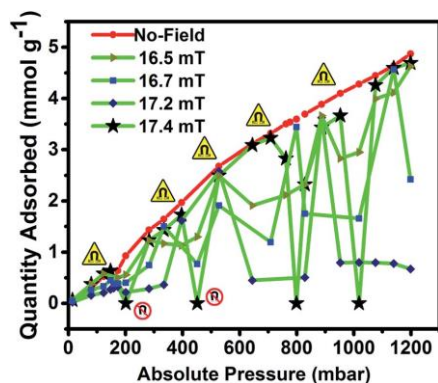


Fig. 4 Effect of magnetic field strengths, 16.5 mT, 16.7 mT, 17.2 mT and 17.5 mT on the release of oxygen molecules from MFC4 composite.

With 200 mbar being the approximate partial pressure of oxygen in air, the periodic switching was set at 200 mbar, 400 mbar, 800 and 1000 mbar.

The concentration of nanoparticles in the composite decided its adsorption and desorption properties. Composites with high content of magnetic nanoparticles affected its adsorption capacities but provided higher heating rates composites with low nanoparticle concentration had good adsorption properties but insufficient heating and therefore could not achieve full desorption. Consequently MFC4, a composite with a comparatively right balance of adsorption properties and heating abilities, was selected to study the effect of magnetic field strengths on the desorption properties of the composites.

The induction coil settings from the temperature rise studies were replicated to heat up the MFC to its maximum of 63.7 °C. However, unlike the room temperature measurement settings, for the oxygen adsorption trials, the sample tube was submerged in a bath of acetone/dry ice bath (Fig. S9b†) which reduced the heating effect of the induction coil causing incomplete desorption of the adsorbed oxygen. To attain the right temperature, the applied field was gradually increased from 16.4 mT to the maximum value of 17.4 mT that caused a full desorption of the oxygen molecules. As demonstrated in Fig. 4, with increase in magnetic field strengths, the desorption capacity of the composites increased with 21%, 49%, 74% and 100% desorption achieved at 16.4, 16.7, 17.2 and 17.4 mT respectively.

For composite MFC2, a desorption efficiency of 16%, 25.8%, 25% and 24.6% was observed whereas for MFC3 it was 71%, 73%, 78% and 72.5% at the preset points of 200, 400, 600 and 800 mbar respectively. MFC4 achieved a full 100% desorption of oxygen molecules at all points. Contrary to the desorption trend established by the composites MFC2 to MFC4, the composite, with 12.6 wt% magnetic nanoparticles, MFC5, achieved a near complete desorption at 200 mbar followed by which it neither adsorbed oxygen nor reacted to the applied magnetic field in any way (Fig. 5).

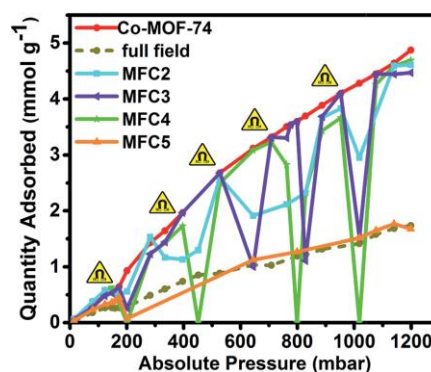


Fig. 5 Results of the triggered release of oxygen molecules from MFC2 to MFC5 by employing a magnetic field of 17.4 mT. The composite MFC4 released 100% of the adsorbed oxygen molecules.

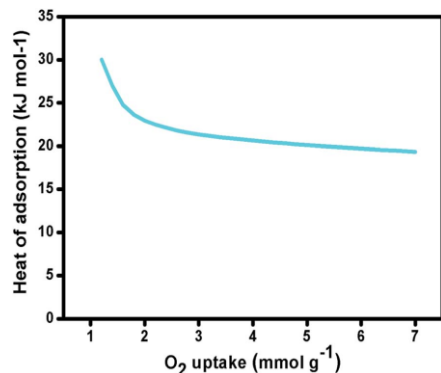


Fig. 6 Isosteric heat of adsorption for oxygen, calculated from the oxygen isotherms of MFC2 collected at 204, 273 and 298 K.

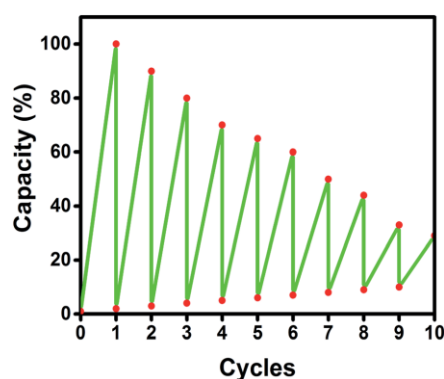


Fig. 7 The results of the oxygen adsorption-desorption cyclic experiments conducted on the composite MFC4, at temperatures of 204 K.

The isosteric heat of adsorption is a measure to understand the intensity of the interaction between the gas molecules and the porous framework and is highly time and temperature dependent. The rate of oxygen adsorption in a MOF is decided by the pore dimensions and the available number of unsaturated metal centers. The initial isosteric heat of adsorption for oxygen was calculated to be -30 kJ mol^{-1} that decreased with surface coverage and stabilized at -19 kJ mol^{-1} . Owing to their higher surface curvatures, at lower loadings, oxygen gets adsorbed into the smaller pores of the MOF and also on the exposed, unsaturated Co^{2+} metal centers. At higher loadings, as all the favorable sites get preferentially occupied, the adsorption proceeds through the larger pores resulting in lower isosteric heat of adsorption (Fig. 6).⁶¹⁻⁶³

To understand the reversibility of the oxygen bindings at temperatures of 204 K, the composite MFC4, was exposed to ten consecutive oxygen adsorption and desorption cycles and with

each cycle a 10% drop in the adsorption capacity was noted (Fig. 7). Even though the adsorptions were carried out at 204 K, where the reversible binding of oxygen in Co^{2+} complexes still exist, the heat from the magnetic nanoparticles that was used to trigger the molecules out of the composite may possibly have caused oxidising of the metal centres. Post-experiment XRD results showed loss of crystallinity and gradual decomposition of the composite.

Conclusions

The high capital and production costs associated with the setup and operations of the current air separation processes has led to the search for a new, better and energy efficient technique for separation of oxygen. This can be provided for by the formation of MFCs that make use of the reactive heating ability of the nanoparticles in a magnetic field to trigger the release of the adsorbed molecules by magnetic induction swing adsorption (MISA).

In this study the capacity of cobalt-based MFCs to adsorb oxygen molecules was evaluated. Desorption trials were conducted by exposing the composites to an alternating magnetic field resulting in release of the bound oxygen molecules. A composite with 12.18 wt% Fe_3O_4 nanoparticles was able to release 100% of the adsorbed oxygen when exposed to a magnetic field of 17.4 mT at 270 kHz. The repetitive adsorption and desorption cycles revealed the dependency of time and temperature on the performance and stability of the composite. This is a proof-of-concept experiment carried out to prove the oxygen adsorption capability of MFCs and to establish the efficiency of the magnetic induction heating in successfully achieving the release of most of the adsorbed oxygen molecules.

Future work will include the study and development of prospective new MOFs for the capture of oxygen, the subsequent synthesis of the MFCs by encapsulation of high magnetization nanoparticles in these MOFs and the stimuli responsive triggering of the oxygen molecules by the MISA process.

Conflicts of interest

There are no conflicts to declare.

References

- 1 J. Emsley, *Nature's building blocks: an AZ guide to the elements*, Oxford University Press, Oxford, England, 2001.
- 2 A. Smith and J. Klosek, *Fuel Process. Technol.*, 2001, **70**, 115-134.
- 3 M. Dobson, *Int. J. Tuberc. Lung Dis.*, 2001, **5**, 520-523.
- 4 Y. Zhu, S. Legg and C. D. Laird, *Comput. Chem. Eng.*, 2010, **34**, 1377-1384.
- 5 W. F. Castle, *Int. J. Refrig.*, 2002, **25**, 158-172.
- 6 K. Watanabe, N. Austin and M. R. Stapleton, *Mol. Simul.*, 1995, **15**, 197-221.
- 7 D. J. Xiao, M. I. Gonzalez, L. E. Darago, K. D. Vogiatzis, E. Haldoupis, L. Gagliardi and J. R. Long, *J. Am. Chem. Soc.*, 2016, **138**, 7161-7170.

- 8 C. Lastoskie, K. E. Gubbins and N. Quirke, *Langmuir*, 1993, **9**, 2693–2702.
- 9 C. R. Reid and K. M. Thomas, *Langmuir*, 1999, **15**, 3206–3218.
- 10 K. Sumida, D. L. Rogow, J. A. Mason, T. M. McDonald, E. D. Bloch, Z. R. Herm, T.-H. Bae and J. R. Long, *Chem. Rev.*, 2011, **112**, 724–781.
- 11 H. S. Koh, M. K. Rana, A. G. Wong-Foy and D. J. Siegel, *J. Phys. Chem. C*, 2015, **119**, 13451–13458.
- 12 Y. Lin, C. Kong, Q. Zhang and L. Chen, *Adv. Energy Mater.*, 2017, **7**, 1601296.
- 13 J.-R. Li, J. Sculley and H.-C. Zhou, *Chem. Rev.*, 2011, **112**, 869–932.
- 14 N. L. Rosi, J. Eckert, M. Eddaoudi, D. T. Vodak, J. Kim, M. Keffe and O. M. Yaghi, *Science*, 2003, **300**, 1127.
- 15 Y. Liu, Z. U. Wang and H.-C. Zhou, *Greenhouse Gases: Sci. Technol.*, 2012, **2**, 239–259.
- 16 M. Rubio-Martinez, C. Avei-Camur, A. W. Thornton, I. Imaz, D. Maspoch and M. R. Hill, *Chem. Soc. Rev.*, 2017, **46**, 3453–3480.
- 17 J. L. Rowsell and O. M. Yaghi, *Angew. Chem., Int. Ed.*, 2005, **44**, 4670–4679.
- 18 H.-C. Zhou, J. R. Long and O. M. Yaghi, *Chem. Rev.*, 2012, **673**–674.
- 19 R. J. Kuppler, D. J. Timmons, Q.-R. Fang, J.-R. Li, T. A. Makal, M. D. Young, D. Yuan, D. Zhao, W. Zhuang and H.-C. Zhou, *Coord. Chem. Rev.*, 2009, **253**, 3042–3066.
- 20 C. M. Doherty, D. Buso, A. J. Hill, S. Furukawa, S. Kitagawa and P. Falcaro, *Acc. Chem. Res.*, 2013, **47**, 396–405.
- 21 R. Ricco, L. Malfatti, M. Takahashi, A. J. Hill and P. Falcaro, *J. Mater. Chem. A*, 2013, **1**, 13033–13045.
- 22 A. K. Adhikari and K.-S. Lin, *Chem. Eng. J.*, 2016, **284**, 1348–1360.
- 23 P. Falcaro, R. Ricco, A. Yazdi, I. Imaz, S. Furukawa, D. Maspoch, R. Ameloot, J. D. Evans and C. J. Doonan, *Coord. Chem. Rev.*, 2016, **307**, 237–254.
- 24 E. D. Bloch, L. J. Murray, W. L. Queen, S. Chavan, S. N. Maximoff, J. P. Bigi, R. Krishna, V. K. Peterson, F. Grandjean and G. J. Long, *J. Am. Chem. Soc.*, 2011, **133**, 14814–14822.
- 25 M. März, R. E. Johnsen, P. D. C. Dietzel and H. Fjellvåg, *Microporous Mesoporous Mater.*, 2012, **157**, 62–74.
- 26 K. Sumida, D. L. Rogow, J. A. Mason, T. M. McDonald, E. D. Bloch, Z. R. Herm, T.-H. Bae and J. R. Long, *Chem. Rev.*, 2012, **112**, 724–781.
- 27 Y.-S. Bae, A. M. Spokoyny, O. K. Farha, R. Q. Snurr, J. T. Hupp and C. A. Mirkin, *Chem. Commun.*, 2010, **46**, 3478–3480.
- 28 L. J. Murray, M. Dinca, J. Yano, S. Chavan, S. Bordiga, C. M. Brown and J. R. Long, *J. Am. Chem. Soc.*, 2010, **132**, 7856–7857.
- 29 N. Tlili, G. Grévilot and C. Vallières, *Int. J. Greenhouse Gas Control*, 2009, **3**, 519–527.
- 30 J. A. Mason, K. Sumida, Z. R. Herm, R. Krishna and J. R. Long, *Energy Environ. Sci.*, 2011, **4**, 3030–3040.
- 31 N. Hedin, L. Andersson, L. Bergström and J. Yan, *Appl. Energy*, 2013, **104**, 418–433.
- 32 M. Songolzadeh, M. Soleimani, M. Takht Ravanchi and R. Songolzadeh, *Sci. World J.*, 2014, **2014**, 828131.
- 33 R. E. Morris and P. S. Wheatley, *Angew. Chem., Int. Ed.*, 2008, **47**, 4966–4981.
- 34 R. Lyndon, K. Konstas, R. A. Evans, D. J. Keddie, M. R. Hill and B. P. Ladewig, *Adv. Funct. Mater.*, 2015, **25**, 4405–4411.
- 35 R. Lyndon, K. Konstas, A. W. Thornton, A. J. Seeber, B. P. Ladewig and M. R. Hill, *Chem. Mater.*, 2015, **27**, 7882–7888.
- 36 R. Lyndon, K. Konstas, B. P. Ladewig, P. D. Southon, P. C. J. Kepert and M. R. Hill, *Angew. Chem., Int. Ed.*, 2013, **52**, 3695–3698.
- 37 P. Falcaro, F. Lapierre, B. Marmiroli, M. Styles, Y. Zhu, M. Takahashi, A. J. Hill and C. M. Doherty, *J. Mater. Chem. C*, 2013, **1**, 42–45.
- 38 O. Lucia, P. Maussion, E. J. Dede and J. M. Burdío, *IEEE Trans. Ind. Electron.*, 2014, **61**, 2509–2520.
- 39 M. Bañobre-López, A. Teijeiro and J. Rivas, *Rep. Pract. Oncol. Radiotherapy*, 2013, **18**, 397–400.
- 40 M. Ma, Y. Zhang, X. Shen, J. Xie, Y. Li and N. Gu, *Nano Res.*, 2015, **8**, 600–610.
- 41 A. Kolhatkar, A. Jamison, D. Litvinov, R. Willson and T. Lee, *Int. J. Mol. Sci.*, 2013, **14**, 15977.
- 42 H. Rudolf, D. Silvio, M. Robert and Z. Matthias, *J. Phys.: Condens. Matter*, 2006, **18**, S2919.
- 43 H. Li, M. M. Sadiq, K. Suzuki, R. Ricco, C. Doblin, A. J. Hill, S. Lim, P. Falcaro and M. R. Hill, *Adv. Mater.*, 2016, **28**, 1839–1844.
- 44 M. M. Sadiq, H. Li, A. J. Hill, P. Falcaro, M. R. Hill and K. Suzuki, *Chem. Mater.*, 2016, **28**, 6219–6226.
- 45 H. Li, M. M. Sadiq, K. Suzuki, C. Doblin, S. Lim, P. Falcaro, A. J. Hill and M. R. Hill, *J. Mater. Chem. A*, 2016, **4**, 18757–18762.
- 46 H. Li, M. M. Sadiq, K. Suzuki, P. Falcaro, A. J. Hill and M. R. Hill, *Chem. Mater.*, 2017, **29**(15), 6186–6190.
- 47 R. Lyndon, K. Konstas, B. P. Ladewig, P. D. Southon, P. C. J. Kepert and M. R. Hill, *Angew. Chem., Int. Ed.*, 2013, **52**, 3695–3698; *Angew. Chem.*, 2013, **3125**, 3783–3786.
- 48 A. C. H. Barreto, V. R. Santiago, R. M. Freire, S. E. Mazzetto, J. C. Denardin, G. Mele, I. M. Cavalcante, M. E. N. P. Ribeiro, N. M. P. S. Ricardo, T. Gonçalves, L. Carbone, T. L. G. Lemos, O. D. L. Pessoa and P. B. A. Fechine, *Int. J. Mol. Sci.*, 2013, **14**, 18269–18283.
- 49 F. Ke, Y.-P. Yuan, L.-G. Qiu, Y.-H. Shen, A.-J. Xie, J.-F. Zhu, X.-Y. Tian and L.-D. Zhang, *J. Mater. Chem.*, 2011, **21**, 3843–3848.
- 50 N. L. Rosi, J. Kim, M. Eddaoudi, B. Chen, M. O’Keeffe and O. M. Yaghi, *J. Am. Chem. Soc.*, 2005, **127**, 1504–1518.
- 51 P. D. Dietzel, V. Besikiotis and R. Blom, *J. Mater. Chem.*, 2009, **19**, 7362–7370.
- 52 P. D. Dietzel, P. A. Georgiev, J. Eckert, R. Blom, T. Strässle and T. Unruh, *Chem. Commun.*, 2010, **46**, 4962–4964.
- 53 P. D. Dietzel, R. E. Johnsen, H. Fjellvåg, S. Bordiga, E. Groppo, S. Chavan and R. Blom, *Chem. Commun.*, 2008, 5125–5127.
- 54 P. D. Southon, D. J. Price, P. K. Nielsen, C. J. McKenzie and C. J. Kepert, *J. Am. Chem. Soc.*, 2011, **133**, 10885–10891.

Published on 14 January 2019. Downloaded by Monash University on 12/20/2020 6:25:24 AM.

- 55 H. Sugimoto, T. Nagayama, S. Maruyama, S. Fujinami, Y. Yasuda, M. Suzuki and A. Uehara, *Bull. Chem. Soc. Jpn.*, 1998, **71**, 2267–2279.
- 56 M. Suzuki, H. Kanatomi and I. Murase, *Chem. Lett.*, 1981, **10**, 1745–1748.
- 57 C. Hui, C. Shen, T. Yang, L. Bao, J. Tian, H. Ding, C. Li and H. J. Gao, *J. Phys. Chem. C*, 2008, **112**, 11336–11339.
- 58 T. Yang, C. Shen, Z. Li, H. Zhang, C. Xiao, S. Chen, Z. Xu, D. Shi, J. Li and H. Gao, *J. Phys. Chem. B*, 2005, **109**, 23233–23236.
- 59 S. Sun, H. Zeng, D. B. Robinson, S. Raoux, P. M. Rice, S. X. Wang and G. Li, *J. Am. Chem. Soc.*, 2004, **126**, 273–279.
- 60 C. Popa, A. Prodan, P. Chapon, C. Turculet and D. Predoi, *J. Nanomater.*, 2015, **2015**, 5.
- 61 D. J. Xiao, M. I. Gonzalez, L. E. Darago, K. D. Vogiatzis, E. Haldoupis, L. Gagliardi and J. R. Long, *J. Am. Chem. Soc.*, 2016, **138**, 7161–7170.
- 62 A. Kloutse, R. Zacharia, D. Cossement, R. Chahine, R. Balderas-Xicohténcatl, H. Oh, B. Streppel, M. Schlichtenmayer and M. Hirscher, *Appl. Phys. A: Mater. Sci. Process.*, 2015, **121**, 2.
- 63 B. Schmitz, U. Müller, N. Trukhan, M. Schubert, G. Férey and M. Hirscher, *ChemPhysChem*, 2008, **9**, 2181–2184.

Supporting Information

Efficient Delivery of Oxygen via Magnetic Framework Composites

Leena Melag, † M. Munir Sadiq, *‡ Stefan J. D. Smith, ‡ Kristina Konstas ‡, Kiyonori Suzuki, *|| and Matthew R. Hill, *†‡

†Department of Chemical Engineering, Monash University, Clayton, VIC 3168, Australia

|| Department of Materials Science and Engineering, Monash University, Clayton, VIC 3168, Australia

‡ CSIRO, Private Bag 33, Clayton South MDC, VIC 3169, Australia

1. Experimental

All reagents and solvents used for the synthesis were obtained from commercial vendors and used as received.

I. Synthesis of Fe₃O₄ Nanoparticles

0.75 g of 2, 5-dihydroxyterephthalic acid (DHTA) and 3.0 g of Co (NO₃)₂·6H₂O were dissolved in 150 mL of DMF. The mixture was sonicated in a 250 mL Duran bottle and placed in an oven at 1100C for 20hrs. On cooling down to room temperature, the mother liquor was decanted, and the products were washed with DMF three times and then immersed in methanol. The methanol was exchanged with fresh methanol for the next six days, and the samples were activated at 2500C under vacuum for 24 hrs and stored in an N₂ glove bag.^{1, 2}

II. Synthesis of Fe₃O₄ Nanoparticles

Hydrophilic Fe₃O₄ nanoparticles were synthesised using a facile one-step method. First, trisodium citrate (1 mmol, C₆H₅Na₃O₇ · 2H₂O), sodium hydroxide (4 mmol), and sodium nitrate (0.2 mmol) were dissolved into deionised water (19 mL) and heated to 100 °C. 1 mL of 2M FeSO₄ · 4H₂O (2mmol) solution was added to the mixture it, and the entire solution was maintained at 100 °C for one hour. After cooling, the black precipitate was magnetically separated from the solvent and redispersed into DI water and can be stored in water for up to a month.³

III. Synthesis of the (Co-MOF-74-Fe₃O₄) composite

The synthesis of Fe₃O₄ nanoparticles had citrate and sodium nitrate salts, resulting in citrate capped Fe₃O₄ nanoparticles. Therefore, no separate attempt was made to functionalised the surfaces of these magnetic nanoparticles. As these nanoparticles having a tendency to agglomerate and settle down, the mixture of Co-MOF-74 precursor and preformed, Fe₃O₄ nanoparticles was subjected to continuous mechanical stirring for the entire duration of 2 and half days at a temperature of 100 °C. For the washing cycles, the composites were magnetically separated from the solvents. For this study, composites with 0.08 wt % (MC1) , 8.8 wt % (MC2) , 11.8 wt % (MC3) , 12.18 wt % (MC4) , 12.6 wt % (MC5) , and 15 wt % (MC6) of magnetic nanoparticles were synthesized.^{1, 2}

2. Powder X-ray diffraction

The phase identification studies were conducted using a Phillips PW-1140 X-ray diffractometer using a Co-K α radiation of wavelength 1.79 Å (λ is the wavelength of the radiation (Co-1.78897 Å), at 40 kV and 25 mA. As shown in Fig. S1 a) and b), the XRD pattern of the synthesised Fe₃O₄ nanoparticles (reference pattern for a cubic spinel Fe₃O₄ lattice) and the composites are in agreement with literature reports. As can be observed from the XRD patterns in Fig. S1 b), there is a gradual shift in the peak positions of composites MC5 and MC6, that have higher concentrations of magnetic nanoparticles.

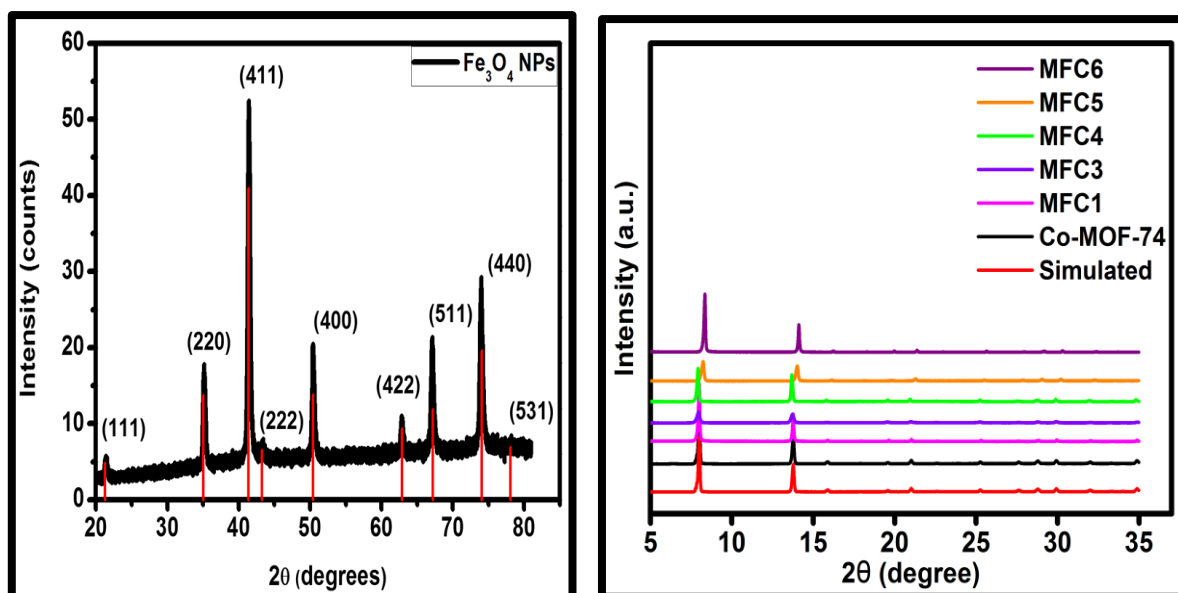


Figure S1: The powder X-ray diffraction patterns of a) the synthesised Fe₃O₄ nanoparticles that can be referenced to the theoretical patterns for a cubic Fe₃O₄ lattice (COD 1011084), and b) the synthesised Co-MOF-74 and simulated data and the composites with varying concentrations of magnetic nanoparticles.

3. Microstructural Analysis

The morphological studies on the samples were carried out using the JOEL 7001F Scanning Electron Microscope. The micrographs show hexagonal-shaped prism aggregates of Co-MOF-74 crystals with solid elongated structures measuring a few μm in length.

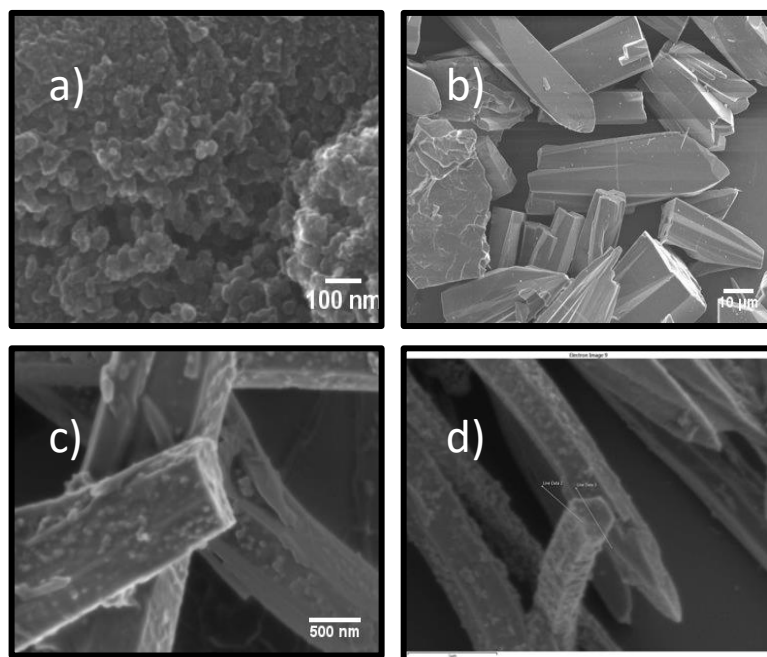


Figure S2: SEM Images of a) the synthesised Fe_3O_4 nanoparticles in size range of 20-100nm. b) hexagonal-shaped prism aggregates of Co-MOF-74 crystals with solid elongated structures measuring a few μm in length, c) and d) the Fe_3O_4 -composite with the magnetic nanoparticles embedded on its surface.

4. Thermogravimetric analysis

For the thermogravimetric analysis, the MOF samples were heated from the room temperature to 600 $^{\circ}\text{C}$ at 20 $^{\circ}\text{C}/\text{min}$ in a nitrogen atmosphere. The thermal treatment on the bare MOF and the composite showed an initial gradual loss in weight for both, but after 300 $^{\circ}\text{C}$, the composite collapsed faster than the bare MOF leading to a more drastic weight loss around 500 $^{\circ}\text{C}$ for the final structural collapse .⁴

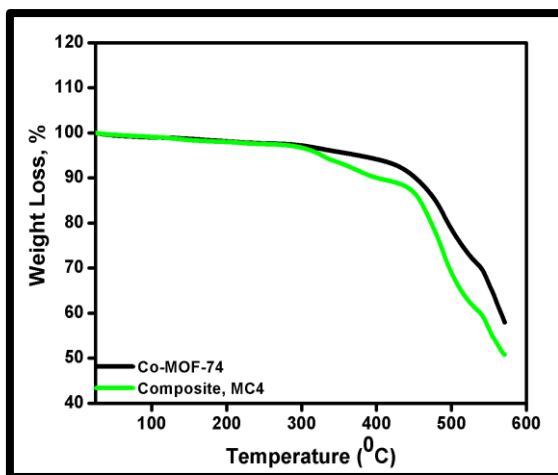


Figure S3: Comparison of the TGA curves of the bare Co-MOF-74 and the Magnetic framework composite, MC4.

5. Low-pressure gas adsorption analysis

To determine the surface area and porosity properties of the bare Co-MOF-74 and the MFCs, 10 - 50 mg of dry sample was transferred into the BET glass tube, it was capped with a transeal and weighed. The tubes were fixed onto a Micrometrics ASAP 2020 gas adsorption analyser where the samples were heated to 250 °C under dynamic vacuum for 24 hrs and weighed again. Low-pressure N₂ adsorption isotherms were carried out at 77K at preset measurement data points to collect the nitrogen adsorption-desorption data over a broad range of pressures.

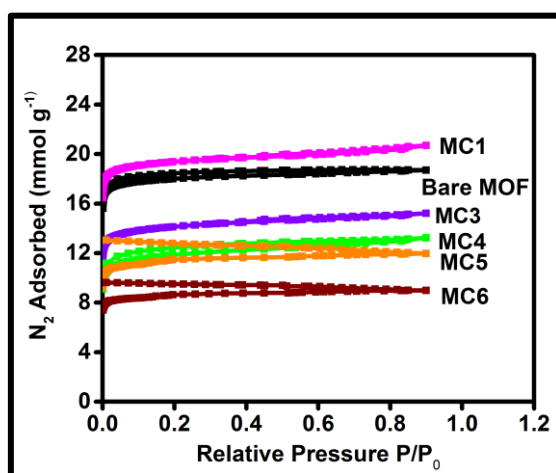


Figure S4: N₂ Adsorption isotherms of Co-MOF-74 and MFCs at 77K.

Table S1: Results from the surface area measurements of the bare Co-MOF-74 and the MFCs.

	Bare MOF	MC1 (0.08 wt. %)	MC3	MC4 (12.18 wt. %)	MC5	MC6 (15 wt. %)
--	----------	----------------------	-----	-----------------------	-----	--------------------

			(11.8 wt. %)		(12.6 wt. %)	
BET (m ² /g)	1449	1478	1082	1008	953	713
Langmuir (m ² /g)	1764	1909	1399	1150	1247	933

In real air separation, 400 ppm of CO₂ is present, and its capture is facilitated in a pre-purification process by using either absorption, adsorption, cryogenic distillation or membrane separation. To understand the effect of trace quantities of CO₂ we carried out the CO₂ adsorption study at 204 K. As expected, the uptake of CO₂ by MOF-74 at 204 K is much higher than of oxygen, particularly at low partial pressures, indicating that a pre-purification step is required to remove carbon dioxide and water from the process.

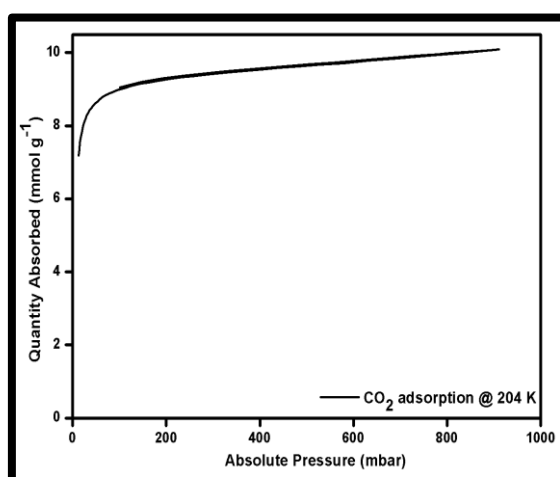


Figure S5: *CO₂ Adsorption isotherms of Co-MOF-74 at 204K.*

6. Vibrating Sample Magnetometer

The saturation magnetization (Ms), coercivity (Hc) and magnetization curves were studied on a vibrating sample magnetometer (VSM, RIKEN DENSHI) operated at room temperature. The samples are prepared by embedding the magnetic nanoparticles in an epoxy resin and hardener mix, and once it was all set, the measurements were carried out. The results of the synthesised Fe₃O₄ nanoparticles show a saturation magnetization of 58 emu/g, and with MFCs, the saturation magnetization values were higher for composites with higher concentrations of magnetic nanoparticles, MC6 (1.6 emu/g), MC5 (1.2 emu/g), MC4 (1 emu/g), MC3 (0.8 emu/g) and MC2 (0.1 emu/g).

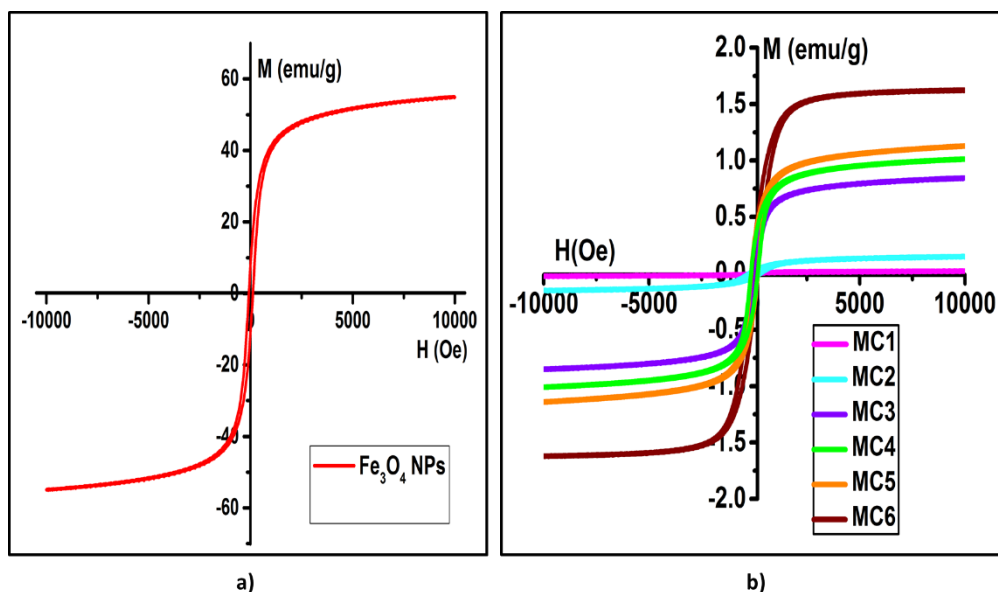


Figure S6: Hysteresis loop of a) Fe_3O_4 nanoparticles and the b) MFCs.

7. Thermo-magneto gravimetric Analysis

The Curie temperature of the Fe_3O_4 nanoparticles was determined using the Thermo-magneto gravimetric analysis, which is a very efficient technique to ascertain the various structural and magnetic transitions in the nanoparticles. Curie point is the temperature at which a sharp change in the magnetic properties is observed, and the otherwise strong magnetic properties of the material are lost, and it becomes paramagnetic. This is derived by measuring the change in weight of the sample as a function of temperature, in an applied magnetic field.^{1,5-7,8} The change in temperatures cause changes in magnetic properties of the samples that is noticed by the change in the weight of the sample. This principle is used to determine the Curie temperature. Here the measurements on a weighed amount of Fe_3O_4 nanoparticles were conducted by heating it from room temperature to 1000 °C in a nitrogen atmosphere using a heating rate of 40 °C/min and the Curie temperature for the synthesised Fe_3O_4 nanoparticles was found to be $T_c=570$ °C. This self-controlling heating property of the magnetic nanoparticles is used in applications as a control to avoid overheating.

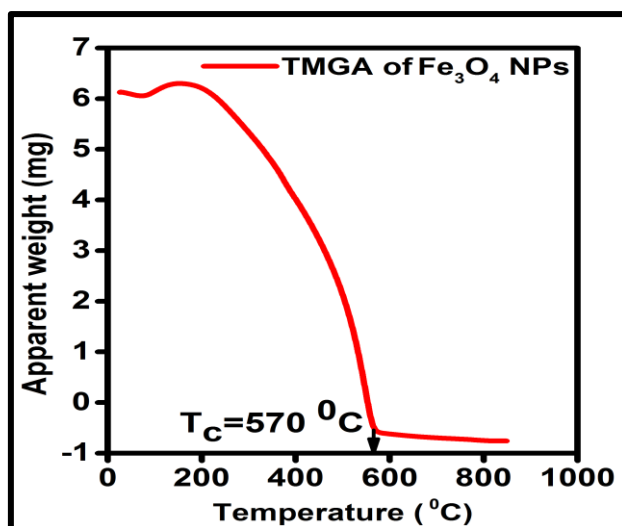


Figure S7: Using Thermo-magneto-gravimetric analysis, the Curie temperature of the synthesised Fe₃O₄ nanoparticles was found to be T_c=570 °C.

8. Specific Absorption Rate (SAR).

Specific Absorption Rate, SAR, describes the heating efficiency of the magnetic materials and indicates the rate at which the magnetic nanoparticles will absorb the magnetic energy and convert it into thermal energy. Apart from the diameter, shape and composition of the nanoparticles, SAR is strongly governed by the frequency of the applied magnetic field. In hyperthermia treatments nanoparticles with high SAR values are preferred because it means a higher absorption rate even at low concentrations.⁷ SAR is calculated by dispersing the particles in a liquid medium and the measuring:

$$SAR = C_s \frac{m_s}{m_m} \left(\frac{dT}{dt} \right)_{t=0} \quad 8.1$$

Where C_s is the specific heat capacity of suspension, dT/dt at t =0 is the initial gradient of the heating curve, m_s and m_m are the specific masses of the suspension and magnetic particles, respectively. The units of SAR are watts per kilogram (W/kg).^{9, 10} To measure SAR, the nanoparticles were dispersed in water at a concentration of 5mg/ml. This magnetic suspension was placed in a dewar flask and exposed to an induction heating system (EASYHEAT 0224–Ambrell) with a heating coil of 8 turns (N) of 2.5

cm diameter (D) and 4 cm in length (L). The amplitude of the AC magnetic field was fixed at $H = 13.09$ kA/m. The temperature rise attained by the samples for the next 30 minutes is noted as the heat generation capacity of the samples. An IR Thermal camera (FLIR E5) was used to capture these changes in the temperatures. With the initial starting temperature of 23.84 °C, and on exposure to an AC magnetic field, the Fe_3O_4 nanoparticles stabilised at a temperature of 85.02 °C, and the MFC exhibited a maximum temperature rise (T_{max}) of 63.7 °C. The SAR values calculated using equation (8.1) are 74.48 W/g for the Fe_3O_4 nanoparticles and 14.19 W/g for the Fe_3O_4 -composite.

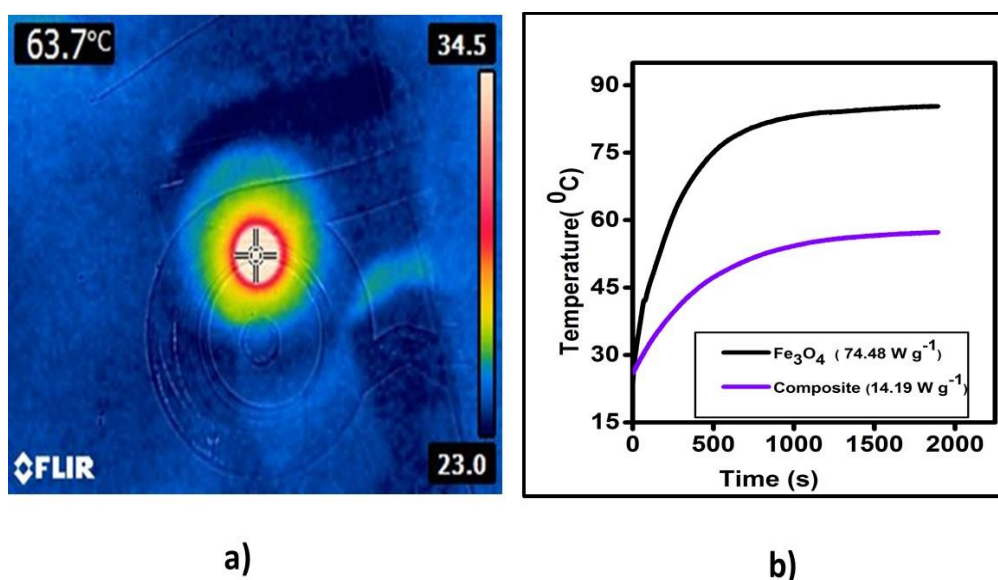


Figure S8: SAR measurements: a) The live image captured by the IR-camera of the temperature rise attained by the MC3 composite, b) The calculated specific absorption rate values of 74.48 W/g for the Fe_3O_4 nanoparticles and 14.19 W/g for the Fe_3O_4 -composite.

9. Set- up for the Magnetic Triggered Release of Oxygen

The triggered release of oxygen from the MFC was achieved using the Tristar Micrometrics adsorption equipment and the EASYHEAT Ambrell induction-heating machine. The setup consisted of a glass tube with the sample in it, which was hooked on to the Tristar Micrometrics adsorption machine. A slightly bigger glass tube, acting as a dewar and containing the acetone+dry ice mixture was encircling the sample tube. This setup was fitted through an induction coil in such a manner that the sample comes

in the center of the 8-turn coil. This ensured uniform exposure of the sample to the magnetic field. The effects of the magnetic field were contained using a Faradays cage.

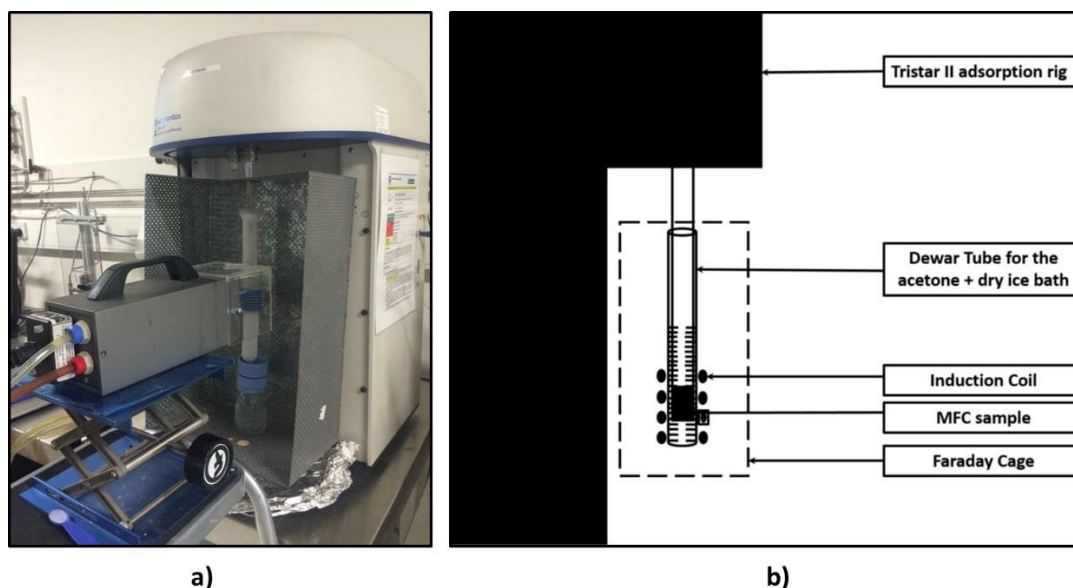


Figure S9: Setup for the triggered release of oxygen, a) The actual setup of the sample tube attached to the Tristar Micrometrics adsorption equipment and the EASYHEAT Ambrell induction-heating machine used to facilitate the heating of the magnetic nanoparticles, b) the graphical representation of the same setup.

During calculations of SAR, using a magnetic field strength of 16.4 mT, the Fe_3O_4 nanoparticles stabilised at a temperature of 63.7 °C. Therefore, to achieve this temperature of 63.7 °C, a current of 78A had to be passed through the 8-turn coil of the EASYHEAT Ambrell induction heating system.

Based on these calculations, the first set of triggered release was carried out by passing 78A current (63.7 °C) through the coils. However, the experiments for calculation of SAR are carried out at room temperature whereas these triggered release experiments are carried out at temperatures of -69 °C. Therefore, due to the cold acetone + dry ice bath encircling the sample, the maximum desorption temperatures were not reached and complete desorption of oxygen molecules was not achieved. To target maximum desorption, the temperatures were increased by increasing the current passing through the coil. Finally, the maximum desorption from the composites was achieved when a current of 83.2 A was passed through the coil generating a magnetic field strength of 17.4 mT to overcome the cold barrier

of the acetone-dry ice bath and cause localised heating of the Fe₃O₄ nanoparticles, which otherwise, in these settings, would have attained the temperatures of 68.5 °C.

Table S2: Magnetic Field Settings

Current through the coil, A	Magnetic Field Strength, mT	Temperature °C
78	16.5	63.8
79.3	16.7	64.8
81.9	17.2	66.9
83.2	17.4	68.5

10. Regeneration energy calculations:

For a cryogenic distillation based Air Separation Unit producing 110 to 350 tonnes of oxygen per day, the specific energy is reported as 1.11 MJ/kg- 1.82 MJ/kg at 40 bar. (Air Liquide Engineering & Construction. Standard Plants. 04-2017).

At this early lab-scale setup it is not possible to directly determine energy use for the process. Still, the energy calculations for the estimated regeneration energy (Q_{thermal}) of our composite per kilogram of O₂ captured can be calculated. Specific regeneration energy (Q_{thermal}) is reported as the sum of the energy required to heat the adsorbent to the desorption temperature, and the energy needed to desorb bound gas species from the adsorbent,¹¹ according to the equation:

$$Q_{\text{thermal}} = \frac{c_p m_{\text{sorbent}} \Delta T + (\Delta h O_2 \Delta q O_2)}{m O_2}$$

Where,

c_p = specific heat capacity of adsorbent (Jg⁻¹K⁻¹)

m_{sorbent} = mass of adsorbent (g)

ΔT = Temperature difference between adsorption and desorption conditions (K)

Δh = heat of adsorption (kJmol⁻¹)

Δq = working capacity, it can be defined as the difference between the O₂ loadings at adsorption and O₂ loadings at the end of desorption¹².

$m O_2$ = Mass of oxygen adsorbed at that pressure (g)

Applying this equation to 0.1320 g of **MFC4**, the MOF composite with **12.18** wt. % of Fe₃O₄ nanoparticles, the energy required to regenerate the amount of oxygen captured at 200 mbar, 400 bar, 800 mbar and 1000 mbar is calculated, and the values are:

Pressure (mbar)	Δq (mmol/g)	Calculated Regeneration energy (MJ/kg)
200	0.93	2.89
400	1.98	1.67
800	3.5	1.20
1000	4.2	1.10

While this calculation does not include process considerations and cooling duty of air from ambient to 204 K, we expect this energy requirement to be less than half of that required for cryogenic distillation at 92 K. Using a suitable fraction of the above quoted energy costs for Cryogenic distillation, and without further improvements to the technology, the total estimated energy cost of the MISA process for capturing oxygen from air from lab scale experiments is broadly competitive to the mature process. However, with orders of magnitude increases in scale, we expect the efficiency using this first generation material to greatly improve. Further efficiencies may be achieved through operation at higher pressures, as is indicated by the trends in working capacity (Δq) and regeneration energy with pressure.

References:

1. Adhikari, A. K.; Lin, K.-S., Improving CO₂ adsorption capacities and CO₂/N₂ separation efficiencies of MOF-74(Ni, Co) by doping palladium-containing activated carbon. *Chem. Eng. J.* **2016**, 284, 1348-1360.
2. Grant Glover, T.; Peterson, G. W.; Schindler, B. J.; Britt, D.; Yaghi, O., MOF-74 building unit has a direct impact on toxic gas adsorption. *Chem. Eng. Sci.* **2011**, 66, (2), 163-170.
3. Hui, C.; Shen, C.; Yang, T.; Bao, L.; Tian, J.; Ding, H.; Li, C.; Gao, H. J., Large-Scale Fe₃O₄ Nanoparticles Soluble in Water Synthesised by a Facile Method. *J. Phys. Chem. C* **2008**, 112, (30), 11336-11339.
4. Howarth, A. J.; Peters, A. W.; Vermeulen, N. A.; Wang, T. C.; Hupp, J. T.; Farha, O. K., Best Practices for the Synthesis, Activation, and Characterisation of Metal–Organic Frameworks. *Chem. Mater.* **2017**, 29, (1), 26-39.
5. Zhang, Y.; Zhai, Y., Magnetic induction heating of nano-sized ferrite particle. In *Adv. Ind. Micro. Heat. Mine. Organ. Mater.*, InTech: 2011.
6. Ebrahimi, M., On the temperature control in self-controlling hyperthermia therapy. *J. Magn. Magn. Mater.* **2016**, 416, 134-140.
7. Kolhatkar, A.; Jamison, A.; Litvinov, D.; Willson, R.; Lee, T., Tuning the Magnetic Properties of Nanoparticles. *Int J Mol Sci* **2013**, 14, (8), 15977.
8. Sun, S.; Liu, C.; Peng, R.; Fu, Z.; Lu, Y., Measuring room-temperature intrinsic multiferroic properties by excluding the secondary magnetic inclusion contribution. *Sci. China. Mater.* **2015**, 58, (10), 791-798.
9. Kekalo, K.; Baker, I.; Meyers, R.; Shyong, J., Magnetic Nanoparticles with High Specific Absorption Rate at Low Alternating Magnetic Field. *Nano LIFE* **2015**, 5, (2), 1550002.

10. Mornet, S.; Vasseur, S.; Grasset, F.; Duguet, E., Magnetic nanoparticle design for medical diagnosis and therapy. *J. Mater. Chem.* **2004**, 14, (14), 2161-2175.
11. Sadiq, M. M.; Li, H.; Hill, A. J.; Falcaro, P.; Hill, M. R.; Suzuki, K., Magnetic Induction Swing Adsorption: An Energy-Efficient Route to Porous Adsorbent Regeneration. *Chem. Mater* **2016**, 28, (17), 6219-6226.
12. Zhang, W.; Liu, H.; Sun, Y.; Cakstins, J.; Sun, C.; Snape, C. E., Parametric study on the regeneration heat requirement of an amine-based solid adsorbent process for post-combustion carbon capture. *Appl. Ener.* **2016**, 168, 394-405.

Appendix B

Performance evaluation of CuBTC composites for room temperature Oxygen storage

Leena Melag, M. Munir Sadiq, Kristina Konstas, Farnaz Zadehahmadi, Kiyonori Suzuki and
Matthew R. Hill



Cite this: *RSC Adv.*, 2020, **10**, 40960

Performance evaluation of CuBTC composites for room temperature oxygen storage†

Leena Melag,^a M. Munir Sadiq,^b Kristina Konstas,^c Farnaz Zadehahmadi,^c Kiyonori Suzuki^b and Matthew R. Hill^{*ac}

Oxygen is commonly separated from air using cryogenic liquefaction. The inherent energy penalties of phase change inspire the search for energy-efficient separation processes. Here, an alternative approach is presented, where we determine whether it is possible to utilise simpler, stable materials in the right process to achieve overall energy efficiency. Adsorption and release by Metal–Organic Frameworks (MOFs) are an attractive alternative due to their high adsorption and storage capacity at ambient conditions. Cu-BTC/MgFe₂O₄ composites were prepared, and magnetic induction swing adsorption (MISA) used to release adsorbed oxygen quickly and efficiently. The 3 wt% MgFe₂O₄ composites exhibited an oxygen uptake capacity of 0.34 mmol g⁻¹ at 298 K and when exposed to a magnetic field of 31 mT, attained a temperature rise of 86 °C and released 100% of adsorbed oxygen. This water vapor stable pelletized system, can be filled and emptied within 10 minutes requiring around 5.6 MJ kg⁻¹ of energy.

Received 17th August 2020
Accepted 27th October 2020

DOI: 10.1039/d0ra07068h

rsc.li/rsc-advances

1. Introduction

The demand for high purity oxygen is on the rise owing to its increased consumption by the healthcare, steel, food, water, chemical, and pharmaceutical industries and this, in turn, has influenced research into more energy-efficient ways to capture, separate and store oxygen.^{1,2} The traditional process of cryogenic liquefaction of air³ produces ultra-high purity oxygen and still dominates the industrial methods of oxygen separation, but the complex plant setups and the energy requirements associated with the entire process limits its use for large scale productions only. The membrane-based separations and adsorption-based processes using zeolites and carbon molecular sieves are simpler, reversible, low cost and easily scalable for small scale separations of oxygen, but their structural rigidity, pore heterogeneity, and low oxygen permeabilities impose limitations on the purity of the oxygen produced.⁴ Once produced, compressed or liquefied oxygen is bottled up in storage tanks for subsequent use in varied applications.^{2,5-7} Taking into account the safety hazards associated with the handling and storing of a highly reactive gas like oxygen, equal emphasis is required on finding alternate means to counter the current high-pressure (*ca.* 140 bar) storage of oxygen; a safe,

lightweight alternative that would store oxygen in high volumes but at much lower pressures.⁸⁻¹⁰

Metal–Organic Frameworks (MOFs) are porous nano-materials that have been explored for gas separations,¹¹⁻¹⁴ catalysis,¹⁵ sensing,^{11,16-23} and drug delivery applications.^{24,25} They are constructed using metal nodes and organic linkers resulting in unique modular structures that are flexible, porous and offer the distinctive chemical tunability needed for gas storage.²⁶⁻²⁸ Their ability to host functional nanoparticles within their structures imparts added diverse functionalities to their existing versatile properties.²⁹ Similar to most adsorption processes, separations in MOFs are based on the guest–host interactions where the adsorbents can either physically adsorb gas molecules on its surface or can bind to them chemically.³⁰ For selective separations using MOFs, the selectivity between the different gas molecules relies on preferential size-selective sieving or favourable quadrupole interactions or strong chemical affinities with either of the adsorbates.³¹ Most oxygen separation processes are nitrogen selective and are based on the adsorption or isolation of nitrogen from the air to separate oxygen. However, using MOFs, selective oxygen separation has been studied through a process that relies on oxygen molecules directly binding to the metal cations in the framework leading to higher selectivity over other gases, mainly nitrogen.³²⁻³⁵

Accordingly, to investigate the role of MOFs in oxygen separation and storage, DeCoste *et al.* conducted simulation studies on 10 000 hypothetical MOFs and recorded NU-125 as the MOF with the highest oxygen adsorption capacity of 17.4 mol kg⁻¹ at 140 bar pressure. Computational studies by Moghadam *et al.* on existing 2932 MOFs reported UCMC-152 as

^aDepartment of Chemical Engineering, Monash University, Clayton, VIC 3168, Australia. E-mail: Matthew.Hill@csiro.au

^bDepartment of Materials Science and Engineering, Monash University, Clayton, VIC 3168, Australia

^cCSIRO, Private Bag 33, Clayton South MDC, VIC 3169, Australia

† Electronic supplementary information (ESI) available. See DOI: 10.1039/d0ra07068h



Paper

the MOF with a deliverable volumetric oxygen capacity of 249 cm³(STP) cm⁻³ and gravimetric oxygen storage of 19.6 mmol kg⁻¹ obtained at 140 bar storage and 5 bar release pressures at 298 K. Similarly, various other MOFs like IRMOFs, UiO-66, Cr₃(BTC)₂,^{33,35,36} Cr-BTT,³⁷ and M₂(dobdc) (M = Cr, Mn, Fe, Co), especially Co₂(dobdc)^{38–40} and Fe₂(dobdc)^{35,41,42} have been investigated in detail as oxygen selective adsorbents for separation and storage. Apart from specially designed and developed MOFs, the existing range of MOFs need to be explored for a simpler, stable, and recyclable solution for room temperature oxygen storage. This paper investigates a widely used copper-based MOF, CuBTC, also known as HKUST-1 or MOF-199, previously identified by both DeCoste *et al.* and Moghadam *et al.* for oxygen storage applications. Owing to its affinity towards oxygen, CuBTC MOFs have been used as cathode catalysts in fuel cell technology that is impeded by a sluggish oxygen reduction reaction (ORR) and catalytic efficiency, cost, and stability. With its large surface area and a large number of sites for the catalytic reactions, CuBTC MOFs have been studied to replace platinum as the non-noble metal ORR catalyst or have been used as the sacrificial template for carbon-based electrocatalysts.^{43–47} CuBTC (copper(ii) benzene-1,3,5-tricarboxylate), is one of the widely explored, easily scalable, and most commercially used MOFs in various applications. Its ease of synthesis, high surface areas (1500–2000 m² g⁻¹), and excellent thermal and structural stability make it applicable for gas adsorption,^{48–52} separation,^{49,53–56} and sensors^{17,57,58} applications.

Temperature Swing Adsorption (TSA) and Pressure Swing Adsorption (PSA) are the most commonly used regeneration processes for MOFs. However, their strong host-guest interactions with the adsorbed molecules, particularly the strong adsorption at lower partial pressures and their thermally insulating nature, limit the uniform transfer of the applied heat throughout the MOF, making the regeneration process very challenging and energy-intensive.^{11,59–63} To address this, our group has demonstrated the potentials of incorporating stimuli-responsive materials in MOFs to achieve energy-efficient release of the trapped gases.^{11,39,59,60,64–68} In this paper, we discuss how rapid and remote heat generation can be achieved through the fabrication of Magnetic Framework Composites (MFCs) and how their interactions with a magnetic field can be used efficiently for release of the adsorbed molecules. Magnetic Induction Swing Adsorption (MISA) is a magnetically induced heating process aimed at regeneration of MOFs.^{69–71} In our previous paper, we have demonstrated the efficiency of the MISA process by desorption of 4.8 mmol g⁻¹ of adsorbed oxygen from Co-MOF-74/Fe₃O₄ systems at 204 K and 1 bar pressure.³⁹ To build upon these results obtained at cryogenic temperatures of 204 K, we intend to explore the possibility of simpler, stabler, cyclable MOFs for oxygen adsorption at room temperature. This paper looks into the relative stability and capacity of CuBTC MOF for oxygen storage, and the feasibility of oxygen release using MISA at room temperatures and 1 bar pressure.

The exposure of CuBTC MFC pellets formed using 3 wt% of MgFe₂O₄ nanoparticles, to a magnetic field of 33 mT, at a frequency of 269 kHz, triggered a 100% release of the

0.30 mmol g⁻¹ oxygen molecules stored at 1 bar pressure. The ease of use and control of the MISA process was demonstrated by triggering an on-demand release of oxygen at 200, 400, 600, 800, and 1000 mbar pressures and achieving 100% desorption each time. Three continuous cycles of adsorption and magnetically triggered desorption cycles helped to establish the structural rigidity, thermal stability, and adsorption capacity of the CuBTC MFC. The effect of atmospheric exposure, and the effect of exposure to water vapour on the structural stability of the MFCs, was also investigated.

2. Experimental

2.1 Materials synthesis

All the reagents including 1,3,5-benzenetricarboxylic acid (H₃BTC), copper acetate monohydrate Cu(OAc)₂·H₂O, sodium acetate trihydrate (CH₃COONa·3H₂O), magnesium chloride hexahydrate (MgCl₂·6H₂O), ferric chloride hexahydrate (FeCl₃·6H₂O), PEG and the solvents, *N,N*-dimethylformamide (DMF) and ethanol used for the synthesis were of analytical grade, obtained from commercial vendors and used as received.

Synthesis of CuBTC MOF. 0.7 g of copper acetate monohydrate (3.5 mmol) dissolved in 14 mL of deionized water was mixed with 0.6 g of trimesic acid (H₃BTC, 2.8 mmol) dissolved in 14 mL of ethanol. This mixture was stirred for 30 min, transferred into an autoclave, and heated to 85 °C for 24 h. On cooling, the blue CuBTC MOF was washed three times with ethanol and dried in a vacuum oven at 140 °C for 24 h.^{55,72}

Synthesis of MgFe₂O₄ nanoparticles. MgFe₂O₄ nanoparticles were synthesized using a solvothermal method by mixing of 3.6 g, 0.027 moles of sodium acetate trihydrate, 2.5 mmol MgCl₂·6H₂O and 5 mmol FeCl₃·6H₂O together and adding 2.00 g of polyethylene glycol (MW = 4000) as a surfactant. The mixture is stirred vigorously to form a homogeneous solution and then heated under reflux at 180 °C for 16 h. On cooling, the black magnetic nanoparticles are magnetically separated and washed alternately with distilled water and ethanol and dried in a vacuum oven at 80 °C for 8 h.⁷³

Fabrication of CuBTC pellets. The objective behind the shaping of MOFs is to pack maximum amounts of adsorbents in the storage tank compactly, to increase the amount of gas stored per unit volume. For practical applications, shaping MOFs is favourable. Still, the shaping technique should not adversely affect the stability and or adsorption capacity of the MOFs, and it should be feasible for large scale productions too. The most common shaping technique, pelletising, can be achieved by either applying a certain amount of pressure on the powdered MOFs to shape them into pellets or by mixing the MOF powder with specific binders (typically, polyvinyl alcohol (PVA)) and solvent to make a paste that can be further extruded into pellets.^{55,72,74} The Cu-BTC/MgFe₂O₄ MFCs were pelletised by extruding a paste made using measured quantities of CuBTC MOF, binder, and MgFe₂O₄ nanoparticles, through a 5 mL syringe. The extruded MFC noodles were cut into 8–10 mm pellets and allowed to dry in ambient air before drying them in a vacuum oven at 140 °C for 24 h. To select an MFC having an optimal balance between adsorption capacities, heating



abilities, and structural stability, different MFCs with varying binder concentrations (1, 2, 3, 4 wt%) and varying magnetic content (1, 2, 3, 4 wt% of MgFe_2O_4 nanoparticles) were fabricated and investigated for their surface area and oxygen adsorption properties.

2.2 Characterisation of materials

The samples were characterised using X-ray Powder Diffraction (XRD), Scanning Electron Microscopy (SEM), Energy Dispersive Spectroscopy (EDS) and thermogravimetric analysis (TGA). Fourier-Transform Infrared (FTIR) spectra for all samples were collected using a Thermo Scientific NICOLET 6700 FT-IR. XRD measurements analysed the crystal structure of the samples on a D8 ADVANCE Eco X-ray powder diffractometer with a Co K_α radiation source of 1.79 Å with a scan rate of 0.05 s per step at 40 kV and 25 mA. JOEL 7001F Scanning Electron Microscope was used for the morphological size-shape study of all the samples. The surface area measurements were carried out using Micromeritics ASAP 2420 instruments, and the oxygen adsorption studies were carried out on a 3Flex surface and catalyst characterisation instrument. For the triggered release experiments, the 3Flex was paired with a radio frequency power supply induction machine (EASY HEAT 0224–Ambrell) operated at 269 kHz with an 8 turns heating coil of 2.5 cm diameter and 4 cm in length.

3. Results and discussion

Fig. 1a presents the diffraction patterns of the synthesized powdered CuBTC MOF, the magnetic nanoparticles, and the MFCs fabricated with 1 wt%, 2 wt%, and 3 wt% MgFe_2O_4 nanoparticles. The diffraction peaks from the synthesized CuBTC sample corresponds to the face centre cubic (FCC) CuBTC structure, which matches well with the peaks of the simulated CuBTC (Fig. S1a†). The clear, distinct sharp peaks confirm the excellent crystallinity of the sample. Due to their low concentrations, peaks corresponding to the magnetic nanoparticles are not visible in the composite XRD. The morphology of the bare CuBTC and composite was investigated with Scanning Electron Microscopy (SEM) analysis. SEM micrographs presented in Fig. 1b and d reveal octahedral shaped CuBTC particles with an average particle size of about 5 μm . Fig. 1c shows a uniform, spherical morphology for MgFe_2O_4 nanoparticles with a diameter of 150–170 nm. The nanoparticles were used to fabricate the MFCs by varying their concentrations during the pelletization process. Fig. 1e is a micrograph of the MFC with 3 wt% MgFe_2O_4 nanoparticles, which reveals the magnetic nanoparticles firmly bound to the surfaces of the MOF particles and Fig. S2c–e† show its elemental distribution. The XRD analysis of the synthesized MgFe_2O_4 nanoparticles (Fig. S2a†) shows the diffraction peaks of planes (2 2 0), (3 1 1), (4 0 0), (5 1 1) and (4 4 0), for a cubic spinel MgFe_2O_4 phase, that matches the standard powder diffraction data (ICSD #00-036-0398) of the MgFe_2O_4 phase from literature⁷³ with a calculated mean crystallite size of 20.2 nm.

Vibrating sample magnetometer (RIKEN DENSHI VSM) was used to study the response of MgFe_2O_4 nanoparticles to an

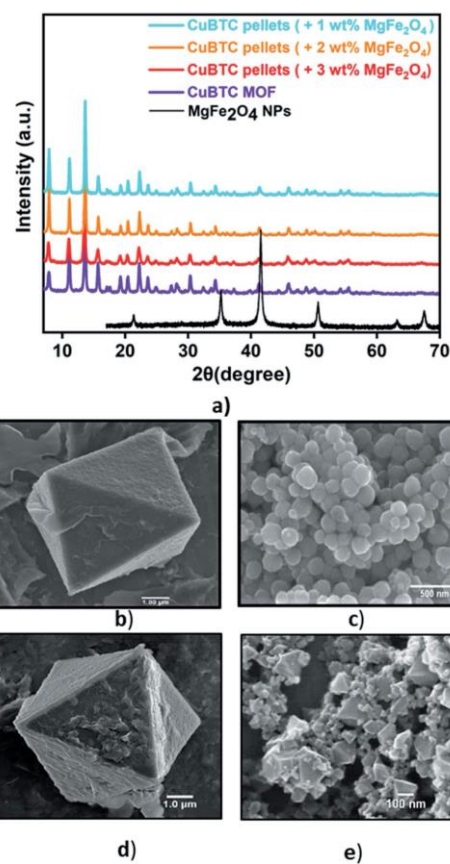


Fig. 1 (a) The powder diffraction pattern of bare CuBTC MOF, MgFe_2O_4 nanoparticles, CuBTC– MgFe_2O_4 composite with 1 wt%, 2 wt%, 3 wt% magnetic content, and SEM images of (b) bare CuBTC (c) the MgFe_2O_4 nanoparticles (d) bare CuBTC (e) 3 wt% CuBTC– MgFe_2O_4 composite.

applied magnetic field. When exposed to an applied magnetic field, the magnetization (M) of the MgFe_2O_4 nanoparticles increases with an increase in the magnetic field until it becomes saturated at 70 emu g^{-1} (Fig. S3a†). The Curie temperature (T_C) of the MgFe_2O_4 nanoparticles, defined as the temperatures above which the ferrimagnetic nanoparticles become paramagnetic,^{12,75–78} was evaluated through thermo-magneto gravimetric analysis (TMGA) (Fig. S4†). This was estimated to be 566 °C. This agrees with T_C values reported in the literature for MgFe_2O_4 .^{59,66,69} Specific adsorption rate, SAR, is a parameter used in estimating the magnitude of the heating effect generated by magnetic nanoparticles when exposed to an alternating current magnetic field.^{11,59,66,69} The SAR is a valuable parameter that can be used to estimate the rate of conversion of the



magnetic field to thermal energy. A high SAR implies rapid heating, with SAR of the synthesized MgFe_2O_4 nanoparticles calculated to be 130 W g^{-1} under an applied field of 25 mT.

For gas adsorption measurements, the CuBTC samples were activated at 140°C for 24 h, and the N_2 adsorption isotherms obtained at 77 K show a type I adsorption that is typically observed in microporous solids. The calculated Brunauer–Emmett–Teller (BET) surface areas of the bare CuBTC MOF and MFCs are summarized in Fig. S5a and Table S1.† The BET surface area of the bare CuBTC MOF was $1495 \text{ m}^2 \text{ g}^{-1}$, and upon addition of 1 wt% binder, a drop of 17% in surface area was noticed. This loss in surface area can be attributed to the process of pelletising where the binders, which are essential to enable cohesion and densification of the MOFs, cause partial blockage of some pores in the MOF resulting in lower surface areas and pore volumes.⁷⁹ Based on such effects of different binder concentrations and varying magnetic contents on the surface area properties of the MFC, the Cu-BTC/MgFe₂O₄ composites with 3 wt% binder concentration and 3 wt% MgFe₂O₄ nanoparticles were selected and fabricated for all experiments.

To evaluate the potential of these Cu-BTC/MgFe₂O₄ MFCs for room temperature oxygen storage applications, it is crucial to establish their moisture stability in ambient atmospheric conditions.⁸⁰ Water adsorption experiments were conducted to test the water stability of the MFCs using Micromeritics 3Flex gas sorption analyser for the range ($P/P_0 = 0.001\text{--}0.9$) at 298 K. Prior to the vapour adsorption measurements, the CuBTC samples were activated at 140°C for 12 h. The initial steep slope (0.001–0.2), the intermediate shallow plateau (0.2–0.7) and the last steep slope (0.7–0.9) of the water adsorption isotherm are all indicative of the strong interactions between the water molecules and the copper centres from the initial adsorption in the CuBTC cages to the final micropore filling of the side pockets. The water vapour adsorption capacity of 28.4 mmol g^{-1} of the CuBTC MOF matches well with the results reported in the literature.⁵⁰ The water vapour adsorption capacity of the 3 wt% CuBTC–MgFe₂O₄ composite pellets was found to be 28.9 mmol g^{-1} . Post water adsorption experiments, the structural stability of the MOF and MFC were analysed by powder X-ray diffraction (PXRD), and the matching XRD peak intensities of the activated samples and the hydrated samples confirm the structural stability (Fig. S6† and 2).

3.1 Oxygen adsorption

To evaluate the oxygen adsorption properties of the CuBTC pellets, single-component oxygen adsorption measurements were carried out at 204, 273, and 298 K (pressures loadings between 0 to 1 bar), on 80 mg of activated CuBTC pellets. The adsorption temperatures of 204, 273, and 298 K were stabilized using acetone and dry-ice bath, ice bath, and water bath, respectively. The results from the oxygen adsorption at these three temperatures reveal that at 204 K, the pellets displayed the highest adsorption capacity of 3.5 mmol g^{-1} of oxygen, followed by 0.45 mmol g^{-1} oxygen at 273 K and 0.34 mmol g^{-1} of oxygen was adsorbed at 298 K (Fig. 3). In CuBTC MOF,¹³ the dimeric copper-tetracarboxylic unit of Cu–Cu (2.628 Å) acts as a centre and is connected by four oxygen atoms from the

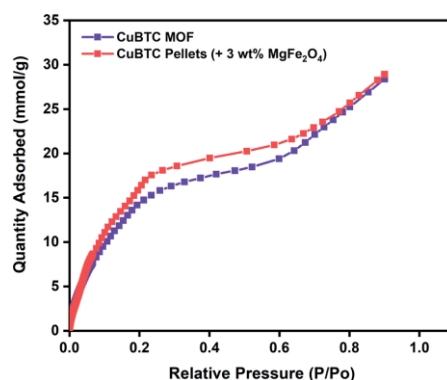


Fig. 2 Water vapour adsorption isotherms of CuBTC MOF and 3 wt% CuBTC–MgFe₂O₄ composite pellets measured at 298 K.

benzenetricarboxylate (BTC) linkers and water molecules.^{81–84} The interconnected Cu(II) paddlewheel unit and tridentate BTC linkers form a three-dimensional octahedral structure with square-shaped main channels of $9 \times 9 \text{ \AA}$ and tetrahedral units of 5 \AA openings that are connected to the main channels by triangular pockets of 3.5 \AA . The isosteric heat of adsorption, Q_{st} , reveals the extent of interaction between the adsorbed molecules and the adsorbate under constant loading conditions and here these interactions are primarily dependant on the reactions at the exposed cationic Cu^{2+} sites and adsorption at the windows sites of the octahedral CuBTC cage is calculated to be $-15.3 \text{ kJ mol}^{-1}$. This near-constant Q_{st} curve of oxygen was plotted using the adsorption data measured at 204, 273, and 298 K (Fig. S8b†) and shows that irrespective of the loading conditions the binding energies remain constant.

To study the reversibility and reusability of the MFC pellets after their interactions with oxygen at room temperature, cyclic

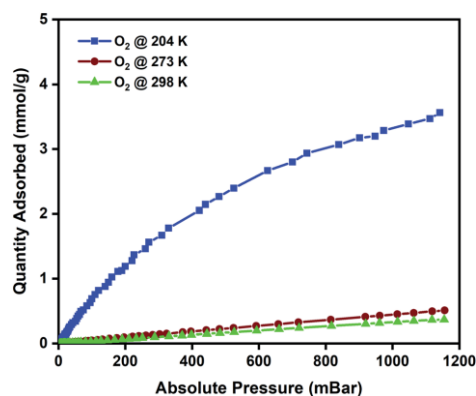


Fig. 3 Oxygen adsorption isotherms of CuBTC MOF measured at 204, 273, and 298 K.



studies were carried out on the same sample. Between every oxygen adsorption cycle, they were regenerated at 140 °C for 12 h. As observed from Fig. 4, over twenty continuous cycles, the MFC pellets displayed a consistent oxygen adsorption capacity. They did not show any signs of material degradation even after the 20th cycle, which was later confirmed by PXRD (Fig. S10†). Thermal stabilities and decomposition temperatures of the samples were also studied by thermal gravimetric analysis (TGA) using weighed samples that were heated from 25 °C to 800 °C at a heating rate of 10 °C min⁻¹ (Fig. S7a†).

3.2 Desorption of oxygen using MISA

Magnetic induction swing adsorption is an innovative technology that harnesses the heating abilities of magnetic nanoparticles to trigger the release of stored gas molecules from the framework in energy-efficient ways. The adsorption potential of the MOFs and the heating abilities of the magnetic nanoparticles are combined to develop the MFCs. This is to enable efficient heat transfer in the MOF by overcoming their low thermal conductivities. It is achieved using ferrimagnetic nanoparticles capable of remote, targeted, and localized heat generation capabilities upon exposure to a magnetic field.^{60,85,86} The heat generation in the nanoparticles is a result of hysteresis observed in the plot of magnetisation vs. the applied field when the ferrimagnets are exposed to an alternating current magnetic field. An irreversible magnetisation–demagnetisation process is induced with the magnitude of the heat generated equivalent to the area within the hysteresis loop.^{69,87,88} Consequently, in MFCs, this rapid and localized heat generation leads to instability in the guest–host bond of the adsorbed gas and the framework that triggers the release of the gas molecules. The selection of the MOF, the ratio of magnetic nanoparticles, and the strength of the applied magnetic field are essential features of the MISA process. The heat generation capability of the MFCs was measured by recording their temperature rise profile while

exposing them to different magnetic field strengths. While studying the 3 wt% Cu-BTC/MgFe₂O₄ MFCs, it was noted that on application of 25 mT magnetic field, from the initial temperatures of 25 °C, the pellets attained a maximum temperature rise of 78 °C, with 31 mT magnetic field the temperature reached was 86 °C and with 33 mT, the MFCs reached a temperature of 92 °C (Fig. S4d†).

The oxygen adsorption isotherms were collected using a Micro metrics 3Flex gas sorption analyser at pre-set equilibration times, allowing enough time for the system to equilibrate at each pressure point, and the targeted pressures for desorption were set at 200, 400, 600, 800, and 1000 mbar. The experiment was designed to alternate between adsorption and desorption phases continuously, with minimal activation and degassing taking place between each cycle. The desorption was induced with an EASY HEAT Ambrell induction machine (Fig. S9†) to trigger the remote, rapid, and localised heating enabling the complete release of the adsorbed oxygen at the desired pressure. Typically, the 3Flex experiment program is run to adsorb oxygen from 0.1 mbar to 1200 mbar. The experiment is monitored, and at 200 mbar pressure range, the remote magnetic heating is activated to trigger the release of the adsorbed oxygen molecules. The process is repeated at 400, 600, 800, and 1000 mbar. For the 3 wt% MFC, a magnetic field of 31 mT was applied, and at 188 mbar, a 100% release of the 0.06 mmol g⁻¹ of adsorbed oxygen was released in 5 minutes. Once complete desorption was achieved, the applied magnetic field was switched off to stop the remote heating process, thereby allowing the MFC to resume the adsorption of oxygen. The MFC pellets showed a similar uptake performance relative to the bare MOF. The triggered release of the MFC was repeated at 400 mbar (0.12 mmol g⁻¹), 600 mbar (0.17 mmol g⁻¹), 800 mbar (0.22 mmol g⁻¹), and 1000 mbar (0.26 mmol g⁻¹) and achieved 100% release of oxygen molecules within 5 min time except for the 1000–1200 mbar range where it took 8–9 min for the adsorption–desorption–adsorption cycle to finish (Fig. 5).

Open Access Article. Published on 10 November 2020. Downloaded on 12/20/2020 6:18:00 AM.
This article is licensed under a Creative Commons Attribution 3.0 Unported Licence.

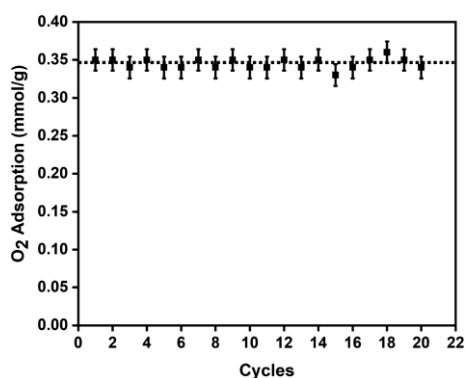


Fig. 4 Twenty oxygen adsorption–desorption cycles on the 3 wt% CuBTC–MgFe₂O₄ composite pellets at 298 K with the error bars representing ± 0.02 standard deviation per cycle.

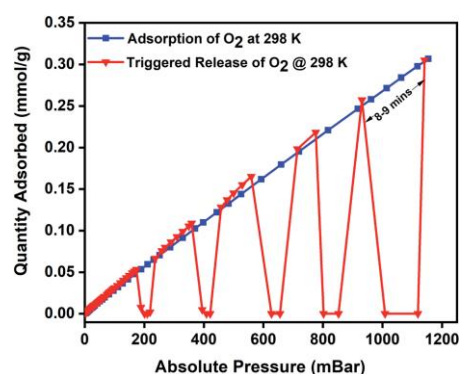


Fig. 5 Oxygen adsorption isotherm of 3 wt% CuBTC–MgFe₂O₄ composite pellets at 298 K and the magnetically triggered desorption at 200, 400, 600, 800, and 1000 mbar.

To investigate the post-MISA stability of the MFC, its regeneration, and adsorption capacities of the MFC pellets, they were activated at 140 °C for 6 h after each triggered release experiment, and after twenty MISA cycles (Fig. 4), the XRD results corroborate their structural stability (Fig. S10†).

To evaluate regeneration capability and the cyclic performance of the composite pellets over multiple closed MISA cycles, upon achieving the maximum oxygen uptake of 0.34 mmol g⁻¹ at 1140 mbar, the pellets were reactivated for 10 minutes by remote magnetic heating at 33 mT (92 °C) and simultaneously evacuating the sample from 1200–0 mbar. Fig. 6 presents the results of three continuous closed MISA cycles on the 3Flex with a sample pressure of 0.007 mbar achieved when the magnetic heating and vacuum activation steps were combined. Upon switching off the magnetic field, oxygen adsorption and MISA-based desorption second cycle continued precisely like the first cycle at 200, 400, 600, 800, and 1000 mbar and 31 mT (86 °C) applied magnetic field. The results from three continuous adsorptions and MISA regeneration of the MFCs revealed that the oxygen adsorption capacity of the composite pellets was not adversely affected by the heat from the nanoparticles and each desorption cycle achieved a consistent result of complete desorption of bound oxygen molecules.

To highlight the easy accessibility of oxygen at any targeted pressures and to signify the versatility of the MISA process in regenerating the MFC after every adsorption cycle, we ran a closed MISA adsorption–desorption–regeneration cyclic run across all pressures. This experiment was planned to alternate between adsorption, desorption, and regeneration between each cycle. The experiment was conducted with the usual oxygen adsorption by the MFCs, that was followed by desorption at 200 mbar using a magnetic field of 31 mT (86 °C), and the 200–0 mbar regeneration was achieved within 6 min by the magnetic heating from 33 mT (92 °C) magnetic field and evacuation from the system. Once 0 mbar pressure was reached, the MFC resumed its oxygen adsorption until the desorption and

regeneration steps were activated again at 400, 600, 800, and 1000 mbar pressures. The regeneration times varied between 6–10 minutes with 200–0 mbar reached in 6 minutes, whereas it took 10 minutes for the 1200–0 mbar step. The 140 °C for 12 h heating plus vacuum reactivation step was replaced with 10 minutes, and 33 mT (92 °C) applied field at the end of each pressure point (downward-facing arrows at 1, 2, 3, 4 and 5 in Fig. 7). The success of this new adsorbent regeneration method can be validated by the consistent oxygen adsorption capacities shown by the composite in consecutive cycles.

3.3 Regeneration energy

For efficient and economic adsorption-based separations, the adsorbent selection is primarily governed by its selectivity, adsorption capabilities, regeneration ability, and stability. The regeneration energy is the energy utilized by the adsorbent to undo the adsorption process. It depends on the heat of adsorption, specific heat capacity, and working capacity of the adsorbents. It is directly proportional to the heat of adsorption because strong interaction between the adsorbent and adsorbate results in a higher heat of adsorption and consequently higher regeneration energy would be required to overcome this strong interaction⁸⁹ leading to a high energy penalty.^{11,89,90} Furthermore, MOFs are generally known to be thermal insulators and require high temperatures to trigger the release of adsorbed species. The remote, localised and targeted heating nature of the MISA process makes it most suitable for oxygen capture and storage applications while minimising the energy penalty required to operate the process.^{11,59,60,91}

Fig. 8 depicts the regeneration energy requirements with varying magnetic fields of 25 mT, 31 mT, and 33 mT. Stronger interactions between the adsorbed molecules and the framework at low pressures require higher regeneration energies for

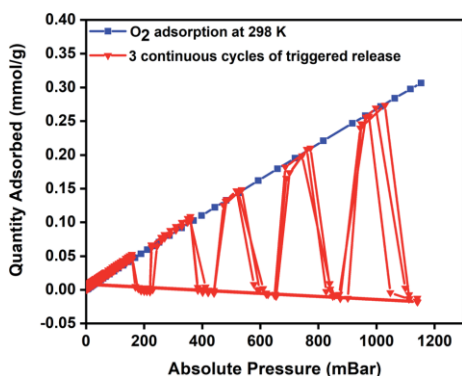


Fig. 6 Oxygen adsorption isotherm of 3 wt% CuBTC–MgFe₂O₄ composite at 298 K and three continuous desorption cycles of oxygen at 200, 400, 600, 800, and 1000 mbar.

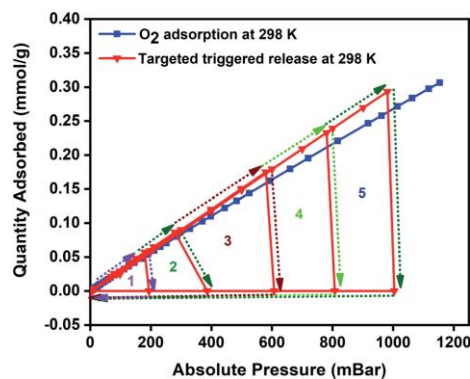


Fig. 7 The performance of 3 wt% CuBTC–MgFe₂O₄ composite at 298 K in a closed MISA cyclic adsorption–desorption–regeneration process with the combined vacuum and magnetic heating triggered desorption at 200, 400, 600, 800 and 1000 mbar and the regeneration from 200–0 mbar (1), 400–0 mbar (2), 600–0 mbar (3), 800–0 mbar (4) and 1000–0 mbar (5).



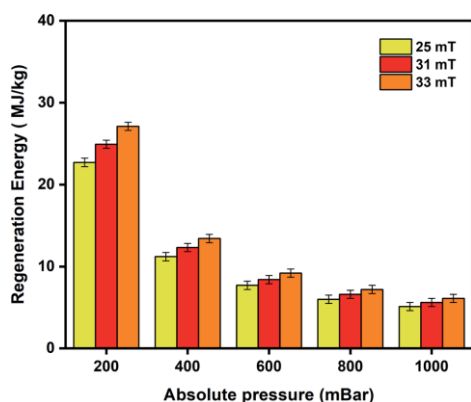


Fig. 8 Regeneration energy as a function of varying magnetic fields of 25 mT, 31 mT, and 33 mT used to trigger desorption of oxygen from the 3 wt% CuBTC-MgFe₂O₄ MFCs.

desorption at 200 mbar. Energy requirements by the MISA process were evaluated for two different masses of the MFC pellets. When 0.3 g and 0.6 g of the 3 wt% MFC pellets were exposed to a magnetic field of 31 mT; the MFC pellets experienced a temperature rise of 86 °C and the energy utilized for the regeneration of 0.26 mmol g⁻¹ of oxygen adsorbed at 1000 mbar was calculated to be 5.1 MJ kg_{O₂}⁻¹ for 0.3 g weight sample and 5.6 MJ kg_{O₂}⁻¹ for 0.6 g sample (Fig. S11b†).

Additionally, the energy used to drive the magnetic induction heating in the MISA process was determined by monitoring the electrical power consumption of the EASY HEAT Ambrell induction machine. A power meter connected to the machine estimated the power consumption when the MFC is in and out of the magnetic field at 25 mT, 31 mT, and 33 mT. For the 0.6 g of the MFC pellets, the energy consumed to regenerate the pellets at 1000 mbar was calculated from the power (W) consumed by the induction unit, the time (s) it took to release the adsorbed molecules and the mass (g) of the released molecules (Table S3†). Despite the relatively high regeneration energy requirement of the MFC pellets, the energy input to the induction system was calculated to be 0.15 kW h kg_{O₂}⁻¹ (Table S2†) highlighting a lower energy requirement when compared to conventional cryogenic oxygen producing systems where energy requirement of 0.3–0.35 kW h kg_{O₂}⁻¹ has been reported.⁹²

4. Conclusions

MOFs are known to be thermally insulating, and this can be overcome by utilizing the rapid, localized, and easily controllable magnetic induction heating effect. MISA is a technology that can be harnessed to achieve an efficient process for on-demand oxygen delivery. Particularly, miniaturized oxygen concentrators can be engineered with MFCs for room temperature oxygen storage and on-demand supply of oxygen. The

results demonstrate the versatility and potential of the MISA process in exploiting a readily available MOF incorporated with magnetic nanoparticles for safe storage and on-demand release of oxygen at ambient conditions. Here, the powdered CuBTC MOF was transformed into CuBTC-MgFe₂O₄ MFCs by mixing them with different amounts of MgFe₂O₄ nanoparticles and pelletising them with the help of a binder. To understand the purity and properties of the synthesized CuBTC MOF, MgFe₂O₄ nanoparticles, and the fabricated CuBTC-MgFe₂O₄ MFCs, they were analysed using different characterisation techniques and depending on the outcome the pellets with 3 wt% magnetic content were selected for further oxygen studies. These pellets showed an adsorption capacity of 0.3 mmol g⁻¹ at 1 bar pressure at 298 K. When they were exposed to a magnetic field of 31 mT at 269 kHz; the MgFe₂O₄ nanoparticles attained a temperature rise to 86 °C causing full desorption of the oxygen molecules. The composite exhibited good thermal stability and excellent cyclability by maintaining its adsorption properties over three continuous adsorption-desorption cycles. Oxygen storage and supply using ambient temperature processes can be made simpler, efficient, safer, and considerably less complex using cyclable MOFs. This, accompanied by the energy-efficient MISA process, can revolutionize the safe storage, handling, transport, and on-demand supply of oxygen.

Conflicts of interest

There are no conflicts of interest to declare with the publication of this manuscript.

Acknowledgements

The authors acknowledge the use of instruments and scientific and technical assistance at the Monash Centre for Electron Microscopy, a Node of Microscopy Australia and the Monash X-ray platform.

References

- 1 R. J. Allam, *Energy Procedia*, 2009, **1**, 461–470.
- 2 M. Dobson, *Int. J. Tuberc. Lung Dis.*, 2001, **5**, 520–523.
- 3 J. Emsley, *Nature's building blocks: an AZ guide to the elements*, Oxford University Press, 2011.
- 4 E. Gulcay and I. Erucar, *Ind. Eng. Chem. Res.*, 2019, **58**, 3225–3237.
- 5 M. Dobson, *Anaesthesia*, 1991, **46**, 217–219.
- 6 E. Arnold, A. Bruton, M. Donovan-Hall, A. Fenwick, B. Dibb and E. Walker, *BMC Pulm. Med.*, 2011, **11**, 9.
- 7 A. Dubois, P. Bodelin and X. Vigor, *US Pat.*, 6, 520, 176, 18 Feb 2003.
- 8 P. Z. Moghadam, T. Islamoglu, S. Goswami, J. Exley, M. Fantham, C. F. Kaminski, R. Q. Snurr, O. K. Farha and D. Fairen-Jimenez, *Nat. Commun.*, 2018, **9**, 1378.
- 9 J. B. DeCoste, M. H. Weston, P. E. Fuller, T. M. Tovar, G. W. Peterson, M. D. LeVan and O. K. Farha, *Angew. Chem., Int. Ed.*, 2014, **53**, 14092–14095.
- 10 M. H. Weston, *US Pat.*, 20150105250, April 16, 2015.



- 11 M. M. Sadiq, K. Suzuki and M. R. Hill, *Chem. Commun.*, 2018, 54, 2825–2837.
- 12 P. Falcaro, F. Lapierre, B. Marmiroli, M. Styles, Y. Zhu, M. Takahashi, A. J. Hill and C. M. Doherty, *J. Mater. Chem. C*, 2013, 1, 42–45.
- 13 J. A. Mason, M. Veenstra and J. R. Long, *Chem. Sci.*, 2014, 5, 32–51.
- 14 D. Bazer-Bachi, L. Assié, V. Lecocq, B. Harbuzaru and V. Falk, *Powder Technol.*, 2014, 255, 52–59.
- 15 J. Kim, H.-Y. Cho and W.-S. Ahn, *Catal. Surv. Asia*, 2012, 16, 106–119.
- 16 R. F. Mendes and F. A. Almeida Paz, *Inorg. Chem. Front.*, 2015, 2, 495–509.
- 17 G. W. Peterson, D. K. Britt, D. T. Sun, J. J. Mahle, M. Browe, T. Demasky, S. Smith, A. Jenkins and J. A. Rossin, *Ind. Eng. Chem. Res.*, 2015, 54, 3626–3633.
- 18 E. D. Bloch, W. L. Queen, R. Krishna, J. M. Zadrozny, C. M. Brown and J. R. Long, *Science*, 2012, 335, 1606–1610.
- 19 H. Li, K. Wang, Y. Sun, C. T. Lollar, J. Li and H.-C. Zhou, *Mater. Today*, 2018, 21, 108–121.
- 20 J.-R. Li, R. J. Kuppler and H.-C. Zhou, *Chem. Soc. Rev.*, 2009, 38, 1477–1504.
- 21 J.-R. Li, J. Sculley and H.-C. Zhou, *Chem. Rev.*, 2011, 112, 869–932.
- 22 M. V. Parkes, D. F. Sava Gallis, J. A. Greathouse and T. M. Nenoff, *J. Phys. Chem. C*, 2015, 119, 6556–6567.
- 23 W. L. Queen, E. D. Bloch, C. M. Brown, M. R. Hudson, J. A. Mason, L. J. Murray, A. J. Ramirez-Cuesta, V. K. Peterson and J. R. Long, *Dalton Trans.*, 2012, 41, 4180–4187.
- 24 K. K. Gangu, S. Maddila, S. B. Mukkamala and S. B. Jonnalagadda, *Inorg. Chim. Acta*, 2016, 446, 61–74.
- 25 F. Ke, Y.-P. Yuan, L.-G. Qiu, Y.-H. Shen, A.-J. Xie, J.-F. Zhu, X.-Y. Tian and L.-D. Zhang, *J. Mater. Chem.*, 2011, 21, 3843–3848.
- 26 O. M. Yaghi, G. Li and H. Li, *Nature*, 1995, 378, 703.
- 27 H. Furukawa, K. E. Cordova, M. O’Keeffe and O. M. Yaghi, *Science*, 2013, 341, 1230444.
- 28 M. Eddaoudi, D. B. Moler, H. Li, B. Chen, T. M. Reineke, M. O’Keeffe and O. M. Yaghi, *Acc. Chem. Res.*, 2001, 34, 319–330.
- 29 C. M. Doherty, D. Buso, A. J. Hill, S. Furukawa, S. Kitagawa and P. Falcaro, *Acc. Chem. Res.*, 2014, 47, 396–405.
- 30 C. H. Hendon, A. J. Rieth, M. D. Korzyński and M. Dincă, *ACS Cent. Sci.*, 2017, 3, 554–563.
- 31 J.-R. Li, R. J. Kuppler and H.-C. Zhou, *Chem. Soc. Rev.*, 2009, 38, 1477–1504.
- 32 D. J. Xiao, M. I. Gonzalez, L. E. Darago, K. D. Vogiatzis, E. Haldoupis, L. Gagliardi and J. R. Long, *J. Am. Chem. Soc.*, 2016, 138, 7161–7170.
- 33 L. J. Murray, M. Dinca, J. Yano, S. Chavan, S. Bordiga, C. M. Brown and J. R. Long, *J. Am. Chem. Soc.*, 2010, 132, 7856–7857.
- 34 P. D. Southon, D. J. Price, P. K. Nielsen, C. J. McKenzie and C. J. Kepert, *J. Am. Chem. Soc.*, 2011, 133, 10885–10891.
- 35 E. D. Bloch, L. J. Murray, W. L. Queen, S. Chavan, S. N. Maximoff, J. P. Bigi, R. Krishna, V. K. Peterson, F. Grandjean, G. J. Long, B. Smit, S. Bordiga, C. M. Brown and J. R. Long, *J. Am. Chem. Soc.*, 2011, 133, 14814–14822.
- 36 E. D. Bloch, W. L. Queen, M. R. Hudson, J. A. Mason, D. J. Xiao, L. J. Murray, R. Flacau, C. M. Brown and J. R. Long, *Angew. Chem., Int. Ed.*, 2016, 55, 8605–8609.
- 37 D. J. Xiao, M. I. Gonzalez, L. E. Darago, K. D. Vogiatzis, E. Haldoupis, L. Gagliardi and J. R. Long, *J. Am. Chem. Soc.*, 2016, 138, 7161–7170.
- 38 H. Nagar, P. Vadthya, N. S. Prasad and S. Sridhar, *RSC Adv.*, 2015, 5, 76190–76201.
- 39 L. Melag, M. M. Sadiq, S. J. D. Smith, K. Konstas, K. Suzuki and M. R. Hill, *J. Mater. Chem. A*, 2019, 7, 3790–3796.
- 40 H. Sugimoto, T. Nagayama, S. Maruyama, S. Fujinami, Y. Yasuda, M. Suzuki and A. Uehara, *Bull. Chem. Soc. Jpn.*, 1998, 71, 2267–2279.
- 41 A. M. P. Moeljadi, R. Schmid and H. Hirao, *Can. J. Chem.*, 2016, 94, 1144–1150.
- 42 M. März, R. E. Johnsen, P. D. C. Dietzel and H. Fjellvåg, *Microporous Mesoporous Mater.*, 2012, 157, 62–74.
- 43 M. Thorseth, C. Tornow, E. Tse and A. Gewirth, *Coord. Chem. Rev.*, 2013, 257, 130–139.
- 44 S. Gonen and L. Elbaz, *Curr. Opin. Electrochem.*, 2018, 9, 179–188.
- 45 S. Gonen, O. Lori, G. Cohen-Taguri and L. Elbaz, *Nanoscale*, 2018, 10, 9634–9641.
- 46 X. F. Lu, B. Y. Xia, S.-Q. Zang and X. W. Lou, *Angew. Chem., Int. Ed.*, 2020, 59, 4634–4650.
- 47 M. Jiang, L. Li, D. Zhu, H. Zhang and X. Zhao, *J. Mater. Chem. A*, 2014, 2, 5323–5329.
- 48 A. I. Skoulidis, *J. Am. Chem. Soc.*, 2004, 126, 1356–1357.
- 49 J. Liu, Y. Wang, A. I. Benin, P. Jakubczak, R. R. Willis and M. D. LeVan, *Langmuir*, 2010, 26, 14301–14307.
- 50 N. Al-Janabi, P. Hill, L. Torrente-Murciano, A. Garforth, P. Gorgojo, F. Siperstein and X. Fan, *Chem. Eng. J.*, 2015, 281, 669–677.
- 51 B. Sun, S. Kayal and A. Chakraborty, *Energy*, 2014, 76, 419–427.
- 52 J. J. Gutiérrez-Sevillano, J. M. Vicent-Luna, D. Dubbeldam and S. Calero, *J. Phys. Chem. C*, 2013, 117, 11357–11366.
- 53 Q. Yang, C. Xue, C. Zhong and J. F. Chen, *AIChE J.*, 2007, 53, 2832–2840.
- 54 Z. Hulvey, K. V. Lawler, Z. Qiao, J. Zhou, D. Fairen-Jimenez, R. Q. Snurr, S. V. Ushakov, A. Navrotsky, C. M. Brown and P. M. Forster, *J. Phys. Chem. C*, 2013, 117, 20116–20126.
- 55 M. Rubio-Martinez, M. P. Batten, A. Polyzos, K.-C. Carey, J. I. Mardel, K.-S. Lim and M. R. Hill, *Sci. Rep.*, 2014, 4, 5443.
- 56 Z. Liang, M. Marshall and A. L. Chaffee, *Energy Fuels*, 2009, 23, 2785–2789.
- 57 N. A. Travlou, K. Singh, E. Rodríguez-Castellón and T. J. Bandosz, *J. Mater. Chem. A*, 2015, 3, 11417–11429.
- 58 M. Hosseini, S. Zeinali and M. Sheikhi, *Sens. Actuators, B*, 2016, 230, 9–16.
- 59 M. M. Sadiq, H. Li, A. J. Hill, P. Falcaro, M. R. Hill and K. Suzuki, *Chem. Mater.*, 2016, 28, 6219–6226.
- 60 H. Li, M. M. Sadiq, K. Suzuki, R. Ricco, C. Doblin, A. J. Hill, S. Lim, P. Falcaro and M. R. Hill, *Adv. Mater.*, 2016, 28, 1839–1844.

Open Access Article. Published on 10 November 2020. Downloaded on 12/20/2020 6:18:00 AM.
 This article is licensed under a Creative Commons Attribution 3.0 Unported Licence.



- 61 B. L. Huang, A. J. H. McGaughey and M. Kaviani, *Int. J. Heat Mass Transfer*, 2007, **50**, 393–404.
- 62 B. L. Huang, Z. Ni, A. Millward, A. J. H. McGaughey, C. Uher, M. Kaviani and O. Yaghi, *Int. J. Heat Mass Transfer*, 2007, **50**, 405–411.
- 63 X. Zhang and J. Jiang, *J. Phys. Chem. C*, 2013, **117**, 18441–18447.
- 64 H. Li, M. M. Sadiq, K. Suzuki, C. Doblin, S. Lim, P. Falcaro, A. J. Hill and M. R. Hill, *J. Mater. Chem. A*, 2016, **4**, 18757–18762.
- 65 H. Li, M. M. Sadiq, K. Suzuki, P. Falcaro, A. J. Hill and M. R. Hill, *Chem. Mater.*, 2017, **29**, 6186–6190.
- 66 M. M. Sadiq, M. Rubio-Martinez, F. Zadehahmadi, K. Suzuki and M. R. Hill, *Ind. Eng. Chem. Res.*, 2018, **57**, 6040–6047.
- 67 R. Ricco, K. Konstas, M. J. Styles, J. J. Richardson, R. Babarao, K. Suzuki, P. Scopece and P. Falcaro, *J. Mater. Chem. A*, 2015, **3**, 19822–19831.
- 68 R. Ricco, L. Malfatti, M. Takahashi, A. J. Hill and P. Falcaro, *J. Mater. Chem. A*, 2013, **1**, 13033–13045.
- 69 A. Kolhatkar, A. Jamison, D. Litvinov, R. Willson and T. Lee, *Int. J. Mol. Sci.*, 2013, **14**, 15977.
- 70 M. Bañobre-López, A. Teijeiro and J. Rivas, *Rep. Pract. Oncol. Radiother.*, 2013, **18**, 397–400.
- 71 I. Harris and A. Williams, *Mater. Sci. Eng., C*, 2009, **2**, 49–84.
- 72 M. Rubio-Martinez, C. Avci-Camur, A. W. Thornton, I. Imaz, D. Maspocho and M. R. Hill, *Chem. Soc. Rev.*, 2017, **46**, 3453–3480.
- 73 S. Maensiri, M. Sangmanee and A. Wiengmoon, *Nanoscale Res. Lett.*, 2009, **4**, 221.
- 74 X.-M. Liu, L.-H. Xie and Y. Wu, *Inorg. Chem. Front.*, 2020, **7**, 2840–2866.
- 75 K. Bakoglidis, K. Simeonidis, D. Sakellari, G. Stefanou and M. Angelakeris, *IEEE Trans. Magn.*, 2012, **48**, 1320–1323.
- 76 S. Sun, H. Zeng, D. B. Robinson, S. Raoux, P. M. Rice, S. X. Wang and G. Li, *J. Am. Chem. Soc.*, 2004, **126**, 273–279.
- 77 A. E. Deatsch and B. A. Evans, *J. Magn. Magn. Mater.*, 2014, **354**, 163–172.
- 78 M. Ebrahimi, *J. Magn. Magn. Mater.*, 2016, **416**, 134–140.
- 79 S. J. Yang, J. Y. Choi, H. K. Chae, J. H. Cho, K. S. Nahm and C. R. Park, *Chem. Mater.*, 2009, **21**, 1893–1897.
- 80 B. S. Gelfand and G. K. H. Shimizu, *Dalton Trans.*, 2016, **45**, 3668–3678.
- 81 S. Bouson, A. Krittayavathananon, N. Phattharasupakun, P. Siwayaprahm and M. Sawangphruk, *R. Soc. Open Sci.*, 2017, **4**, 170654.
- 82 A. Vishnyakov, P. I. Ravikovitch, A. V. Neimark, M. Bülow and Q. M. Wang, *Nano Lett.*, 2003, **3**, 713–718.
- 83 K.-S. Lin, A. K. Adhikari, C.-N. Ku, C.-L. Chiang and H. Kuo, *Int. J. Hydrogen Energy*, 2012, **37**, 13865–13871.
- 84 W. W. Lestari, M. Adreane, C. Purnawan, H. Fansuri, N. Widiastuti and S. B. Rahardjo, 2016.
- 85 B. Mu and K. S. Walton, *J. Phys. Chem. C*, 2011, **115**, 22748–22754.
- 86 S. K. Bhardwaj, N. Bhardwaj, R. Kaur, J. Mehta, A. L. Sharma, K.-H. Kim and A. Deep, *J. Mater. Chem. A*, 2018, **6**, 14992–15009.
- 87 H. Rudolf, D. Silvio and Z. Matthias, *Nanotechnology*, 2010, **21**, 015706.
- 88 H. W. Sung and C. Rudowicz, arxiv preprint cond-mat/0210657, 2002.
- 89 J. A. Mason, K. Sumida, Z. R. Herm, R. Krishna and J. R. Long, *Energy Environ. Sci.*, 2011, **4**, 3030–3040.
- 90 H. Li, M. M. Sadiq, K. Suzuki, C. Doblin, S. Lim, P. Falcaro, A. J. Hill and M. R. Hill, *J. Mater. Chem. A*, 2016, **4**, 18757–18762.
- 91 M. M. Sadiq, M. Rubio-Martinez, F. Zadehahmadi, K. Suzuki and M. R. Hill, *Ind. Eng. Chem. Res.*, 2018, **57**, 6040–6047.
- 92 A. C. Twort, *Water supply*, London: Arnold/IWA Pub., London, 5th edn, 2000.

Open Access Article. Published on 10 November 2020. Downloaded on 12/20/2020 6:18:00 AM.
This article is licensed under a Creative Commons Attribution 3.0 Unported Licence.



Supporting Information

Performance evaluation of CuBTC composites for room temperature Oxygen storage.

Leena Melag,[†] M. Munir Sadiq,[‡] Kristina Konstas,[‡] Farnaz Zadehahmadi, Kiyonori Suzuki,^{*||} and Matthew R. Hill,^{**‡}

[†]Department of Chemical Engineering, Monash University, Clayton, VIC 3168, Australia

^{||}Department of Materials Science and Engineering, Monash University, Clayton, VIC 3168, Australia

[‡]CSIRO, Private Bag 33, Clayton South MDC, VIC 3169, Australia

Powder X-Ray Diffraction and FTIR spectroscopy of CuBTC MOF:

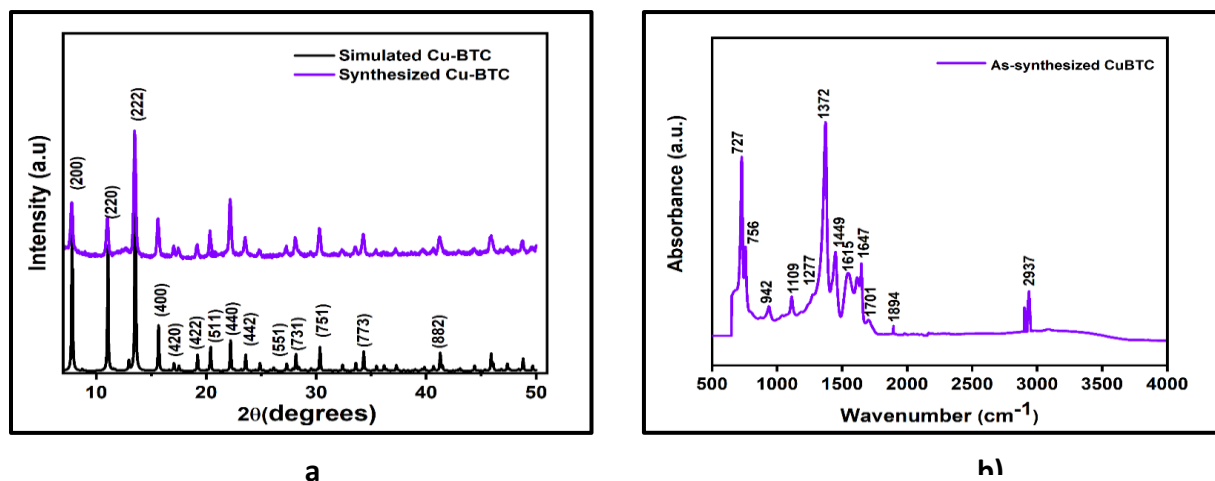


Figure S1: a) The XRD patterns of the synthesised CuBTC MOF are a perfect match with the simulated XRD pattern of CuBTC, b) The FTIR spectra of the synthesised CuBTC to detect the functional groups in the sample.

The XRD pattern of the synthesised Cu-BTC is shown in Fig S1, and it is characteristic of a face-centred cubic (FCC) CuBTC crystal lattice and the reflection peaks of (200), (220), (222), (400), (420), (511), (440), (442), (551), (731), (751), (773), and (882) match the reflections of the simulated CuBTC pattern. Fourier-Transform Infrared (FTIR) spectra for all samples were collected using a Thermo Scientific NICOLET 6700 FT-IR and was used to detect the functional groups in the samples. The FTIR spectrum of samples match closely with the ones reported in the literature^{1, 2} with the significant peaks observed at 580-727 cm^{-1} attributed to the vibrational bond involving the Cu-O, the peaks around 1449 and 1372 cm^{-1} due to the symmetric stretching modes and the one around 1647 cm^{-1} due to the asymmetric stretching of carboxylate groups in the BTC linker.

Powder X-Ray Diffraction and SEM on MgFe_2O_4 nanoparticles :

As shown in Fig. S2, a), the XRD pattern of the synthesised MgFe_2O_4 nanoparticles with diffraction peaks of planes (2 2 0), (3 1 1), (4 0 0), (5 1 1) and (4 4 0), for a cubic spinel MgFe_2O_4 phase, matches the standard powder diffraction data (ICSD #00-036-0398) of the MgFe_2O_4 phase from literature³. The mean crystallite size of 10.2 nm was calculated from the peak broadening of the diffraction planes and used in the Scherrer's equation, $d = K\lambda/(\beta \cos\theta)$, where d is the crystallite size, λ is the wavelength of the X-ray radiation (Co-1.78897 Å), K is a shape factor with values in between 0.9-1, θ is the Bragg peak in degrees and β is the line broadening (full width at half maximum). Scanning electron microscope (SEM) analysis on the samples was carried out on a JEOL JSM-7001F microscope and, as shown in Figure S2, b), the images show uniform, spherical, and agglomerated MgFe_2O_4 nanospheres

Appendix B- Performance evaluation of CuBTC composites for room temperature Oxygen storage

with a diameter of about 150-160 nm.

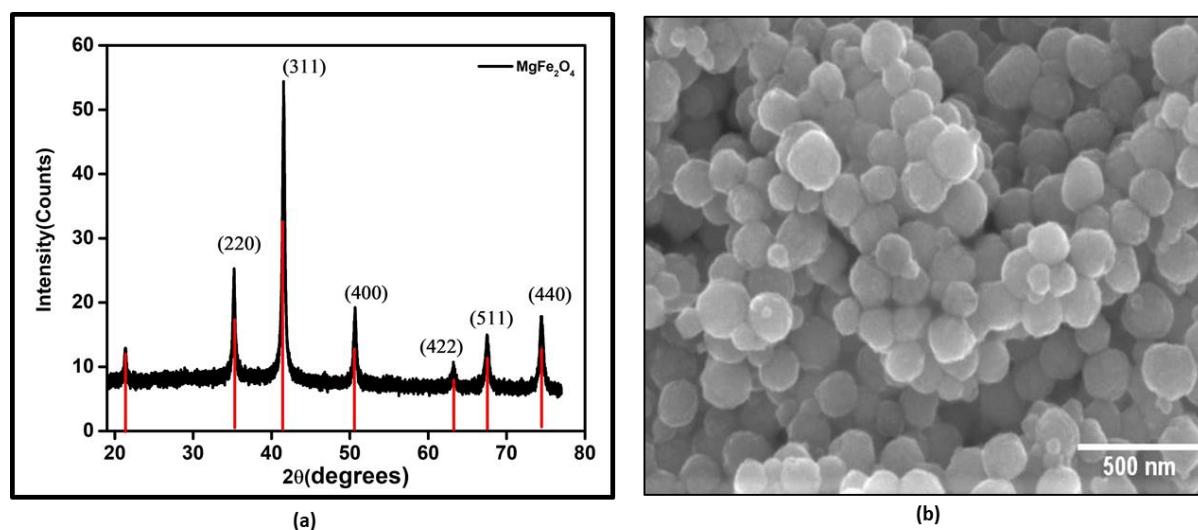


Figure S2: (a) XRD patterns for a cubic spinel $MgFe_2O_4$ phase that matches the standard powder diffraction data (ICSD #00-036-0398). (b) SEM images showing the spherical, uniform $MgFe_2O_4$ nanospheres.

Vibrating Sample Magnetometer:

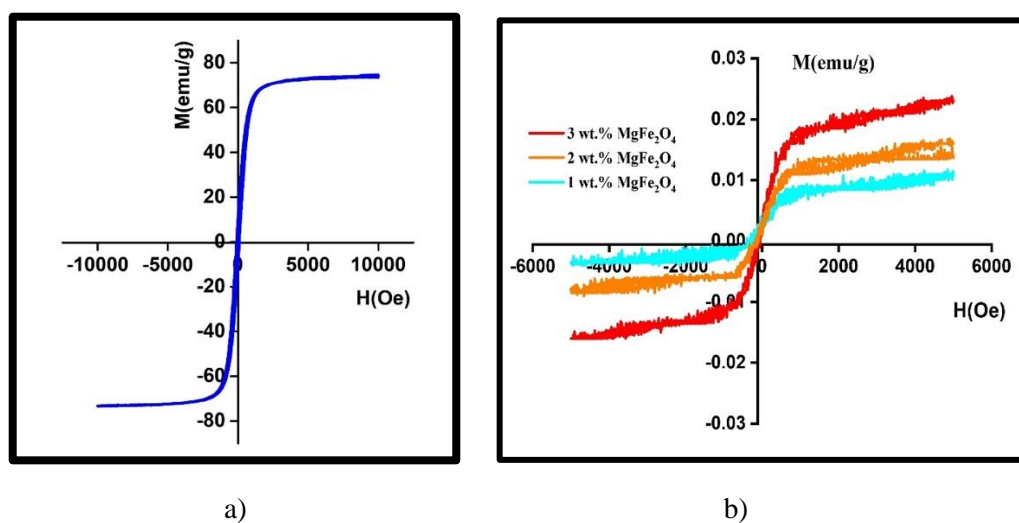


Figure S3: a) The magnetic hysteresis loops of bare $MgFe_2O_4$ showing a saturation magnetization of 65 emu/g and b) the magnetic hysteresis loops of the CuBTC- $MgFe_2O_4$ composites with varying magnetic contents.

The saturation magnetization (M_s), coercivity (H_c), and magnetization curves were studied on a vibrating sample magnetometer (VSM, RIKEN DENSHI) operated at room temperature. The samples are prepared by embedding the magnetic nanoparticles in an epoxy resin and hardener mix, and once it was all set, the measurements were carried out. The results of the $MgFe_2O_4$ nanospheres synthesised show a saturation magnetization of 65 emu/g. With MFCs, the saturation magnetization values were

Appendix B- Performance evaluation of CuBTC composites for room temperature Oxygen storage

higher for composites with higher concentrations of magnetic nanoparticles with 3 wt.% CuBTC-MgFe₂O₄ composite showing 0.025 emu/g.

Thermo-magneto gravimetric analysis

Curie point is a temperature at which magnetic materials undergo loss of their magnetic properties and become paramagnetic. This sharp change in magnetic properties is measured by measuring the samples' weight changes as a function of temperature. The Curie temperature of the MgFe₂O₄ nanoparticles was determined using the Thermo-magneto gravimetric analysis, which is a very efficient technique to ascertain the magnetic transitions in the nanoparticles. A weighed amount of MgFe₂O₄ nanoparticles were heated from room temperature to 800 °C in a nitrogen atmosphere using a heating rate of 40 °C/min, and the Curie temperature was found to be T_c=566 °C.

Specific Absorption Rate (SAR):

The rate at which the magnetic nanoparticles will absorb the magnetic energy and convert it into thermal energy can be predicted using a Specific adsorption rate (SAR). Apart from the diameter, shape, and composition of the nanoparticles, SAR is strongly governed by the frequency of the applied magnetic field. High SAR values are preferred because it means higher heating efficiency. Magnetic nanoparticles with higher SAR values are ideal for an efficient MISA process.

SAR is calculated by dispersing the particles in a liquid medium and the measuring:

$$SAR = C_s \frac{m_s}{m_m} \left(\frac{dT}{dt} \right)_{t=0}$$

Where C_s is the specific heat capacity of suspension, dT/dt at t =0 is the initial gradient of the heating curve, m_s, and m_m are the specific masses of the suspension and magnetic particles, respectively. The units of SAR are watts per kilogram (W/kg). The SAR of the synthesised MgFe₂O₄ nanoparticles was calculated using the temperature rise profile by dispersing 10 mg of the MgFe₂O₄ nanoparticles in 1ml of water and exposing it to a 25 mT magnetic field. As seen in figure S4-b, the temperature stabilised at 74 °C, and the SAR was calculated to be 130.6 W/g.

Temperature Rise Profile:

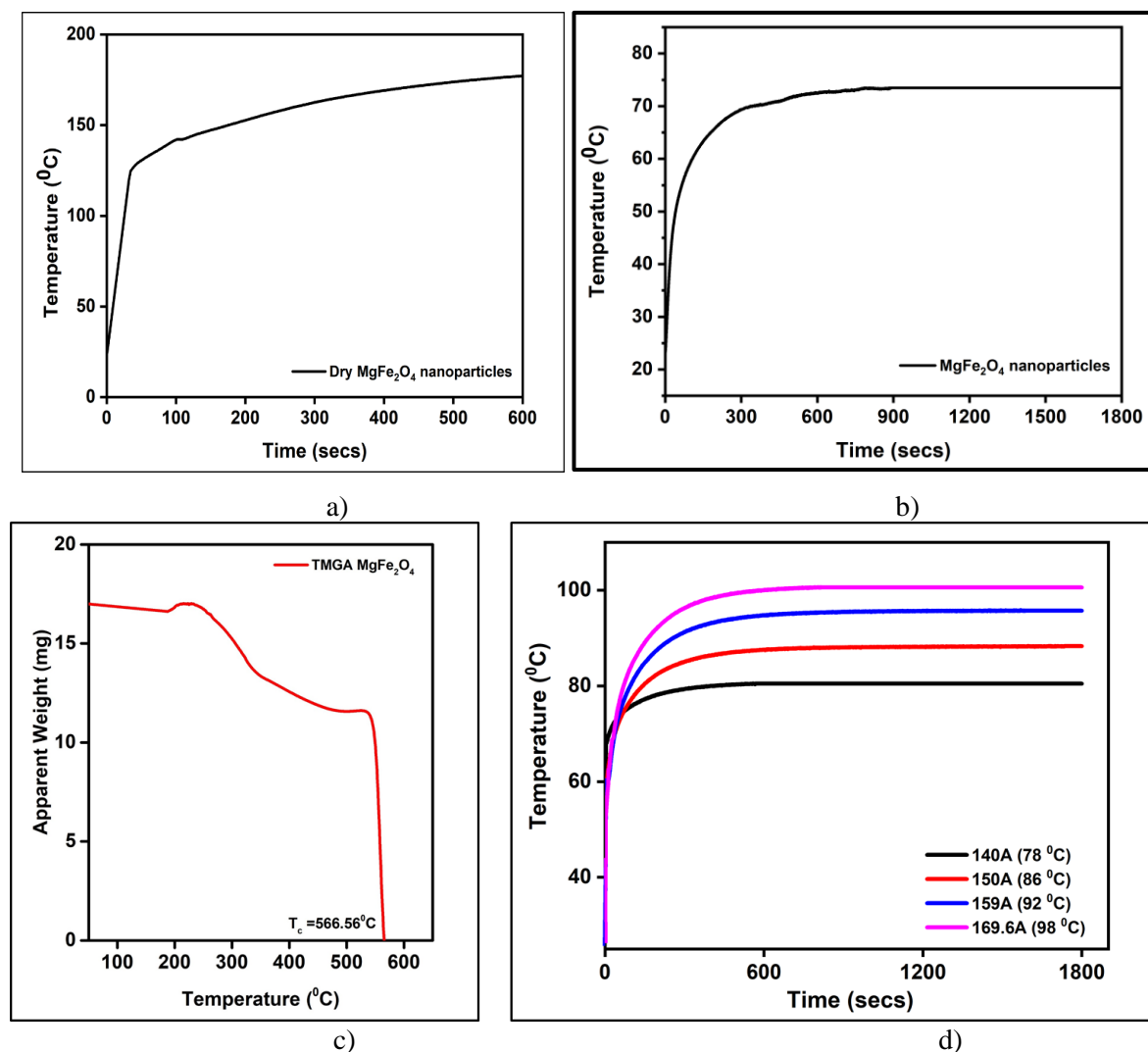


Figure S4: a) Temperature rise profile of dry MgFe₂O₄ nanoparticles, b): Temperature rise profile of 10 mg of the synthesised MgFe₂O₄ nanoparticles dispersed in 1 ml of water at 25 mT, c) The curie point of the MgFe₂O₄ was measured to be 566 °C using the thermo-magneto gravimetric analysis, d) Temperature rise attained by the 3 wt. % CuBTC-MgFe₂O₄ composites when exposed to varying magnetic fields.

To determine the maximum heating capacity of the MFC composites, the samples were placed in a dewar flask and exposed to varying magnetic fields, and their responsive temperature rise profile was measured for the next 30 mins. After the initial rise in temperatures, depending on the magnetic content in the samples and the magnetic field strength, the samples stabilise at a particular temperature. This highlights the maximum heating ability of the nanoparticles or composites at that particular magnetic

Appendix B- Performance evaluation of CuBTC composites for room temperature Oxygen storage

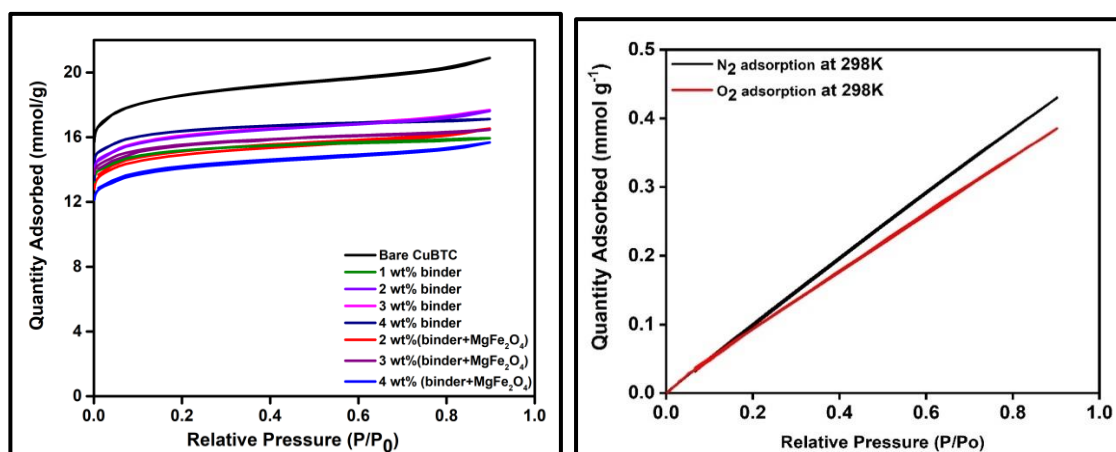
field. This works as a controller and helps determine the strength of the magnetic field to be applied for a particular sample for the given application.

Current through the coil, A	Magnetic Field Strength, mT	Temperature °C
140	25	78
150	31	86
160	33	92

A current of 150 A through the induction coil generates a magnetic field of 31 mT and heats the composite to around 86 °C, and with a current of 160 A, a magnetic field of 33 mT is generated. The temperature rise attained due to it is around 92 °C. In the current experiment, these are the two magnetic fields that trigger the release of oxygen molecules from the 3 wt. % CuBTC-MgFe₂O₄ composites.

Porosity and Surface Area Measurements:

Micrometric ASAP 2420 machine was used to measure the porosity and surface area properties of the sample. Initially, empty BET sample tubes were weighed, then they were filled with the CuBTC samples sealed with Transeals caps and then weighed again. The samples were heated under vacuum to 140 °C for 24 hrs and reweighed again to calculate the actual mass of the degassed samples. The sample tubes were then attached to the ASAP ports for N₂ studies at 77K temperatures. The effect of the addition of binders and effect of binders as well as the magnetic nanoparticles is studied using the N₂ uptake isotherms.



Appendix B- Performance evaluation of CuBTC composites for room temperature Oxygen storage

a)

b)

Figure S5: The BET surface area measurements of the composites by Nitrogen adsorption at 77 K, b) The Nitrogen and oxygen uptake by the 3 wt.% CuBTC-MgFe₂O₄ composite at 298 K.

Table S1. Summary of the BET surface areas of the CuBTC MOF before and after pelletising.

Sample	BET surface area (m ² /g)	Langmuir Surface Area: (m ² /g)
CuBTC MOF (powder form)	1495	1939
Pellets (1 wt.% binder)	1163	1505
Pellets (2 wt.% binder)	1228	1590
Pellets (3 wt.% binder)	1235	1600
Pellets (3 wt.% binder + 1 wt.% MgFe ₂ O ₄)	1143	1481
Pellets (3 wt.% binder + 2 wt.% MgFe ₂ O ₄)	1189	1539
Pellets 3 wt.% binder + 3 wt.% MgFe ₂ O ₄)	1080	1401

Moisture stability of CuBTC MOF and composite:

Appendix B- Performance evaluation of CuBTC composites for room temperature Oxygen storage

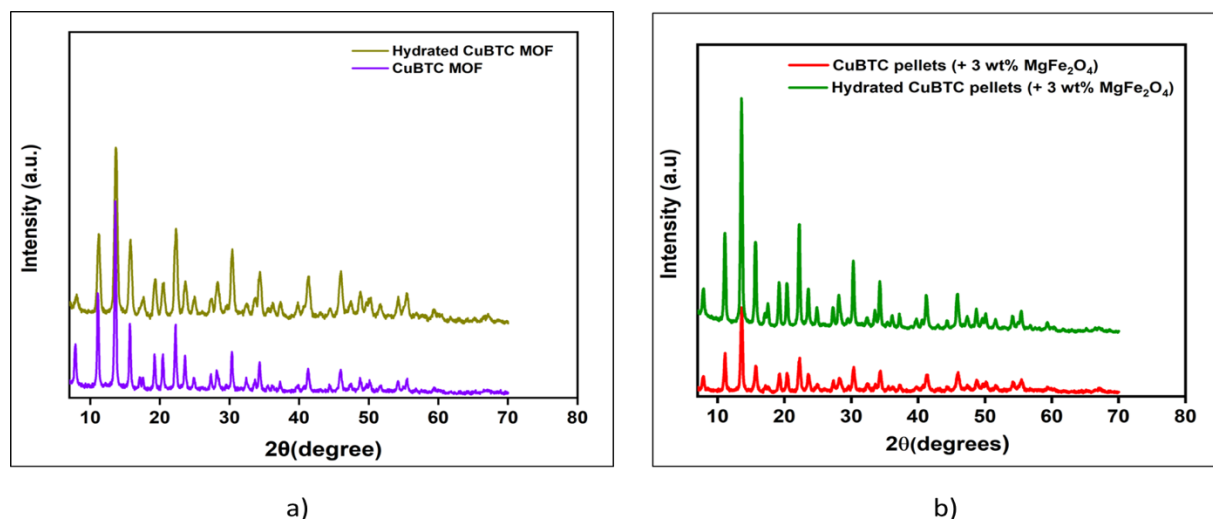


Figure S6: XRD patterns for a) CuBTC MOF and b) the 3 wt.% CuBTC-MgFe₂O₄ composite before and after water vapour adsorption at 298 K.

Thermal Stability and Atmospheric Stability of the composites:

Thermal stabilities of the samples were studied by thermal gravimetric analysis (TGA) using weighed samples that were heated from 25 °C to 800 °C using a heating rate of 10 °C min⁻¹. As observed in Figure S5-a), the TGA of bare as-synthesised CuBTC MOF, TGA of 3 wt.% CuBTC-MgFe₂O₄ composite pellets and TGA of the same sample after exposure of the environment for 30 days has been plotted. In all three samples, the two significant weight losses are observed, the first one corresponds to the evaporation of the solvent, and the second weight loss corresponds to the decomposition of MOF and or composites. Apart from the weight losses corresponding to the decomposition of the MOFs, the thermal stabilities of the CuBTC MOF and the 3 wt.% CuBTC-MgFe₂O₄ composites are very similar, indicating that the use of binders and the shaping procedure has not adversely affected its stability. As confirmed by other characterisation techniques, atmospheric exposure has reduced the thermal stability of the composite. The XRD of the exposed sample shows some peaks broadening corresponding to either the introduction of defects in the MOF framework or the slow degradation of the framework.

Appendix B- Performance evaluation of CuBTC composites for room temperature Oxygen storage

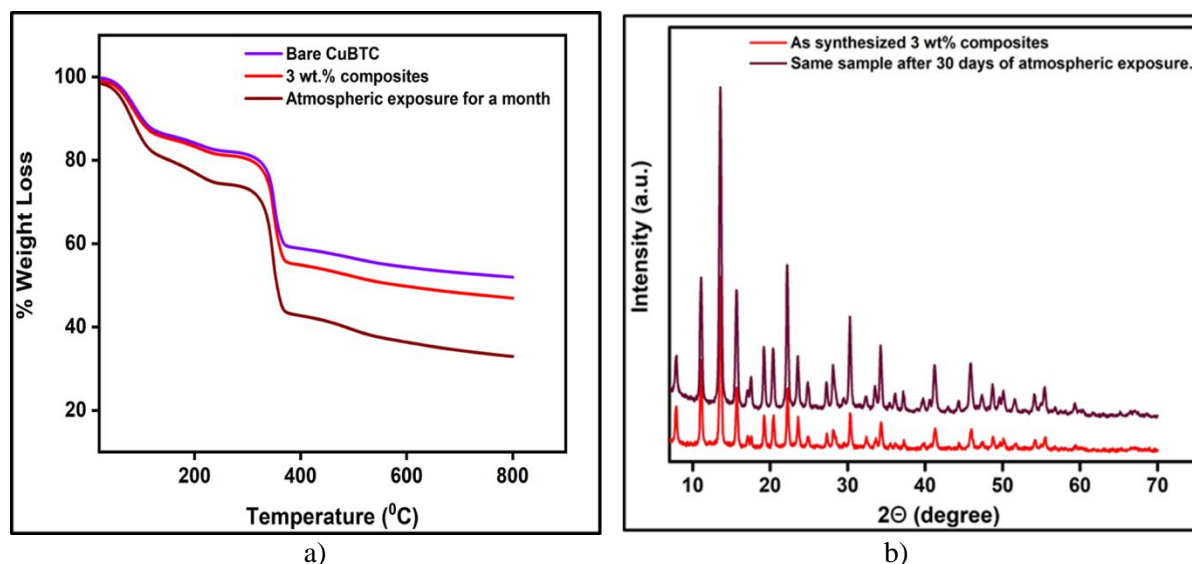


Figure S7: a) TGA analysis of the synthesised CuBTC MOF, the 3 wt.% CuBTC-MgFe₂O₄ composite, and the 3 wt.% CuBTC-MgFe₂O₄ composite after exposure to atmosphere for 30 days, b) XRD of the 3 wt.% CuBTC-MgFe₂O₄ composite before and after atmospheric exposure.

Isosteric Heat of Adsorption:

The isosteric heats of adsorption, Q_{st} , reveals the extent of interaction between the adsorbed molecules and the adsorbate under constant loading conditions. In the case of CuBTC MOF, this interaction that is dependant on the reactions at the exposed cationic Cu²⁺ sites and adsorption at the windows sites of the octahedral CuBTC cage is calculated to be -15.3 kJ mol⁻¹ (Figure S6-b). This near-constant Q_{st} curve was plotted using the adsorption data measured at 204 K, 273, and 298 K (Figure S6-a) and shows that irrespective of the low or loading conditions the binding energies remain the same.

Appendix B- Performance evaluation of CuBTC composites for room temperature Oxygen storage

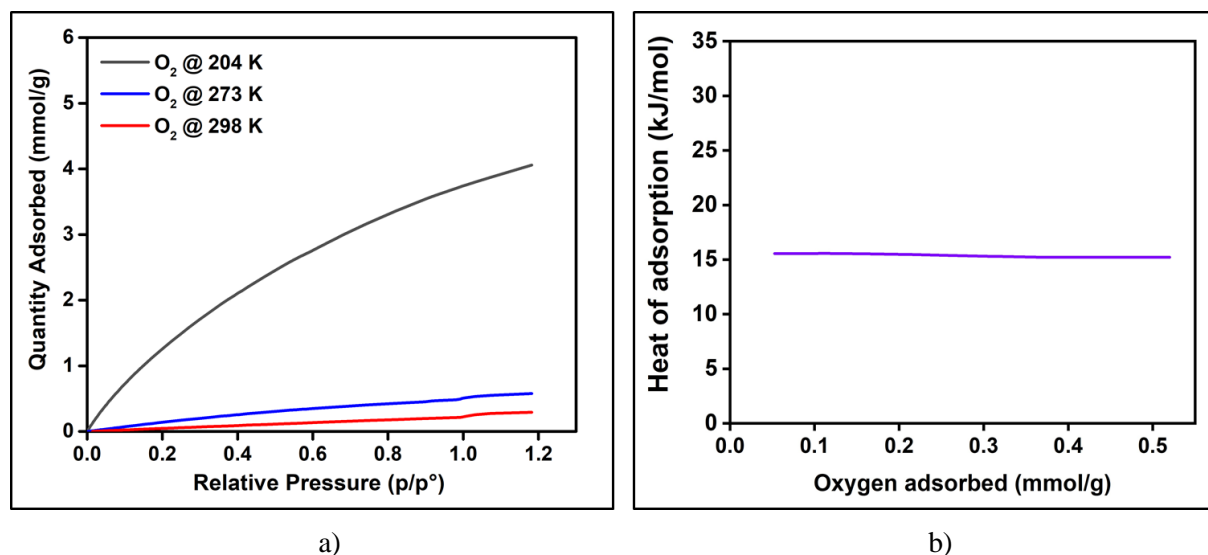


Figure S8: a) Oxygen adsorption isotherm of CuBTC MOF at 204 K, 273 K, and 298 K, b) The heat of adsorption curve, Q_{st} curve, plotted using the adsorption data measured at 204 K, 273 and 298 K.

Oxygen Adsorption Measurements & Triggered Release Experiments:

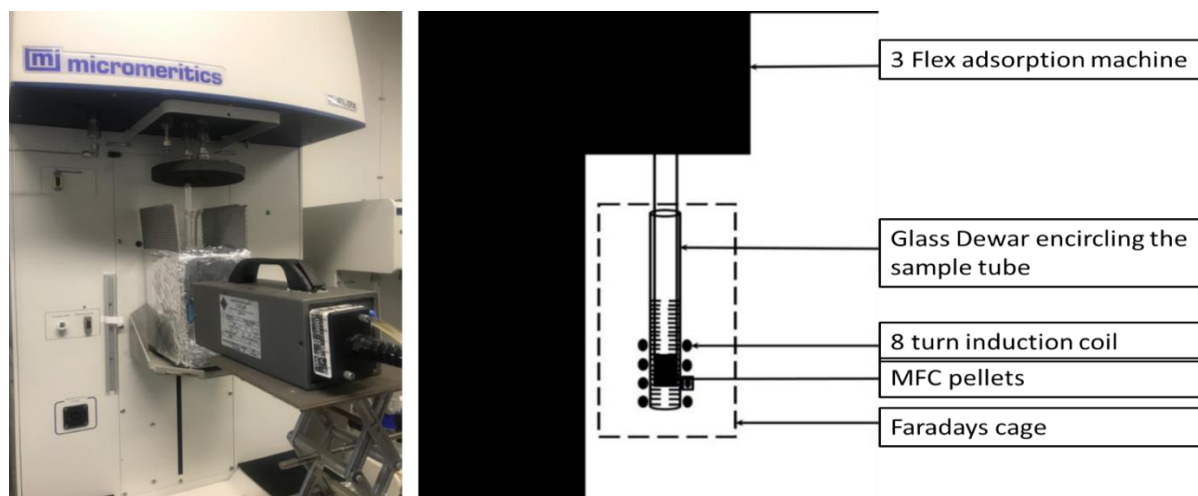


Figure S9: a) The setup for oxygen adsorption measurements consists of the 3Flex machine and the EASY HEAT Ambrell induction machine with an 8 turn coil that is strategically placed around the sample tube so that the sample is uniformly exposed to the magnetic field, b) the graphical representation of the triggered release experiments.

The oxygen adsorption studies were carried out on a Micromeritics 3Flex surface and catalyst characterisation instrument. The triggered release setup consisted of the activated and weighed CuBTC

Appendix B- Performance evaluation of CuBTC composites for room temperature Oxygen storage

pellets filled in a 3flex tube and attached to the 3flex machine while a slightly wider glass dewar encircled it.

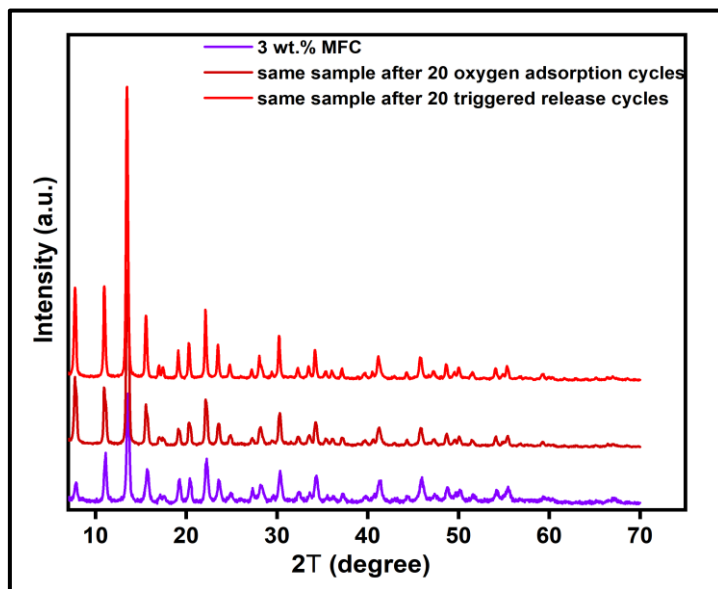


Figure S10: XRD patterns the 3 wt.% CuBTC-MgFe₂O₄ composite before and after 20 oxygen adsorption and triggered release cycles.

Regeneration Energy using the MISA process:

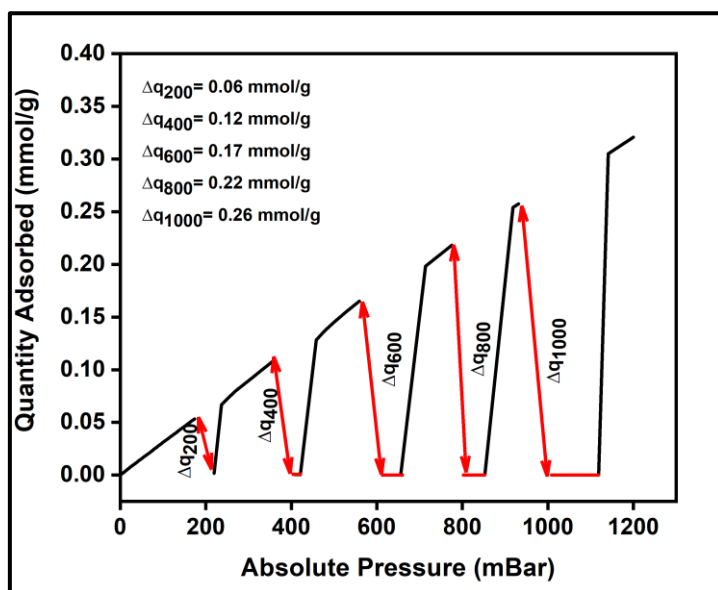


Figure S10: Working capacity is the difference in oxygen adsorbed under normal adsorption conditions, and the oxygen retained after desorption.

Appendix B- Performance evaluation of CuBTC composites for room temperature Oxygen storage

At this lab-scale setup, it is not possible to directly determine energy use for the process, but the energy calculations for the estimated regeneration energy ($Q_{thermal}$) of our composite per kilogram of O_2 captured can be calculated. Specific regeneration energy ($Q_{thermal}$) is reported as the sum of the energy required to heat the adsorbent to the desorption temperature, and the energy required to desorb bound gas species from the adsorbent, according to the equation:

$$Q_{thermal} = \frac{c_p m_{sorbent} \Delta T + (\Delta h_{O_2} \Delta q_{O_2})}{m_{O_2}}$$

Where,

C_p = specific heat capacity of adsorbent ($Jg^{-1}K^{-1}$)

$m_{sorbent}$ = mass of adsorbent (g)

ΔT = Temperature difference between adsorption and desorption conditions (K)

Δh = heat of adsorption ($kJmol^{-1}$)

Δq = working capacity, it can be defined as the difference between the O_2 loadings at adsorption and O_2 loadings at the end of desorption.

m_{O_2} = Mass of oxygen adsorbed at that pressure (g)

Applying this equation to the values in Table S2, the energy required to regenerate the amount of oxygen captured at 200 mbar, 400 bar, 800 mbar and 1000 mbar is calculated, and the values are:

Table S2: The estimated regenerative energy and power calculations for 0.6 gms of 3 wt.% CuBTC-MgFe₂O₄ composite pellets at 25mT, 31 mT, and 33mT.

Magnetic field Strength	25 (mT)					31(mT)					33(mT)				
	Regeneration Pressure (mBar)	200	400	600	800	1000	200	400	600	800	1000	200	400	600	800
Adsorption Temperature (°C)	25	25	25	25	25	25	25	25	25	25	25	25	25	25	25
Regeneration Temperature (°C)	86	86	86	86	86	92	92	92	92	92	96	96	96	96	96

Appendix B- Performance evaluation of CuBTC composites for room temperature Oxygen storage

Regeneration Time (s)	362	360	359	360	359	300	300	300	300	300	180	180	180	180	180
Amount of O ₂ desorbed (mmol/g)	0.04	0.10	0.14	0.19	0.23	0.06	0.12	0.17	0.22	0.26	0.06	0.12	0.17	0.22	0.26
Regeneration Energy (Q) (MJ/kg)	22.71	11.26	7.74	6.05	5.14	24.90	12.34	8.4	6.6	5.6	27.07	13.43	9.23	7.22	6.13
Energy Consumption (kWh/kg o ₂)	1.47	0.71	0.50	0.37	0.31	0.65	0.37	0.24	0.18	0.15	0.51	0.27	0.18	0.14	0.11

Table S3. The calculated energy required to regenerate the 3 wt.% CuBTC-MgFe₂O₄ composite pellets using magnetic fields of 25 mT, 31 mT, and 33 mT.

Absolute pressure (mBar)	Regeneration energy (MJ/kg)		
	25 mT magnetic field	31 mT magnetic field	33 mT magnetic field
200	22.7	24.9	27.1
400	11.2	12.3	13.4
600	7.7	8.4	9.2
800	6.0	6.6	7.2
1000	5.1	5.6	6.1

To establish the energy efficiency of the MISA process, power calculations were done using a power meter to measure the power required by the induction coil at varying magnetic fields of 25 mT, 31 mT, and 33 mT. To determine the power required to regenerate a weighed amount of sample, these calculations were done without exposing the samples to the magnetic fields and with samples being exposed to the magnetic fields (Figure S11-a). The power required was calculated from the output readings from the power meter, the time required for the samples to desorb all the adsorbed molecules,

Appendix B- Performance evaluation of CuBTC composites for room temperature Oxygen storage

and the mass of the desorbed molecules. Based on these calculations it was determined that using a magnetic field strength of 31 mT, that triggered a temperature rise of 86 °C in the 0.6gms of 3 wt.% CuBTC-MgFe₂O₄ composite, 0.65 kWh/kgO₂ power was consumed to desorb 0.3 mmol/g of adsorbed oxygen molecules. To understand how the weight of the sample influences the regeneration energies, using a magnetic field strength of 31 mT, the calculations were done using two samples weighing 0.33 gms and 0.64 gms each, and for 0.33 gms sample 5.1 MJ kg⁻¹ is required at 1000 mbar, and for 0.64 gms of the same sample, 5.6 MJ kg⁻¹ of energy is required at 1000 mbar(Figure S11-b).

Table- S4: Estimated energy required to regenerate 0.33gms and 0.6 gms of 3 wt.% CuBTC-MgFe₂O₄ composite pellets using magnetic fields of 31 mT.

Absolute pressure (mbar)	Regeneration energy (MJ/kg)	
	Using 31 mT magnetic field	
	0.33 gms	0.66 gms
200	22	24.9
400	11.2	12.34
600	7.7	8.4
800	5.8	6.6
1000	5.1	5.6

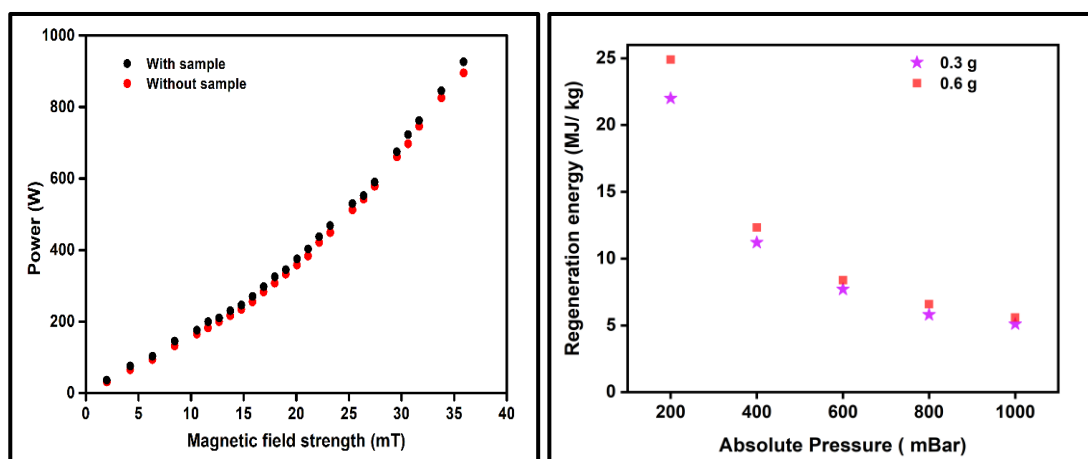


Figure S11: a) Power calculations done using the Magnetic induction setup for power consumed with and without the sample. b) To study the regeneration energy required for different amounts of samples, 0.3 gms of the sample, and 0.6 gms of samples.

Appendix B- Performance evaluation of CuBTC composites for room temperature Oxygen storage

References:

1. S. Bouson, A. Krittayavathananon, N. Phattharasupakun, P. Siwayaprahm and M. Sawangphruk, *R. Soc. Open Sci*, 2017, **4**, 170654.
2. S. Homayoonnia and S. Zeinali, *Sens. Actuators, B*, 2016, **237**, 776-786.
3. S. Maensiri, M. Sangmanee, and A. Wiengmoon, *Nanoscale Res. Lett*, 2009, **4**, 221.

Appendix C

Supporting Information for

The potential of bimetallic FeCo-MOF-74 for Oxygen adsorption at room temperature

Leena Melag,[†] M. Munir Sadiq,[†] Kristina Konstas,[‡] Kiyonori Suzuki,^{||} J. S. Garitaonandia,[†] and Matthew R. Hill,^{*†‡}

[†]Department of Chemical Engineering, Monash University, Clayton, VIC 3168, Australia

^{||}Department of Materials Science and Engineering, Monash University, Clayton, VIC 3168, Australia

[†]Department of Applied Physics II, Faculty of Science & Technology, University of the Basque Country UPV/EHU, Basque Country (Spain)

[‡]CSIRO, Private Bag 33, Clayton South MDC, VIC 3169, Australia

Appendix C- The potential of bimetallic FeCo-MOF-74 for Oxygen adsorption at room temperature

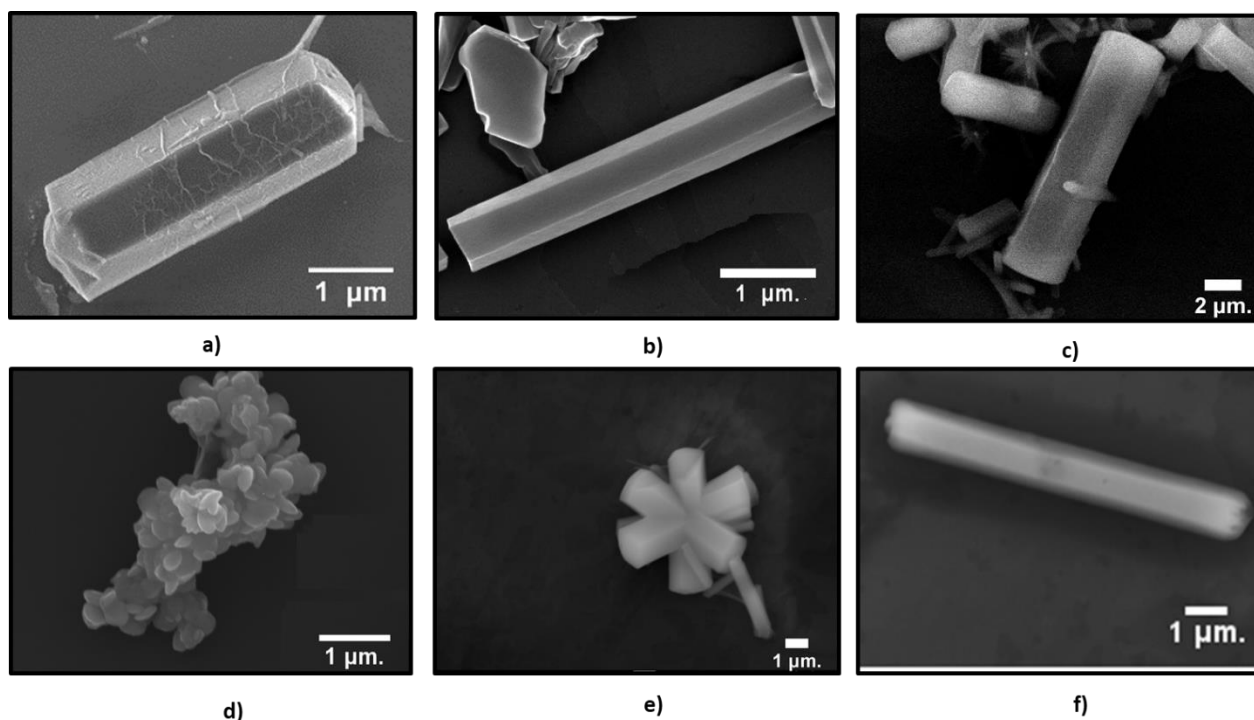


Figure S-1: The SEM images of the synthesised a) Co-MOF-74, b) Fe-MOF-74, c) and hexagonal bimetallic $Fe_{0.9}Co_{0.1}$ -MOF-74 nanorods, d) the spherical $Fe_{0.9}Co_{0.1}$ -MOF-74, and e) the $Fe_{0.5}Co_{0.5}$ -MOF-74, f) the $Fe_{0.1}Co_{0.9}$ -MOF-74.

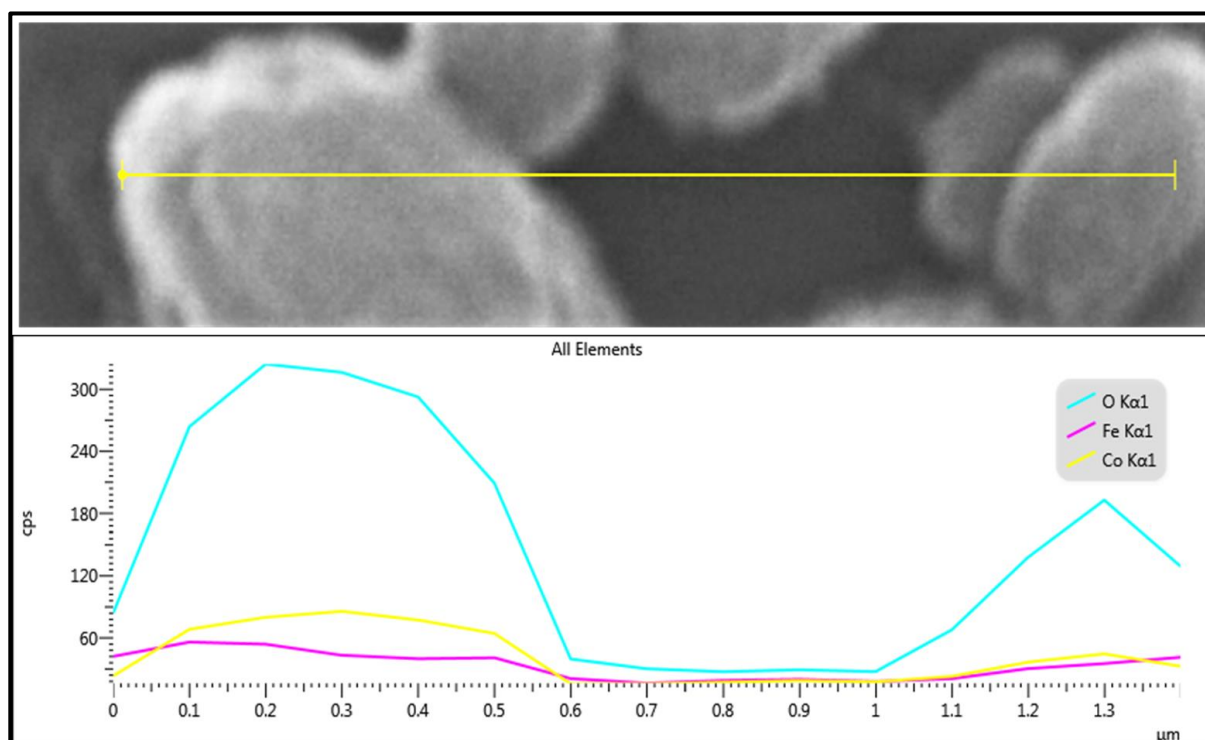


Figure S-2: The EDX line mapping of the spherical $Fe_{0.9}Co_{0.1}$ -MOF-74 confirms the presence of cobalt and iron in the MOF crystals.

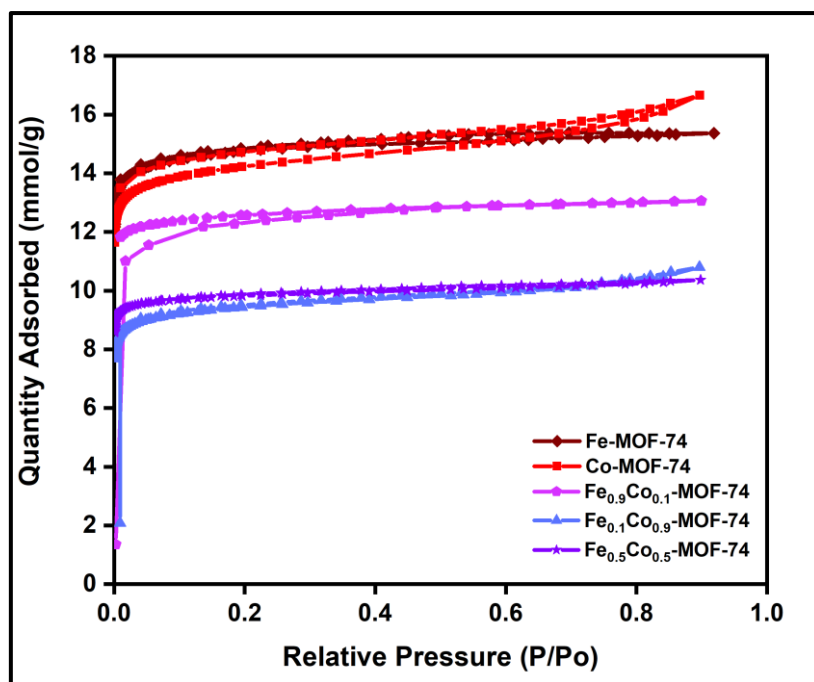


Figure S3: The nitrogen adsorption isotherms of the series of synthesised Fe-MOF-74, Co-MOF-74, and the bimetallic Fe_{0.9}Co_{0.1}-MOF-74, Fe_{0.5}Co_{0.5}-MOF-74, Fe_{0.1}Co_{0.9}-MOF-74 measured at 77 K.

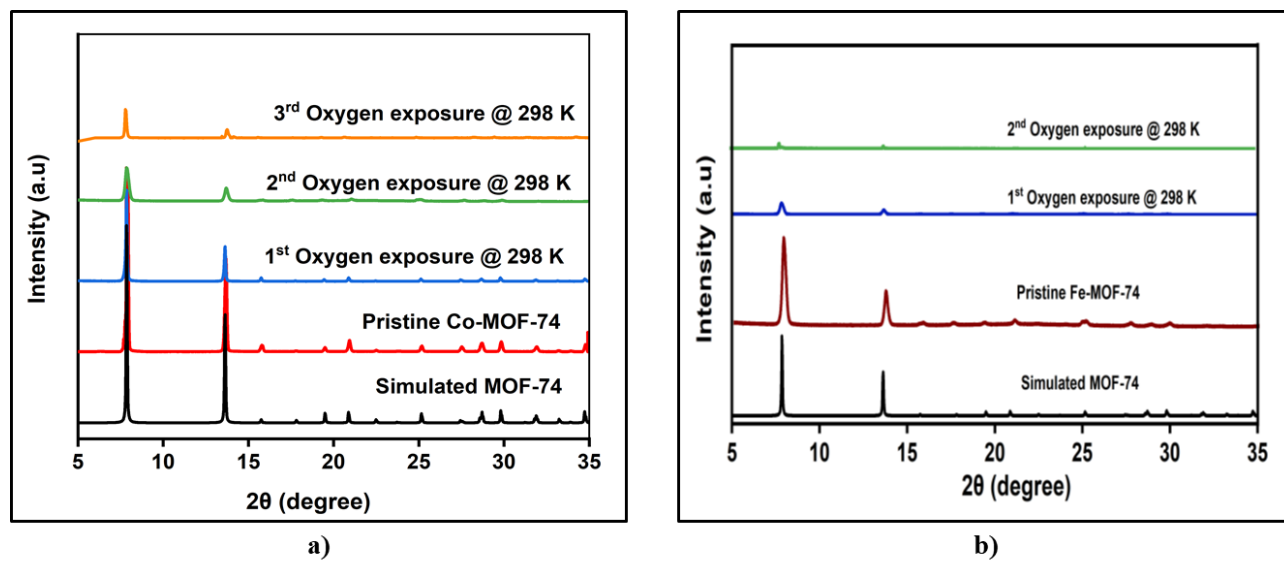


Figure S4: The XRD patterns of the a) Co-MOF-74 and b) Fe-MOF-74 before and after O₂ adsorption cycles at 298 K.

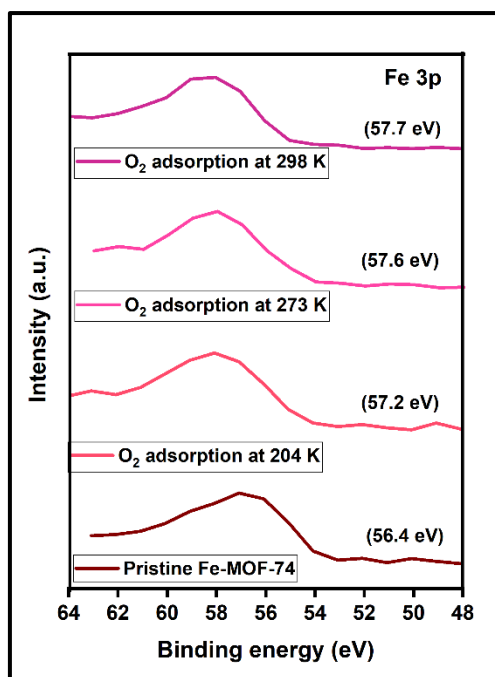


Figure S5: The XPS spectra of Fe 3p of Pristine Fe-MOF-74 before and after exposure to Oxygen at 204 K, 273 K and 298 K.

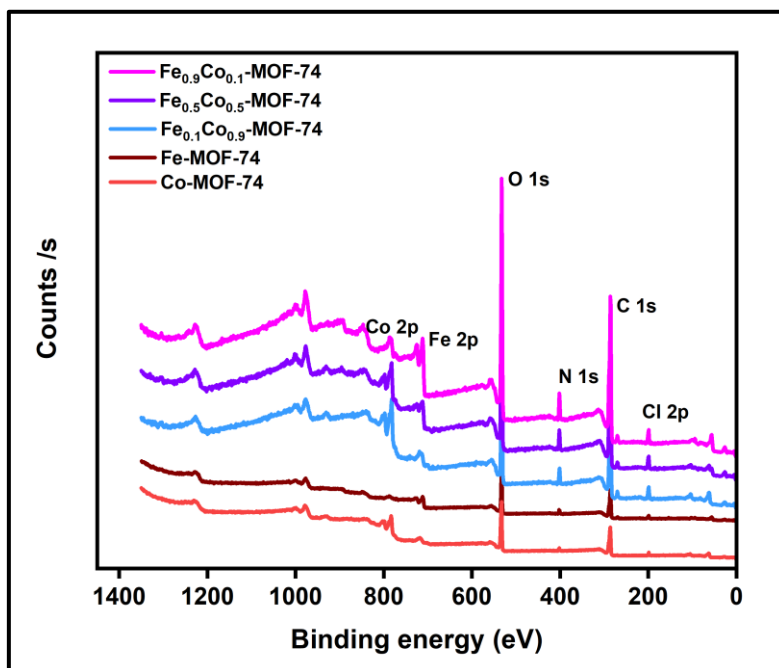


Figure S6: The survey spectrum of Co-MOF-74, Fe-MOF-74 and the bimetallic Fe_xCo_{1-x}-MOF-74s confirms the presence of Fe, Co, O, C and N.

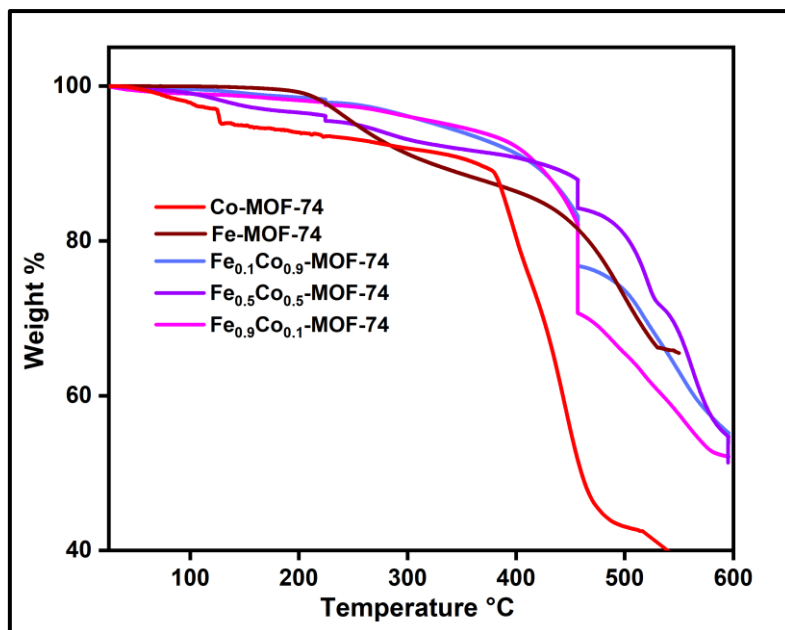


Figure S7: TGA of Co-MOF-74, Fe-MOF-74 and the bimetallic Fe_xCo_{1-x}-MOF-74s.

Appendix D

References

1. Pépin, J.-L.;Barjhoux, C. E.;Deschaux, C. and Brambilla, C.,*Long-term oxygen therapy at home: compliance with medical prescription and effective use of therapy*, Chest, 1996, **109**, 1144–1150.
2. Hardavella, G.;Karampinis, I.;Frille, A.;Sreter, K. and Rousalova, I.,*Oxygen devices and delivery systems*, Breathe, 2019, **15**, e108.
3. Thakur, N.;Blanc, P. D.;Julian, L. J.;Yelin, E. H.;Katz, P. P.;Sidney, S.;Iribarren, C. and Eisner, M. D.,*COPD and cognitive impairment: the role of hypoxemia and oxygen therapy*, Int J Chron Obstruct Pulmon Dis, 2010, **5**, 263.
4. Lynes, D. and Kelly, C.,*Long-term, ambulatory and short-burst oxygen therapy in the community*, Prim. Health Care, 2009, **19**, 40–46.
5. Baukal Jr, C. E., CRC press, 2010.
6. Skeen, S.;Yablonsky, G. and Axelbaum, R.,*Characteristics of non-premixed oxygen-enhanced combustion: I. The presence of appreciable oxygen at the location of maximum temperature*, Combust. Flame, 2009, **156**, 2145-2152.
7. Cui, Y.;Van der Lans, R. and Luyben, K. C. A.,*Effects of dissolved oxygen tension and mechanical forces on fungal morphology in submerged fermentation*, Biotechnol. Bioeng., 1998, **57**, 409-419.
8. Brahmhatt, S., *Journal*, 2010.
9. Englezos, V.;Cravero, F.;Torchio, F.;Rantsiou, K.;Ortiz-Julien, A.;Lambri, M.;Gerbi, V.;Rolle, L. and Cocolin, L.,*Oxygen availability and strain combination modulate yeast growth dynamics in mixed culture fermentations of grape must with Starmerella bacillaris and Saccharomyces cerevisiae*, Food Microbiol., 2018, **69**, 179-188.
10. Cekic, S.;Filik, H. and Apak, R.,*Simultaneous spectrophotometric determination of paracetamol and p-aminophenol in pharmaceutical products with tiron using dissolved oxygen as oxidant*, J. Anal. Chem., 2005, **60**, 1019-1023.
11. Gavriilidis, A.;Constantinou, A.;Hellgardt, K.;Hii, K. K. M.;Hutchings, G. J.;Brett, G. L.;Kuhn, S. and Marsden, S. P.,*Aerobic oxidations in flow: opportunities for the fine chemicals and pharmaceuticals industries*, React. Chem. Eng., 2016, **1**, 595-612.
12. Hone, C. A.;Roberge, D. M. and Kappe, C. O.,*The use of molecular oxygen in pharmaceutical manufacturing: is flow the way to go?*, ChemSusChem, 2017, **10**, 32-41.
13. Collivignarelli, M.;Bertanza, G.;Sordi, M. and Pedrazzani, R.,*High-strength wastewater treatment in a pure oxygen thermophilic process: 11-year operation and monitoring of different plant configurations*, Water Sci. Technol., 2015, **71**, 588-596.
14. Kumar, K. V.;Gadipelli, S.;Wood, B.;Ramisetty, K. A.;Stewart, A. A.;Howard, C. A.;Brett, D. J. L. and Rodriguez-Reinoso, F.,*Characterization of the adsorption site energies and heterogeneous surfaces of porous materials*, J. Mater. Chem. A, 2019, **7**, 10104–10137.
15. Han, I.-S. and Chung, C.-B.,*Performance prediction and analysis of a PEM fuel cell operating on pure oxygen using data-driven models: A comparison of artificial neural network and support vector machine*, Int. J. Hydrogen Energy, 2016, **41**, 10202-10211.
16. Nemitallah, M. A.;Habib, M. A.;Badr, H. M.;Said, S. A.;Jamal, A.;Ben-Mansour, R.;Mokheimer, E. M. and Mezghani, K.,*Oxy-fuel combustion technology: current status, applications, and trends*, Int. J. Energy Res., 2017, **41**, 1670-1708.
17. Sengodan, S.;Lan, R.;Humphreys, J.;Du, D.;Xu, W.;Wang, H. and Tao, S.,*Advances in reforming and partial oxidation of hydrocarbons for hydrogen production and fuel cell applications*, Renew. Sust. Energ. Rev., 2018, **82**, 761-780.
18. Smith, A. and Klosek, J.,*A review of air separation technologies and their integration with energy conversion processes*, Fuel Process. Technol., 2001, **70**, 115–134.

19. Van der Ham, L. and Kjelstrup, S., *Exergy analysis of two cryogenic air separation processes*, Energy, 2010, **35**, 4731–4739.
20. Murali, R. S.;Sankarshana, T. and Sridhar, S., *Air Separation by Polymer-based Membrane Technology*, Sep. Purif. Rev, 2013, **42**, 130–186.
21. Nagar, H.;Vadthya, P.;Prasad, N. S. and Sridhar, S., *Air separation by facilitated transport of oxygen through a Pebax membrane incorporated with a cobalt complex*, RSC Adv., 2015, **5**, 76190–76201.
22. Watanabe, K.;Austin, N. and Stapleton, M. R., *Investigation of the Air Separation Properties of Zeolites Types A, X and Y by Monte Carlo Simulations*, Mol Simul, 1995, **15**, 197–221.
23. Cavenati, S.;Grande, C. A. and Rodrigues, A. E., *Adsorption equilibrium of methane, carbon dioxide, and nitrogen on zeolite 13X at high pressures*, J. Chem. Eng. Data, 2004, **49**, 1095–1101.
24. Santos, J.;Magalhaes, F. and Mendes, A., *Contamination of zeolites used in oxygen production by PSA: effects of water and carbon dioxide*, Ind. Eng. Chem. Res., 2008, **47**, 6197–6203.
25. Morris, R. E. and Wheatley, P. S., *Gas Storage in Nanoporous Materials*, Angew. Chem. Int. Ed., 2008, **47**, 4966–4981.
26. Gulcay, E. and Erucar, I., *Biocompatible MOFs for Storage and Separation of O₂: A Molecular Simulation Study*, Ind. Eng. Chem. Res., 2019, **58**, 3225–3237.
27. Demir, H.;Stoneburner, S. J.;Jeong, W.;Ray, D.;Zhang, X.;Farha, O. K.;Cramer, C. J.;Siepmann, J. I. and Gagliardi, L., *Metal–Organic Frameworks with Metal–Catecholates for O₂/N₂ Separation*, J. Phys. Chem. C, 2019, **123**, 12935–12946.
28. Moghadam, P. Z.;Islamoglu, T.;Goswami, S.;Exley, J.;Fantham, M.;Kaminski, C. F.;Snurr, R. Q.;Farha, O. K. and Fairen-Jimenez, D., *Computer-aided discovery of a metal–organic framework with superior oxygen uptake*, Nat. Commun., 2018, **9**, 1378.
29. Weston, M. H., *Metal-organic frameworks for oxygen storage and air separation*, U.S. Patent 20150105250, April 16, 2015.
30. Eddaoudi, M.;Moler, D. B.;Li, H.;Chen, B.;Reineke, T. M.;O’Keeffe, M. and Yaghi, O. M., *Modular Chemistry: Secondary Building Units as a Basis for the Design of Highly Porous and Robust Metal–Organic Carboxylate Frameworks*, Acc. Chem. Res., 2001, **34**, 319–330.
31. Howarth, A. J.;Peters, A. W.;Vermeulen, N. A.;Wang, T. C.;Hupp, J. T. and Farha, O. K., *Best Practices for the Synthesis, Activation, and Characterization of Metal–Organic Frameworks*, Chem. Mater., 2017, **29**, 26–39.
32. Yaghi, O. M. and Li, Q., *Reticular Chemistry and Metal-Organic Frameworks for Clean Energy*, MRS Bull., 2011, **34**, 682–690.
33. Mendes, R. F. and Almeida Paz, F. A., *Transforming metal-organic frameworks into functional materials*, Inorg. Chem. Front, 2015, **2**, 495–509.
34. Yaghi, O. M. L., Guangming;Li, Hailian, *Selective binding and removal of guests in a microporous metal-organic framework*, Nature, 1995, **378**, 703.
35. Sumida, K.;Rogow, D. L.;Mason, J. A.;McDonald, T. M.;Bloch, E. D.;Herm, Z. R.;Bae, T.-H. and Long, J. R., *Carbon Dioxide Capture in Metal–Organic Frameworks*, Chem. Rev., 2012, **112**, 724–781.
36. Bae, Y.-S.;Spokoyny, A. M.;Farha, O. K.;Snurr, R. Q.;Hupp, J. T. and Mirkin, C. A., *Separation of gas mixtures using Co(ii) carborane-based porous coordination polymers*, Chem. Commun., 2010, **46**, 3478–3480.
37. Grant Glover, T.;Peterson, G. W.;Schindler, B. J.;Britt, D. and Yaghi, O., *MOF-74 building unit has a direct impact on toxic gas adsorption*, Chem. Eng. Sci., 2011, **66**, 163–170.
38. Britt, D.;Furukawa, H.;Wang, B.;Glover, T. G. and Yaghi, O. M., *Highly efficient separation of carbon dioxide by a metal-organic framework replete with open metal sites*, PNAS, 2009, **106**, 20637–20640.
39. Guo, Z.;Wu, H.;Srinivas, G.;Zhou, Y.;Xiang, S.;Chen, Z.;Yang, Y.;Zhou, W.;O’Keeffe, M. and Chen, B., *A metal–organic framework with optimized open metal sites and pore spaces for high methane storage at room temperature*, Angew. Chem. Int. Ed., 2011, **50**, 3178–3181.
40. Kapelewski, M. T.;Geier, S. J.;Hudson, M. R.;Stück, D.;Mason, J. A.;Nelson, J. N.;Xiao, D. J.;Hulvey, Z.;Gilmour, E.;FitzGerald, S. A.;Head-Gordon, M.;Brown, C. M. and Long, J.

- R., *M₂(m-dobdc) (M = Mg, Mn, Fe, Co, Ni) Metal–Organic Frameworks Exhibiting Increased Charge Density and Enhanced H₂ Binding at the Open Metal Sites*, *J. Am. Chem. Soc.*, 2014, **136**, 12119–12129.
41. Zhou, W.;Wu, H. and Yildirim, T.,*Enhanced H₂ Adsorption in Isostructural Metal–Organic Frameworks with Open Metal Sites: Strong Dependence of the Binding Strength on Metal Ions*, *J. Am. Chem. Soc.*, 2008, **130**, 15268–15269.
 42. Connolly, B. M.;Aragones-Anglada, M.;Gandara-Loe, J.;Danaf, N. A.;Lamb, D. C.;Mehta, J. P.;Vulpe, D.;Wuttke, S.;Silvestre-Albero, J.;Moghadam, P. Z.;Wheatley, A. E. H. and Fairen-Jimenez, D.,*Tuning porosity in macroscopic monolithic metal-organic frameworks for exceptional natural gas storage*, *Nat. Commun.*, 2019, **10**, 2345.
 43. Ahmed, I. and Jhung, S. H.,*Composites of metal–organic frameworks: Preparation and application in adsorption*, *Mater. Today*, 2014, **17**, 136–146.
 44. Villajos, J. A.;Jagorel, N.;Reinsch, S. and Emmerling, F. L.,*Increasing exposed metal site accessibility in a Co-MOF-74 material with induced structure-defects*, *Front. Mater.*, 2019, **6**, 230.
 45. Vitillo, J. G.;Regli, L.;Chavan, S.;Ricchiardi, G.;Spoto, G.;Dietzel, P. D.;Bordiga, S. and Zecchina, A.,*Role of exposed metal sites in hydrogen storage in MOFs*, *J. Am. Chem. Soc.*, 2008, **130**, 8386–8396.
 46. Díaz-García, M.;Mayoral, Á.;Díaz, I. and Sánchez-Sánchez, M.,*Nanoscaled M-MOF-74 Materials Prepared at Room Temperature*, *Cryst. Growth Des.*, 2014, **14**, 2479–2487.
 47. Moeljadi, A. M. P.;Schmid, R. and Hirao, H.,*Dioxygen binding to Fe-MOF-74: microscopic insights from periodic QM/MM calculations*, *Can. J. Chem.*, 2016, **94**, 1144–1150.
 48. Parkes, M. V.;Sava Gallis, D. F.;Greathouse, J. A. and Nenoff, T. M.,*Effect of metal in M₃ (btc) 2 and M₂ (dobdc) MOFs for O₂/N₂ separations: A combined density functional theory and experimental study*, *J. Phys. Chem. C*, 2015, **119**, 6556–6567.
 49. Bloch, E. D.;Murray, L. J.;Queen, W. L.;Chavan, S.;Maximoff, S. N.;Bigi, J. P.;Krishna, R.;Peterson, V. K.;Grandjean, F.;Long, G. J.;Smit, B.;Bordiga, S.;Brown, C. M. and Long, J. R.,*Selective Binding of O₂ over N₂ in a Redox–Active Metal–Organic Framework with Open Iron(II) Coordination Sites*, *J. Am. Chem. Soc.*, 2011, **133**, 14814–14822.
 50. Li, J.-R.;Kuppler, R. J. and Zhou, H.-C.,*Selective gas adsorption and separation in metal–organic frameworks*, *Chem. Sov. Rev.*, 2009, **38**, 1477–1504.
 51. Zhang, W.;Banerjee, D.;Liu, J.;Schaef, H. T.;Crum, J. V.;Fernandez, C. A.;Kukkadapu, R. K.;Nie, Z.;Nune, S. K. and Motkuri, R. K.,*Redox-Active Metal–Organic Composites for Highly Selective Oxygen Separation Applications*, *Adv. Mater.*, 2016, **28**, 3572–3577.
 52. Xiao, D. J.;Gonzalez, M. I.;Darago, L. E.;Vogiatzis, K. D.;Haldoupis, E.;Gagliardi, L. and Long, J. R.,*Selective, Tunable O₂ Binding in Cobalt(II)–Triazolate/Pyrazolate Metal–Organic Frameworks*, *J. Am. Chem. So.*, 2016, **138**, 7161–7170.
 53. Sugimoto, H.;Nagayama, T.;Maruyama, S.;Fujinami, S.;Yasuda, Y.;Suzuki, M. and Uehara, A.,*Thermodynamic study on dioxygen binding of diiron (II) and dicobalt (II) complexes containing various dinucleating ligands*, *Bull. Chem. Soc. Jpn.*, 1998, **71**, 2267–2279.
 54. Sladekova, K.;Campbell, C.;Grant, C.;Fletcher, A. J.;Gomes, J. R. B. and Jorge, M.,*The effect of atomic point charges on adsorption isotherms of CO₂ and water in metal organic frameworks*, *Adsorption*, 2020, **26**, 663–685.
 55. Melag, L.;Sadiq, M. M.;Smith, S. J. D.;Konstas, K.;Suzuki, K. and Hill, M. R.,*Efficient delivery of oxygen via magnetic framework composites*, *J. Mater. Chem. A*, 2019, **7**, 3790–3796.
 56. Xu, W.;Tu, B.;Liu, Q.;Shu, Y.;Liang, C.-C.;Diercks, C. S.;Yaghi, O. M.;Zhang, Y.-B.;Deng, H. and Li, Q.,*Anisotropic reticular chemistry*, *Nature Reviews Materials*, 2020, **5**, 764–779.
 57. DeCoste, J. B.;Weston, M. H.;Fuller, P. E.;Tovar, T. M.;Peterson, G. W.;LeVan, M. D. and Farha, O. K.,*Metal–organic frameworks for oxygen storage*, *Angew. Chem. Int. Ed.*, 2014, **53**, 14092–14095.
 58. Al-Janabi, N.;Hill, P.;Torrente-Murciano, L.;Garforth, A.;Gorgojo, P.;Siperstein, F. and Fan, X.,*Mapping the Cu-BTC metal–organic framework (HKUST-1) stability envelope in the presence of water vapour for CO₂ adsorption from flue gases*, *Chem. Eng. J.*, 2015, **281**, 669–677.

59. Vishnyakov, A.;Ravikovitch, P. I.;Neimark, A. V.;Bülow, M. and Wang, Q. M.,*Nanopore structure and sorption properties of Cu– BTC metal– organic framework*, Nano Lett., 2003, **3**, 713–718.
60. Gutiérrez-Sevillano, J. J.;Vicent-Luna, J. M.;Dubbeldam, D. and Calero, S.,*Molecular Mechanisms for Adsorption in Cu-BTC Metal Organic Framework*, J. Phys. Chem. C, 2013, **117**, 11357–11366.
61. Kim, J.;Cho, H.-Y. and Ahn, W.-S.,*Synthesis and Adsorption/Catalytic Properties of the Metal Organic Framework CuBTC*, Catal. Surv. Asia, 2012, **16**, 106–119.
62. Lin, K.-S.;Adhikari, A. K.;Ku, C.-N.;Chiang, C.-L. and Kuo, H.,*Synthesis and characterization of porous HKUST-1 metal organic frameworks for hydrogen storage*, Int. J. Hydrog. Energy, 2012, **37**, 13865–13871.
63. Supronowicz, B.;Mavrandonakis, A. and Heine, T.,*Interaction of small gases with the unsaturated metal centers of the HKUST-1 metal organic framework*, J. Phys. Chem. C, 2013, **117**, 14570–14578.
64. Majchrzak-Kuceba, I. and Bukalak-Gaik, D.,*Regeneration performance of metal–organic frameworks*, J. Therm. Anal. Calorim., 2016, **125**, 1461-1466.
65. Hayashi, S.;Kawai, M. and Kaneko, T.,*Dynamics of high purity oxygen PSA*, Gas Sep. Purif., 1996, **10**, 19–23.
66. Ma, M.;Zhang, Y.;Shen, X.;Xie, J.;Li, Y. and Gu, N.,*Targeted inductive heating of nanomagnets by a combination of alternating current (AC) and static magnetic fields*, Nano Res., 2015, **8**, 600–610.
67. Kolhatkar, A.;Jamison, A.;Litvinov, D.;Willson, R. and Lee, T.,*Tuning the Magnetic Properties of Nanoparticles*, Int. J. Mol, 2013, **14**, 15977.
68. Rudolf, H.;Silvio, D.;Robert, M. and Matthias, Z.,*Magnetic particle hyperthermia: nanoparticle magnetism and materials development for cancer therapy*, J. Phys. Condens. Matter, 2006, **18**, S2919.
69. Doherty, C. M.;Buso, D.;Hill, A. J.;Furukawa, S.;Kitagawa, S. and Falcaro, P.,*Using functional nano- and microparticles for the preparation of metal–organic framework composites with novel properties*, Acc. Chem. Res., 2013, **47**, 396–405.
70. Ricco, R.;Malfatti, L.;Takahashi, M.;Hill, A. J. and Falcaro, P.,*Applications of magnetic metal–organic framework composites*, J. Mater. Chem. A, 2013, **1**, 13033–13045.
71. Doherty, C. M.;Buso, D.;Hill, A. J.;Furukawa, S.;Kitagawa, S. and Falcaro, P.,*Using functional nano- and microparticles for the preparation of metal-organic framework composites with novel properties*, Acc. Chem. Res., 2014, **47**, 396-405.
72. Falcaro, P.;Lapierre, F.;Marmioli, B.;Styles, M.;Zhu, Y.;Takahashi, M.;Hill, A. J. and Doherty, C. M.,*Positioning an individual metal–organic framework particle using a magnetic field*, J Mater Chem C, 2013, **1**, 42–45.
73. Zhao, X.;Liu, S.;Tang, Z.;Niu, H.;Cai, Y.;Meng, W.;Wu, F. and Giesy, J. P.,*Synthesis of magnetic metal-organic framework (MOF) for efficient removal of organic dyes from water*, Sci. Rep., 2015, **5**, 11849.
74. Sadiq, M. M.;Li, H.;Hill, A. J.;Falcaro, P.;Hill, M. R. and Suzuki, K.,*Magnetic Induction Swing Adsorption: An Energy Efficient Route to Porous Adsorbent Regeneration*, Chem. Mater., 2016, **28**, 6219–6226.
75. Li, H.;Sadiq, M. M.;Suzuki, K.;Ricco, R.;Doblin, C.;Hill, A. J.;Lim, S.;Falcaro, P. and Hill, M. R.,*Magnetic Metal–Organic Frameworks for Efficient Carbon Dioxide Capture and Remote Trigger Release*, Adv. Mater., 2016, **28**, 1839–1844.
76. Li, H.;Sadiq, M. M.;Suzuki, K.;Doblin, C.;Lim, S.;Falcaro, P.;Hill, A. J. and Hill, M. R.,*MaLISA—a cooperative method to release adsorbed gases from metal–organic frameworks*, J. Mater. Chem. A, 2016, **4**, 18757–18762.
77. Bloch, E. D.;Queen, W. L.;Hudson, M. R.;Mason, J. A.;Xiao, D. J.;Murray, L. J.;Flacau, R.;Brown, C. M. and Long, J. R.,*Hydrogen Storage and Selective, Reversible O₂ Adsorption in a Metal–Organic Framework with Open Chromium(II) Sites*, Angew. Chem. Int. Ed, 2016, **55**, 8605–8609.

78. Xiao, D. J.;Gonzalez, M. I.;Darago, L. E.;Vogiatzis, K. D.;Haldoupis, E.;Gagliardi, L. and Long, J. R.,*Selective, tunable O₂ binding in cobalt (II)–triazolate/pyrazolate metal–organic frameworks*, J. Am. Chem. Soc, 2016, **138**, 7161–7170.
79. Murray, L. J.;Dinca, M.;Yano, J.;Chavan, S.;Bordiga, S.;Brown, C. M. and Long, J. R.,*Highly-selective and reversible O₂ binding in Cr³⁺ (1, 3, 5-benzenetricarboxylate) 2*, J. Am. Chem. Soc., 2010, **132**, 7856–7857.
80. Huang, B. L.;McGaughey, A. J. H. and Kaviani, M.,*Thermal conductivity of metal-organic framework 5 (MOF-5): Part I. Molecular dynamics simulations*, Int. J. Heat Mass Transfer, 2007, **50**, 393-404.
81. Huang, B. L.;Ni, Z.;Millward, A.;McGaughey, A. J. H.;Uher, C.;Kaviani, M. and Yaghi, O.,*Thermal conductivity of a metal-organic framework (MOF-5): Part II. Measurement*, Int. J. Heat Mass Transfer, 2007, **50**, 405-411.
82. Zhang, X. and Jiang, J.,*Thermal Conductivity of Zeolitic Imidazolate Framework-8: A Molecular Simulation Study*, J. Phys. Chem. C, 2013, **117**, 18441-18447.
83. Babaei, H.;DeCoster, M. E.;Jeong, M.;Hassan, Z. M.;Islamoglu, T.;Baumgart, H.;McGaughey, A. J. H.;Redel, E.;Farha, O. K.;Hopkins, P. E.;Malen, J. A. and Wilmer, C. E.,*Observation of reduced thermal conductivity in a metal-organic framework due to the presence of adsorbates*, Nat. Commun., 2020, **11**, 4010.
84. Sun, L.;Liao, B.;Sheberla, D.;Kraemer, D.;Zhou, J.;Stach, E. A.;Zakharov, D.;Stavila, V.;Talin, A. A. and Ge, Y.,*A microporous and naturally nanostructured thermoelectric metal-organic framework with ultralow thermal conductivity*, Joule, 2017, **1**, 168-177.
85. Sadiq, M. M.;Suzuki, K. and Hill, M. R.,*Towards energy efficient separations with metal organic frameworks*, Chem. Commun., 2018, **54**, 2825–2837.
86. Sadiq, M. M.;Rubio-Martinez, M.;Zadehahmadi, F.;Suzuki, K. and Hill, M. R.,*Magnetic Framework Composites for Low Concentration Methane Capture*, Ind. Eng. Chem. Res., 2018, **57**, 6040-6047.
87. Falcaro, P.;Ricco, R.;Yazdi, A.;Imaz, I.;Furukawa, S.;MasPOCH, D.;Ameloot, R.;Evans, J. D. and Doonan, C. J.,*Application of metal and metal oxide nanoparticles@MOFs*, Coord. Chem. Rev., 2016, **307**, 237–254.
88. Ke, F.;Yuan, Y.-P.;Qiu, L.-G.;Shen, Y.-H.;Xie, A.-J.;Zhu, J.-F.;Tian, X.-Y. and Zhang, L.-D.,*Facile fabrication of magnetic metal-organic framework nanocomposites for potential targeted drug delivery*, J. Mater. Chem., 2011, **21**, 3843–3848.
89. Ricco, R.;Konstas, K.;Styles, M. J.;Richardson, J. J.;Babarao, R.;Suzuki, K.;Scopece, P. and Falcaro, P.,*Lead (II) uptake by aluminium based magnetic framework composites (MFCs) in water*, J. Mater. Chem. A, 2015, **3**, 19822–19831.
90. Allam, R. J.,*Improved oxygen production technologies*, Energy Procedia, 2009, **1**, 461–470.
91. Rao, P. and Muller, M., 2007.
92. Arnold, E.;Bruton, A.;Donovan-Hall, M.;Fenwick, A.;Dibb, B. and Walker, E.,*Ambulatory oxygen: why do COPD patients not use their portable systems as prescribed? A qualitative study*, BMC Pulm. Med., 2011, **11**, 9.
93. Dobson, M.,*Oxygen concentrators and cylinders*, Int J Tuberc Lung Dis, 2001, **5**, 520–523.
94. Zieliński, J.;Tobiasz, M.;Hawrytkiewicz, I.;Sliviński, P. and Palasiewicz, G.,*Effects of long-term oxygen therapy on pulmonary hemodynamics in COPD patients: a 6-year prospective study*, Chest, 1998, **113**, 65–70.
95. Organization, W. H., *Oxygen sources and distribution for COVID-19 treatment centres: interim guidance*, 4 April 2020, World Health Organization, 2020.
96. Dubois, A.;Bodelin, P. and Vigor, X.,*Portable oxygen concentrator.*, US Patent 6,520,176, 18 Feb. 2003.
97. Hui, D. S.;Hall, S. D.;Chan, M. T.;Chow, B. K.;Ng, S. S.;Gin, T. and Sung, J. J.,*Exhaled air dispersion during oxygen delivery via a simple oxygen mask*, Chest, 2007, **132**, 540-546.
98. Vensel, R. R., *Journal*, 1977.
99. Baukal Jr, C. E., *Oxygen-enhanced combustion*, CRC press, 2013.
100. Thompson, D. R.;Bool, L. E. and Chen, J. C., *Oxygen enhanced combustion for NO_x control*, Praxair Inc, 2004.

101. Chen, W.;Chen, C.-s.;Bouwmeester, H. J.;Nijmeijer, A. and Winnubst, L.,*Oxygen-selective membranes integrated with oxy-fuel combustion*, J. Membr. Sci., 2014, **463**, 166-172.
102. Li, Z.-s.;Zhang, T. and Cai, N.-s.,*Experimental study of O₂– CO₂ production for the oxyfuel combustion using a Co-based oxygen carrier*, Ind. Eng. Chem. Res., 2008, **47**, 7147-7153.
103. Toftegaard, M. B.;Brix, J.;Jensen, P. A.;Glarborg, P. and Jensen, A. D.,*Oxy-fuel combustion of solid fuels*, Prog. Energy Combust. Sci., 2010, **36**, 581-625.
104. Adolf, S. G. and Walter, H., *Journal*, 1967.
105. George, A., *Journal*, 1966.
106. Hubert, H., *Journal*, 1953.
107. Barker, D. J.;Mannucchi, G. A.;Salvi, S. M. and Stuckey, D. C.,*Characterisation of soluble residual chemical oxygen demand (COD) in anaerobic wastewater treatment effluents*, Water Res., 1999, **33**, 2499-2510.
108. Ning, Y.-F.;Chen, Y.-P.;Shen, Y.;Zeng, N.;Liu, S.-Y.;Guo, J.-S. and Fang, F.,*A new approach for estimating aerobic–anaerobic biofilm structure in wastewater treatment via dissolved oxygen microdistribution*, Chem. Eng. J., 2014, **255**, 171-177.
109. Skinner, S. J. and Kilner, J. A.,*Oxygen ion conductors*, Mater. Today, 2003, **6**, 30-37.
110. Baukal Jr, C. E., *Oxygen-enhanced combustion*, CRC press, 2010.
111. Fernández-Castro, P.;Vallejo, M.;San Román, M. F. and Ortiz, I.,*Insight on the fundamentals of advanced oxidation processes. Role and review of the determination methods of reactive oxygen species*, Journal of Chemical Technology & Biotechnology, 2015, **90**, 796-820.
112. Wolfbeis, O. S.,*Luminescent sensing and imaging of oxygen: Fierce competition to the Clark electrode*, BioEssays, 2015, **37**, 921-928.
113. Banaszkiwicz, T.;Chorowski, M. and Gizicki, W., 2014.
114. Smith, A. and Klosek, J.,*A review of air separation technologies and their integration with energy conversion processes*, Fuel processing technology, 2001, **70**, 115–134.
115. Mehrpooya, M.;Sharifzadeh, M. M. M. and Rosen, M. A.,*Optimum design and exergy analysis of a novel cryogenic air separation process with LNG (liquefied natural gas) cold energy utilization*, Energy, 2015, **90**, 2047-2069.
116. How air separation works, Messergroup.com. (2020). Retrieved 3 December 2020, www.messergroup.com/sr_RS_latin/production-of-air-gases?inheritRedirect=true.
117. Sircar, S. and Kratz, W. C.,*Oxygen Production by Pressure Swing Adsorption*, Sep. Sci. Technol., 1989, **24**, 429-440.
118. Mercea, P. V. and Hwang, S.-T.,*Oxygen separation from air by a combined pressure swing adsorption and continuous membrane column process*, J. Membr. Sci., 1994, **88**, 131-144.
119. Ruthven, D. M.;Farooq, S. and Knaebel, K. S., *Pressure swing adsorption*, VCH publishers New York, 1994.
120. Santos, J.;Cruz, P.;Regala, T.;Magalhaes, F. and Mendes, A.,*High-purity oxygen production by pressure swing adsorption*, Ind. Eng. Chem. Res., 2007, **46**, 591-599.
121. Buckingham, A.;Disch, R.-L. and Dunmur, D.,*Quadrupole moments of some simple molecules*, Journal of the American Chemical Society, 1968, **90**, 3104-3107.
122. Hackett, C. and Hammond, K. D.,*Simulating the effect of the quadrupole moment on the adsorption of nitrogen in siliceous zeolites*, Microporous. Mesoporous. Mater., 2018, **263**, 231-235.
123. Koh, D.-Y.;Pimentel, B. R.;Babu, V. P.;Stephenson, N.;Chai, S. W.;Rosinski, A. and Lively, R. P.,*Sub-ambient air separation via Li⁺ exchanged zeolite*, Microporous. Mesoporous. Mater., 2018, **256**, 140-146.
124. Pérez-Pellitero, J. and Pirngruber, G. D.,*Industrial Zeolite Applications for Gas Adsorption and Separation Processes*, 2020.
125. Tlili, N.;Grévillet, G. and Vallières, C.,*Carbon dioxide capture and recovery by means of TSA and/or VSA*, International Journal of Greenhouse Gas Control, 2009, **3**, 519–527.
126. Pan, M.;Omar, H. M. and Rohani, S.,*Application of Nanosize Zeolite Molecular Sieves for Medical Oxygen Concentration*, Nanomaterials, 2017, **7**, 195.
127. Jee, J.-G.;Kim, M.-B. and Lee, C.-H.,*Pressure swing adsorption processes to purify oxygen using a carbon molecular sieve*, Chem. Eng. Sci., 2005, **60**, 869-882.

128. Ruthven, D. M., *Diffusion of oxygen and nitrogen in carbon molecular sieve*, Chem. Eng. Sci., 1992, **47**, 4305-4308.
129. Kim, M.-B.;Jee, J.-G.;Bae, Y.-S. and Lee, C.-H., *Parametric study of pressure swing adsorption process to purify oxygen using carbon molecular sieve*, Ind. Eng. Chem. Res., 2005, **44**, 7208-7217.
130. Chen, Y.;Yang, R. and Uawithya, P., *Diffusion of oxygen, nitrogen and their mixtures in carbon molecular sieve*, AIChE journal, 1994, **40**, 577-585.
131. *Adsorption technology Grasys.com. (2020). Retrieved 3 December 2020, from <https://www.grasys.com/technologies/adsorption/>.*
132. Chong, K.;Lai, S.;Thiam, H.;Teoh, H. and Heng, S., *Recent progress of oxygen/nitrogen separation using membrane technology*, J. Eng. Sci. Technol, 2016, **11**, 1016-1030.
133. Haraya, K. and Hwang, S.-T., *Permeation of oxygen, argon and nitrogen through polymer membranes*, J. Membr. Sci., 1992, **71**, 13-27.
134. Rousseau Ronald, W., *Journal*, 1987, 1-1.
135. Sanders, D. F.;Smith, Z. P.;Guo, R.;Robeson, L. M.;McGrath, J. E.;Paul, D. R. and Freeman, B. D., *Energy-efficient polymeric gas separation membranes for a sustainable future: A review*, Polymer, 2013, **54**, 4729-4761.
136. Zhu, X.;Wang, H. and Yang, W., *Novel cobalt-free oxygen permeable membrane*, Chem. Commun., 2004, 1130-1131.
137. Badwal, S. P. and Ciacchi, F. T., *Ceramic membrane technologies for oxygen separation*, Advanced materials, 2001, **13**, 993-996.
138. Sunarso, J.;Baumann, S.;Serra, J.;Meulenberg, W.;Liu, S.;Lin, Y. and Da Costa, J. D., *Mixed ionic–electronic conducting (MIEC) ceramic-based membranes for oxygen separation*, J. Membr. Sci., 2008, **320**, 13-41.
139. Hashim, S. M.;Mohamed, A. R. and Bhatia, S., *Current status of ceramic-based membranes for oxygen separation from air*, Adv. Colloid Interface Sci., 2010, **160**, 88-100.
140. Bouwmeester, H. J. and Burggraaf, A. J., in *Membrane science and technology*, Elsevier, 1996, vol. 4, pp. 435-528.
141. Zhang, Z.;Zhou, W.;Chen, Y.;Chen, D.;Chen, J.;Liu, S.;Jin, W. and Shao, Z., *Novel approach for developing dual-phase ceramic membranes for oxygen separation through beneficial phase reaction*, ACS applied materials & interfaces, 2015, **7**, 22918-22926.
142. Chorowski, M. and Gizicki, W., *Technical and economic aspects of oxygen separation for oxy-fuel purposes*, Archives of Thermodynamics, 2015, **36**.
143. Yaghi, O. M.;Li, G. and Li, H., *Selective binding and removal of guests in a microporous metal-organic framework*, Nature, 1995, **378**, 703.
144. Gándara, F.;Furukawa, H.;Lee, S. and Yaghi, O. M., *High Methane Storage Capacity in Aluminum Metal–Organic Frameworks*, Journal of the American Chemical Society, 2014, **136**, 5271–5274.
145. Konstas, K.;Osl, T.;Yang, Y.;Batten, M.;Burke, N.;Hill, A. J. and Hill, M. R., *Methane storage in metal organic frameworks*, J. Mater. Chem., 2012, **22**, 16698–16708.
146. Liu, J.;Tian, J.;Thallapally, P. K. and McGrail, B. P., *Selective CO₂ Capture from Flue Gas Using Metal–Organic Frameworks—A Fixed Bed Study*, J. Phys. Chem. C, 2012, **116**, 9575–9581.
147. Furukawa, H.;Cordova, K. E.;O’Keeffe, M. and Yaghi, O. M., *The chemistry and applications of metal-organic frameworks*, Science, 2013, **341**, 1230444.
148. Rowsell, J. L. and Yaghi, O. M., *Strategies for hydrogen storage in metal–organic frameworks*, Angewandte Chemie International Edition, 2005, **44**, 4670–4679.
149. Yaghi, O. M.;O’keeffe, M.;Ockwig, N. W. and Chae, H. K., *Reticular synthesis and the design of new materials*, Nature, 2003, **423**, 705.
150. Li, H.;Eddaoudi, M.;O’Keeffe, M. and Yaghi, O. M., *Design and synthesis of an exceptionally stable and highly porous metal-organic framework*, Nature, 1999, **402**, 276–279.
151. Kuppler, R. J.;Timmons, D. J.;Fang, Q.-R.;Li, J.-R.;Makal, T. A.;Young, M. D.;Yuan, D.;Zhao, D.;Zhuang, W. and Zhou, H.-C., *Potential applications of metal-organic frameworks*, Coord. Chem. Rev., 2009, **253**, 3042–3066.

152. Zhou, H.-C.; Long, J. R. and Yaghi, O. M., *Journal*, 2012.
153. Li, H.; Sadiq, M. M.; Suzuki, K.; Doblin, C.; Lim, S.; Falcaro, P.; Hill, A. J. and Hill, M. R., *MaLISA – a cooperative method to release adsorbed gases from metal–organic frameworks*, *J. Mater. Chem. A*, 2016, **4**, 18757–18762.
154. Li, J.-R.; Sculley, J. and Zhou, H.-C., *Metal–organic frameworks for separations*, *Chem. Rev.*, 2011, **112**, 869–932.
155. Li, H.; Wang, K.; Sun, Y.; Lollar, C. T.; Li, J. and Zhou, H.-C., *Recent advances in gas storage and separation using metal–organic frameworks*, *Mater. Today*, 2018, **21**, 108–121.
156. Bao, Z.; Chang, G.; Xing, H.; Krishna, R.; Ren, Q. and Chen, B., *Potential of microporous metal-organic frameworks for separation of hydrocarbon mixtures*, *Energy Environ. Sci.*, 2016, **9**, 3612–3641.
157. Zeng, L.; Guo, X.; He, C. and Duan, C., *Metal–Organic Frameworks: Versatile Materials for Heterogeneous Photocatalysis*, *ACS Catalysis*, 2016, **6**, 7935–7947.
158. Alshammari, A.; Jiang, Z. and Cordova, K. E., *Metal organic frameworks as emerging photocatalysts*, *Semiconductor Photocatalysis: Materials, Mechanisms and Applications*, 2016, 302–341.
159. Peterson, G. W.; Britt, D. K.; Sun, D. T.; Mahle, J. J.; Browe, M.; Demasky, T.; Smith, S.; Jenkins, A. and Rossin, J. A., *Multifunctional Purification and Sensing of Toxic Hydride Gases by CuBTC Metal–Organic Framework*, *Ind. Eng. Chem. Res.*, 2015, **54**, 3626–3633.
160. Bloch, E. D.; Queen, W. L.; Krishna, R.; Zadrozny, J. M.; Brown, C. M. and Long, J. R., *Hydrocarbon separations in a metal-organic framework with open iron (II) coordination sites*, *Science*, 2012, **335**, 1606–1610.
161. Queen, W. L.; Bloch, E. D.; Brown, C. M.; Hudson, M. R.; Mason, J. A.; Murray, L. J.; Ramirez-Cuesta, A. J.; Peterson, V. K. and Long, J. R., *Hydrogen adsorption in the metal-organic frameworks Fe₂(dobdc) and Fe₂(O₂)(dobdc)*, *Dalton Trans*, 2012, **41**, 4180–4187.
162. Gangu, K. K.; Maddila, S.; Mukkamala, S. B. and Jonnalagadda, S. B., *A review on contemporary Metal–Organic Framework materials*, *Inorg. Chim. Acta*, 2016, **446**, 61–74.
163. Sadiq, M. M.; Rubio-Martinez, M.; Zadehahmadi, F.; Suzuki, K. and Hill, M. R., *Magnetic Framework Composites for Low Concentration Methane Capture*, *Ind. Eng. Chem. Res.*, 2018, **57**, 6040–6047.
164. Stephanie Gnewuch, O. U.
165. Dey, C.; Kundu, T.; Biswal, B. P.; Mallick, A. and Banerjee, R., *Crystalline metal-organic frameworks (MOFs): synthesis, structure and function*, *Acta Crystallogr B Struct Sci Cryst Eng Mater*, 2014, **70**, 3–10.
166. Yaghi, O. M.; O’Keeffe, M.; Ockwig, N. W.; Chae, H. K.; Eddaoudi, M. and Kim, J., *Reticular synthesis and the design of new materials*, *Nature*, 2003, **423**, 705–714.
167. Stock, N. and Biswas, S., *Synthesis of Metal–Organic Frameworks (MOFs): Routes to Various MOF Topologies, Morphologies, and Composites*, *Chem. Rev*, 2012, **112**, 933–969.
168. Rubio-Martinez, M.; Avci-Camur, C.; Thornton, A. W.; Imaz, I.; Maspoch, D. and Hill, M. R., *New synthetic routes towards MOF production at scale*, *Chem. Soc. Rev.*, 2017, **46**, 3453–3480.
169. Zhang, B.; Zhang, J.; Tan, X.; Shao, D.; Shi, J.; Zheng, L.; Zhang, J.; Yang, G. and Han, B., *MIL-125-NH₂@ TiO₂ core–shell particles produced by a post-solvothermal route for high-performance photocatalytic H₂ production*, *ACS applied materials & interfaces*, 2018, **10**, 16418–16423.
170. Tan, B.; Luo, Y.; Liang, X.; Wang, S.; Gao, X.; Zhang, Z. and Fang, Y., *Mixed-solvothermal synthesis of MIL-101 (Cr) and its water adsorption/desorption performance*, *Ind. Eng. Chem. Res.*, 2019, **58**, 2983–2990.
171. Cai, X.; Lin, J. and Pang, M., *Facile synthesis of highly uniform Fe-MIL-88B particles*, *Crystal Growth & Design*, 2016, **16**, 3565–3568.
172. McRoberts, K., University of St Andrews, 2018.
173. Adhikari, A. K. and Lin, K.-S., *Improving CO₂ adsorption capacities and CO₂/N₂ separation efficiencies of MOF-74(Ni, Co) by doping palladium-containing activated carbon*, *Chem. Eng. J.*, 2016, **284**, 1348–1360.

174. Becker, T. M.;Heinen, J.;Dubbeldam, D.;Lin, L.-C. and Vlugt, T. J. H.,*Polarizable Force Fields for CO₂ and CH₄ Adsorption in M-MOF-74*, J. Phys. Chem. C, 2017, **121**, 4659–4673.
175. Mason, J. A.;Sumida, K.;Herm, Z. R.;Krishna, R. and Long, J. R.,*Evaluating metal-organic frameworks for post-combustion carbon dioxide capture via temperature swing adsorption*, Energy Environ. Sci., 2011, **4**, 3030–3040.
176. Sun, H.;Ren, D.;Kong, R.;Wang, D.;Jiang, H.;Tan, J.;Wu, D.;Chen, S. and Shen, B.,*Tuning 1-hexene/n-hexane adsorption on MOF-74 via constructing Co-Mg bimetallic frameworks*, Microporous Mesoporous Mater., 2019, **284**, 151-160.
177. Sun, J.;Zhang, X.;Zhang, A. and Liao, C.,*Preparation of Fe–Co based MOF-74 and its effective adsorption of arsenic from aqueous solution*, Int. J. Environ. Sci, 2019, **80**, 197–207.
178. Bae, S.;Zaini, N.;Kamarudin, K. S. N.;Yoo, K. S.;Kim, J. and Othman, M. R.,*Rapid solvothermal synthesis of microporous UiO-66 particles for carbon dioxide capture*, Korean J. Chem. Eng., 2018, **35**, 764-769.
179. Lozano, L. A.;Iglesias, C. M.;Faroldi, B. M.;Ulla, M. A. and Zamaro, J. M.,*Efficient solvothermal synthesis of highly porous UiO-66 nanocrystals in dimethylformamide-free media*, Journal of Materials Science, 2018, **53**, 1862-1873.
180. Feng, D.;Gu, Z. Y.;Li, J. R.;Jiang, H. L.;Wei, Z. and Zhou, H. C.,*Zirconium-metalloporphyrin PCN-222: mesoporous metal–organic frameworks with ultrahigh stability as biomimetic catalysts*, Angewandte Chemie International Edition, 2012, **51**, 10307-10310.
181. Gao, Q.;Xie, Y.-B.;Li, J.-R.;Yuan, D.-Q.;Yakovenko, A. A.;Sun, J.-H. and Zhou, H.-C.,*Tuning the formations of metal–organic frameworks by modification of ratio of reactant, acidity of reaction system, and use of a secondary ligand*, Crystal growth & design, 2012, **12**, 281-288.
182. Park, J.;Feng, D.;Yuan, S. and Zhou, H. C.,*Photochromic metal–organic frameworks: reversible control of singlet oxygen generation*, Angew. Chem., 2015, **127**, 440-445.
183. Chen, B.;Wang, X.;Zhang, Q.;Xi, X.;Cai, J.;Qi, H.;Shi, S.;Wang, J.;Yuan, D. and Fang, M.,*Synthesis and characterization of the interpenetrated MOF-5*, J. Mater. Chem., 2010, **20**, 3758-3767.
184. Liu, D.;Purewal, J.;Yang, J.;Sudik, A.;Maurer, S.;Mueller, U.;Ni, J. and Siegel, D.,*MOF-5 composites exhibiting improved thermal conductivity*, Int. J. Hydrogen Energy, 2012, **37**, 6109-6117.
185. Tranchemontagne, D. J.;Hunt, J. R. and Yaghi, O. M.,*Room temperature synthesis of metal-organic frameworks: MOF-5, MOF-74, MOF-177, MOF-199, and IRMOF-0*, Tetrahedron, 2008, **64**, 8553-8557.
186. Majano, G. and Pérez-Ramírez, J.,*Scalable room-temperature conversion of copper (II) hydroxide into HKUST-1 (Cu₃(btc)₂)*, Advanced Materials, 2013, **25**, 1052-1057.
187. Zhuang, J. L.;Ceglarek, D.;Pethuraj, S. and Terfort, A.,*Rapid room-temperature synthesis of metal–organic framework HKUST-1 crystals in bulk and as oriented and patterned thin films*, Advanced functional materials, 2011, **21**, 1442-1447.
188. Huo, J.;Brightwell, M.;El Hankari, S.;Garai, A. and Bradshaw, D.,*A versatile, industrially relevant, aqueous room temperature synthesis of HKUST-1 with high space-time yield*, J. Mater. Chem. A, 2013, **1**, 15220-15223.
189. Zhang, H.;Liu, D.;Yao, Y.;Zhang, B. and Lin, Y.,*Stability of ZIF-8 membranes and crystalline powders in water at room temperature*, J. Membr. Sci., 2015, **485**, 103-111.
190. Zhu, M.;Venna, S. R.;Jasinski, J. B. and Carreon, M. A.,*Room-temperature synthesis of ZIF-8: the coexistence of ZnO nanoneedles*, Chem. Mater., 2011, **23**, 3590-3592.
191. Mueller, U.;Schubert, M.;Teich, F.;Puetter, H.;Schierle-Arndt, K. and Pastre, J.,*Metal–organic frameworks—prospective industrial applications*, J. Mater. Chem., 2006, **16**, 626-636.
192. Taddei, M.;Steitz, D. A.;van Bokhoven, J. A. and Ranocchiari, M.,*Continuous-Flow Microwave Synthesis of Metal–Organic Frameworks: A Highly Efficient Method for Large-Scale Production*, Chemistry–A European Journal, 2016, **22**, 3245-3249.
193. Lestari, W. W.;Adreane, M.;Purnawan, C.;Fansuri, H.;Widiastuti, N. and Rahardjo, S. B., 2016.
194. Al-Kutubi, H.;Gascon, J.;Sudhölter, E. J. and Rassaei, L.,*Electrosynthesis of metal–organic frameworks: challenges and opportunities*, ChemElectroChem, 2015, **2**, 462-474.

195. Campagnol, N.;Van Assche, T. R.;Li, M.;Stappers, L.;Dincă, M.;Denayer, J. F.;Binnemans, K.;De Vos, D. E. and Fransaeer, J.,*On the electrochemical deposition of metal–organic frameworks*, J. Mater. Chem. A, 2016, **4**, 3914-3925.
196. Li, M. and Dincă, M.,*On the Mechanism of MOF-5 Formation under Cathodic Bias*, Chem. Mater., 2015, **27**, 3203-3206.
197. Yang, H.-m.;Xian, L.;Song, X.-l.;Yang, T.-l.;Liang, Z.-h. and Fan, C.-m.,*In situ electrochemical synthesis of MOF-5 and its application in improving photocatalytic activity of BiOBr*, Transactions of Nonferrous Metals Society of China, 2015, **25**, 3987-3994.
198. Yang, H.;Song, X.;Yang, T.;Liang, Z.;Fan, C. and Hao, X.,*Electrochemical synthesis of flower shaped morphology MOFs in an ionic liquid system and their electrocatalytic application to the hydrogen evolution reaction*, RSC Adv., 2014, **4**, 15720-15726.
199. Ma, W.;Jiang, Q.;Yu, P.;Yang, L. and Mao, L.,*Zeolitic imidazolate framework-based electrochemical biosensor for in vivo electrochemical measurements*, Anal. Chem., 2013, **85**, 7550-7557.
200. Worrall, S. D.;Mann, H.;Rogers, A.;Bissett, M. A.;Attfield, M. P. and Dryfe, R. A.,*Electrochemical deposition of zeolitic imidazolate framework electrode coatings for supercapacitor electrodes*, Electrochim. Acta, 2016, **197**, 228-240.
201. Jhung, S.-H.;Lee, J.-H. and Chang, J.-S.,*Microwave synthesis of a nanoporous hybrid material, chromium trimesate*, Bull. Korean Chem. Soc., 2005, **26**, 880-881.
202. Khan, N. A.;Kang, I. J.;Seok, H. Y. and Jhung, S. H.,*Facile synthesis of nano-sized metal-organic frameworks, chromium-benzenedicarboxylate, MIL-101*, Chem. Eng. J., 2011, **166**, 1152-1157.
203. Khan, N. A. and Jhung, S. H.,*Synthesis of metal-organic frameworks (MOFs) with microwave or ultrasound: Rapid reaction, phase-selectivity, and size reduction*, Coord. Chem. Rev., 2015, **285**, 11-23.
204. Choi, J.-S.;Son, W.-J.;Kim, J. and Ahn, W.-S.,*Metal–organic framework MOF-5 prepared by microwave heating: Factors to be considered*, Microporous. Mesoporous. Mater., 2008, **116**, 727-731.
205. Ni, Z. and Masel, R. I.,*Rapid production of metal-organic frameworks via microwave-assisted solvothermal synthesis*, J Am Chem Soc, 2006, **128**, 12394-12395.
206. Fujii, K.;Garay, A. L.;Hill, J.;Sbircea, E.;Pan, Z.;Xu, M.;Apperley, D. C.;James, S. L. and Harris, K. D. M.,*Direct structure elucidation by powder X-ray diffraction of a metal–organic framework material prepared by solvent-free grinding*, Chem. Commun., 2010, **46**, 7572-7574.
207. Friščić, T.;Childs, S. L.;Rizvi, S. A. A. and Jones, W.,*The role of solvent in mechanochemical and sonochemical cocrystal formation: a solubility-based approach for predicting cocrystallisation outcome*, CrystEngComm, 2009, **11**, 418-426.
208. Yuan, W.;Friscić, T.;Apperley, D. and James, S. L.,*High reactivity of metal-organic frameworks under grinding conditions: parallels with organic molecular materials*, Angew. Chem. Int. Ed. Engl., 2010, **49**, 3916-3919.
209. Beldon, P. J.;Fábián, L.;Stein, R. S.;Thirumurugan, A.;Cheetham, A. K. and Friščić, T.,*Rapid room-temperature synthesis of zeolitic imidazolate frameworks by using mechanochemistry*, Angew. Chem., 2010, **122**, 9834-9837.
210. Friščić, T.;Reid, D. G.;Halasz, I.;Stein, R. S.;Dinnebier, R. E. and Duer, M. J.,*Ion-and liquid-assisted grinding: improved mechanochemical synthesis of metal–organic frameworks reveals salt inclusion and anion templating*, Angew. Chem., 2010, **122**, 724-727.
211. Feng, X.;Jia, C.;Wang, J.;Cao, X.;Tang, P. and Yuan, W.,*Efficient vapor-assisted aging synthesis of functional and highly crystalline MOFs from CuO and rare earth sesquioxides/carbonates*, Green Chemistry, 2015, **17**, 3740-3745.
212. Julien, P. A.;Mottillo, C. and Friščić, T.,*Metal–organic frameworks meet scalable and sustainable synthesis*, Green Chemistry, 2017, **19**, 2729-2747.
213. James, S. L.;Adams, C. J.;Bolm, C.;Braga, D.;Collier, P.;Friščić, T.;Grepioni, F.;Harris, K. D.;Hyett, G. and Jones, W.,*Mechanochemistry: opportunities for new and cleaner synthesis*, Chem. Soc. Rev., 2012, **41**, 413-447.

214. Batten, M. P.;Rubio-Martinez, M.;Hadley, T.;Carey, K.-C.;Lim, K.-S.;Polyzos, A. and Hill, M. R.,*Continuous flow production of metal-organic frameworks*, Current Opinion in Chemical Engineering, 2015, **8**, 55-59.
215. Rubio-Martinez, M.;Hadley, T. D.;Batten, M. P.;Constanti-Carey, K.;Barton, T.;Marley, D.;Mönch, A.;Lim, K.-S. and Hill, M. R.,*Scalability of Continuous Flow Production of Metal–Organic Frameworks*, ChemSusChem, 2016, **9**, 938-941.
216. Myers, R. M.;Fitzpatrick, D. E.;Turner, R. M. and Ley, S. V.,*Flow chemistry meets advanced functional materials*, Chemistry–A European Journal, 2014, **20**, 12348-12366.
217. He, B.;Sadiq, M. M.;Batten, M. P.;Suzuki, K.;Rubio-Martinez, M.;Gardiner, J. and Hill, M. R.,*Continuous Flow Synthesis of a Zr Magnetic Framework Composite for Post-Combustion CO₂ Capture*, Chemistry–A European Journal, 2019, **25**, 13184-13188.
218. Ameloot, R.;Vermoortele, F.;Vanhove, W.;Roeflaers, M. B.;Sels, B. F. and De Vos, D. E.,*Interfacial synthesis of hollow metal–organic framework capsules demonstrating selective permeability*, Nature chemistry, 2011, **3**, 382-387.
219. Sachse, A.;Ameloot, R.;Coq, B.;Fajula, F.;Coasne, B.;De Vos, D. and Galarneau, A.,*In situ synthesis of Cu–BTC (HKUST-1) in macro-/mesoporous silica monoliths for continuous flow catalysis*, Chem. Commun., 2012, **48**, 4749-4751.
220. Faustini, M.;Kim, J.;Jeong, G.-Y.;Kim, J. Y.;Moon, H. R.;Ahn, W.-S. and Kim, D.-P.,*Microfluidic approach toward continuous and ultrafast synthesis of metal–organic framework crystals and hetero structures in confined microdroplets*, Journal of the American Chemical Society, 2013, **135**, 14619-14626.
221. Rubio-Martinez, M.;Batten, M. P.;Polyzos, A.;Carey, K.-C.;Mardel, J. I.;Lim, K.-S. and Hill, M. R.,*Versatile, High Quality and Scalable Continuous Flow Production of Metal-Organic Frameworks*, Sci. Rep., 2014, **4**, 5443.
222. Chen, L.;Wang, H.-F.;Li, C. and Xu, Q.,*Bimetallic metal–organic frameworks and their derivatives*, Chem Sci, 2020, **11**, 5369-5403.
223. Yang, X. and Xu, Q.,*Bimetallic metal–organic frameworks for gas storage and separation*, Crystal Growth & Design, 2017, **17**, 1450-1455.
224. Yuan, Q.;Yu, Y.;Sherrell, P. C.;Chen, J. and Bi, X.,*Fe/Co-based bimetallic MOF-derived Co₃Fe₇@ NCNTFs bifunctional electrocatalyst for high-efficiency overall water splitting*, Chem. Asian J., 2020, **15**, 1728-1735.
225. Zhong, M.;Yang, D.-H.;Kong, L.-J.;Shuang, W.;Zhang, Y.-H. and Bu, X.-H.,*Bimetallic metal–organic framework derived Co₃O₄–CoFe₂O₄ composites with different Fe/Co molar ratios as anode materials for lithium ion batteries*, Dalton Trans., 2017, **46**, 15947-15953.
226. Li, B.;Liu, J.;Liu, Q.;Chen, R.;Zhang, H.;Yu, J.;Song, D.;Li, J.;Zhang, M. and Wang, J.,*Core-shell structure of ZnO/Co₃O₄ composites derived from bimetallic-organic frameworks with superior sensing performance for ethanol gas*, Appl. Surf. Sci., 2019, **475**, 700-709.
227. Schubert, M.;Kahlich, M.;Feldmeyer, G.;Hüttner, M.;Hackenberg, S.;Gasteiger, H. and Behm, R.,*Bimetallic PtSn catalyst for selective CO oxidation in H₂-rich gases at low temperatures*, Physical Chemistry Chemical Physics, 2001, **3**, 1123-1131.
228. Sun, Q.;Liu, M.;Li, K.;Han, Y.;Zuo, Y.;Chai, F.;Song, C.;Zhang, G. and Guo, X.,*Synthesis of Fe/M (M= Mn, Co, Ni) bimetallic metal organic frameworks and their catalytic activity for phenol degradation under mild conditions*, Inorg. Chem. Front, 2017, **4**, 144-153.
229. Wang, L. J.;Deng, H.;Furukawa, H.;Gándara, F.;Cordova, K. E.;Peri, D. and Yaghi, O. M.,*Synthesis and characterization of metal–organic framework-74 containing 2, 4, 6, 8, and 10 different metals*, Inorg. Chem., 2014, **53**, 5881-5883.
230. Gul-E-Noor, F.;Jee, B.;Mendt, M.;Himsl, D.;Pöppl, A.;Hartmann, M.;Haase, J.;Krautscheid, H. and Bertmer, M.,*Formation of Mixed Metal Cu_{3-x}Zn_x(btc)₂ Frameworks with Different Zinc Contents: Incorporation of Zn²⁺ into the Metal–Organic Framework Structure as Studied by Solid-State NMR*, J. Phys. Chem. C, 2012, **116**, 20866-20873.
231. Gotthardt, M. A.;Schoch, R.;Wolf, S.;Bauer, M. and Kleist, W.,*Synthesis and characterization of bimetallic metal–organic framework Cu–Ru-BTC with HKUST-1 structure*, Dalton Trans., 2015, **44**, 2052-2056.

232. Cao, Y.;Zhao, Y.;Song, F. and Zhong, Q.,*Alkali metal cation doping of metal-organic framework for enhancing carbon dioxide adsorption capacity*, J. Energy Chem., 2014, **23**, 468-474.
233. Kim, Y.;Das, S.;Bhattacharya, S.;Hong, S.;Kim, M. G.;Yoon, M.;Natarajan, S. and Kim, K.,*Metal-Ion Metathesis in Metal–Organic Frameworks: A Synthetic Route to New Metal–Organic Frameworks*, Chemistry – A European Journal, 2012, **18**, 16642-16648.
234. Smith, S. J. D.;Ladewig, B. P.;Hill, A. J.;Lau, C. H. and Hill, M. R.,*Post-synthetic Ti Exchanged UiO-66 Metal-Organic Frameworks that Deliver Exceptional Gas Permeability in Mixed Matrix Membranes*, Sci. Rep., 2015, **5**, 7823.
235. Kim, D. and Coskun, A.,*Template-Directed Approach Towards the Realization of Ordered Heterogeneity in Bimetallic Metal–Organic Frameworks*, Angew. Chem., 2017, **129**, 5153-5158.
236. Tang, J.;Salunkhe, R. R.;Liu, J.;Torad, N. L.;Imura, M.;Furukawa, S. and Yamauchi, Y.,*Thermal Conversion of Core–Shell Metal–Organic Frameworks: A New Method for Selectively Functionalized Nanoporous Hybrid Carbon*, Journal of the American Chemical Society, 2015, **137**, 1572-1580.
237. Song, X.;Jeong, S.;Kim, D. and Lah, M. S.,*Transmetalations in two metal–organic frameworks with different framework flexibilities: Kinetics and core–shell heterostructure*, CrystEngComm, 2012, **14**, 5753-5756.
238. Guo, W.;Xia, W.;Cai, K.;Wu, Y.;Qiu, B.;Liang, Z.;Qu, C. and Zou, R.,*Kinetic-Controlled Formation of Bimetallic Metal–Organic Framework Hybrid Structures*, Small, 2017, **13**, 1702049.
239. Fukushima, T.;Horike, S.;Kobayashi, H.;Tsujiimoto, M.;Isoda, S.;Foo, M. L.;Kubota, Y.;Takata, M. and Kitagawa, S.,*Modular design of domain assembly in porous coordination polymer crystals via reactivity-directed crystallization process*, Journal of the American Chemical Society, 2012, **134**, 13341-13347.
240. Mason, J. A.;Veenstra, M. and Long, J. R.,*Evaluating metal–organic frameworks for natural gas storage*, Chem Sci, 2014, **5**, 32–51.
241. Bazer-Bachi, D.;Assié, L.;Lecocq, V.;Harbuzaru, B. and Falk, V.,*Towards industrial use of metal-organic framework: Impact of shaping on the MOF properties*, Powder Technology, 2014, **255**, 52–59.
242. Dincă, M.;Dailly, A.;Liu, Y.;Brown, C. M.;Neumann, D. A. and Long, J. R.,*Hydrogen Storage in a Microporous Metal–Organic Framework with Exposed Mn²⁺ Coordination Sites*, J. Am. Chem. Soc, 2006, **128**, 16876–16883.
243. Chowdhury, P.;Bikkina, C.;Meister, D.;Dreisbach, F. and Gumma, S.,*Comparison of adsorption isotherms on Cu-BTC metal organic frameworks synthesized from different routes*, Microporous. Mesoporous. Mater., 2009, **117**, 406–413.
244. Zeitler, T. R.;Van Heest, T.;Sholl, D. S.;Allendorf, M. D. and Greathouse, J. A.,*Predicting low-pressure O₂ adsorption in nanoporous framework materials for sensing applications*, Chemphyschem, 2013, **14**, 3740-3750.
245. Parkes, M.;Gallis, D.;Greathouse, J. and Nenoff, T.,*Effect of Metal in M₃(btc)₂ and M₂(dobdc) MOFs for O₂/N₂ Separations: A Combined Density Functional Theory and Experimental Study*, J. Phys. Chem. C, 2015, **119**, 6556-6567.
246. Wang, Y.;Yang, J.;Li, Z.;Zhang, Z.;Li, J.;Yang, Q. and Zhong, C.,*Computational study of oxygen adsorption in metal–organic frameworks with exposed cation sites: effect of framework metal ions*, RSC Adv., 2015, **5**, 33432-33437.
247. Sava Gallis, D. F.;Parkes, M. V.;Greathouse, J. A.;Zhang, X. and Nenoff, T. M.,*Enhanced O₂ Selectivity versus N₂ by Partial Metal Substitution in Cu-BTC*, Chem. Mater., 2015, **27**, 2018-2025.
248. Verma, P.;Maurice, R. and Truhlar, D. G.,*Identifying the Interactions That Allow Separation of O₂ from N₂ on the Open Iron Sites of Fe₂(dobdc)*, J. Phys. Chem. C, 2015, **119**, 28499-28511.
249. Bloch, E. D.;Queen, W. L.;Hudson, M. R.;Mason, J. A.;Xiao, D. J.;Murray, L. J.;Flacau, R.;Brown, C. M. and Long, J. R.,*Hydrogen storage and selective, reversible O₂ adsorption in*

- a metal–organic framework with open chromium (II) sites*, *Angew. Chem.*, 2016, **128**, 8747-8751.
250. Xiao, D. J.;Gonzalez, M. I.;Darago, L. E.;Vogiatzis, K. D.;Haldoupis, E.;Gagliardi, L. and Long, J. R.,*Selective, Tunable O₂ Binding in Cobalt(II)–Triazolate/Pyrazolate Metal–Organic Frameworks*, *Journal of the American Chemical Society*, 2016, **138**, 7161-7170.
251. Li, Y. and Yang, R. T.,*Gas Adsorption and Storage in Metal–Organic Framework MOF-177*, *Langmuir*, 2007, **23**, 12937-12944.
252. Hedin, N.;Andersson, L.;Bergström, L. and Yan, J.,*Adsorbents for the post-combustion capture of CO₂ using rapid temperature swing or vacuum swing adsorption*, *Applied Energy*, 2013, **104**, 418–433.
253. Songolzadeh, M.;Soleimani, M.;Takht Ravanchi, M. and Songolzadeh, R.,*Carbon Dioxide Separation from Flue Gases: A Technological Review Emphasizing Reduction in Greenhouse Gas Emissions*, *The Scientific World Journal*, 2014, **2014**, 828131.
254. Barreto, A. C. H.;Santiago, V. R.;Freire, R. M.;Mazzetto, S. E.;Denardin, J. C.;Mele, G.;Cavalcante, I. M.;Ribeiro, M. E. N. P.;Ricardo, N. M. P. S.;Gonçalves, T.;Carbone, L.;Lemos, T. L. G.;Pessoa, O. D. L. and Fachine, P. B. A.,*Magnetic Nanosystem for Cancer Therapy Using Oncocalyxone A, an Antitumour Secondary Metabolite Isolated from a Brazilian Plant*, *Int. J. Mol*, 2013, **14**, 18269–18283.
255. Munuera, C.;Shekhah, O.;Wang, H.;Woll, C. and Ocal, C.,*The controlled growth of oriented metal-organic frameworks on functionalized surfaces as followed by scanning force microscopy*, *Physical Chemistry Chemical Physics*, 2008, **10**, 7257–7261.
256. Chughtai, A. H.;Ahmad, N.;Younus, H. A.;Laypkov, A. and Verpoort, F.,*Metal–organic frameworks: versatile heterogeneous catalysts for efficient catalytic organic transformations*, *Chem. Soc. Rev.*, 2015, **44**, 6804–6849.
257. Harris, I. and Williams, A.,*Magnetic materials*, *Mater. Sci. Eng. C*, 2009, **2**, 49–84.
258. Jeong, U.;Teng, X.;Wang, Y.;Yang, H. and Xia, Y.,*Superparamagnetic Colloids: Controlled Synthesis and Niche Applications*, *Advanced Materials*, 2007, **19**, 33–60.
259. Sung, H. W. F.;Rudowicz, C.;Physics, C. U. o. H. K. D. o. and Science, M., *A Closer Look at the Hysteresis Loop for Ferromagnets: A Survey of Misconceptions and Misinterpretations in Textbooks*, City University of Hong Kong, Department of Physics and Materials Science, 2002.
260. Goldman, A., *Modern ferrite technology*, Springer Science & Business Media, 2006.
261. Hergt, R.;Dutz, S. and Zeisberger, M.,*Validity limits of the Néel relaxation model of magnetic nanoparticles for hyperthermia*, *Nanotechnology*, 2009, **21**, 015706.
262. Bakoglidis, K.;Simeonidis, K.;Sakellari, D.;Stefanou, G. and Angelakeris, M.,*Size-dependent mechanisms in AC magnetic hyperthermia response of iron-oxide nanoparticles*, *IEEE Trans. Magn*, 2012, **48**, 1320–1323.
263. Zhang, Y. and Zhai, Y., in *Advances in Induction and Microwave Heating of Mineral and Organic Materials*, InTech, 2011.
264. Deatsch, A. E. and Evans, B. A.,*Heating efficiency in magnetic nanoparticle hyperthermia*, *J. Magn. Mater*, 2014, **354**, 163–172.
265. Kekalo, K.;Baker, I.;Meyers, R. and Shyong, J.,*Magnetic Nanoparticles with High Specific Absorption Rate at Low Alternating Magnetic Field*, *Nano LIFE*, 2015, **5**, 1550002.
266. Mornet, S.;Vasseur, S.;Grasset, F. and Duguet, E.,*Magnetic nanoparticle design for medical diagnosis and therapy*, *J. Mater. Chem.*, 2004, **14**, 2161–2175.
267. Ebrahimi, M.,*On the temperature control in self-controlling hyperthermia therapy*, *J. Magn. Mater*, 2016, **416**, 134–140.
268. Hui, C.;Shen, C.;Yang, T.;Bao, L.;Tian, J.;Ding, H.;Li, C. and Gao, H. J.,*Large-Scale Fe₃O₄ Nanoparticles Soluble in Water Synthesized by a Facile Method*, *J. Phys. Chem. C*, 2008, **112**, 11336–11339.
269. Maensiri, S.;Sangmanee, M. and Wiengmoon, A.,*Magnesium ferrite (MgFe₂O₄) nanostructures fabricated by electrospinning*, *Nanoscale Res. Lett*, 2009, **4**, 221.
270. Zhao, X.;Pattengale, B.;Fan, D.;Zou, Z.;Zhao, Y.;Du, J.;Huang, J. and Xu, C.,*Mixed-Node Metal–Organic Frameworks as Efficient Electrocatalysts for Oxygen Evolution Reaction*, *ACS Energy Lett.*, 2018, **3**.

271. Monshi, A.;Foroughi, M. R. and Monshi, M. R.,*Modified Scherrer equation to estimate more accurately nano-crystallite size using XRD*, WJNSE, 2012, **2**, 154-160.
272. Hasier, J.;Riolo, M. A. and Nash, P.,*Curie temperature determination via thermogravimetric and continuous wavelet transformation analysis*, EPJ Tech Instrum, 2017, **4**, 5.
273. Watts, J. F., *An introduction to surface analysis by XPS and AES*, Chichester, West Sussex, England, New York, NY : J. Wiley ,2003
274. Mu, B. and Walton, K. S.,*Thermal Analysis and Heat Capacity Study of Metal–Organic Frameworks*, J. Phys. Chem. C, 2011, **115**, 22748–22754.
275. Bhardwaj, S. K.;Bhardwaj, N.;Kaur, R.;Mehta, J.;Sharma, A. L.;Kim, K.-H. and Deep, A.,*An overview of different strategies to introduce conductivity in metal–organic frameworks and miscellaneous applications thereof*, J. Mater. Chem. A, 2018, **6**, 14992-15009.